Numerical modelling of performance and failure criteria for surfacing seals

by

Johan Andries Kritzinger Gerber

Dissertation presented for the degree of Doctor of Philosophy in the faculty of Civil Engineering at the University of Stellenbosch

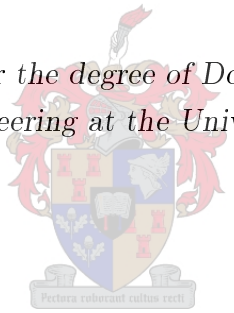

Department of Civil Engineering,
University of Stellenbosch,
Private Bag X1, Matieland 7602, South Africa.

Promoter: Prof. K.J. Jenkins

March 2016

Declaration

By submitting this dissertation electronically, I declare that the entirety of the work contained therein is my own, original work, that I am the sole author thereof (save to the extent explicitly otherwise stated), that reproduction and publication thereof by Stellenbosch University will not infringe any third party rights and that I have not previously in its entirety or in part submitted it for obtaining any qualification.

Signature: .....
J.A.K. Gerber

Date: 05 January 2016 .....

Abstract

Numerical modelling of performance and failure criteria for surfacing seals

J.A.K. Gerber

Department of Civil Engineering,
University of Stellenbosch,
Private Bag X1, Matieland 7602, South Africa.

Dissertation: PhD

March 2016

Finite element modelling of complex structures such as bituminous surfacing seals has become a viable practice to obtain insight into the structure's response behaviour. These responses are difficult, if not impossible to measure in the field and are used to explain seal failure mechanisms. The three major failure mechanisms include: surface ravelling, surface cracking and surface texture loss. Surface cracking and ravelling contributes to surface deterioration which manifests permeability, allowing vertical moisture ingress into the underlying pavement structure. Moisture ingress has a detrimental effect on the pavement surface resulting in potholing, while surface texture loss reduces skid resistance in wet conditions. Since existing damage models are outdated and largely empirical, finite element modelling of seals can be used in the development of improved damage models for seals. Conducting finite element simulations on single, double and cape seals, established the groundwork from which a seal response model was developed for each seal type and failure mechanism. Applying laboratory developed damage functions to the response model, quantified each response type in terms of load repetitions to failure which was validated with empirical and field data. The outcome of this study is a verified primary seal response model that is capable of providing a failure response, based on actual seal design variables. The primary seal response model provides information to improve existing deterioration models for seals, such as the Highway Development and Management (HDM-4) models. It further facilitates the selection of the most appropriate seal for specific environmental and traffic conditions.

Uittreksel

Numeriese modellering van vertoongedrag en falingsmaatstawwe vir plaveiselseëls

J.A.K. Gerber

Departement Siviele Ingenieurswese,
Universiteit van Stellenbosch,
Privaatsak X1, Matieland 7602, Suid Afrika.

Proefskrif: PhD

Maart 2016

Eindige-element modellering van ingewikkelde strukture soos bitumenplaveiselseëls is 'n bruikbare metode vir waarnemings en insig van die struktuur se vertoongedrag. Hierdie vertoongedrag is moeilik, al dan nie onmoontlik om in die veld te meet en word gebruik om die seël se falingsmeganismes te verduidelik. Die drie hoof falingsmeganismes sluit in: klipverlies, ryoppervlak-krake en tekstuurverlies van die ryoppervlak. Ryoppervlak-krake en klipverlies dra by tot ryoppervlak agteruitgang, wat lui tot vog deurlaatbaarheid en vog indringing op die kroonlaag. Vog indringing het 'n nadelige effek op die ryoppervlak en lui tot die vorming van slaggate, terwyl ryoppervlak tekstuurverlies die glyweerstand verlaag in nat toestande. Omdat bestaande skade modelle verouderd en hoofsaaklik empiries is, kan eindige-element modellering van seëls gebruik word in die ontwikkeling en verbetering van skade modelle vir seëls. Eindige–element simulasies van enkel, dubbel en kaapse-seëls het die grondslag gevorm waarvan 'n seël vertoongedragsmodel ontwikkel is vir elke seël tipe en falingsmeganisme. Toepassing van laboratorium ontwikkelde oordragfunksies op die vertoongedragsmodel, het gelui tot kwantifisering van elke vertoongedragstipe na lasherhalings tot faling en is bekragtig met veld en empiriese data. Die uiteinde van hierdie studie 'n is verifieerde primêre seël vertoongedragsmodel wat seël vertoongedrag verskaf, gebaseer op werklike seëlontwerp veranderlikes. Die primêre seël vertoongedragsmodel verskaf inligting wat gebruik kan word om verbeteringe mee te bring aan bestaande seël agteruitgangsmodelle, soos die Highway Development and

Management (HDM-4) modelle. Dit vergemak ook die besluitnemingsproses van die mees toepaslike seël vir ‘n spesifieke klimaatstreek en verkeerstoestande.

Contents

List of Figures

List of Tables

Nomenclature

Abbreviations

ALD	Average Least Dimension
BBS	Bitumen Bond Strength
BPT	Ball Penetration Test
CBR	California Bearing Ratio
CDM	Continuum Damage Mechanics
CFD	Computational Fluid Dynamics
CSIR	Council for Scientific and Industrial Research
CSRA	Committee of State Road Authorities
DEM	Discrete Element Method
DSR	Dynamic Shear Rheometer
DV	Dependent Variable
E80	Equivalent 80 kN Dual Wheel Axle
ELT	Effective Layer Thickness
ELV	Equivalent Light Vehicles
ETC	Environmental Test Chamber
FACT	Fines Aggregate Crushing Value
FE	Finite Element
FEM	Finite Element Method
FWD	Falling Weight Deflectometer

G-R	Glover-Rowe Parameter
GUI	Graphical User Interface
HDM-4	Highway Development and Management Manual
HU	Hounsfield Unit
HV	Heavy Vehicle
HVS	Heavy Vehicle Simulator
ICA	Time to Initiation of Structural Cracking
IRV	Time to Initiation of Ravelling
ITS	Indirect Tensile Strength
IV	Independent Variable
LV	Light Vehicle
LVDT	Linear Variable Displacement Transducer
LVE	Linear Viscoelsatic
MTS	Material Testing Machine
OMC	Optimum Moisture Content
PAC	Porous Asphalt Concrete
PAV	Pressure Aging Vessel
PSRM	Primary Seal Response Model
RBPT	Repeated Ball Penetration Tests
RMSE	Root Mean Square Error
ROC	Radius of Curvature
RTD	Retained Texture Depth
SANRAL	South African National Road Agency SOC LTD
SARDS	South African Roads Design System
SBR	Styrene-Butadiene-Rubber

SBS	Styrene-Butadiene-Styrene
SHRP	Strategic Highway Research Program
SIM	Stress In Motion
SN	AASHTO Structural Number
SNP	Adjusted Structural Number
TETs	Tetrahedral Elements
TiP	Tyre Inflation Pressure
TRH3	Technical Recommendations for Highways Manual 3
UCS	Unconfined Compressive Strength

Symbols

α_i	Prony Series: Stiffness Reduction of the i^{th} Maxwell Element
ν	Prony Series: Poisson's Ratio
τ	Fatigue Transfer Function: Shear stress
τ_i	Prony Series: Relaxation Rate of the i^{th} Maxwell Element
$a,\ b$	Fatigue Transfer Function: Model parameter
E^*	Complex Elastic Modulus
E_∞	Prony Series: Relaxation Modulus
F_r	Tyre Dynamics: Rolling Resistance Force
F_x	Tyre Dynamics: Longitudinal Traction Force
F_y	Tyre Dynamics: Transverse Traction Force
F_z	Tyre Dynamics: Vertical (Normal) Contact Force
F_{fric}	Tyre Dynamics: Tyre-Rubber Friction Force
G^*	Complex Shear Modulus
K_n	Adhesive Zone: Normal Stiffness Response Parameter

K_s	Adhesive Zone: Shear Stiffness Response Parameter
N_f	Fatigue Transfer Function: Repetitions to failure initiation
P	Tyre Dynamics: Texture Dependent Vertical Contact Stress

1. Introduction

"The first rule of business; protect your investment" (Etiquette of the Banker, 1775). Infrastructure investment is big business and with an estimated South African road network stretching a distance of 750 000 km, it needs a significant amount of protection (Kannemeyer, 2014). Since a road is constructed in layers of different materials, protection comes in the form of a durable final layer such concrete, asphalt or bituminous seals. These roads are known as *paved* roads and make up just over a fifth of the total road network. Putting that into perspective, South Africa has a paved road network that can wrap four times around the earth.

The total road replacement cost is roughly two trillion rand, with new construction ranging from $R5\ 000\ 000$ to $R10\ 000\ 000$ [1] per kilometre. Maintaining existing paved roads comes at a much cheaper price than reconstructing it, since resealing i.e. constructing only a new protective bituminous seal layer, costs between $R500\ 000$ and $R1\ 000\ 000$ per kilometre (Kannemeyer, 2014). Seals are therefore a fundamental aspect of the South African National Road Agency's (SANRAL) asset management strategy in providing a good level of service for all road users, which promotes social and economic well-being.

The level of service is determined by the pavements service life which is governed by its relations to various distress types. Distress affects a pavement's ability to fulfil its functional and structural requirements. The main functions of a bituminous seal are to: provide a waterproof cover to the underlying pavement; provide a safe all-weather, dust-free riding surface for traffic with adequate skid resistance; protect the underlying layer from the abrasive and destructive forces of traffic and the environment (TRH3, 2007).

For decades have practitioners observed distress phenomena on surfacing seals. Only in more recent years have researches decided to develop numerical models of seals in an attempt to obtain insights into the mechanisms of distress. These mechanisms serve as the basis for improvements to an outdated and largely empirical seal deterioration model (Theyse, 2008). Merging recent mechanistic developments with existing empirical seal deterioration ideology, advances the science of seal design from a pure

[1] The USD/ZAR exchange rate at time of publication was \$1.00 = R12.50

empirical approach to a mechanistic-empirical method. The latter is a gradual process and evolves as the mechanistic component is being developed. Therefore, the following section presents background information on the development of numerical seal models.

1.1 Background information

Seals fail via a variety of distress mechanisms with the more prominent cases being: surface cracking, surface ravelling and surface texture loss. Practitioners utilises surfacing deterioration models in scheduling timely surface maintenance. Research on defining and improving these models is encumbered by the problems associated with constructing realistic seals in the laboratory (Henderson *et al.*, 2006). A large number of variables are included such as the binder application rate, nozzle spraying characteristics and temperature, aggregate grading and spread, base characteristics etc. An alternative approach is therefore explored in this section.

1.1.1 The need for numerical seal modelling

Producing several full scale seal test samples in the laboratory is an expensive and time consuming exercise and becomes impractical if several variables are to be examined (Henderson *et al.*, 2006). An alternative approach is to construct numerical models of the various seal sections. Such models would provide information on the stress and strain conditions within the seal layer which can be utilised in the prediction of seal deterioration and failure.

A numerical seal model, in simple terms, is the transformation of a physical seal structure into a virtual seal structure. By applying a numerical time-stepping procedure; it is possible to obtain the model's behaviour over time. The virtual seal structure is basically a system of mathematical equations of which the finite element method (FEM) is one of the earlier developments.

The Highway Development and Management Models (HDM-4) make provision for empirical surface deterioration models which includes: Surface crack initiation and progression, surface ravelling initiation and progression, potholing initiation and progression and surface texture loss development (Theyse, 2008). However, caution should be exercised when applying these models, since the material and empirical model parameters of the HDM-4 need to be calibrated and adjusted for South African conditions. Since full scale testing is impractical, finite element (FE) seal models can be used to calibrate or improve the existing HDM-4 surfacing deterioration models.

1.1.2 Early developments in seal modelling

FE modelling of bituminous seals was in many ways pioneered by Milne (2004) in collaboration with Delft University of Technology. Milne realised that obtaining new insight into the stress and displacement dynamics of a seal would require a model consisting of individual components on a micro scale. A joint effort was therefore embarked on by Huurman *et al.* (2003) in developing algorithms that can generate a FE model of individual aggregates in a surrounding bitumen layer.
The result was a single layer of spherical aggregates packed in a hexagonal structure surrounded by bitumen, resembling a thin open graded asphalt-like structure. The model, not only gave insight into the stress and displacement characteristics of the adhesive bond between the aggregates and bitumen, but also indicated the stress magnitudes obtained within the bitumen. This model was termed the *prototype seal surfacing model* and served as a reference for future model developments. Huurman (2010) made improvements to the prototype model which allowed insight into the permanent vertical deformation of the aggregates on the supporting substrate.

1.1.3 Recent developments in seal modelling

Initial models were developed with idealised generated geometries, while a recent shift in developments incline more towards computer tomography as an origin for seal model geometries. Computer tomography is radiography (x-rays) in which a 3D image of a structure is constructed by computer from a series of plane cross-sectional images, thereby, obtaining the original geometry of the scanned specimen.
In a preliminary study to evaluate the potential advantages of a mechanistic seal design method, Henderson *et al.* (2006) developed 2D FE models from scanned seal core samples by selecting representative cross-sectional images of the respected seal cores. Distinct material properties were attributed to the binder, aggregate and substructure. The model results indicated that the maximum Von Mises stess and strain conditions occur in thin bitumen regions immediately adjacent to the seal aggregate. The study postulated that the high stresses obtained in the bitumen films indicate that the behaviour of the bitumen will govern the failure mechanisms of the respected seal.
In another preliminary study, a 3D FE seal model was developed by Kathirgamanathan *et al.* (2012) from a scanned core sample in a quest to explore the stress and strain conditions within that layer. The study resonates with the findings of Henderson *et al.* (2006) and highlights the complexity of simulating a tyre load on the seal surface. Both studies indicated that aggregate to aggregate contact reduced the stress levels observed in the binder component.

1.2 Problem statement

Developments in FE seal modelling contributes in the attempt to describe and quantify surface distress mechanisms of seals which is very difficult, if not currently impossible to measure in the field. The major surface distress phenomena that affect the functional requirements of a seal are surface ravelling, surface cracking and surface texture loss.

1.2.1 Surface ravelling

Surface ravelling is an event where the seal aggregate dislodges from the surface when subject to traffic. This is also loosely defined as stripping or stone loss. The mechanism at work is a development of stress within the binder-aggregate adhesive bond. This bond is broken in one of two ways: either instantly, with a force greater than the bond strength or over time, due to bond fatigue. Although some of the previous FE seal models are able to give insight into the magnitude of the adhesive-bond stress, no quantification in terms failure time for seals has been reported.

1.2.2 Surface cracking

The formation of cracks on the seal surface is divided into two categories: reflective cracking and fatigue cracking. Reflective cracking is the crack progression to the surface, emanating in the substrate. It is therefore not a surface distress phenomenon, rather a base distress problem and is not further discussed in this study. Fatigue cracking however, is the damage and disintegration of the bitumen continuum when subject to repetitive mechanical and environmental loading. This phenomenon, also known as cohesive fatigue cracking, is detrimental to the functional requirements of a seal, since cracks allow the seepage of surface water into the substrate. Similar to the surface ravelling phenomenon, previous seal models are able to give insight into the magnitude of binder stresses, but provide no quantification in terms of fatigue life.

1.2.3 Surface texture loss

Surface texture loss of a seal is a functional consideration based on the reduction in the adequate skid resistance provided in wet conditions. The mechanism at work is fourfold and consists of aggregate orientation, aggregate embedment, aggregate wear and binder rise. No current seal model can account for the entire surface texture loss process, but Huurman's (2010) improvements to the prototype model did provide initial embedment growth quantities.

This study acknowledges the difficulty in developing and constructing FE seal models in which ever manner. Presently, the output of these FE models serve merely as a rating tool, where stress and strain results are compared against a reference result. The real challenge is the conversion of the distress mechanism outputs i.e. the stress and strain into verifiable time estimates of failure. Achieving this advances the feasibility of a mechanistic component which can be used to address the inadequacies of empirical deterioration models for seals.

1.3 Research scope

This research study forms part of a greater seal research project, Project PB/2006/D-1 (Milne, 2010), which in turn is one of many building blocks in the improved South African Roads Design System (SARDS). The seal research project includes three parallel study mandates: Improved response and damage characterisation of bituminous materials; Numerical modelling of bituminous surfacing seals; Empirical data analysis on the performance of bituminous surfacing seals.
The mandates are entwined and complement each other in attaining the outcome of the seal building block. This study is the second mandate, where aspects of the first and third mandate contribute in achieving the research objectives of this study.

1.3.1 Research hypothesis

Current seal designs are based on empirical approaches that have proven to work well in the past. The advent of modified binders, increased traffic volumes and a desire of practitioners to seal during cold, previously embargoed periods, resulted in a disconnect between the old proven empirical seal approach and current demands. It is the hypothesis of this study that seals can be modelled with numerical methods to reflect reality, thereby bridging the disconnect and advancing seal design by improving deterioration models to meet current industry demands.

1.3.2 Research objectives

Motivated by the discussion on the research hypothesis, four objectives are set out for this study. Each objective is numbered and discussed as follows:

Objective 1

Develop a system of algorithms that is capable of generating the architecture for a numerical seal model analysis. The architecture must be able to differentiate between single, double and cape seal structures. Each structure should have user

adaptable input parameters for the seal geometry, material characteristics and load case properties.

Objective 2

Simulate each seal type for a predefined list of variables and obtain adhesive, cohesive and embedment response parameters. Quantify the model responses in terms of time to failure and validate the quantification. Modify embedment to represent surface texture loss.

Objective 3

Develop a conceptual approach to quantify aggregate embedment.

Objective 4

Identify the critical response parameters and develop the primary seal response model (PSRM). This model, in turn, is implementable in the SARDS recursive performance simulation.

1.3.3 Research delineations

With the exception of Objective 3, no other laboratory or field testing will be conducted in this study. All the bituminous material characteristics would be obtained from research study one (mandate one). In the unfortunate case where mandate one fails to provide vital bituminous characteristics, alternative characteristics would be obtained from literature. All the non-essential material characteristics would also be obtained from literature.

This study is not responsible for the collection and analysis of field data, although this study requires field data for validation and verification purposes. Only field and empirical data obtained in research study three (mandate three) will be utilised in the validation and verification processes of this study.

The numerical seal model development is limited to the three structures as stipulated in Objective 1, with the intention to provide three types of response parameters. These parameters include adhesive, cohesive and embedment response types. Variations of these models with reference to geometry, material type and load cases are limited and a detail discussion follows in Section 3.3.

The number of simulation per seal type will also be contained to a factorial approach from a predefined matrix of variables. This study will therefore not simulate all the possible combinations of seal variables, since time is also a constrain. The establish-

ment where this study is conducted allow a three to five year study period. Thesis submission must occur within that time frame.

1.3.4 Research significance

The significance of this study can be divided into its theoretical and practical contribution to bituminous seal science. When considering the theoretical aspects, it is worth mentioning that this is the first study which will develop FE seal model of the single, double and cape seals. Previous studies have focussed on modelling only the single seal, therefore in this study direct comparisons between the three will be possible. Model responses will also be quantified in terms of time to failure for the various modes of failure. Other theoretical aspects such as design assumptions will be addressed. Typical assumptions are a 40:1 equivalent damage factor for light vehicles in comparison to heavy vehicles and a notion that 50% of embedment occurs during seal construction.
The practical contribution of this study would be the finalisation of Objective 4. The PSRM can be described as a model of models and is the summation of the FE seal modelling process translated into a response model. Theoretical as it may sound, the practical implication is its contribution to the seal building block of SARDS as discussed in the research scope.

1.4 Dissertation outline

This dissertation consists of eleven chapters. This section presents a brief discussion on the dissertation outline and concludes this chapter with a flow diagram thereof (Figure 1.1).

Chapter 1: Introduction

This chapter introduces the topic of investigation; numerical modelling of surfacing seals and presents background information on the developments of numerical seal modelling. This chapter further outlines the study objectives, major limitations and significance of the research.

Chapter 2: Literature review

The literature review presents and discusses subject areas related to numerical modelling of seals. Subject areas include: road seal theory, tyre contact stress and the modelling of surface layers.

Chapter 3: Methodology

This chapter presents the research approach and explains the methodology with which the objectives will be achieved. There is also a detailed discussion on the research limitations.

Chapter 4: Binder characterisation

This chapter presents and illustrates the results of the binder testing program as pertaining to this study and identified in mandate one. Binder and bituminous material characterisation do not form part of this study, but the characteristics are required by this study to attain the objectives as discussed in Section 1.3.2.

Chapter 5: Embedment characterisation

A conceptual embedment model emanating from FE modelling and laboratory testing is presented and discussed in this chapter. The model is used in the quantification process of surface texture loss.

Chapter 6: Field data analyses

Field data analyses required in the verification and validation processes of the FE seal model results are presented in this chapter. These analyses form part of mandate three and thus, do not form part of this study, but are required by this study to attain the objectives as discussed in Section 1.3.2.

Chapter 7: Single seal analysis

The single seal analysis presents the model response characteristics and quantified damage characteristics for adhesive, cohesive and embedment failure.

Chapter 8: Double seal analysis

The double seal analysis presents the model response characteristics and quantified damage characteristics for adhesive, cohesive and embedment failure.

Chapter 9: Cape seal analysis

The cape seal analysis presents the model response characteristics and quantified damage characteristics for adhesive, cohesive and embedment failure.

Chapter 10: Comparative analysis

This chapter compares the results of the single, double and cape seal analyses with reference to the three failure mechanisms. Developments on the PSRM are also presented in this chapter.

Chapter 11: Conclusions and recommendations

This chapter summarises the major findings with reference to the research objectives and presents recommendations which may lead to even more findings in future work.

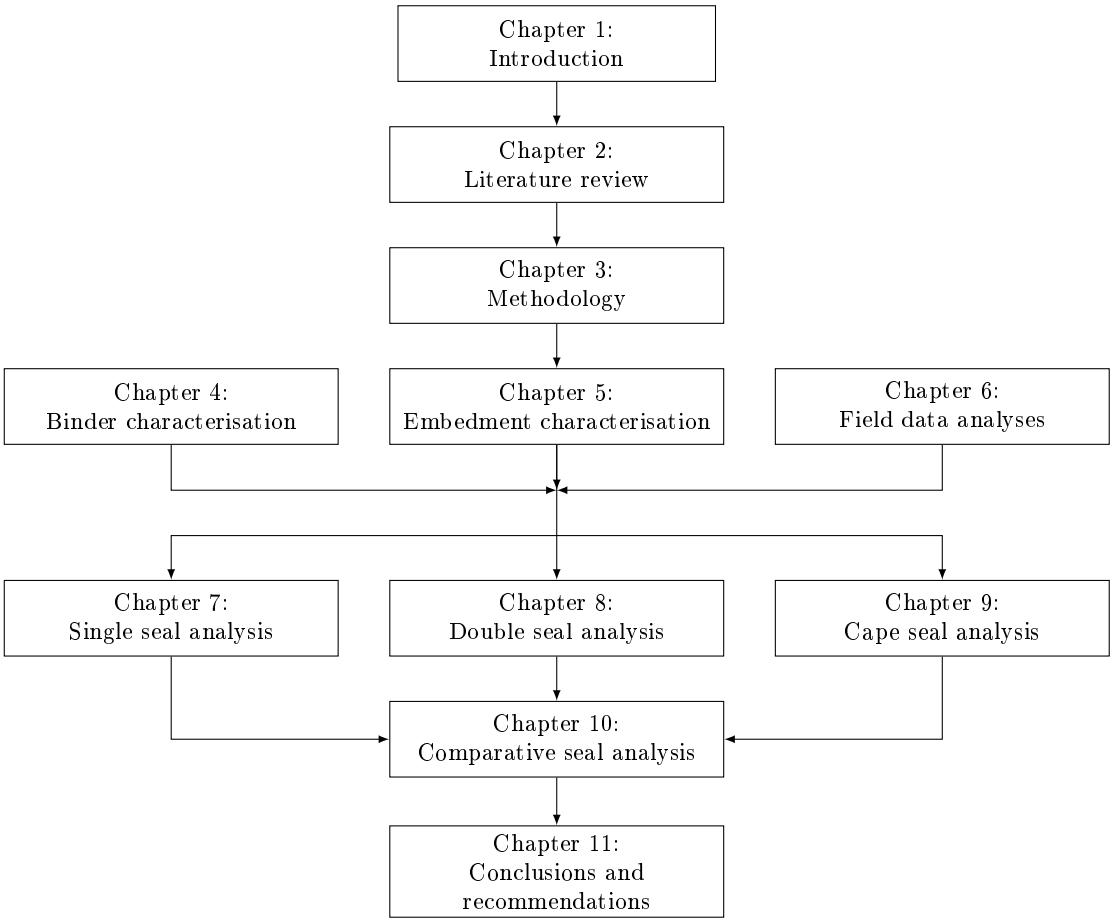

Figure 1.1: Chapter description and layout of this study.

2. Literature review

Literature relevant to multi-scale modelling of surfacing seals is presented in this chapter. The components of seal modelling are of interest, therefore a basic overview of seal design principles are discussed, followed by insights into the dynamics of pneumatic tyre loads. Thereafter, the crux of this literature review is presented with discussions on numerical modelling of seals and inadequacies of current empirical seal deterioration models. This chapter concludes with a brief summary of the works presented.

2.1 Bituminous seal theory

Surfacing seals are a cost-effective technique in constructing a surface layer that fulfils the requirements with regard to traffic accommodation and climatic conditions. This section highlights the basic design principles, discusses the construction materials and provides insight into the failure mechanisms of seals.

2.1.1 Design principles

Seals are cover layers constructed on roads to perform two main functions. Firstly, a seal serves as protection for sub-layers against water ingress and the abrasive effects of traffic and environmental forces. Secondly, it provides road users with durable skid resistance in all-weather conditions. Seals can be constructed on newly build roads or on existing roads. The latter process is referred to as resealing. Seal construction in its simplest form consists of a bitumen coat, sprayed on top of a base course, covered with single sized aggregates (TRH3, 2007). This type of structure conforms to a single seal.

There are different kinds of seal structures. Common structures are: single seals, double seals, cape seals, slurry seals and sand seals. According the seal design guide, Technical Recommendations for Highways Manual 3 (TRH3), lesser constructed structures include: geotextile seals, split seals, chocked seals, inverted double seals and graded aggregate seals. The various structures are depicted in Figure 2.1.

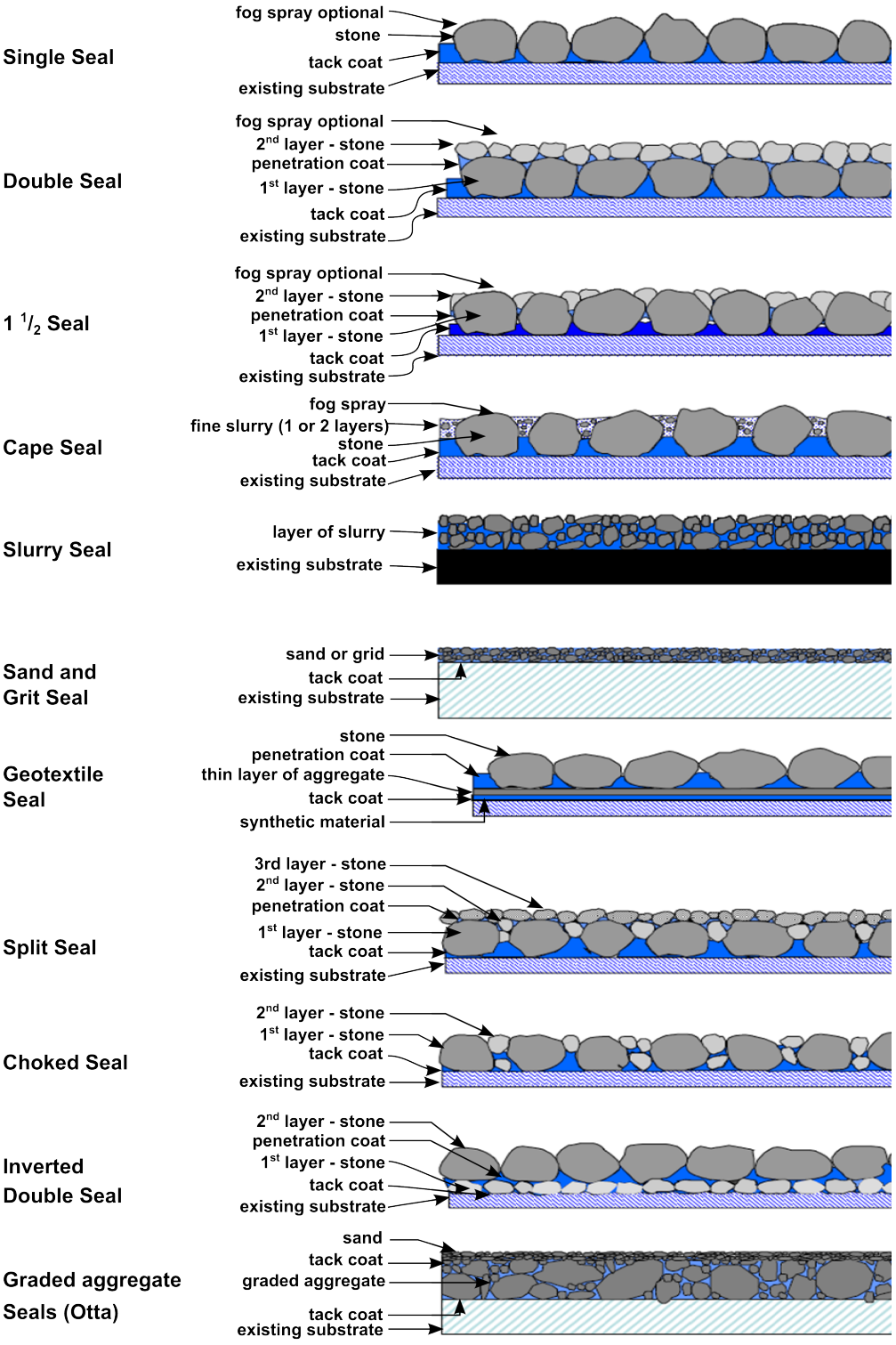

Figure 2.1: Schematic illustration of seal structures (TRH3, 2007).

Seal construction in South Africa evolved from Hanson's (1934) original volumetric approach of partially filling the voids obtained in the aggregate layer. His method in the 1930's singled out the average least dimension (ALD) of the seal aggregate as a fundamental design parameter. Hanson utilised the ALD in determining the volume of the aggregate cover, associated air voids and related bitumen application rate (Milne, 2004). Regional road authorities in South Africa practised variations of this method. Variations were due to climatic conditions, bitumen binder sources and disagreement on the ideal aggregate packing matrices. The committee of state road authorities (CSRA) accommodated these variations within the volumetric design approach producing the TRH3 (2007), a guideline for designing and constructing surfacing seals in South Africa. The TRH3 is routinely updated and specifies the following basic design principles:

a) Minimum voids to be filled with binder to prevent stone loss in the case of no embedment is 42% for single seals and 55% for double seals. (Wetting 30% of the aggregate height requires approximately 42% of the voids to be filled. See Figure 2.2).

b) Amount of stone wear due to traffic depends on the stone hardness and traffic volume. An assumption is made that the hardness is not less than 210 kN at 10% of the fines aggregate crushing value (FACT).

c) Required minimum surface texture depth to provide adequate skid resistance is 0.7 mm. Design charts make provision for texture depths of 0.3 mm, 0.5 mm, 0.7 mm and 1.0 mm.

d) Embedment during construction is estimated at 50% of service life embedment. Total potential embedment is determined from the corrected ball-penetration test (SANS-3001-BT10:2013, 2013).

e) Effective layer thickness (ELT) of a single seal is a function of the ALD. $ELT = 0.85679 \times ALD + 0.46715\ mm$.

f) ELT of a double seal is a function of the ALD sum for the two aggregate layers. $ELT_d = 0.86028 \times ELT1 + ELT2 + 0.1988\ mm$.

g) Estimated voids of a single seal (%) $= 45.3333 - 0.333 \times ELT$.

h) Estimated voids of a double seal (%) $= 63.01263 - 0.04743 \times {ELT_d}^2 - 2.41172 \times ELT_d$.

The design principles combined practical experience with theory, resulting in a design process that is adaptable depending on the climatic region and availability of construction materials.

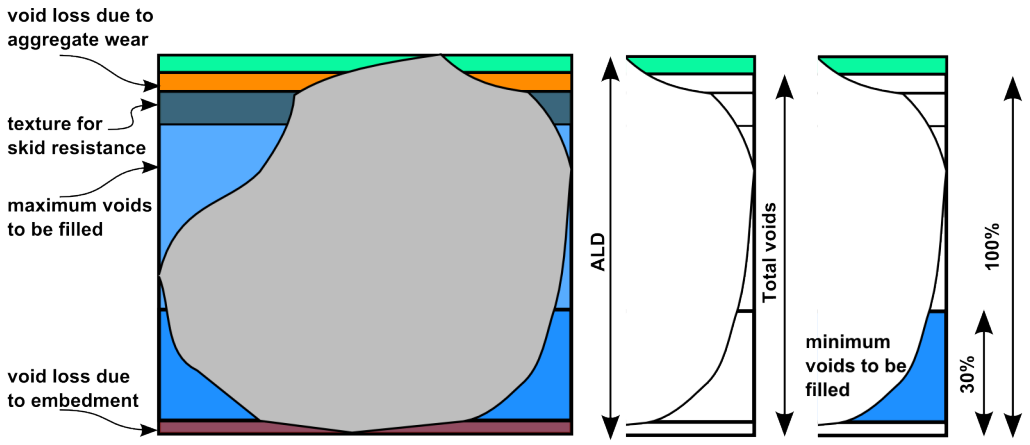

Figure 2.2: Principles of design for binder application rates (TRH3, 2007).

2.1.2 Construction materials

The primary materials used in seal construction are crushed aggregates and bitumen binder. The aggregates protect the underlying structure from the abrasive forces of traffic, thus it needs to comply with certain hardness specifications. The bitumen binder holds the aggregate in place an is waterproofing the substructure. Binder properties should comply with the required performance range of the region in which the seal is constructed.

Aggregates

Single size aggregate fractions are mainly used in seal construction. In practice the term, *nominal size*, is widely used. The nominal size pertains to the sieve size of the passing fraction. Four nominal sizes are used in South Africa: 19 mm, 13.2 mm, 9.5 mm and 6.7 mm. Components defining the shape of the aggregate are the nominal size, ALD and the flakiness index. The flakiness index indicates the measure of aggregate elongation. Although round, smooth (not crushed) aggregates can be used in seal construction as indicated by Thomas *et al.* (2006), the South African industry makes use of crushed aggregates. Fractured surfaces result in better aggregate interlock and bitumen bond strength than smooth surfaces (Paige-Green *et al.*, 2009). Cubical shapes are preferred over flaky aggregates. The latter is more susceptible to bleeding and stone loss.

Some aggregates are harder than others, yet all considered aggregates must comply with industry standards of 10% FACT at 210 kN. This standard ensures that aggregates can withstand the construction process and wear due to traffic within excepted tolerances. Scholars (Paige-Green *et al.*, 2009; Thothela *et al.*, 2011) queried the rigid enforcement of this standard, indicating that useful local material is being

disregarded. As a result relaxed aggregate specifications for low volume roads were included in the TRH3 (2007).

Seal aggregates can be categorised by the state of their hydrophilicity and acidity. Hydrophilic aggregates have an electro-negative charge. Aggregates that are hydrophilic includes: silica, quarts and sandstone. Hydrophobic aggregates have an electro-positive charge. Aggregates that are hydrophobic includes: limestone, dolomite, basalt and calcareous rocks (Milne, 2004). Rocks are acid if the acidic components (SiO_2 *and* CO_2) exceed 50% of their chemical mass composition. Crushed basic and acid crystalline rocks as well as high silica and diamictites are used as surfacing aggregates in Southern Africa (SAPEM, 2014; Paige-Green *et al.*, 2009). In cases such as granite (acid crystalline) and quartzite (high silica), caution should be exercised if the aggregates exhibit a glassy texture. This may cause bitumen adhesion problems.

Adhesion of binder to aggregate is influenced by: moisture, dust, porosity, mineralogy, acidity and surface tension. Dust adversely affects the adhesion of binder to aggregate. Moist aggregates do not adhere properly to binders with the exception of emulsions. Weak adhesion results in aggregate loss when the road is opened for traffic. Acidic rocks such as quartzites are known to have poor adhesion. Precoating these materials increase the adhesion bond and prevent the problems encountered with dust, moisture and acidity. Porous aggregate absorbs the lighter fraction of the binder. As a result the binder becomes to brittle and unable to bind the seal on the road and stone loss occurs. Precoating porous aggregate reduces the binder absorption and it is recommended to use modified binders instead of conventional binders for the tack coat (TRH3, 2007).

Binders

Bitumen is a viscous material that occurs naturally or as a by-product during the crude oil refinement process. Bitumen is used to bind the seal aggregates to one another and to the underlying base, therefore termed *bitumen-binder* or *binder*. Binders are divided into two categories. The first category is conventional binders. These binders obtain its chemical and compositional properties from the crude oil refinement process. The second category is modified binders. These are binders of which the chemical compositions are altered after the refinement process by adding polymers or modifiers.

Modified binders are subdivided into two compositional groups of which the first is homogeneous binders and the second non-homogeneous binders. Homogeneous binders are defined as a blend of polymer and bitumen where two distinct phases cannot be detected (TG1, 2007). Non-homogeneous binders are defined as a blend

of modifier and bitumen where there are two distinctly detectable phases in the final product (TG1, 2007). The phases refer to the material phases of the polymer or modifier and bitumen. The physical properties of binders are controlled by the fundamental properties related to viscosity, temperature and phase transition (TG1, 2007). Binders are modified to improve bonding properties, resistance to aging, binder resilience and reduce temperature susceptibility (Milne, 2004). Exposure to ultraviolet light and subsequent evaporation of the volatiles, cause the binder to harden and become brittle over time. This is known as binder hardening or aging.
Conventional binders that are widely used in seal construction are: penetration grade binders, cut-back binders and emulsions. Similarly modified binders include: Styrene-Butadiene-Styrene (SBS) binders, Styrene-Butadiene-Rubber (SBR) binders, bitumen rubber and modified emulsions. SBS and SBR are homegenous binders, while bitumen rubber is a non-homogeneous binder.
Proper bonding of the seal aggregate can comprise of multiple binder applications. These applications consist of: prime coats, tack coats, penetration coats, slurries, fog sprays and in some cases aggregate precoats. On a newly constructed base, prime coats are applied, preparing the base for the seal layer. These coats are not essential but promote the adhesion between the base and the seal (TRH3, 2007). Prime coats also provide the base with temporary protection against construction traffic and adverse weather effects. Prime coats can consist of cutback binders or emulsions. A tack coat is the thin layer of binder that holds the seal stone on the underlying structure. Conventional and modified binders are used for tack coats. In the case of a double seal where multiple aggregate layers are used, a penetration coat is introduced between the first and second aggregate applications to bind the layers. In most cases the penetration coat will be the same binder as the tack coat, but in some instances it may differ.
A fog spray is a diluted emulsion sprayed on top of a newly constructed seal, providing *shoulder* bonds (Figure 2.4) and reducing the risk of aggregate loss. Cationic emulsions are electro positive while anionic emulsions are electro negative. Cationic emulsion are generally preferred for sprayed seal applications and anionic emulsions are largely used in slurry seals (van Zyl *et al.*, 2012). Slurry is a mixture of graded aggregates, emulsion, active filler and water. In the case of a cape seal the slurry paste is worked into the voids that exist between the aggregates.
Aggregate precoats consist of low viscosity bitumen containing cutters and a chemical adhesion agent. The purpose of the precoat is to improve the adhesion of the aggregate to the binder (SAPEM, 2014). Weak bonds lead to stone loss under traffic which is one of three major failure mechanisms in seal design philosophy.

2.1.3 Failure mechanisms

Failure mechanisms define the underlying cause of failure by isolating the components responsible for the defect in the functionality of the seal. These mechanisms are adhesive failure, cohesive failure and embedment as illustrated in Figure 2.3.

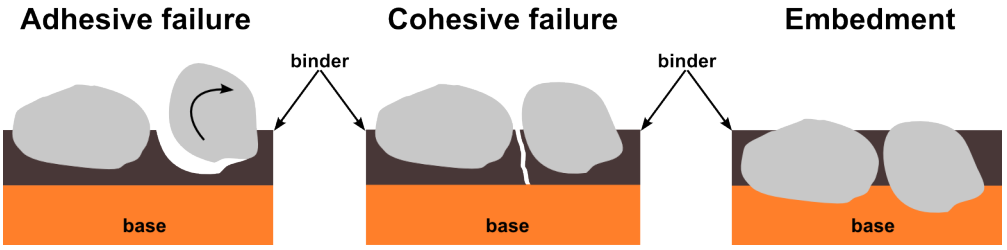

Figure 2.3: Seal failure mechanisms.

Adhesive failure

Adhesion refers to the bond at the binder-aggregate interface. This bond is the component responsible for adhesive failure. Weak bonds are due to faulty binders, too low binder application rates, cold temperatures and excessive delay in aggregate placing (TRH3, 2007). The sensitivity of this bond depends on the aggregate size, aggregate spread and the position of the binders. A single seal with an open spread and minimum binder application is highly sensitive in comparison to the same seal with a close or interlocked spread. Even less sensitive is the same interlocked single seal with a fog spray on top. The fog spray creates a shoulder bond that contributes to the adhesive bond.

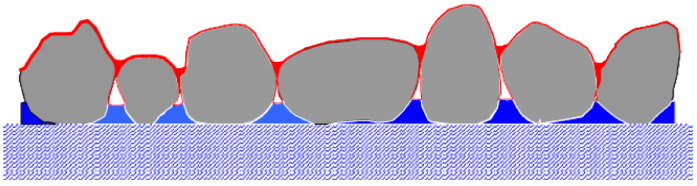

Figure 2.4: Shoulder bond created by fog spray application (TRH3, 2007).

Separation of this bond in the presence of water is known as stripping. According to Bagampadde (2005), stripping is influenced by aggregate surface characteristics like chemical stability, pore size distribution, polarity and surface energy. Stripping is thus chemical of nature and leads to stone loss under traffic. Mo (2010) indicates that although non mechanical effects such as moisture, aging, chemical differences etc. may enhance the development of ravelling, ravelling remains directly related to

fatigue damage of the adhesive bond. Ravelling is thus defined as stone loss due to fatigue of the binder-aggregate interface bond when subjected traffic.
In practice stone loss occurs in the period after construction when the road opens for traffic. The adhesive failure mechanism is thus associated with an early service life failure. In exceptional circumstances, ravelling can also occur at an advanced stage of a seal's service life, but this would be unusual.

Cohesive failure

Mo (2010) defines cohesive failure as cracks that initiate within the binder material. Practical experience as documented in the TRH3 (2007), categorises seal cracks as active cracks and passive cracks. Active cracks occur as reflection cracks on the surface and do not originate within the binder material. Passive cracks in the form of crocodile cracks and secondary cracks are due to binder fatigue. These cracks are situated within the binder material while the underlying support structure is still in good condition. Repetitive mechanical loading, binder hardening (aging) and temperature changes are the driving factors behind binder fatigue which results cohesive failure. As bituminous materials oxidise they become harder, less ductile and more prone to cracking. Another factor of fatigue cracking was observed by Rowe *et al.* (2014) whilst conducting low temperature bitumen ductility tests. The development of non-mechanical loading i.e. thermal related cracking was reported. Cohesive failure is therefore associated with mechanical and environmental fatigue cracking and can be described as an end of service life phenomenon.

Embedment

Embedment is probably best explained in the context of surface texture depth loss. Texture loss consists of four phases which occur simultaneously during the service life of the seal. These phases include stone orientation, embedment, binder rise and aggregate wear as illustrated in Figure 2.5.
Stone orientation is the repositioning of the aggregates within the binder in an attempt to come at rest in its ALD. Although most orientation occurs beneath the rollers during proper construction, in some cases this phase continues for a couple of weeks when subject to traffic. When the aggregates orientate the binder height increases which results in texture loss.
Embedment is the process where the seal aggregate permanently deforms the underlying substrate by penetrating into it when subject to load. As the aggregates embed, the relative depth of the binder with respect to aggregate asperities reduces and results in texture loss. In some cases the aggregate penetrates through the tack coat film as it embeds into the base. This phenomenon is known as *punching*.

Binder rise is a phenomenon resulting from the upsurge of existing moisture in the substrate. This upsurge of moisture that in some cases accumulates into a vapour beneath the seal, forces the binder upward, resulting in binder rise and texture loss. This phenomenon occurs particularly in soft and unoxidised binders.

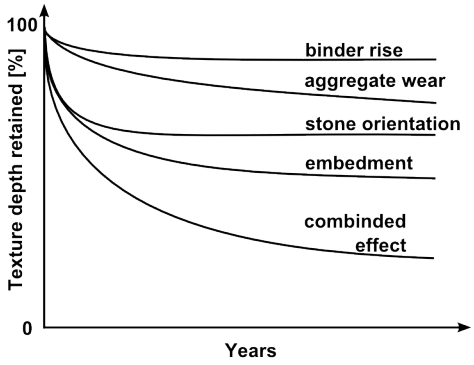

Figure 2.5: Schematic representation of the surface texture loss phases.

Aggregate wear is simply a reduction in the aggregate vertical dimension due to the abrasive effect of traffic, which leads to texture loss. The net effect of the four phases at any given time, results in the total loss of surface texture depth and is a measurable component which constitutes the criteria for embedment failure. The target minimum surface texture required for adequate skid resistance in wet conditions is set to 0.7 *mm* (TRH3, 2007). Thus, the initial surface texture after construction will be greater than the target minimum and gradually reduce towards the design minimum as embedment takes place (van Zyl, 2007). If the surface texture reduces below the design minimum due to embedment it will result in bleeding. Bleeding is the heaving of binder onto the surface due to the diminishing of voids in the seal structure as a result of texture loss, off which embedment is a major contributor.
Surface texture decay is non-linear with time. Woodward *et al.* (2005) indicates that there are three phases of decay:

a) Rapid decay of texture. Mechanisms at work are stone orientation, embedment and abrasion of aggregate asperities until a stable mosaic is formed.

b) Slow decay of texture. Seal structure is stable with gradual loss of macro texture due to embedment.

c) Erratic behaviour where texture continues to decay but at variable rates.

Factors such as seal aggregate size, base support and temperature affect the embedment. Laboratory testing by Woodward *et al.* (2005) indicated that larger seal aggregates have greater percentage of texture loss than smaller aggregates given the

same base and under the same loading conditions. This correlates with the TRH3 (2007) that suggests the construction of an inverted double seal on soft bases which are susceptible to embedment. The smaller stone acts as an *armouring* layer in this particular situation.

Embedment susceptibility can be detected with the Ball Penetration Test. The test was developed in an attempt to quantify the expected embedment and thereby the expected reduction of voids in the seal system (Milne, 2004). The Ball Penetration Test is used extensively in seal construction and consists of a standard Marshall hammer, dropped from a specified height onto a 19 *mm* steel ball. Temperature adjustments are made to the Ball Penetration readings depending on the base type. Base types that include bituminous materials show embedment increase with temperature as was found by Yaacob *et al.* (2007) on soft sand asphalt bases.

Embedment as a failure mechanism is considered to occur within the first phase as described by Woodward *et al.* (2005). Milne (2004) documented that aggregate orientation occurs under the rollers (construction) and that surface texture depths stabilises within a couple of months after construction. Embedment failure is therefore associated with early service life failure.

2.2 Contact stress of pneumatic tyres

The original inventors of the pneumatic tyre were inspired by the concept of riding on a cushion of air to provide riding comfort. As vehicle speeds increased and manoeuvring requirements became more severe, lateral and directional wheel stability attained equal importance to riding comfort (Moore, 1975). Directional wheel stability is largely determined by the tyre-road interface. Therefore, this section explores the dynamics of a rolling wheel, the influences of the tyre-road interface on the tyre-road contact forces and a means of measuring these forces.

2.2.1 Rolling wheel dynamics

For a wheel to roll in a longitudinal (straight line) direction, it requires either a torque or an external force driving the motion. This motion cannot exist without a frictional component at the tyre-road interface. Resulting from friction, longitudinal and transverse traction forces are formed. These forces are related to the corresponding normal force of the wheel.

Normal force

The vertical reaction vector exerted by a tyre load on the road's surface is known as the normal force F_z. The magnitude and position of the normal force mainly

depends on the total weight of the vehicle, the wheel's location with reference to the vehicle's centre of gravity, the slope of the road and the longitudinal acceleration of the vehicle. As the tyre rotates it is subjected to deformation in the contact patch. The tyre material is deflected vertically as it enters the contact patch and bounces back as it exits the contact patch. The energy spent deforming the tyre is not completely recovered as it returns to its original shape, resulting in internal damping (Rajamani, 2011). The loss of energy results in an asymmetric vertical load and is represented by a force on the tyre known as the *rolling resistance* F_r (Figure 2.6). Haney (2003) states that the asymmetry becomes more exaggerated with speed.

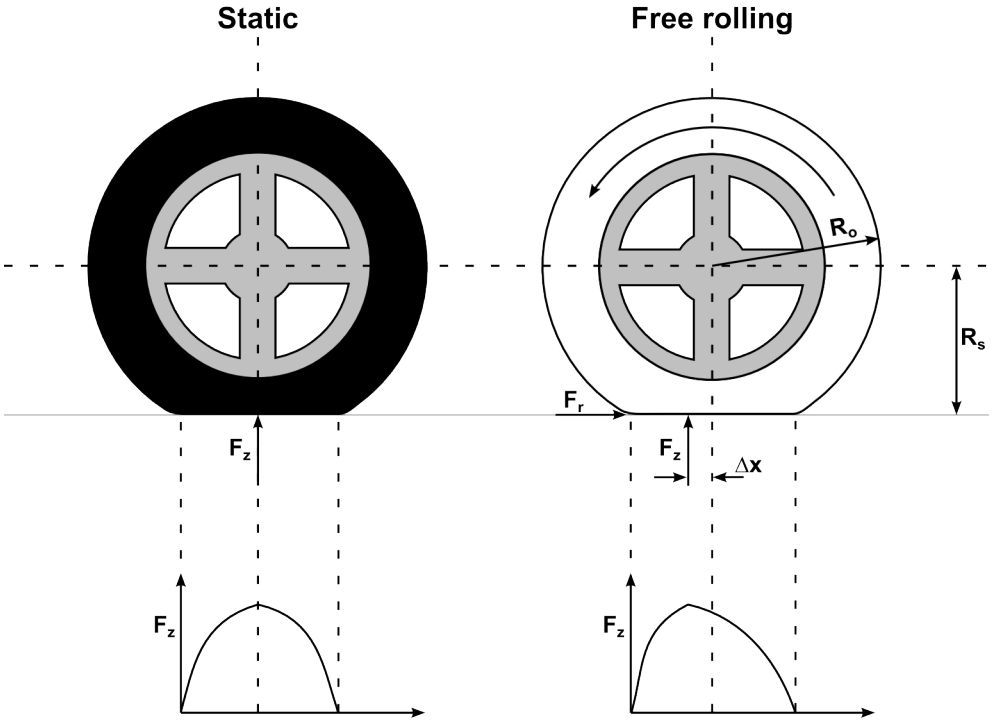

Figure 2.6: Tyre normal force.

Rolling resistance is in the opposite direction to the vehicle's motion an can be calculated with Equation 2.1. The variable Δx is not easily measurable and therefore scholars such as Rajamani (2011) and Moore (1975) indicate that F_r is simply taken as a proportionate of F_z with a constant rolling resistance coefficient f. According to Rajamani (2011) f has a range of 0.01 to 0.04 and has a typical value of 0.015 for passenger vehicles.

$$F_r = \frac{F_z(\Delta x)}{R_s} \tag{2.1}$$

Longitudinal traction force

As the tyre rolls and deflects in the contact patch, a reduction of the undeflected radius R_o results in the formation of traction forces F_x in the longitudinal direction between the tread rubber and the road. Moore (1975) explains the shape of the traction force as follows: Due to the change in radius, an effective radius R_e is selected to calculate the forward velocity V. If ω denotes the angular velocity of the wheel V is calculated with Equation 2.2. It is apparent that $R_s < R_e < R_o$.

$$V = \omega \times R_e \tag{2.2}$$

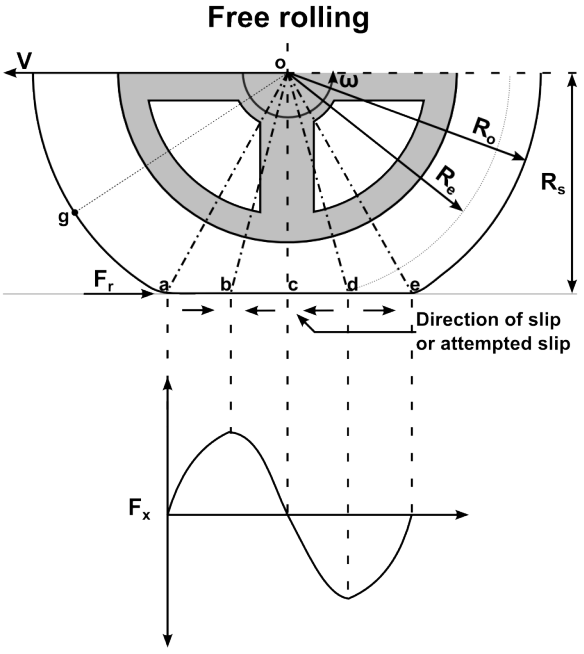

Figure 2.7: Tyre longitudinal traction force.

The tangential velocity of point g on the undeflected tread surface is given by $\omega \times R_o$, relative to the wheel centre o. As g approaches the entry point a of the contact patch, its velocity decreases causing circumferential compression in the tread band, hence the velocity of point a relative to o exceeds the underlying road velocity, $\omega \times R_e$. This causes rearward longitudinal slip or attempted slip in the region a to b (Figure 2.7). Slip is thus defined as the difference in the axle velocity V and the equivalent rotational velocity $\omega \times R$. From b to centre of contact c and to point d (the mirror image of b), the effective rolling radius is marginally less than R_e. This results in a limited amount of forward slip. Within the last quarter of the contact patch from d to

e, the velocity of the tread elements increases resulting in rearward slip or attempted slip.
This slip direction reverses a number of times and is represented by a sinusoidal-like wave form with a positive and a negative peak. Tielking and Roberts (1987) indicated that the slip direction changed again at the exit point of the contact patch, resulting in a second positive peak value. The absolute difference of the peak values is equal to the rolling resistance F_r. De Beer *et al.* (2005) indicate that the longitudinal stress is approximately 12% of the associated vertical stress.

Transverse traction force

Deflection and bending of the tyre side walls during rolling cause inward lateral movement of the tread rubber. The tread rubber assumes an hourglass shape over the distance of the contact patch. The lateral movement results in an outward shear stress distribution over the length and across the width of the contact patch (Figure 2.8). The magnitude of the transverse shear depends on tyre construction, tread rubber, vertical load and inflation pressures. Under inflated tyres and heavy load

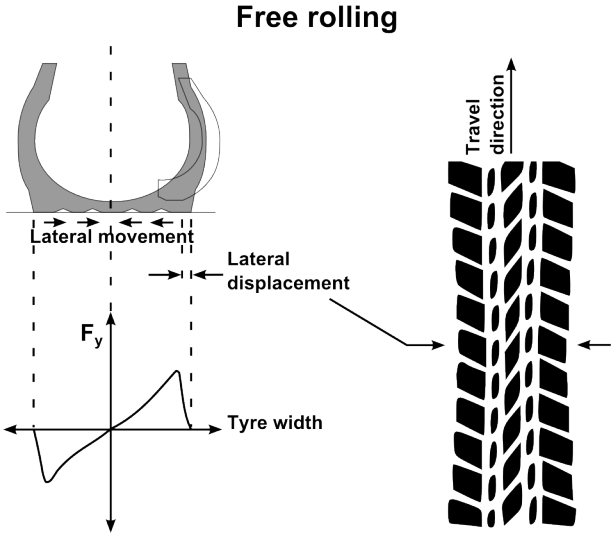

Figure 2.8: Tyre transverse traction force.

conditions are the major contributors to the transverse traction force F_y (De Beer *et al.*, 2005). Scholars such as Tielking and Roberts (1987) and De Beer *et al.* (2005) indicate that the transverse traction stresses are greater than longitudinal traction stresses. De Beer *et al.* (2005) estimated the transverse traction stress at 17% of the associated vertical stress which is 5% more than the longitudinal traction stress.

Braking and acceleration

With the onset of braking the rolling resistance increases F_r to a substantially greater breaking force F_b (Figure 2.10). The severity of braking is measured by the brake slip ratio s_b and is defined in Equation 2.3, where w_{ro} is the angular velocity of the wheel in free rolling and w_{br} the angular velocity of the wheel in braking (Moore, 1975).

$$s_b = \frac{w_{ro} - w_{br}}{w_{ro}}|_{v=constant} \tag{2.3}$$

A braking torque T_b applied to the wheel reduces the angular velocity below the free rolling value, resulting in a positive brake slip ratio. Brake slip ratio is zero for free rolling and unity for locked-wheel braking (Moore, 1975). The variation of a braking force coefficient F_b/F_z with slip ratio is illustrated in Figure 2.9 and peaking at approximately 0.2 to 0.3. According to Moore (1975) braking within the vicinity of zero to point A is desirable since directional stability is preserved by rolling rather than locked-wheel sliding. Once point A is reached, s_b rapidly reaches unity, resulting in tyre slide or locked-wheel braking. Miller *et al.* (2001) indicated that general wheel slip is between 0% and 3% under normal driving conditions.

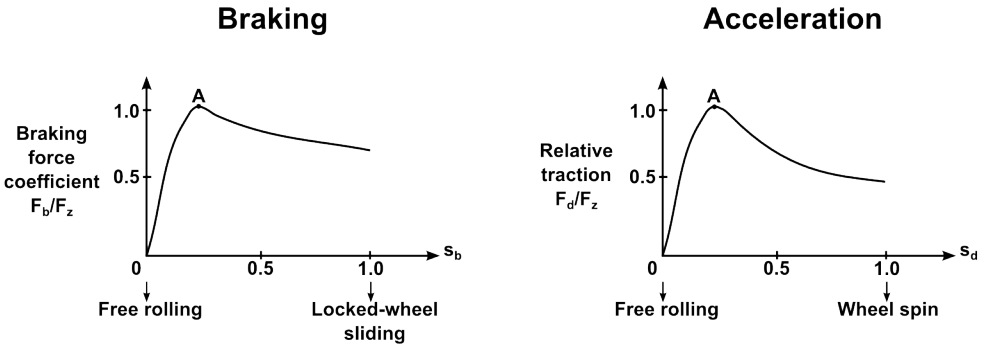

Figure 2.9: Relationship between F_b/F_z and s_b; F_d/F_z and s_d (Moore, 1975).

During braking the axle to ground height R_s reduces in comparison to free rolling conditions. The distribution of vertical pressure shifts more towards the front half of the contact patch, increasing the asymmetry offset Δx. The braking force F_b has an approximated triangular distribution over the contact patch and the total longitudinal traction force consists of F_b superimposed on F_r (Figure 2.10).
Acceleration is in many aspects similar to braking though in the opposite direction. Instead of wheel-lock once point A (Figure 2.9) is reached, the drive slip ratio s_d rapidly reaches unity resulting in wheel spin. The drive slip ratio is defined in Equation 2.4, where w_{ro} is the angular velocity of the wheel in free rolling and w_{dr}

the angular velocity of the wheel subject to a driving torque (Moore, 1975).

$$s_d = \frac{w_{dr} - w_{ro}}{w_{dr}}|_{v=constant} \tag{2.4}$$

The driving torque T_d results in a longitudinal traction force F_d with a similar distribution along the contact patch as F_b, but the motion is in the direction of travel as illustrated in Figure 2.10. The total longitudinal traction force consists of F_d superimposed on F_r.

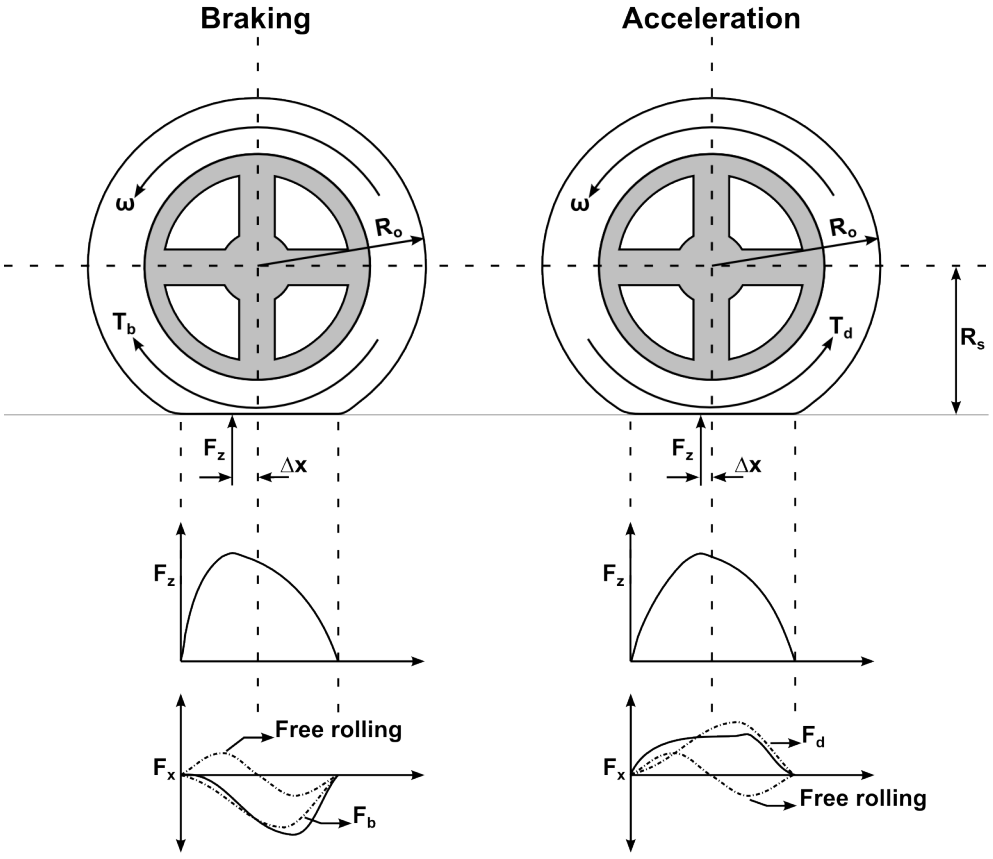

Figure 2.10: Distribution of F_z and F_x for braking and acceleration.

2.2.2 Pavement texture and tyre friction

Pavement surface texture is perhaps the most important variable which determines the magnitude of frictional forces between a tyre and the road, especially in wet conditions. At the sliding interface a rubber frictional force F_{fric} is generated. The friction force F_{fric} consist of an adhesive F_{ad} and deformation F_{def} component as defined in Equation 2.5.

$$F_{fric} = F_{ad} + F_{def} \tag{2.5}$$

Adhesion

According to Moore (1975), the adhesive frictional component F_{ad} is due to a molecular-kinetic, thermally activated, stick-slip mechanism of rubber at the sliding interface (Figure 2.11). The mechanism may be attributed to a molecular bonding of exposed surface atoms in both members, followed by a stretch, break and relaxation cycle of events (Moore, 1975). Sliding of the tread rubber causes these bonds to stretch, rupture and relax before new bonds are made. Adhesive friction is dependent on the contact area and micro texture of the road. On dry, smooth macro textures it is the major contributor of the friction force F_{fric}.

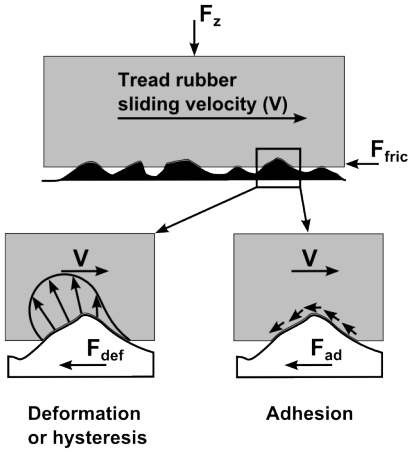

Figure 2.11: Components of rubber friction.

Deformation

Adhesive friction forces decrease dramatically when lubricants such as water, oil, dust or ice are present on the road's surface. The viscoelastic properties of the tread rubber produce asymmetrical draping around the asperities in the presence of relative sliding between the tread and the road. This draping opposes the sliding motion and results in the hysteresis or deformation friction force F_{def}. The major influencing factors on F_{def} are the tread rubber properties and the pavement roughness.

Pavement roughness

The term *micro texture* refers to the surface roughness of the crushed seal aggregates which have typical amplitudes of 10 to 100 microns. *Macro texture* refers to surface roughness of the road. Pavement macro roughness comprise of four terms: size, shape, spacing and asperity hight distribution (Moore, 1975).
The macro texture primarily influences the relationship (slope) of slip velocity V

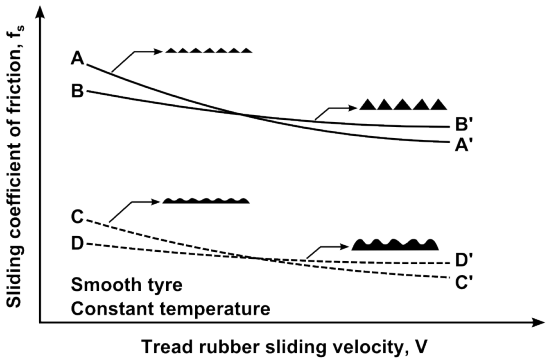

Figure 2.12: Relationships of friction, velocity and surface texture (Moore, 1975).

and the friction force as illustrated in Figure 2.12. Comparing AA' and BB' or CC' and DD' in Figure 2.12, it is evident that the larger macro texture has a smaller rate of decay for the relationship of frictional coefficient f_s with tread rubber slip velocity V. However, the magnitude of the frictional coefficient is dependent on the micro texture of the aggregates. Smooth round aggregates such as CC' or DD' have smaller coefficients of friction than the angular crushed aggregates of AA' or BB'. A higher coefficient of friction f_s results in a greater longitudinal force F_x at the tyre-road interface.

The macro texture influences the area of the tyre contact patch, thus indirectly affects the normal force F_z at the tyre-road interface. Moore (1975) explains the phenomenon as follows: The assumed or apparent contact area A_{app} is illustrated in Figure 2.13. On rough surfaces this is an over estimation, because the actual area A_{act} is equal to the sum of the contact areas at the asperity tips $A_{act} = \sum A_i$. Therefore, rougher macro textures reduce tyre contact area, resulting in an increase of the vertical stress P (Equation 2.6).

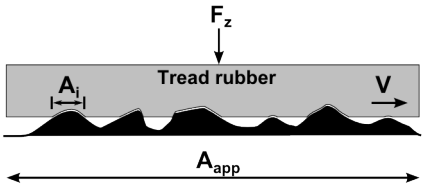

Figure 2.13: Draping of tread rubber around road asperities

$$P = \left[\frac{A_{app}}{A_{act}}\right] P_{app} \tag{2.6}$$

Moore's (1975) observation was confirmed by Cesbron *et al.* (2008) who measured the static vertical pressure at the tyre-road interface on various macro surfaces with

a Tekscan pressure sensor. Cesbron *et al.* (2008) found that on random macro textures, pressure was distributed irregularly and higher pressures were measure on courser textures. Earlier literature (Woodside *et al.*, 1992) also substantiate these findings. Woodside *et al.* (1992) investigated the static stress situations experienced by seal aggregate at different macro textures with contact stress transducers. An increase in the vertical hight of the transducers (greater macro texture) resulted in a reduction of actual tyre contact area and higher observations of stress due to increased contact pressures. Quantification of these type of pressures resulted in the development of a stress in motion (SIM) device by De Beer and Fisher (2013).

2.2.3 Stress in motion approach

Developed as a quantification device, the stress in motion (SIM) system measures the tri-axial force (F_x, F_y and F_z) of a rolling tyre. The SIM pad is designed with a permanent macro surface texture. Software emanating from SIM data can manipulate the artificial surface texture, resulting in scaled tri-axial forces.

Characteristics of the SIM pad

The dimensions of the SIM pad measures 750 mm x 375 mm x 120 mm of which the base plate is a 50 mm thick steel plate providing rigid support. The width of the SIM pad accommodates a single tyre. A second SIM pad can be mounted alongside the first SIM pad for dual wheel measurements. Each SIM pad consists of 1041 conical, hollow, steel pins, 21 of which are sensor pins and 1020 supporting pins. The sensor pins are aligned transversely in the middle of the pad. The supporting pins serve a function of tyre conditioning, associating the tread rubber to the SIM pad surface. All the pins are 50 mm in length, have a 9.7 mm top diameter and a 14.0 mm bottom diameter. The pins are spaced as depicted in Figure 2.14 and each pin represents an effective area of 250.28 mm^2, which is a geometrical constant of the SIM system (De Beer and Fisher, 2013).
The SIM pad measures the contact forces with the sensor pins and converts the results to stresses by using the effective area. Designed to measure loads up to 200 kN and speeds ranging from 0 km/h to 120 km/h, the SIM system give insight to a wide range of tyre contact forces (De Beer and Fisher, 2013). However, all SIM published works were done at creep speeds of which the majority of the works were conducted at 0.3 $m.s^{-1}$. Testing was primarily conducted with the heavy vehicle simulator (HVS), which operates at low speeds. At higher speeds, in excess of 30 km/h, a 20% reduction in the tyre contact area was observed by Cesbron *et al.* (2009) by means of the Tekscan pressure sensor on various surface textures.

SIM pad texture

SIM pad texture is defined by De Beer and Fisher (2013) as the difference in area of a pin head and the related effective area 250.28 mm^2 − 73.9 mm^2 = 176.38 mm^2. These gaps surrounding the pins allow the penetration of the pins into the tread rubber. Force acting on the existing pin head area results in contact stress for a condition termed *neutral texture*. If the force intensity is expressed in terms of a smaller, figurative pin head area, it results in and increase of the gaps surrounding the pins and an increase in the contact stress. Therefore, manipulating the ratio of effective area to pin head area produce an artificial texture condition termed *positive texture*. Force data obtained with positive texture is a scale value of the measured data at neutral texture. Positive texture is indicative of coarse macro surfaces, where neutral texture represents smoother surfaces such as dry asphalt or a seal (De Beer and Fisher, 2013).

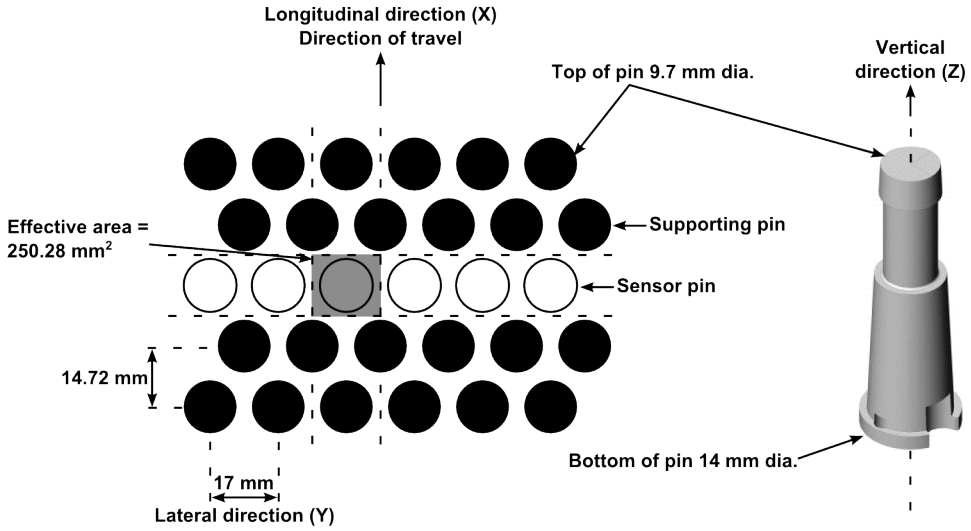

Figure 2.14: Schematic layout of a SIM system section, positions of the supporting and sensor pins, effective area and the conical steel pin (De Beer and Fisher, 2013).

Micro texture of the steel pins was tested with the Pendulum Skid Resistance Tester. Skid resistant values of 76 for dry conditions and 37 in wet conditions were obtained. As a result the SIM system represents a potentially slippery road ($value < 45$) in wet conditions and good skid resistance in dry conditions therefore, according to De Beer and Fisher (2013), it is unlikely that the SIM system underestimates the longitudinal and transverse forces in dry conditions. Various tests were conducted in dry conditions and compiled into software packages.

SIM software

Data measured at 0.3 $m.s^{-1}$ in dry conditions was compiled in the software package, *TyreStress SEAL version 1.0.0.2*. The software contains data of five different tyres, two of which are heavy vehicle (HV) tyres and three passenger or light vehicle (LV) tyres. Data for the HV tyres range from 15 kN to 100 kN (vertical load) at inflation pressures of 520 kPa to 1000 kPa. Each LV tyre has a single vertical load value and tyre inflation pressure.

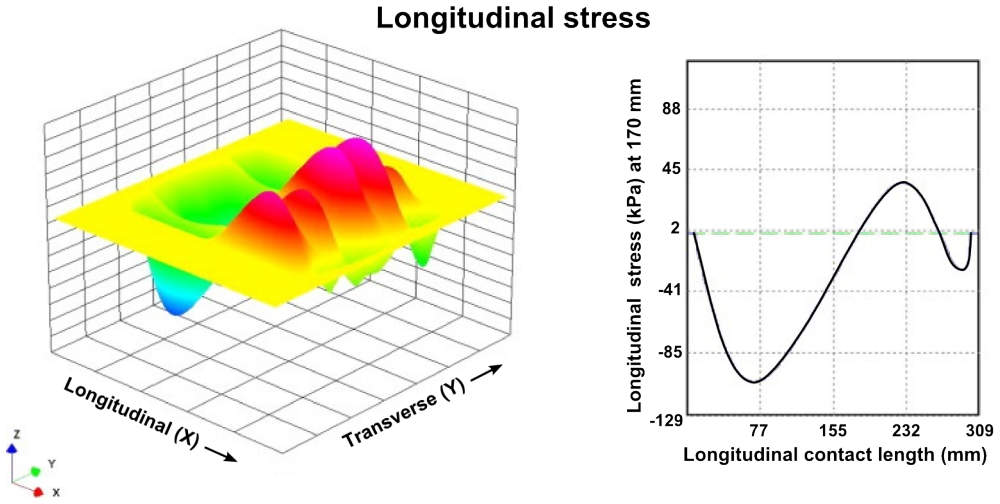

Figure 2.15: SIM 3D longitudinal tyre contact patch stress.

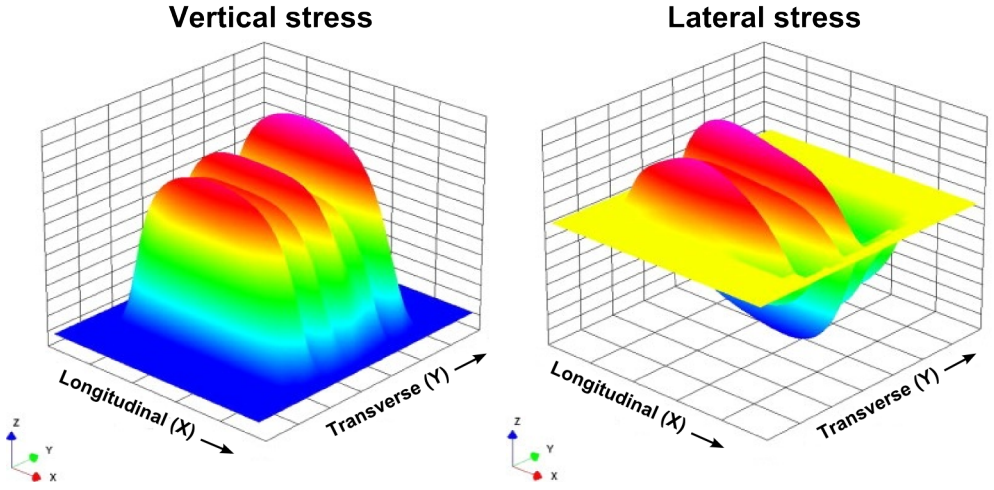

Figure 2.16: SIM 3D vetrical and transverse tyre contact patch stresses.

TyreStress SEAL includes a positive texture option, which allows scaling of the contact forces for representation of courser macro textures. Quantification of the courser texture remains to be investigated. Typical tyre contact patch stresses obtained with TyreStress SEAL are depicted in Figure 2.15 and Figure 2.16. Outputs can either be in force N or stress kPa. The vertical, longitudinal and transverse load distributions are a significant factor in the numerical modelling process of surface layers.

2.3 Numerical modelling of bituminous surface layers

Numerical models are defined as mathematical equations, which govern the dynamic response of a physical system and are characterised by three attributes: the model's geometry, material properties and applied load. The model's response translates the information of the attributes to a state of stress and strain by using theories. The significance of insight obtained by analysing the stress and strain depends on the type of theory and the scale of modelling.

2.3.1 Computational modelling approach and scale

The scale of modelling is determined by the size (dimensions) of the model. Typical scales for pavement modelling are macro-scale, bulk-scale, meso-scale and micro-scale. A schematic representation of a road is depicted in the far left-hand side of Figure 2.17. The road consists of multiple composite material layers, constructed to withstand the bearing capacity of traffic. Insights into pavement bearing capacity occur at a macro-scale, with the assumption that these layers are infinite, isotropic and homogeneous. Elastic multilayer theory is the vehicle or tool which evaluates the macro-scale design indicating whether the design would fulfil bearing capacity requirements.

Layers on a macro-scale require material response properties. The responses properties are obtained during laboratory bulk-scale testing. Bulk samples such as asphalt beams for the four point bending tests, asphalt briquettes for indirect tensile tests, triaxial samples etc. are assumed to be homogeneous materials. The empirical relationship between the test procedure and test sample constitutes the bulk response model. Therefore, insight obtained in a specific scale can address problems that manifest on a larger scale.

Meso-scale models are developed to address phenomena that occurs at bulk-scale testing. According to Woldekidan (2011), meso-scale analyses include the heterogeneous nature of the specimen. Therefore, different material properties are assigned to the bitumen and aggregate components in an asphalt specimen. Authors, Huurman (2008) and Mo (2010) agree that meso-scale models represent the structure

of a specimen. The interaction of the structural components dictates the bulk-scale responses. The finite element method (FEM) and discrete element method (DEM) serve as mechanistic tools to obtain insight into the component response and damage and is referred to as meso-mechanics.

Insight into component interaction such as the bitumen-aggregate interface is conducted on a micro-scale. Here, the heterogeneous natures of the individual materials are considered. Theories in micro-mechanics are used explain observations made in meso-scale. Each measurement or response in a certain scale can explain or give insight to phenomena observed in a larger scale if an appropriate tool or theory exists to transfer the data. However, loads in a model at certain scale can be derived from loading results of an upper scale. Systems incorporating multiple models of different scales to define a problem are termed *multi-scale models*.

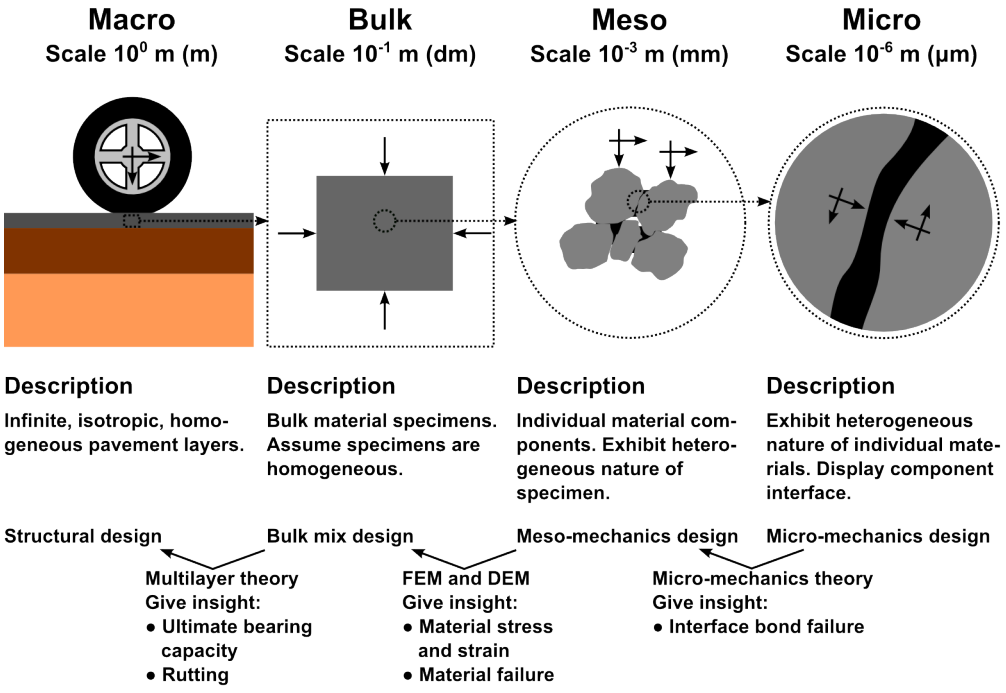

Figure 2.17: Modelling approach and scale for asphalt pavements.

2.3.2 Geometry of multi-scale models

A great challenge in spatial modelling is the translation of physical geometries to multi-scale models. Models need to reflect reality, but not exceed the limits of available computational power. It is this compromise that results in the two main approaches of geometry representations. The approaches are idealised geometry and x-ray image geometry.

Idealised geometry

Representing complex geometries such as aggregates with idealised spherical shapes, simplifies multi-scale modelling. This was the approach to Huurman's (2008) 2D and 3D porous asphalt concrete (PAC) models for evaluating ravelling. Huurman indicated that ravelling was a material damage phenomenon, therefore the PAC models distinguished between aggregates, mortar (mixture of bitumen, sand and filler), air voids and adhesive zones (Figure 2.18).

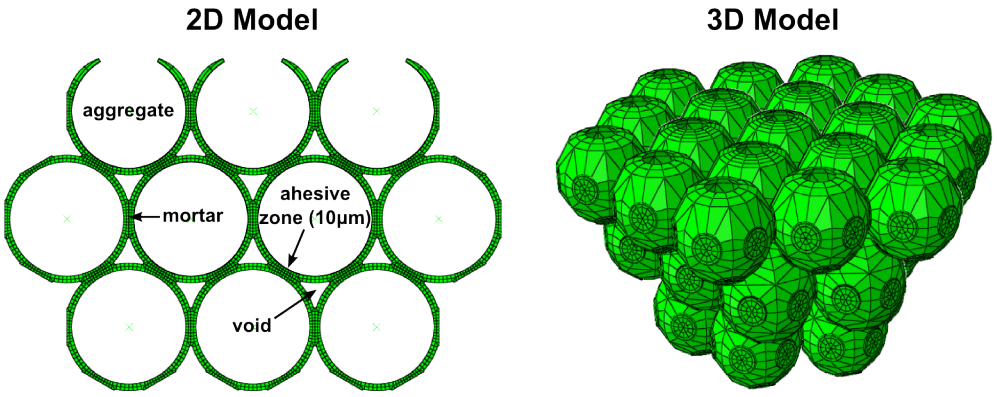

Figure 2.18: Idealised 2D and 3D PAC models (Huurman, 2008).

Aggregates were represented by equivalent circles or spheres based on the volumetric proportions of the PAC mix, while the mortar was presented as a homogeneous film. The thickness of the adhesive zone was not relevant from a spatial perspective since it was modelled as part of the mortar, however a thickness of 0.01 mm was assumed. This assumption was made with reference to the micro texture of the aggregates and sand particle sizes in the mortar. The structure of the models comprised of three layers of aggregates bound by mortar films. Air voids were situated between the aggregates. The percentage of voids could be adjusted by adjusting the the thickness of the mortar film.

Huurman *et al.* (2003) assisted Milne (2004) in developing a 3D prototype performance model for road seals. Milne's model comprised of aggregates bound by bitumen and an interface layer that represented the aggregate-bitumen adhesive bond (Figure 2.19). The aggregates had a spherical shape with heights based on the ALD and widths representing the nominal size of a 13.2 mm single seal. The model setup accommodated either equivalent aggregate sizes or normally distributed aggregates sizes within the first standard deviation. The latter setup is more representative of single size aggregates used in seal construction. Edge-to-edge spacing of these aggregates ranged from 0 mm to 6.1 mm. A homogeneous binder layer filled the spaces

between the aggregates and represented a 1.2 l/m^2 application rate. The interface layer was estimated at 0.2 mm. The model had no base layer, but had boundary conditions that simulated an elastic foundation. At a later stage, Huurman (2010) improved the model by adding a base layer for the evaluation of embedment (Figure 2.20). Other improvements were redesigning the interface layer to 0.01 mm and adjusting the spaces between aggregates that exceeded observations in practise. Both models however, do not accommodate the existence of air voids in the structure.

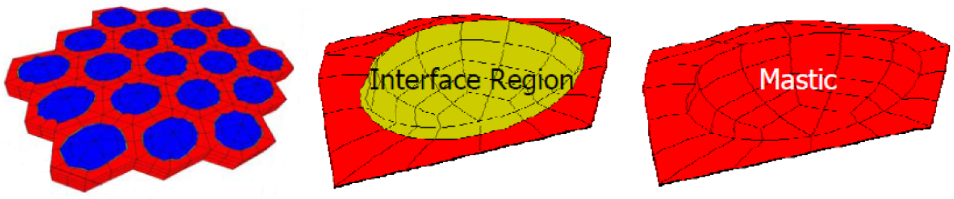

Figure 2.19: 3D Prototype performance model for surfacing seals (Milne, 2004).

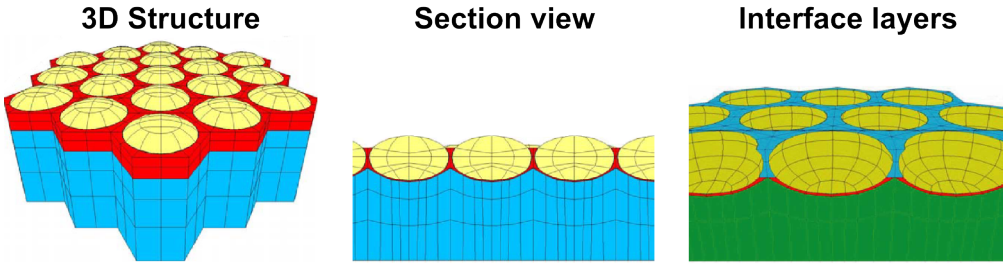

Figure 2.20: Adjusted 3D performance model for surfacing seals (Huurman, 2010).

Air voids are intentionally created during a PAC mix, resulting in a permeable surface layer which allows moisture flow through the inter-connected pores. According to Kringos (2007) the moisture flow results in physical damage of the mastic (mixture of bitumen and filler) by weakening the cohesive properties of the mastic and reducing the aggregate-mastic adhesive bond. The introduction of traffic increases the pore pressure in the PAC resulting in increased mechanically induced stresses. Kringos (2007) developed a computational model to simulate physical and mechanical moisture induced damage on PAC. The model was verified with a 2D FEM approach. The approach consisted of two aggregates bound by a mastic film, a macro pore containing water and an aggregate mastic interface (Figure 2.21).
Based on the approach of Kringos (2007), hardening (aging) of the mastic due to air flow was investigated by Das *et al.* (2013). Atmospheric oxygen and temperature act as a catalyst in the mastic hardening process. Das *et al.* (2013) developed a 3D finite element (FE) model consisting of spherical aggregates covered with mastic in

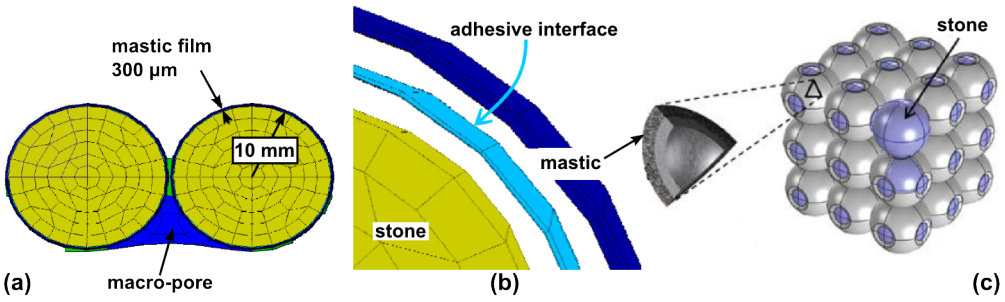

Figure 2.21: Moisture flow damage and mastic hardening FE models: (a) 2D Moisture flow model, (b) Adhesive interface, (c) 3D Mastic hardening model.

a cubical packing formation (Figure 2.21). This packing allows the air flow through the interconnected pores of the 3D structure.

The importance of aggregate packing was observed by Mo *et al.* (2008) in developing PAC models with Huurman (2008). Mo *et al.* (2008) found that the aggregate packing affected the overall stress levels in the 2D models (Figure 2.18). The results of the 2D models were compared with the 3D models (Figure 2.18) and greater stress values were observed within the mortar and adhesive zones of the 3D models in comparison to the 2D models. The reason for the higher stresses in the 3D models was attributed to greater loading of the model due to a larger effective loading area of the 3D model. Huurman (2008) observed a similar phenomenon and cautioned that the 2D PAC model can overestimate the PAC service life to ravelling.

Tehrani *et al.* (2013) conducted a study on the complex modulus response of mastic and mortar through 2D and 3D FE simulations. An in-house program, MOA (French acronym for Random Object Generator), was used to generate the mastic and mortar structural models. MOA generates random sized 3D particles inside a delineated volume such as a cube or cylinder. The particles shapes are either spherical or polyhedral. Particles can be separated or allowed to be intact. The voids between the partials are filled with bitumen in the case of mastic and with mastic in case of mortar. The surface geometry of the 3D model constitutes the 2D model (Figure 2.22).

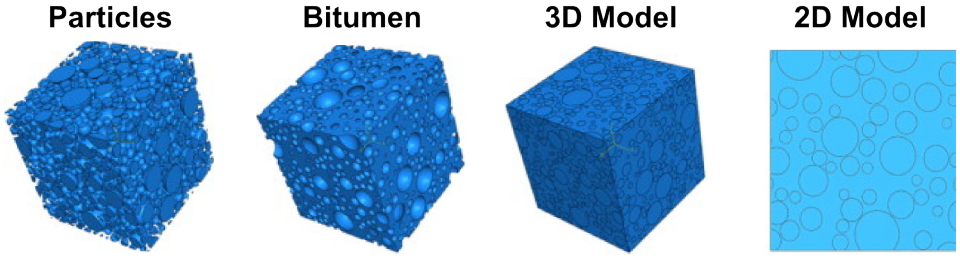

Figure 2.22: 2D and 3D Micro structural models (Tehrani *et al.*, 2013).

The 2D and 3D mastic models under estimated the stiffness of the mixture compared to the measured complexed modulus. The 3D model results were closer to the measured results with a discrepancy of 25% between the 3D and 2D model results. A similar trend was observed for the mortar model, but the discrepancy reduced to 16%. Therefore a reduction in the geometrical heterogeneity resulted in a decrease of the discrepancy obtained in the transition from the 3D model to the 2D model. It is known that micro-mechanical models under estimate the stiffness of asphalt mixtures, as aggregate interlock is not captured in the approach (Tehrani *et al.*, 2013). Aggregate interlock can be accommodated by means of image processing techniques to identify the aggregate to aggregate contact areas.

X-ray image geometry

Computerised tomography scanning (CT-scans), also known as X-ray imaging, was originally developed for the medical practice, but proved to be an effective method in obtaining the in situ geometry of road surface specimens. X-ray images are based on the Hounsfield unit (HU) scale which is a quantitative scale for describing the radio-density of a material. The HU range of an image stack is converted to a grayscale for interpretation purposes. Less dense materials are displayed in darker shades, while denser materials are displayed in lighter shades. In a seal specimen, voids (air) will be black while the aggregates are white.
A 3D FE seal model based on X-ray images was the approach followed by Kathirgamanathan *et al.* (2012) to investigate the effect of seal aggregate to aggregate contact. Aggregate to aggregate interaction which enables the seal to withstand traffic stresses are critical for the distribution of horizontal loads over the seal's surface (Kathirgamanathan *et al.*, 2012). Scans of a seal core sample were taken at 1.0 *mm* intervals and reconstructed using image processing techniques (Figure 2.23). The resolution of the images dictates the quality of the images. Accurately defining the

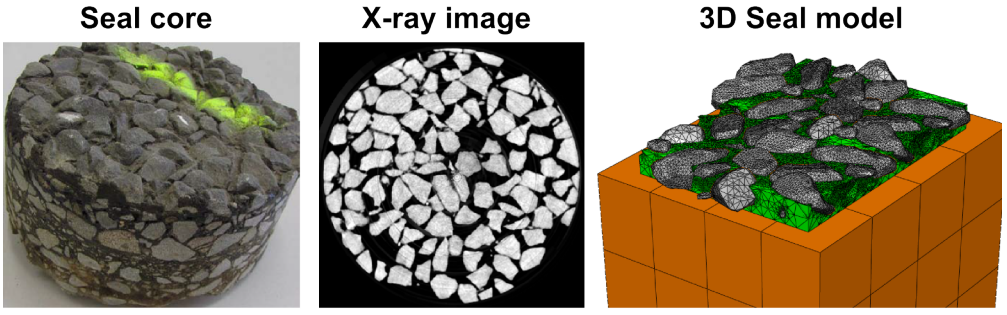

Figure 2.23: 3D X-ray seal FE model (Kathirgamanathan *et al.*, 2012).

threshold (grayscale range) of the binder-aggregate interface largely depends on the resolution of the images. Zelelew and Papagiannakis (2011) described an approach to identify this threshold. Kathirgamanathan *et al.* (2012) used a *water shedding* segmentation technique in defining the aggregate boundaries. Aggregates need to have individual boundaries. This means that there should be at least one pixel between adjacent aggregates else if aggregates share boundaries it will result in a *super aggregate*. A super aggregate is the term used for two or more aggregates acting as one. Kathirgamanathan *et al.* (2012) model consisted of 26 aggregates, bitumen and an artificial base (Figure 2.23). Embedment was simulated by slightly raising the artificial base allowing the bottom aggregates to penetrate the base. Aggregates smaller than 2 *mm* were treated as part of the bitumen phase. No adhesive interface layer was considered to represent the bitumen-aggregate bond.
Huurman (2008) recognised the importance of an adhesive interface and manually assigned these interfaces in PAC FE models. Inspired by the X-ray FE model technique; Huurman (2008) constructed 2D FE models from colour photos taken of PAC sample cross section cuts. To enhance the presence of voids in the photo plane, the PAC samples were submerged into a gypsum solution filling the voids. When allowed to dry, it clearly indicated the position of the voids in the cross section cuts. This facilitated the manual construction process of the 2D FE models (Figure 2.24). Similar to the idealised models (Figure 2.18), the photo models consisted of aggregates, mortar, voids and adhesive zones. The photo models were constructed to quantify the feasibility of representing the PAC structure with idealised geometry. According to Huurman (2008) the geometrical comparisons were troublesome due to the stochastic response of the photo model structure. However, the results of the 2D PAC idealised and photo models were in the same order.

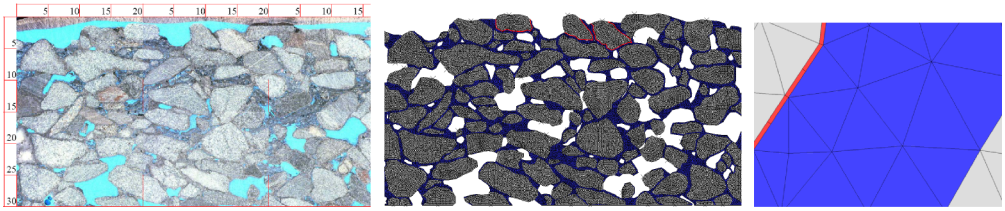

Figure 2.24: 2D PAC FE photo model (Huurman, 2008): (a) PAC cross section photo with gypsum filled voids, (b) 2D FE model, (c) Adhesive interface layer.

A 3D PAC FE model was developed by Onifade *et al.* (2013). The model was constructed to be included in an uniaxial compression analysis. The test results displayed the aggregate to aggregate load-transfer zones and confirmed the significance of the PAC internal structure to load response. A 100 *mm* diameter PAC core with

a hight of 80 mm was scanned at a resolution of 1949×1799 with a slice thickness of 59 μm, which resulted in 1932 images. A subsample of 60 $mm \times 60$ $mm \times 60$ mm was selected to generate the FE mesh (Figure 2.25). The mesh consisted of approximately 98 million tetrahedral elements (TETs). Onifade *et al.* (2013) indicated that a reduction in the resolution, by resampling the images, will reduce the number of tets in the FE mesh. The resampling resolution of the images was set to 400 μm which reduced the number of TETs to approximately 12.4 million without losing a considerable amount of image detail. However due to computing constrains the cube was further reduced to a 30 $mm \times 30$ $mm \times 30$ mm subsample which consisted of 254000 tets (Figure 2.25).

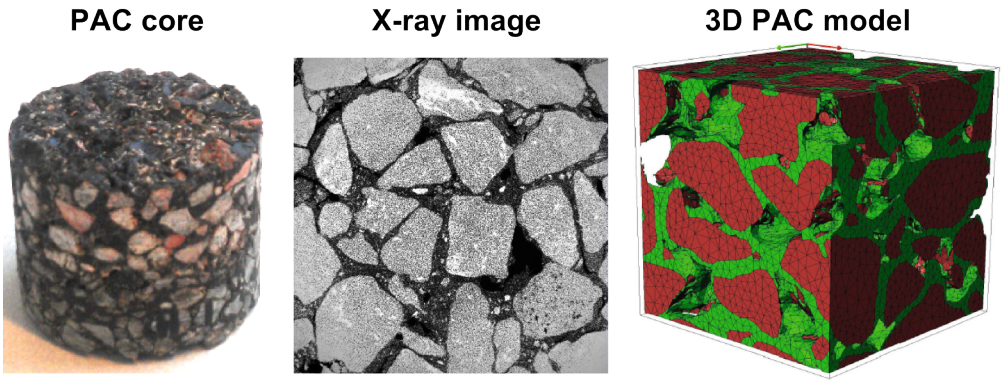

Figure 2.25: 3D PAC FE model (Onifade *et al.*, 2013).

Zelelew *et al.* (2013) investigated the viability of modelling permanent deformation in asphalt samples by developing 2D DEM models of Superpave gyratory compacted specimens through the X-ray imaging process. Zelelew *et al.* (2013) agree with Onifade *et al.* (2013) that asphalt behaviour is dominated by the interaction between the mastics and distinct aggregate particles and further indicate that asphalt's plastic deformation properties are greatly influenced by the mastic rheology, aggregate properties and micro structure of the mixture constituents. Micro-mechanics based on DEM are commonly used in large strain simulations and ideally suited to describe particle contact interaction. The DEM models included mastic-to-mastic, mastic-to-aggregate and aggregate-to-aggregate contact interactions. The models also allowed *clumping* of similar adjacent materials, thus avoiding force-displacement calculation between them (Zelelew *et al.*, 2013).

Although DEM and FEM are used in multi-scale modelling, DEM is suitable for analysing systems by modelling the translational and rotational behaviour of the individual particles. FEM is a continuum approach and is better suited for applications in material performance models. In these models the ability of the materials to

sustain repeated loads are predicted (Woldekidan, 2011). The outcome of the model is thus dependent on constitutive material models.

2.3.3 Material modelling

A structural analysis in continuum mechanics is governed by mathematical expressions which relate the response of the structure (body) under external loads to stress and strain. The analysis needs to fulfil the requirement of three basic equations which are; the kinematic equation, equilibrium equation and constitutive equation. The kinematic equation relates displacements and deformations within the body to strain, while the equilibrium equation deals with the force balance thereof (Woldekidan, 2011). The constitutive equation defines the relationship of stress with strain inside the body. Kinematic and equilibrium laws are common for all materials, regardless of type or form. Therefore, the fundamental mechanical response of a material is reflected in its constitutive stress-strain relation. Within asphalt or a seal structure, different constitutive relations are assigned to the individual components. These components include: aggregates, bitumen or mastic, adhesive interface, air voids and the supporting base layer.

Aggregates

Aggregates are considered as a linear elastic material with reference to multi-scale modelling. Scholars including Milne (2004), Huurman (2010) and Onifade *et al.* (2013) have adopted this assumption. Kringos (2007) however, assumed hyper elastic aggregate properties. Elastic aggregates cannot exhibit wear, be crushed or permanently deformed. Since these phenomena were not the primary interests of the structural models, elasticity was considered an effective assumption.
If computational constraints are of concern, aggregates can be considered as rigid bodies. This was the approach of Huurman (2008) (Figure 2.18) and Kathirgamanathan *et al.* (2012) (Figure 2.23). Assigning a rigid body property to an aggregate implicate that the aggregate cannot deform, it can only translate and rotate. Thus, no stress-strain relationship exist for such a body, reducing the computational time.
Apart from the constitutive material model, an interaction relationship (contact algorithm) on the aggregate edge needs to be specified if aggregate-to-aggregate interactions are of interest. These algorithms dramatically increase computational time and can be addressed with the assumption that aggregates are always covered with a thin film of bitumen (or mastic), therefore no direct aggregate-to-aggregate contact exist in the structure.

Bitumen

With reference to bituminous materials, cognisance of the different deformation types associated with continuum mechanics is important. A summary of the deformation types are presented in Table 2.1. Bitumen exhibits time dependent mechanical behaviour when subjected to deformation and displays elastic and viscous material characteristics, hence the term *viscoelastic*. Viscoelastic materials manifest *creep* and *relaxation* when subjected to loading. While creep represents an increase of deformation with time, relaxation refers to the decrease in stress with time under a constant deformation (Woldekidan, 2011).

Table 2.1: Types of deformations in a continuum (Poulikakos, 2011).

Deformation	Characteristics	Molecular level
Elastic	Time independent. Deformation occurs the instance stress is applied or released. Reversible. Energy is not dissipative (recoverable).	Deformation due to bond length of atoms. Long molecular chains are frozen in position.
Plastic	Time independent. Irreversible. Energy dissipative. Yield stress.	Atoms rearrange permanently.
Viscoelastic	Instantaneous elastic strain. Viscous time dependent strain. Elastic recoverable strain upon release.	Same as elastic with time dependence.
Viscoplastic	Time dependent. Irreversible. Energy dissipative.	Atoms rearrange permanently.
Viscous flow	Deformation is not instantaneous. Time dependant. Irreversible upon release. Energy dissipative.	Chain motion intensifies. Chain segments vibrate and rotate independently of one another.

Bitumen response behaviour is divided into two categories. If the applied load within the binder is small the assumption is made that the material exhibits a linear viscoelastic response, however with larger loads the material displays a nonlinear viscoelastic response. The linear viscoelastic mechanical analogies can be represented by a system consisting of linear springs and viscous dashpots. Two common systems are the Maxwell model (Figure 2.26) and the Kelvin-Voigt model (Figure 2.27).
The Maxwell model assumes a uniform distribution of stress in the system. Stress in the spring is equal to the stress in the dashpot $\sigma(t) = \sigma_s(t) = \sigma_d(t)$. However, the total deformation of the system is equal to the sum of the individual elements $\epsilon(t) = \epsilon_s(t) + \epsilon_d(t)$. The subscripts s and d refers to the spring and dashpot respectively. Figure 2.26 illustrates the response of the Maxwell model when subjected to a con-

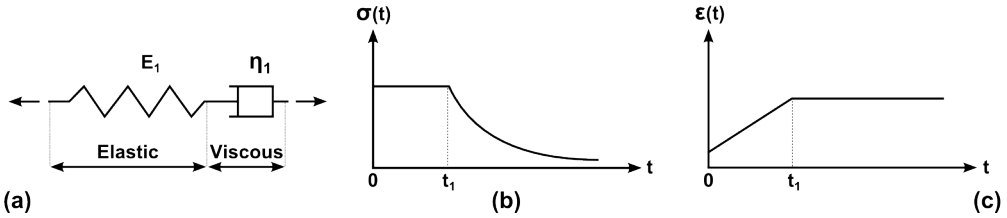

Figure 2.26: Maxwell model: (a) Elastic spring and viscous dashpot, (b) Load response with time, (c) Strain response with time.

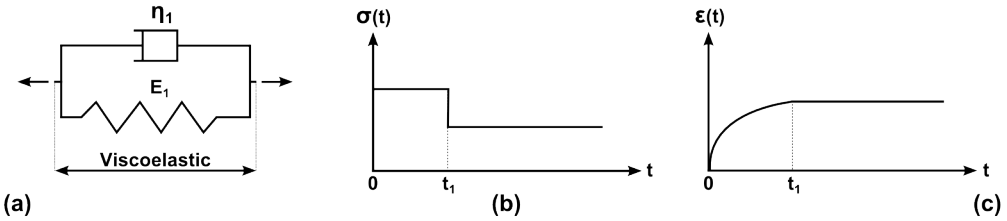

Figure 2.27: Kelvin-Voigt model: (a) Linear Eelastic spring and viscous dashpot, (b) Load response with time, (c) Strain response with time.

stant stress and a constant strain. A constant stress is applied for a time duration of $0 < t < t_1$ which results in a linear strain response. If the strain remains constant at time t_1 for a duration $t > t_1$, an exponential stress decay is observed.

The Kelvin-Voigt model assumes a uniform distribution of strain in the system. Strain in the spring is equal to the strain in the dashpot $\epsilon(t) = \epsilon_s(t) = \epsilon_d(t)$. The total stress in the system is equal to the sum of the individual elements $\sigma(t) = \sigma_s(t) + \sigma_d(t)$. Figure 2.27 illustrates the response of the Kelvin-Voigt model when subjected to a constant stress and a constant strain. A constant stress is applied for a time duration of $0 < t < t_1$ which results in a non-linear strain response. If the strain remains constant at time t_1 for a duration $t > t_1$, it results in a constant stress. According to Woldekidan (2011) the Kelvin-Voigt model does not simulate stress decay and is therefore not suitable for modelling materials exhibiting relaxation behaviour. Milne (2004) and Huurman (2010) addressed the stress decay constraint by defining an incremental formulation of the Generalised Burgers' model for the bitumen constitutive material model, in their FE seal models. The Generalised Burgers' model consists of a series of Kelvin-Voigt elements as illustrated in Figure 2.28. The single spring response E_0 is obtained by setting the related dashpot viscosity to zero. Similarly a single dashpot response is obtained by setting the related spring stiffness to zero. The model's instantaneous response is captured by the single spring element. Creep evolution is captured by the by the series of Kelvin-Voigt elements and the single dashpot element captures the viscous deformation. A version of this model with a single Kelvin-Voigt element is referred to as *Burgers' model* or *equation*.

With the application of a constant stress, the Generalised Burgers' model exhibits an instantaneous strain response, followed by an increase in strain over the time duration $t_0 < t < t_1$ (Figure 2.28). The increased strain rate becomes linear with time. When the load is removed an instant elastic recovery is observed, followed by a delayed recovery. The unrecoverable deformation is termed *viscous deformation*. The viscoelastic constitutive equations and incremental formulations for the Generalised Burgers' model as presented in Collop *et al.* (2003) are summarised as follows: The total strain in the system is equal to the sum of the strain components as defined in Equation 2.7.

$$\epsilon(t) = \epsilon_{el}(t) + \epsilon_{ve}(t) + \epsilon_{vp}(t) \tag{2.7}$$

where:

t = time
ϵ = total strain component
ϵ_{el} = elastic strain component
ϵ_{ve} = viscoelastic strain component
ϵ_{vp} = viscoplastic strain component

The elastic strain component can be calculated with Equation 2.8 and its incremental formulation is defined in Equation 2.9.

$$\epsilon_{el}(t) = \frac{\sigma(t)}{E_0} \tag{2.8}$$

where:

σ = applied stress
E_0 = elastic modulus of spring element

$$\Delta\epsilon_{el} = \frac{\Delta\sigma}{E_0} \tag{2.9}$$

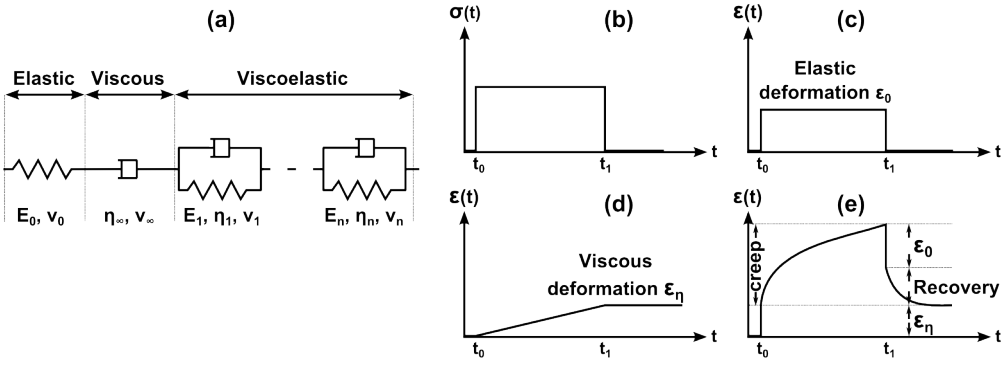

Figure 2.28: Generalised Burgers' model and the model's response to load: (a) Generalised Burgers' model (b) Applied load, (c) Elastic deformation, (d) Viscous deformation, (e) Viscoelastic deformation.

where:

$\Delta\epsilon_{el}$ = elastic strain increment

$\Delta\sigma$ = stress increment

The viscoelastic strain component can be calculated using the hereditary integral formulation presented in Equation 2.10 and its incremental formulation is defined in Equation 2.11.

$$\epsilon_{ve}(t) = J_{ve}(0)\sigma(t) + \int_0^t \frac{dJ_{ve}(t-t')}{d(t-t')}\sigma t' dt' \tag{2.10}$$

where:

J_{ve} = viscoelastic creep compliance

t' = dummy integration variable

$$\Delta\epsilon_{ve} \cong \sum_{i=1}^{N} \left\{ {}^t\epsilon_{ve}^i (e^{-\Delta t/\tau_i} - 1) + \frac{\Delta t}{\eta_i} e^{-\Delta t/2\tau_i} \left({}^t\sigma + \frac{\Delta\sigma}{2} \right) \right\} \tag{2.11}$$

where:

N = number of Kelvin-Voigt elements

$\tau_i = \dfrac{\eta_i}{E_i}$ = relaxation time constant of the i^{th} Kelvin-Voigt element

η_i = viscosity of the i^{th} Kelvin-Voigt element

E_i = elastic modulus of the i^{th} Kelvin-Voigt element

${}^t\epsilon_{ve}^i$ = viscoelastic strain of the i^{th} Kelvin-Voigt element at time t

Δt = time increment

The viscoplastic strain component is also calculated using the hereditary integral formulation as presented in Equation 2.12 and its incremental formulation is defined in Equation 2.13.

$$\epsilon_{vp}(t) = J_{vp}(0)\sigma(t) + \int_0^t \frac{dJ_{vp}(t-t')}{d(t-t')}\sigma t' dt' \tag{2.12}$$

where:

J_{vp} = viscoplastic creep compliance

$$\Delta\epsilon_{vp} \cong \frac{\Delta t}{\eta_\infty}({}^t\sigma + \frac{\Delta\sigma}{2}) \tag{2.13}$$

where:

η_∞ = viscosity of the viscoplastic element

At the onset of creep testing by Collop *et al.* (2003), constant permanent strain accumulation was observed. According Collop *et al.* (2003), the strain accumulation dramatically increased at the later stages (tertiary creep) of the tests. This

observation implies that the effective viscosity is decreasing as the material becomes progressively damaged. Collop *et al.* (2003) proposed a scaler quantity D, to include this effect in a continuum damage mechanics (CDM) approach. Parameter D range from 0 (undamaged) to 1 (fully damaged). The CDM approach is an expression which defines the growth of D, often termed the *evolution* of D. The expression of the CDM approach on the viscoplastic element is presented in Equation 2.14 and the incremental formulation of D is defined in Equation 2.15.

$$\eta_{\infty} = \eta_{uni}(T)(\frac{\sigma_e}{\sigma_0})^{1-n}10^{B(\eta+1/3)}(1-D)^m \qquad (\sigma_e > \sigma_0) \tag{2.14a}$$

$$\eta_{\infty} = \eta_{uni}(T)10^{B(\eta+1/3)}(1-D)^m \qquad (\sigma_e \leq \sigma_0) \tag{2.14b}$$

where:

η_{uni} = uniaxial viscosity
T = temperature
σ_e = Von Mises equivalent stress
σ_0, B, m, n = material parameters

$$\Delta D \cong (1 - {}^{t}D) - \left[(1 - {}^{t}D)^{\mu+1} - (\mu-1)\left(\frac{{}^{t}\sigma_e + \Delta\sigma_e/2}{\tilde{C}}\right)^{v}\Delta t\right]^{\frac{1}{\mu+1}} \tag{2.15}$$

The Generalised Burgers' model is widely used for modelling bituminous materials. If a sufficient number of Kelvin-Voigt elements are selected it describes the response behaviour of viscoelastic materials very accurately (Woldekidan, 2011).
Another common rheological model is obtained by placing a number of Maxwell elements in parallel. This format is known as the *Generalised Maxwell model* and a variation of this model known as the *Prony series* is obtained by including a spring element (Figure 2.29). The Prony series is used by numerous scholars (Huurman (2008), Kathirgamanathan *et al.* (2012), Onifade *et al.* (2013), Tabatabaee and Bahia (2014)) to define the bituminous response characteristics in FE modelling.

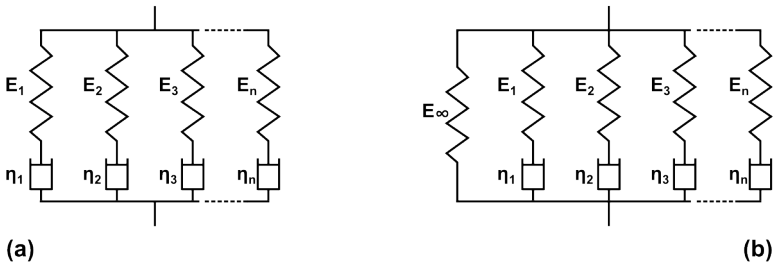

Figure 2.29: (a) Generalised Maxwell model, (b) Prony series

The model parameters required for a Prony series are the relaxation time, the realaxation modulus and the instantaneous material stiffness. Since deformation in the elements is equal, the relaxation function of the system is obtained as a summation of the individual elements. The expression of the relaxation modulus is presented in Equation 2.16 and its incremental formulation, needed for FE modelling, is defined in Equation 2.17 (Huurman and Woldekidan, 2007).

$$E(t) = E_\infty \left[1 - \sum_{i=1}^{N} \alpha_i \left(1 - e^{\frac{-t}{\tau_i}}\right)\right] \tag{2.16}$$

where:

E = relaxation modulus

E_∞ = infinite relaxation modulus

α_i = normalised stiffness reduction of the i^{th} Maxwell element

t = time

τ_i = relaxation rate of the i^{th} Maxwell element

N = number of Maxwell elements

$$\Delta\sigma = E_0 \left(\Delta\epsilon - \sum_{i=1}^{N} \alpha_i^E \Delta\epsilon_i\right) \tag{2.17}$$

where:

$\Delta\epsilon$ = difference in total strain of the i^{th} Maxwell element

$\Delta\epsilon_i$ = difference in viscous strain of the i^{th} Maxwell element

$$\Delta\epsilon_i = \frac{t_i}{\Delta t}\left(\frac{\Delta t}{t_i} + e^{-\Delta t/t_i} - 1\right)\Delta\epsilon + \left(1 - e^{-\Delta t/t_i}\right)\left({}^t\epsilon - {}^t\epsilon_i\right) \tag{2.18}$$

where:

Δt = time increment

${}^t\epsilon$ = total strain at the end of previous increment

${}^t\epsilon_i$ = viscous strain of the i^{th} Maxwell element at the end of previous increment

The popularity of the Prony series is attributed to its inclusion in the commercially available FE software, Abaqus. The series is a response model and has no damage component. Mo (2010) developed a model which translates these responses to damage for bituminous materials. The damage model was based on the dissipated energy principle. Dissipated energy is characterised by a hysteresis loop of a material's stress-strain relationship when subjected to cyclic loading. According to Mo (2010), the energy dissipated in the initial cycle is an indication of the material's fatigue damage. The fatigue damage is related to the number of equivalent loading cycles to failure as defined in Equation 2.19.

$$N_f = \left[\frac{W_{in}}{W_0}\right]^{-b} \tag{2.19}$$

where:

N_f = number of cycles to fatigue failure
W_{in} = dissipated energy during the initial cycle
W_0 = reference energy
b = model constant

$$W_{in}(\epsilon) = \int \sigma_{ij} d\epsilon_{ij} \tag{2.20}$$

where:

σ_{ij} = stress components
ϵ_{ij} = strain components

An altered version of the Prony series layout (Figure 2.29) formed the basis of the constitutive mastic material model developed by Kringos (2007). By adding a plastic component to the elastic element of Figure 2.29 (b), a transformation from an elastic element to an elastoplastic element was achieved. The model termed, *elasto-visco-plastic*, consisted of an elastoplastic element and numerous viscoelastic (Maxwell) elements. The elasto-visco-plastic response characteristics interact with one another in a 3D domain. Effects in a single direction were therefore not a simple summation equation. The deformation tensor which determines the total deformation response of the system was formulated via a process known as *multiplicative decomposition*. The concept of multiplicative decomposition provides an elegant tool for describing the 3D response of the elasto-visco-plastic material models consisting of elastoplastic and viscoelastic components (Kringos, 2007).
The mastic response model included thus a damage component and was developed to operate in finite (i.e. large) strains. Therefore, it had no restrictions on the range of strain in which the material could be modelled. Kringos (2007) indicated that although the model was developed for mastics, it could be used to simulate the effect of the aggregate-mastic adhesive interface.

Adhesive interface

The adhesive interface, also referred to as the adhesive zone or bond, is an aggregate-binder interaction property which is modelled as a material component with a finite thickness as illustrated in Figure 2.30 (a). The interface thickness (film thickness), temperature and loading rate are the main factors that influence the bond strength. The tensile strength of thin bitumen films decrease as the film thickness increase

and approaches a constant value, even if the the film thickness increases further (Mo, 2010). Similarly does the reduction of temperature increase the bond strength, but the reduction in the loading rate reduces the bond strength.

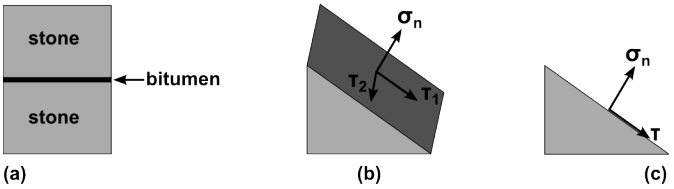

Figure 2.30: Schematic illustration of the bitumen-aggregate interface: (a) Idealised adhesive zone, (b) 3D stress components (c) 2D stress components (Mo, 2010).

Since the adhesive interface is modelled as a material component, it requires material properties. Milne (2004) defined the adhesive interface properties as directional stiffness per film thickness. The magnitude of the directional stiffness ranged from a lower extreme represented by the bitumen's elastic modulus to an upper extreme represented by the elastic modulus of the aggregate. Huurman (2008) followed a similar approach to Milne (2004) and indicated that the directional stiffness response parameters of the adhesive interface, can be determined from the complex moduli of the bitumen as defined in Equation 2.21 and Equation 2.22.

$$K_n = \frac{E^*}{film \quad thickness} \tag{2.21}$$

$$K_s = \frac{G^*}{film \quad thickness} \tag{2.22}$$

where:

K_n = normal stiffness response parameter
K_s = shear stiffness response parameter
E^* = complex elastic modulus
G^* = complex shear modulus

The interface region is extremely thin in comparison to the surrounding regions, therefore it exhibits a slightly different state of stress when subjected to loading. The state of stress is illustrated in Figure 2.30 (b) and indicates that the interface region produces a normal component and two tangential components when subjected to loading. Mo (2010) related the normal component to the tangential components as presented in Equation 2.23. According to this relation, the bond strength increases with compression stress. The compression stress opposes the shear stresses which act along the fracture plane prompting adhesive failure.

$$\tau = -\sigma_n \tan \phi_t + c \tag{2.23}$$

where:

τ = shear stress $\tau = (\tau_1^2 + \tau_2^2)^{0.5}$

σ_n = normal stress (positive for tension)

ϕ_t = angle of internal material friction

c = material cohesion

It is evident from Equation 2.23 that normal and shear stress coexist at the adhesive interface. Therefore, an adhesive fatigue model developed by Mo (2010) relates the combination of interface stresses to an equivalent tensile stress σ_e. The fatigue model is based on a Mohr-Coulomb like failure envelope and determines the damage accumulation at the adhesive interface subject to cyclic loading. According to Mo, the damage accumulation of the initial cycle is an indication of the number of equivalent load cycles to failure (Equation 2.24).

$$N_f = \frac{1}{D_1} \tag{2.24}$$

where:

N_f = number of cycles to fatigue failure

D_1 = damage accumulation of the initial cycle

$$D(t) = \int_0^t \dot{D}(\sigma) dt \tag{2.25}$$

where:

D = damage accumulation of the cycle

$\dot{D}$ = damage accumulation rate

$$\dot{D}(\sigma_e) = \left(\frac{\sigma_e}{\sigma_0}\right)^{n_0} \tag{2.26}$$

where:

σ_e = equivalent tensile stress

$\sigma_e > 0$, otherwise $\dot{D}(\sigma_e) = 0$ if $\sigma_e \leq 0$

σ_0 = tensile strength

n_0 = material parameter

$$\sigma_e = \sigma_n + \frac{\tau}{\tan\phi} \tag{2.27}$$

where:

σ_n = normal stress (positive for tension)

ϕ = angle of internal material friction
τ = shear stress

The fatigue model was verified and adequately simulated the susceptibility of the adhesive interface response to temperature variations. The model however, was not sensitive to the effect of moisture at the adhesive interface. The presence of moisture in a pavement can be ascribed to possible water ingress through existing voids in the structure.

Voids

Although voids form part of asphalt or a surfacing seal structure, they are generally not included as material components. Voids are therefore visible in a structural model (Figure 2.25), but have no assigned properties. Kringos (2007) however, did assign material properties to the voids in developing a model to simulate combined mechanical and moisture induced damage in PAC structures. Voids formed part of the mesh and were termed *macro-pores* (Figure 2.21) which were allowed to hold water. The presence of water in the model resulted in moisture infused damage of the surrounding mastic and underlying base material.

Base

In the context of FE seal modelling, the base component not only provides structural support for the seal aggregate, but should be included to determine the measure of aggregate embedment for a seal subjected to loading. As previously stated, Milne (2004) included boundary conditions which simulated an elastic support layer and did, therefore, not investigate aggregate embedment. Huurman's (2010) improvement to the model did include a homogeneous base. The relation of Burgers' model as defined by Collop *et al.* (2003) was included by Huurman to simulate a granular base, while traffic loads as discussed by Woodside *et al.* (1992) were applied to the seal aggregate. Unbound materials exhibit stress-dependent behaviour and initial calculations by Huurman indicated that stress estimations in the upper part of the base, close to the surface of the seal ranged as follows: $\sigma_1 = 1.8$ MPa, $\sigma_2 = \sigma_3 = 1.0$ MPa for a $Mr - \theta$ model. Emanating from these estimations, base properties with Burger's model were calculated as presented in Table 2.2.
Other seal model inputs were; two different binder types ($70 - 100$ pen and 7% SBS mod) and two different aggregates shapes (smooth and rough). The models were limited to a maximum of 10000 cycles or 2.5 mm embedment. The results displayed no significant differences in the embedment rates and a maximum difference of less than 5% was obtained. Therefore, according to Huurman (2010), the results indicate

that the embedment rate primarily depends on the properties of the base which was not varied for the simulations.

Table 2.2: Base properties (Huurman, 2010).

Free rolling: 22 $m.s^{-1}$	**Acceleration:** 5.5 $m.s^{-1}$
E_0 = 1100 MPa	E_0 = 1100 MPa
E_1 = 100000 MPa	E_1 = 100000 MPa
η_1 = 100000 MPa.s	η_1 = 100000 MPa.s
η_{inu} = 500000 MPa.s	η_{inu} = 2000000 MPa.s
σ_0 = 0.497 MPa	σ_0 = 0.497 MPa
n = 0.855	n = 0.855
B = 1.384	B = 1.384

According to the TRH3 (2007), the properties in the upper part of the base close to the seal surface can be quantified with the ball penetration test (BPT). A FE model of the test was developed by Li and Liu (2011) to gain insight into the deformation characteristics. An asphalt layer served as the base layer and had a Drucker-Prager elastic-plastic constitutive model assigned to it. Although the standard weight and free falling height of the ball penetration test are 4.53 kg and 457 mm, Li and Liu (2011) used 13.61 kg and 800 mm respectively. Furthermore, the impact pulse distribution of the elastic collision between the weight and the 19 mm ball was assumed to be triangular, with a contact time of 0.01 seconds. The outcome of the model coupled the permanent deformation of the steel ball impact, with the resulting stresses and strains in the upper part of the base. This approach possesses the ability to quantify the contribution of the ball penetration test, as a method to determine the susceptibility of a base to embedment when subjected to traffic loads.

2.3.4 Traffic load applications

Measured tyre-road contact stresses, such as the SIM data (De Beer and Fisher, 2013), can be converted to load time functions for FEM implementation. Typical functions developed in such a manner were utilised by Milne (2004) to simulate the traffic load component for a 3D FE seal model. The normalised functions as illustrated in Figure 2.31 (a), represent the longitudinal stress distribution (TF2), transverse stress distribution (TF1) and vertical stress distribution (TF1) with time. The magnitudes of the functions are based on directional stress ratios with reference to the maximum vertical bulk stress σ_z. Milne (2004) applied the following directional stress ratios for free-rolling wheels:

a) Longitudinal stress $\sigma_x(t)$ was equal to 30% of σ_z distributed with TF2, superimposed on 2.5% of σ_x distributed with TF1 which represented rolling resistance.

b) Transverse stress $\sigma_y(t)$ was equal to 15% of σ_z distributed with TF1.

c) Vertical stress $\sigma_z(t)$ was equal to 100% of σ_z distributed with TF1.

In the case of a driven wheel, a σ_{driven} component was superimposed on the longitudinal stress. The component σ_{driven} was calculated with Equation 2.28 and distributed with TF1.

$$\sigma_{driven} = PP_{op}\frac{1 - loss}{v} \times \frac{1}{A} \tag{2.28}$$

where:

P = engine power output
P_{op} = engine operational output
$loss$ = power losses in gearbox and drive shafts
v = constant travelling velocity
A = tyre contact area

Implementation of the time functions requires translation of the bulk stresses to forces. These forces are assigned to individual aggregates. Milne (2004) translated bulk-scale stresses to a meso-scale forces per aggregate by multiplying the bulk stresses with the surface area of the aggregate. On that basis $\sigma_x(t)$, $\sigma_y(t)$ and $\sigma_z(t)$ were translated to $F_x(t)$, $F_y(t)$ and $F_z(t)$ as illustrated in Figure 2.31.

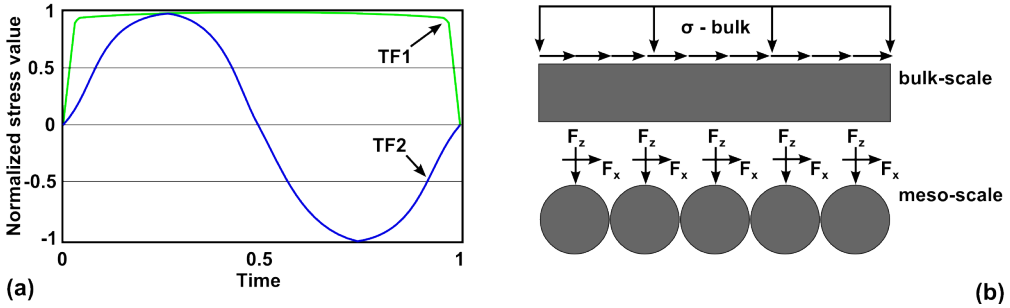

Figure 2.31: (a) Load time functions LT1 and LT2, (b) Bulk stress translation to meso-scale forces (Milne, 2004).

The exact position of the meso-scale forces are different for various scholars. Milne (2004) and Kringos (2007) distributed the force across the existing nodes in the upper part of the aggregate (Figure 2.32), while Huurman (2008) translated the total force to a single node at the pinnacle of the aggregate surface. Furthermore, assigning load time functions to the aggregates at linear time offsets, resulted in a rolling wheel effect across the surface of the FE models. Huurman (2008) and Mo *et al.* (2008) had similar load time functions to Milne (2004), while, Kringos (2007) selected compressive and shear pulses to represent $\sigma_z(t)$ and $\sigma_x(t)$ in the 2D plane. Kringos (2007)

indicated that the applied loads did not represent actual tyre-pavement loading, but were chosen to highlight the punishment of the individual model components and resulting stress and strain.

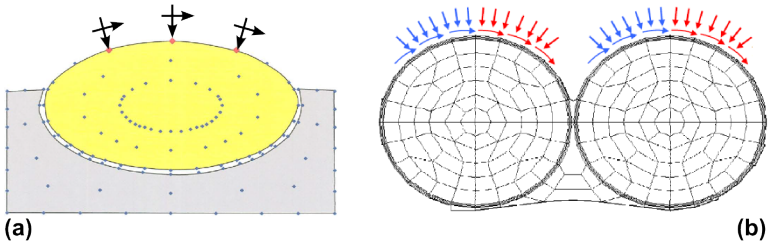

Figure 2.32: Meso-scale model load positions: (a) Section view of Milne's (2004) 3D Model, (b) 2D Model of Kringos (2007).

The traffic simulations in the models of numerous scholars consisted of load time functions with intermediate rest periods. The rest period is the time interval between successive loads and is dependent on the axle offset of the vehicle. However, according to Milne (2004), the rest period of a HV was typically 13 times the length of the load time function and therefore an excessive amount of computation time must be allocated in calculating the relaxation of the bitumen which occurs during this interval. This is unnecessary and inefficient, therefore scholars assume a rest period of two to three times the load time function.

2.4 Bituminous seal deterioration models

Empirical deterioration models for seals were developed by the University of Birmingham in an attempt to predict the asset's decay in condition (ISOHDM, 2004). Practitioners can thereby determine the time intervals of necessary maintenance to keep the asset at an acceptable standard. This process is illustrated in Figure 2.33. These models are commonly referred to as HDM-4 deterioration models. The HDM-4 deterioration models of particular interest with regard to this study include: structural crack initiation, ravelling initiation and surface texture loss. A discussion on each follows in this section with additional information presented in Appendix A.

2.4.1 Structural crack initiation

Structural cracking is effectively load, age and environmental associated cracking (ISOHDM, 2004). The model calculates the surface deterioration in two phase. The fist phase calculates the number of years to crack initiation. The second phase determines the crack progression as a percentage of total carriageway area. The

HDM-4 makes further distinction by characterising the severity of the crack width as follows:

a) Class 1: Crack width $\leq$ 1 mm

b) Class 2: 1 mm $<$ Crack width $\leq$ 3 mm

c) Class 3: Crack width $>$ 3 mm without spalling

d) Class 4: Crack width $>$ 3 mm spalling

Separate models are provided for the initiation and progression of 'all' and 'wide' cracking classes. The crack initiation and progression models for 'wide' structural cracking are extensions of the models for 'all' structural cracking. Wide structural cracking and the crack progression models are not considered in this study since fatigue cracking i.e. initiation of material micro cracking is the focus area with respect to the cohesive failure criterion. Calculations for wide cracking and crack progression models can be found elsewhere (ISOHDM, 2004).

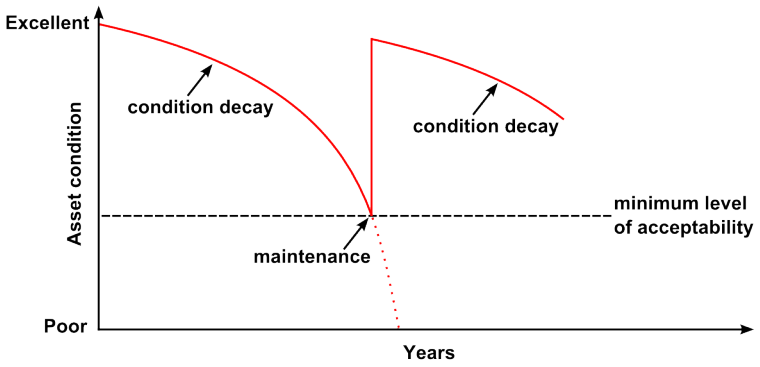

Figure 2.33: Application of deterioration models as a maintenance indication for asset management.

Figure 2.34 illustrates the logic for calculating the crack initiation for all structural cracks. The input variables presented in Figure 2.34 are direct input variables while other variables are derived as illustrated in Appendix A. Key definitions for all crack initiation models are summarised in Table 2.3. More variable definitions on all crack initiation models are presented in Appendix A. Crack initiation Classes 1 and 2 severe as a good indication for the commencement of surface maintenance. Negligence of maintenance intervention can result in perilous surface and subsurface deterioration, since these cracks allow vertical moisture ingress. The main discussion is therefore situated around Equation A.1, reprinted as Equation 2.29 for convenience.

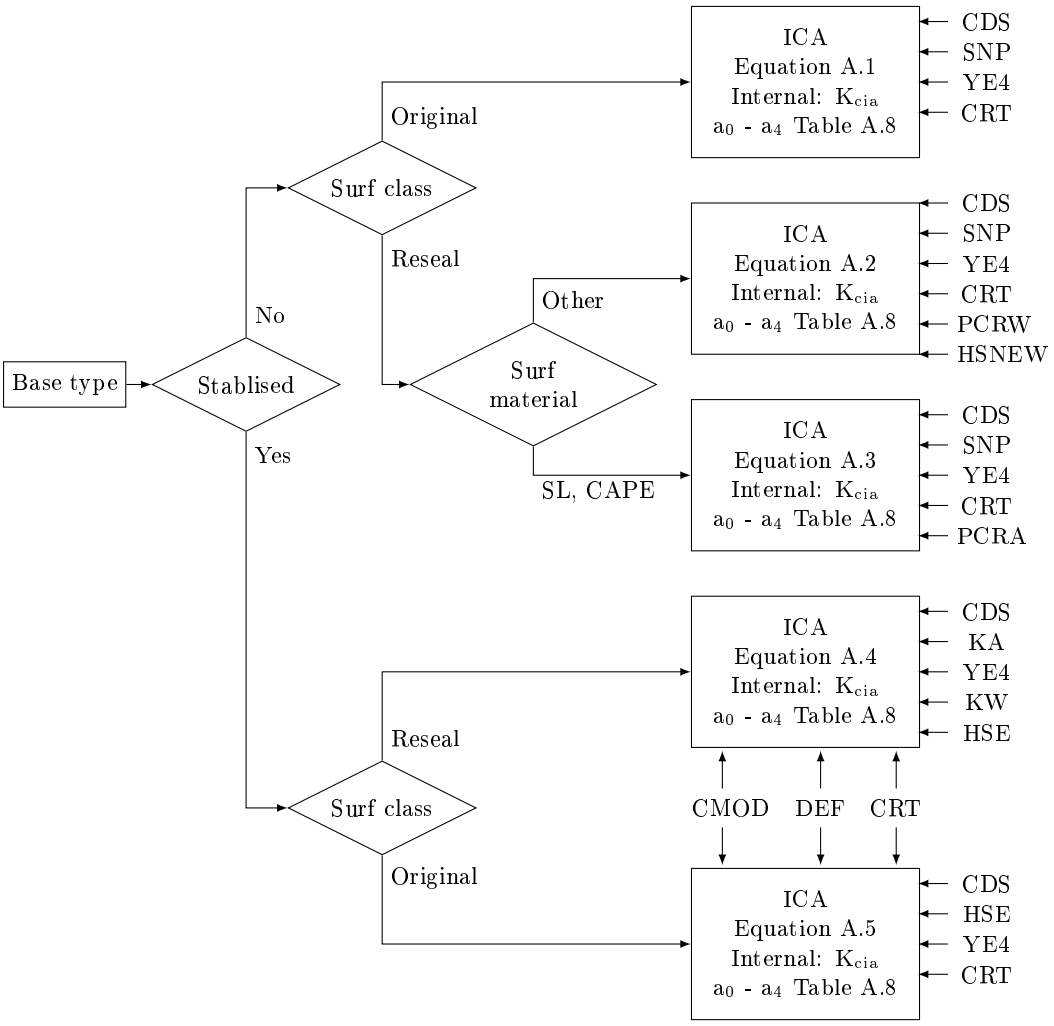

Figure 2.34: Flowchart for the HDM-4 crack initiation models - all structural cracks.

Table 2.3: Definitions of variables utilised in the crack initiation models (ICA).

Description	Variable
Time (years) to crack initiation for all structural cracks	ICA
Construction defects indicator for seals	CDS
Annual number of equivalent standard axles (millions/lane)	YE4
Average annual adjusted structural number of pavement	SNP
Mean Benkelman beam deflection in both wheel paths (mm)	DEF
Resilient modulus of stabilised material (GPa)	CMOD
Thickness of most resent surfacing (mm)	HSNEW
Combined thickness of previous underlying surfacing layers (mm)	HSOLD
Area of all structural cracking before most recent reseal (%)	PCRA
Area of wide structural cracking before most recent reseal (%)	PCRW
Crack retardation time (years) due to maintenance	CRT

Equation 2.29 determines the time in years for the initiation of structural cracks of an original seal on a non-stabilised base.

$$ICA = K_{cia}\{CDS^2 a_0 e^{\left[a_1 SNP + a_2\left(\frac{YE4}{SNP^2}\right)\right]} + CRT\} \tag{2.29}$$

The crack initiation model (Equation 2.29) relies heavily on the adjusted structural number (SNP) of the pavement. The SNP is derived from the AASHTO structural number method (SN). Although the SN parameter is relatively easy to calculate and simple to apply, it is highly empirical and was developed for material conditions foreign to South Africa. It is not sensitive to quality of the base material or pavement balance (SAPEM, 2014). Layer positions can be switched without obtaining a difference in the SN.

The crack initiation model does include different surface dressings, but does not consider the effects of binder types and application rates or aggregate spread rates. A construction defects indicator value (CDS-value) is included to address the quality of materials and workmanship. It is in the light of this variability and selection of material combinations where a FE seal model can contribute in determining the deterioration process. FE models can be used to simulate crack initiation intervals of seals for a range of material combinations and traffic conditions.

2.4.2 Ravelling initiation

The risk to seal ravelling in practice is associated with the period after construction when the road is opened for traffic. The HDM-4 ravelling initiation model addresses therefore the risk criterion and corresponds to the definition of adhesive failure for seals as discussed in Section 2.1.3. The logic for the HDM-4 ravelling initiation is illustrated in Figure 2.35, while the variables used in the model are listed in Table 2.4. The ravelling initiation calculation includes a ravelling retardation factor RRF which is a function of maintenance (Equation 2.30).

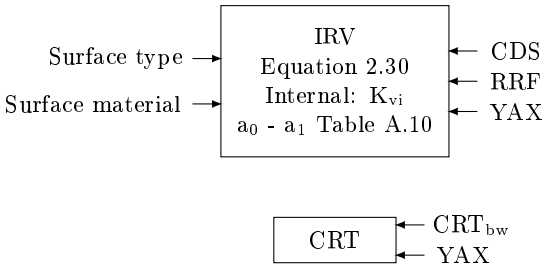

Figure 2.35: Flowchart for the HDM-4 ravelling initiation model.

$$IRV = K_{vi}(CDS)^2 a_0 (RRF) e^{a_1 YAX} \tag{2.30}$$

Table 2.4: Definitions of variables utilised in the ravelling initiation model.

Description	Variable
Time (years) to ravelling initiation	IRV
Construction defects indicator for seals	CDS
Annual number of axles for all vehicle classes (million/lane) in analysis year	YAX
Ravelling retardation factor	RRF

The sensitivity of the Equation 2.30 is source of concern. As previously mentioned, the risk to ravelling for seals follows the period during the initial stages of trafficking, while the IRV determines the time to ravelling in a measure of years. The CDS value describes the binder condition, but differentiation between binder type, surface temperature, aggregate size and vehicle speed are factors that are not considered in Equation 2.30. FE models can be used to determine ravelling initiation that includes the latter factors.

2.4.3 Texture depth loss

The initial surface texture depth emanates from the sand patch test. The logic for the HDM-4 texture depth loss model is illustrated in Figure 2.36, while Table 2.5 defines the variables that are utilised in the texture depth deterioration model. Equations 2.31 and 2.32 relies on equivalent light vehicle (ELV) passes. It therefore requires the assumed equivalency factor of 40 (TRH3, 2007) to convert HV traffic to LV traffic. Both equations do not consider the extend of emebement during construction, the base type or seal aggregate size. The latter are important factors which contributes to surface texture loss.

Table 2.5: Definitions for variables in the HDM-4 texture depth loss model.

Description	Variable
Texture depth (mm) measured at the time of design investigation	TD_s
Initial value of the texture depth (mm) used in simulation	TD_i
Initial texture depth (mm) at the time of surfacing layer construction	ITD
Rate of texture depth change	$\triangle$TDT
Number of equivalent light vehicle passes since construction of surface layer	NELV
Number of equivalent light vehicle passes for analysis year	$\triangle$NELV
Texture depth (mm) at the start of the analysis year	TD_a
Texture depth (mm) at the end of the analysis year	TD_b
Incremental change (mm) in the texture depth for the analysis year	$\triangle$TD
Annual average texture depth for the analysis year	TD_{av}

$$TD_i = ITD(1 - \triangle TDTlogNELV) \tag{2.31}$$

$$\triangle TD = K_{td}\{ITD - TD_a - a_0 ITDlog(10^{\frac{ITD-TD_a}{a_0 ITD}} + \triangle NELV)\} \tag{2.32}$$

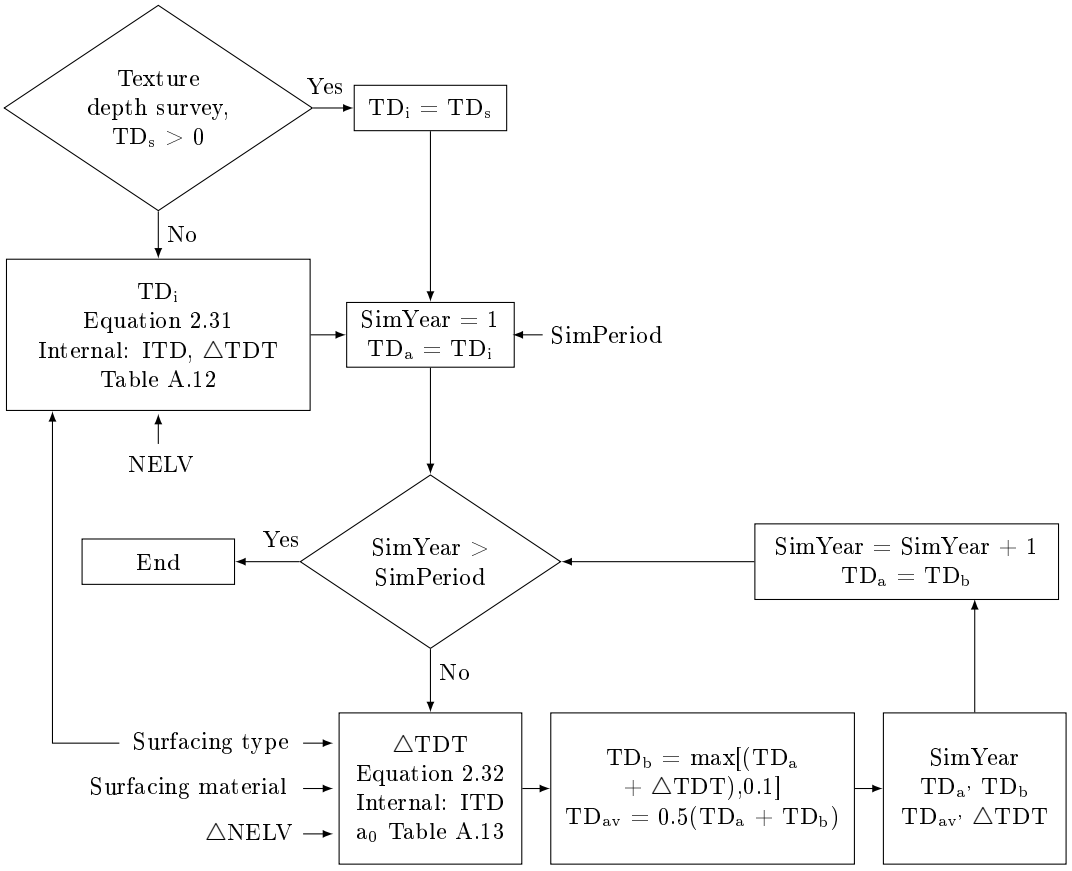

Figure 2.36: Flowchart for the HDM-4 texture loss model.

2.5 Closure

With reference to the literature review, seal design has an adaptive, empirical approach which is generally dependent on the climatic region and construction materials. Single size crushed aggregates and bitumen binders are the main components of a seal structure which is constructed on top of an existing base, providing skid resistance and a waterproof cover layer. The seal layer is susceptible to adhesive failure which causes stone loss and cohesive failure which causes fatigue cracks, resulting in water ingress. Soft base layers result in embedment which causes a reduction in surface texture, therefore a loss of skid resistance in wet conditions. These failure mechanisms can be influenced by a combination of factors which are not easily measured, therefore, an alternative approach is required to observe the phenomena.

Researchers are turning towards FEM and DEM modelling to gain insight and knowledge on the damage mechanics of seals. A typical model is constructed on meso-scale where unique geometries and material properties are allocated for the aggregates, binder, supporting base and binder-aggregate adhesive bond. Model geometry consists either of idealised shapes representing the individual components or X-ray image deduced shapes. Both approaches are simulated in the 2D plane or in a 3D continuum, each having advantages and disadvantages. A 2D simulation is computationally less expensive, therefore promoting a greater number of component combination simulations in comparison to a 3D simulation. A 3D simulation is a more realistic representation of the physical structure, but is also computationally more demanding and in many cases requires additional hardware. A 3D simulation includes vertical, longitudinal and lateral load components, while a 2D simulation manages only two components.

Pneumatic tyre loads have three directional stress components, each having a unique load time function. The load time functions are translated to meso-scale forces and applied to aggregate nodes reserved for loading. Factors that have an influence on the load magnitude are the axle weight, tyre inflation pressure, road surface texture, tyre rubber properties and the wheel motion. Linear time offsetting of the load time functions creates a rolling wheel effect on the seal model surface, resulting in stress and strain in the various components. From these stresses and strains insights into the damage mechanics of seals are obtained.

Insights can be used to adjust or develop new surface deterioration models. Current models exist for surface structural cracking, ravelling and surface texture loss. These models however, were not developed for South African conditions and require calibration or modifications.

3. Methodology

The purpose of this study was the development and simulation of FE seal models that provided phenomenological insights into the structural response of seals. These responses are transformed by further developments to determine the service life of a seal. This chapter details thus the sequence of developments by providing an overall research approach, a detailed methodology and the limitations of this study.

3.1 Research approach

An integrated research process, utilising different techniques resulted in obtaining the objectives of this study. The integrated process consisted of three parallel studies which were: this study, a study by Mukandila (2015) and a study by van Zyl (2015). The contributions of Mukandila (2015) and van Zyl (2015) towards this study are summarised in Chapter 4 and Chapter 6 respectively, while the interactions among the three parallel studies are illustrated in Figure 3.1. Laboratory experiments, computer model simulations, field measurements and observations, and comparative analyses were the fundamental techniques utilised in obtaining the objectives of this study. Each technique is briefly discussed in this section with reference to its appropriateness, strengths and weaknesses. A detailed description of the application and the researcher responsible for each technique is presented in the research methodology, Section 3.2.

3.1.1 Laboratory experiments

Laboratory experiments were conducted for material characterisation of the seal components and the traffic load functions. Material characterisation was related to constitutive models which were implemented with the traffic load functions into computer model simulations of seals.

Laboratory testing influencing factors and material variability are controllable. Defining appropriate sampling sizes result in a true representation of a population which credits the observations made in the laboratory. The main advantage of laboratory

testing is the ability to isolate specific phenomena for measurement or observation. In some cases this may lead to the purchasing of expensive instruments which need calibration and maintenance for accurate measurements. Damaged or broken instruments result in time losses and some instruments may not be able to measure the phenomenon of interest. It must also be noted that some experiments are time consuming and may not be repeatable within a certain time frame.

3.1.2 Computer model simulations

Computer model simulations were conducted to observe the response features of the various seal structures with reference to the material characteristics and traffic loading. Structural response phenomena that are difficult or in some case impossible to measure can be observed with simulations, where the developmental environment is fully controllable. Simulation output data is objective and not influenced by measuring instruments or the malfunctioning thereof. It is therefore an exact reflection of the model setup i.e. what goes in is what comes out.
Although models aim to represent reality, they provide an idealised simplification of it, consequently yielding simplified results. Robust results require sound, accurate and reliable theories which can be formulated by sufficient and qualitative data. Obtaining this kind of input data can be both time consuming and expensive. The output of the simulations needs to be verified and validated, therefore alternative data is required.

3.1.3 Field measurements and observations

Field measurements and observations of road seal response and distress phenomena were conducted for verification and validation of the computer simulations. The measured data and observations represent reality, but interpretation thereof can in some cases be subjective. Field variables and influencing factors are not controllable, only observable and therefore it is not always possible to isolate and measure the phenomenon of interest or obtain data on all the factors influencing it. Quality of the data depends on the type and accuracy of the measuring instrument and also in some cases the competency of the instrument operator. Field testing sites are not always readily accessible which may result in time losses. When measurements are conducted on roads it is of utmost importance to be visible at all times and fully comply with the safety requirements and precautions of the test site.

3.1.4 Comparative analysis

Comparative analyses of the various seal structures, material characteristics and traffic loading were conducted subsequent the verification and validation processes to fulfil the objectives of this study. A comparative analysis indicates the differences and similarities of an item with reference to similar background conditions. This knowledge facilitates the decision process of selecting one item over another.
Altering background conditions produce different results. Therefore, comparing two items with different background conditions can be misleading in a selection process. Comparisons cannot be made with incomplete data sets.

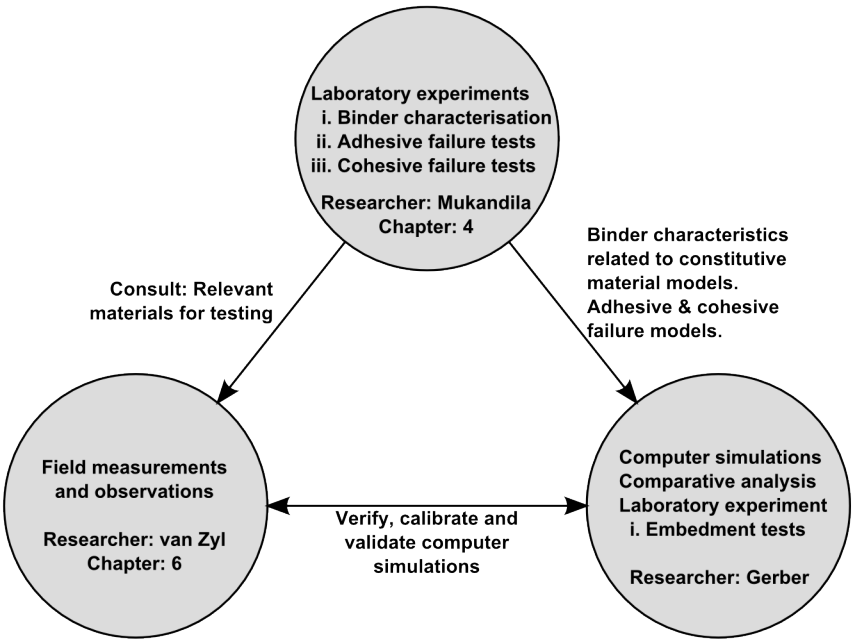

Figure 3.1: Schematic layout of the integrated research approach.

3.2 Research methodology

The research methodology can be compared to an academic production line, where ideas, knowledge and theories serve as raw material, while the objectives serve as the product. In between the raw material and final product a number of processes occur. These processes represent the research methodology and in this study consist of: material characterisation, finite element (FE) seal model development, traffic model formulation, seal model verification and validation, and a comparative analysis. This section elaborates on each of these processes.

3.2.1 Material characterisation

The seal structure was separated into meso-scale material components which included: aggregates, binders, slurry, adhesive interfaces, air voids and base layers. In this section the characterisation process of each material component is discussed. Due to the integrated process, reference is made to the researcher responsible for the development of each component and the relation of the characteristics to the various constitutive material models, which were implemented in the computer modelling phase.

Aggregates

Characterisation of the aggregates pertaining to this study in the context of seal modelling was deduced from literature. Similar to Milne (2004), Huurman (2010) and Onifade *et al.* (2013) this study assumed linear elastic properties for all the aggregates. The properties consisted of an elastic modulus and a Poisson's ratio for each aggregate type as presented in Table 3.1. The aggregates included quartzite, dolerite and granite which are typical aggregates in the seal construction process.

Table 3.1: Mechanical properties of rocks (Budavari, 1983).

Material	Elastic modulus [GPa]	Poisson's ratio[i]
Quartzite	68-78	0.15-0.35
Dolerite	71-86	0.15-0.35
Granite	17-75	0.15-0.35

[i] select $\nu = 0.15$ for parent rock

Due to the assumption of linear elasticity, aggregates cannot exhibit wear, be crushed or permanently deformed. Since these phenomena were not the interests of the structural models, elasticity was considered an effective assumption.

Binders and slurry

Laboratory characterisation of binders was conducted by Mukandila (2015) and the procedures are summarised as follows: Binder response and binder fatigue characteristics were of interest, therefore the Dynamic Shear Rheometer (DSR) was selected as the testing instrument. The DSR is commonly used to determine rheological properties of viscoelastic materials and the machine selected for testing (Physica MCR 301) was equipped with an environmental test chamber (ETC). The ETC allowed temperature control based on electrical heating and liquid nitrogen gas cooling. A

standard test procedure known as the *parallel plate* test was conducted to characterise the binder response properties. A modified test procedure known as *binder column* tests characterised the fatigue properties of the binder.

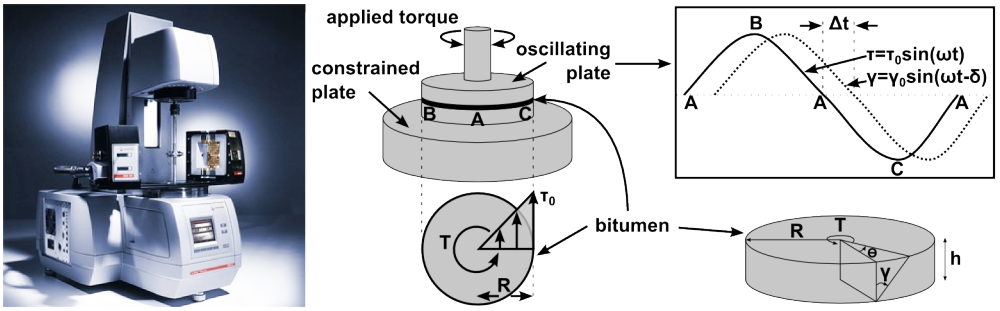

Figure 3.2: Depiction of the DSR equipped with an ETC and schematic layout of the parallel plate test setup for bitumen (Woldekidan, 2011).

A parallel plate test consists of a binder film wedged between two plates as illustrated in Figure 3.2. The dimensions of the plates and the thickness of the binder film depend on the testing temperature. Typically for high to intermediate temperatures a plate diameter of 25 mm and a 1 mm film thickness is used. For intermediate to cold temperatures the plate diameter changes to 8 mm with a 2 mm film thickness. A defined oscillating torque T is applied to the top plate while the bottom plate remains fully constrained. The angular rotation per cycle θ is measured. Interpretation of the applied torque and measured deformation γ provide the fundamental material response properties for the specimen such as the complex shear modulus G^*, complex shear compliance J^* and the phase angle δ. The position of interpretation is at the edge of the specimen and the DSR software automatically adjusts the data to include the effects of inertia and machine compliance factors. The basic response relations are presented in Equation 3.1 to Equation 3.5.

$$\gamma_{max} = \frac{\theta R}{h} \quad and \quad \tau_{max} = \frac{2T}{\pi R^3} \tag{3.1}$$

where:

θ = radial rotation
R = specimen radius
h = film thickness
T = applied torque

$$|G^*(\omega)| = \frac{\tau_{max}}{\gamma_{max}} \tag{3.2}$$

where:

τ_{max} = maximum shear stress

γ_{max} = maximum shear strain

$$G^*(\omega) = |G^*(\omega)| \cos(\delta) + i|G^*(\omega)| \sin(\delta) = G' + iG'' \tag{3.3}$$

where:

$|G^*|$ = magnitude of the dynamic shear modulus
G' = storage shear modulus
G'' = loss shear modulus
δ = phase angle
i = complex notation

$$\delta = \omega \triangle t = \arctan G''/G' \tag{3.4}$$

where:

ω = angular velocity
$\triangle t$ = time lag between stress and stain signals

It is therefore apparent that the dynamic shear modulus $|G^*|$ is the amplitude of the complex shear modulus G^* and is defined in Equation 3.5.

$$|G^*| = \sqrt{(G')^2 + (G'')^2} \tag{3.5}$$

When stress controlled tests are conducted with the DSR, the creep compliance of the bitumen is of interest. The creep compliance is defined in Equation 3.6.

$$J^*(\omega) = |J^*(\omega)| \cos(\delta) + i|J^*(\omega)| \sin(\delta) = J' + iJ'' \tag{3.6}$$

where:

$|J^*|$ = magnitude of the complex creep compliance
J' = storage creep compliance
J'' = creep compliance

The shear stress and strain are not uniformly distributed across the cylindrical specimen. The specimen setup assumes that low stress levels are applied in the region where the material exhibits linear viscoelastic responses. Higher stresses result in non-linear responses and at these ranges binder column fatigue tests (Figure 3.3) were conducted.

Binder column test specimens consist of a 20 mm column of binder, with steel rings enclosing the column ends. The steel rings have a diameter of 8 mm and allow the mounting of the specimen onto the DSR with a unique clamping mechanism. Similar to the parallel plate setup, the bottom ring of the binder column is fully restrained

while an oscillating torque is applied to the top ring. Due to the modification in test specimen geometry, transfer functions are utilised for the interpretation of the applied toque and measured deformation. The transfer functions relate the applied torque to shear stress and shear strain to angular deformation as defined in Equation 3.7 and Equation 3.8 respectively.

$$\tau_{max} = k_1 \frac{2T}{\pi R^3} \tag{3.7}$$

$$\gamma_{max} = k_2 \frac{\theta R}{h_{eff}} \tag{3.8}$$

where:

θ = radial rotation
R = specimen radius
h_{eff} = effective sample height
T = applied torque
$k_1,\ k_2$ = transfer function constants

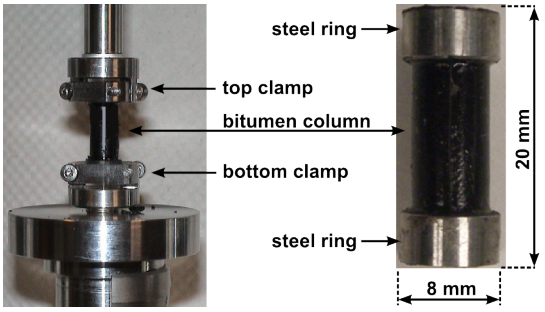

Figure 3.3: DSR bitumen column test setup (Woldekidan, 2011).

Two different binders were characterised by Mukandila (2015) and included in the FE seal model architecture. The binders included: 70-100 penetration grade binder (Pen 70-100) and cationic rapid set emulsion 60% spray grade (CRS-60). In the context of seal construction: Pen 70-100 binders are typically applied as tack coats and penetration coats. Emulsions can be used for the tack coat and penetration coat applications, but can also be diluted with water and applied as cover sprays (fog sprays). Emulsions serve as the binder component in slurry mixtures where ionic stable grade emulsions are generally preferred. Slurry layers are applied in the construction of cape seals and Mukandila's (2015) conducted trial tests on a slurry mixture, but indicated that the graded crushed aggregate fraction inhibits proper sample preparation which affects the test results. Slurry testing was therefore discontinued and Mukandila (2015) recommended that the aggregate fraction be replaced

with crusher dust in future testing. This would effectively reduce the slurry mixture to a mortar-like mixture. For the purpose of this study, mortar characteristics as defined by the LOT program (Huurman, 2008) were used as a substitute for the slurry behaviour. A summary of the laboratory testing as pertaining to this study is presented in Table 3.2.

Table 3.2: DSR response and fatigue testing for binders (Mukandila, 2015).

Test	Binder	Binder condition	Temp. [$^{\circ}C$]
Parallel plate	Pen 70-100	V[i]	0, 10, 25, 50
Parallel plate	Pen 70-100	V + WC[ii], PAV[iii], PAV+WC	25
Parallel plate	CRS-60	V, V + WC, PAV, PAV+WC	25
Parallel plate	Field recovered	No laboratory conditioning	25
Binder column	Pen 70-100	V	10, 25

[i] Virgin [ii] Virgin & Water Conditioned [iii] Pressure Aging Vessel (100 $^{\circ}C$, 24 hours)

The binders were subjected to four material conditions. These conditions include: virgin (V) binder from the refinery, virgin binder conditioned with water (V + WC), virgin binder conditioned with the pressure aging vessel (PAV) and PAV binder conditioned with water (PAV + WC). The objective of the PAV is the simulation of long term field aging and the standard procedures as described in AASHTO R28 or ASTM D6521-08 result in aged samples of approximately 7 to 10 years for asphalt binders (Bahia and Anderson, 1995). However, to verify the PAV aged specimens for seals, Mukandila (2015) conducted tests on field recovered 70-100 penetration grade binders of known ages. No short term aging (Rolling Thin Film Oven) was conducted prior to PAV conditioning.

Interpretation and analysis of the response and fatigue data with reference to seal modelling followed laboratory testing. The response data was translated to an existing constitutive material model, ready for implementation into the Abaqus FE package. The existing constitutive material model is the Prony series which is a modified representation of the Generalised Maxwell model. The relaxation modulus of the Prony series in the time domain is presented in Equation 3.9. The relaxation modulus is then rearranged in terms of the instantaneous shear modulus G_0 as defined in Equation 3.10. From Equation 3.5, the formulation of G^* with the Prony series in terms of the storage and loss moduli in the frequency domain is defined in Equation 3.11 and Equation 3.12 respectively.

$$G(t) = G_{\infty} + \sum_{i=1}^{N} G_i e^{\frac{-t}{\tau_i}} \tag{3.9}$$

$$G(t) = G_0 \left[1 - \sum_{i=1}^{N} \alpha_i \left(1 - e^{\frac{-t}{\tau_i}}\right)\right] \tag{3.10}$$

$$G'(\omega) = G_0 \left[1 - \sum_{i=1}^{N} \alpha_i\right] + G_0 \left[\sum_{i=1}^{N} \frac{\alpha_i \tau_i^2 \omega^2}{1 + \tau_i^2 \omega^2}\right] \tag{3.11}$$

$$G''(\omega) = G_0 \left[\sum_{i=1}^{N} \frac{\alpha_i \tau_i \omega}{1 + \tau_i^2 \omega^2}\right] \tag{3.12}$$

where:

G_∞ = infinite relaxation modulus
G_0 = instantaneous shear modulus
α_i = normalised stiffness reduction of the the i^{th} Maxwell element
τ_i = relaxation rate of the the i^{th} Maxwell element
ω = angular frequency
N = number of Maxwell elements
t = time

$$G_0 = G_\infty + \sum_{i=1}^{N} G_i \tag{3.13}$$

$$\alpha_i = \frac{G_i}{G_0} \tag{3.14}$$

$$G = \frac{E}{2(\nu + 1)} \tag{3.15}$$

where:

G = shear modulus
E = elastic modulus
ν = Poisson's ratio

A Prony series consisting of one elastic element and approximately nine Maxwell elements was developed for each binder, binder condition and testing temperature. The Prony series parameters are thus E_0, α_i, τ_i and ν. A Poisson's ratio of 0.5 was assumed for al binder material calculations. The binder column fatigue data was converted to end of life transfer functions per test temperature in the format as defined in Equation 3.16.

$$\tau = a(1 + N_f)^b \tag{3.16}$$

where:

τ = constant shear stress
N_f = number of DSR load cycles to failure
$a,\ b$ = material parameters

Each transfer function relates the number of DSR cycles N_f to cohesive fatigue at a constant applied load τ. The application of the fatigue model with reference to the FE seal model is addressed Section 3.2.4.

Adhesive interface

Laboratory characterisation of the binder-aggregate adhesive interface was also conducted by Mukandila (2015) and the procedures are summarised as follows:
Similar to the binder fatigue characterisation, the binder-aggregate adhesive fatigue characterisation was conducted with the DSR utilising a different test specimen. The test specimens termed *stone column* specimens, consisted of two 11 mm diameter aggregate cores, each having a height of approximately 15 mm which were bound by a 100 μm binder film as illustrated in Figure 3.4. The specimens were mounted to the DSR with the same clamp system utilised for binder column fatigue testing. The bottom clamp was fully constrained while the top clamp was constrained in all the degrees of freedom except for rotation around the vertical axis to which an oscillating torque was applied.

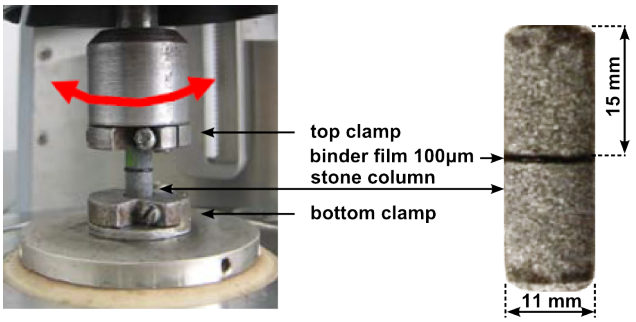

Figure 3.4: DSR stone column test setup (Huurman, 2008).

According to Frolov *et al.* (1983), a reduced film thickness in the ranges of 20 μm to 35 μm yields optimum adhesive stress results. An increase to the film thickness, as is the case with Mukandila, results in a reduction of the failure stress, but more so can invoke multiple failure mechanism simultaneously i.e. adhesive and cohesive failure. Mukandila (2015) conducted stone column tests with 70-100 penetration grade binder and dolerite aggregate. A summary of the stone column adhesive testing, as pertaining to this study, is presented in Table 3.3.

Table 3.3: DSR stone column adhesive interface fatigue testing (Mukandila, 2015).

Aggregate	Binder	Binder condition	Temp. [°C]
Dolerite	Pen 70-100	Virgin	10, 25

The stone column test was designed to address the adhesive failure mechanism by exhibiting phenomenological insights into the fatigue failure of the adhesive interface. The test is therefore a comprehensive approach, where factors such as the aggregate surface texture and surface energy contributions are empirically included in the fatigue relationship. Characterisation of the adhesive interface response was deduced from the complex modulus and not from the stone column tests. Similar to the approaches of Huurman (2008) and Mo (2010), the adhesive interface response was represented by a linear traction separation model as defined in Equation 3.17 to Equation 3.19. The input parameters are therefore the directional stiffness response parameters K_{nn}, K_{ss}, K_{tt}.

$$\mathbf{t} = \begin{Bmatrix} t_n \\ t_s \\ t_t \end{Bmatrix} = \begin{bmatrix} K_{nn} & & \\ & K_{ss} & \\ & & K_{tt} \end{bmatrix} \begin{Bmatrix} \epsilon_n \\ \epsilon_s \\ \epsilon_t \end{Bmatrix} = \mathbf{K}\epsilon \tag{3.17}$$

where:

$\mathbf{t}$ = nominal traction stress vector

$$K_{nn} = \frac{E^*}{film \quad thickness} \tag{3.18}$$

$$K_{ss,tt} = \frac{G^*}{film \quad thickness} \tag{3.19}$$

where:

K_{nn} = normal stiffness response parameter

$K_{ss,tt}$ = shear stiffness response parameters

E^* = complex elastic modulus

G^* = complex shear modulus

Interpretation and analysis of the stone column fatigue data followed a similar procedure to the binder column fatigue data. The stone column fatigue data was converted to end of life transfer functions per test temperature in the format as defined in Equation 3.20.

$$\tau = a(1 + N_f)^b \tag{3.20}$$

where:

τ = constant shear stress

N_f = number of DSR load cycles to failure

$a,\ b$ = material parameters

Each transfer function relates the number of DSR cycles N_f to adhesive fatigue at a constant applied load τ. The application of the fatigue model with reference to the FE seal model is addressed Section 3.2.4.

Air voids

General seal design practice assumes that the spaces between the seal aggregates are neatly filled with bitumen in a bottom-up process during binder application. Van Zyl (2015) however, indicates that air voids still exist in some seal layers where it was assumed that the binder would completely fill the available air volumes. Air voids were assigned to certain seal structures, but without any material characteristics. Air voids represent thus empty spaces within the seal model environment.

Base

Triaxial and California bearing ratio (CBR) tests are well known test methodologies in obtaining the bulk response properties of unbound base layers. Similarly, unconfined compressive strength (UCS) tests and indirect tensile strength (ITS) tests are standard procedures for acquiring the bulk response characteristics of bound materials. None of these tests are able to characterise the behaviour of the upper part of the base layer with reference to seal aggregate embedment. In the interest of completing the computer simulations (Figure 3.1), the outstanding base material characterisation component of the upper 30 mm of an unbound base layer was conducted within the ambit of this study.

Standard laboratory Ball Penetration Tests (BPTs) and a modified version thereof termed, *Repeated Ball Penetration Tests* (RBPT), were conducted to gain insight into the embedment phenomenon. The laboratory setup of the standard BPT (TMH6: Method ST4) is illustrated in Figure 3.5. Specimens were prepared and tested inside a 150 mm diameter steel mould which was attached onto a steel base plate. The base plate was affixed to the laboratory floor during testing. Embedment was measured with a HBM linear variable displacement transducer (LVDT) that was connected to a QuantumX MX840A (8-channel universal amplifier) data acquisition system.

Interpretation of the ball penetration values with a single Marshall hammer blow on crushed stone bases are troublesome and vary in practice. If the initial blow results in a neat half-moon shape, it should be used as the ball penetration value. However, if aggregate breakage or lateral material displacement occurs with the initial blow, it should be interpreted as a seating blow and a secondary blow must be applied. In such instances, the difference between the first and the second blow results in the ball penetration value.

Restrictions on the LVDT did not allow accurate time measurements of the elastic collision between the sliding weight and 19 mm steel ball, therefore an electrical circuit was connected to the steel ball and the foot-piece in separate tests to measure the contact time t_c. A thin film of isolation material was placed between the ball and the foot-piece creating an open circuit (9 volt). Dropping the weight resulted

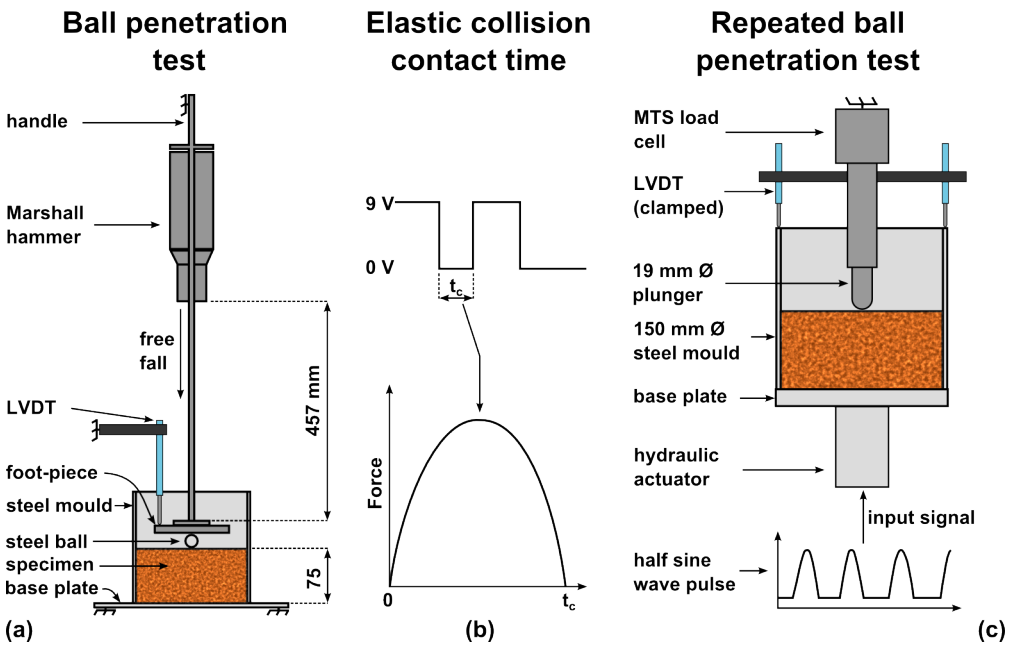

Figure 3.5: (a) Ball penetration test setup, (b) Contact time of the collision between the Marshall hammer and steel ball, (c) Repeated ball penetration setup.

in the foot-piece piercing through the isolation film and closing the circuit (0 volt). The elastic impact caused a small recoil allowing a momentarily open circuit before coming to rest (closed circuit) as illustrated in Figure 3.5. Contact time measurements were conducted on concrete (hard) and sand seal (soft) surfaces. Both cases resulted in measurements of 0.048 to 0.056 seconds, therefore t_c was approximated to be 0.052 seconds.

Test specimens inside the steel mould were also attached to the base plate of the material testing machine (MTS), mounted on top of the hydraulic actuator which has a testing range of 1 kN to 100 kN. A 19 mm diameter steel plunger, representing the 19 mm steel ball, was connected to the MTS load cell as illustrated in Figure 3.5. Three LVDTs were mounted around the top edge of the steel mould to capture the permanent deformation data of the test specimen.

The applied load shape was defined by the input signal, which consisted of a continuous half sine wave pulse with rest periods. Testing was conducted around the lower limit of the MTS and therefore a low frequency wave pulse of 1 Hz was applied to increase the accuracy of the applied loads. This resulted in a loading time of 0.5 seconds followed by a rest period of also 0.5 seconds. The pulse period represents vehicle speeds of less than 5 km/h, similar to the SIM data measurements. Load controlled tests were conducted at 0.5 kN, 1.0 kN and 5.0 kN. Each test consisted of a new specimen, an initial seating load with a magnitude of 0.1 kN followed by 10 000 cycles of the applied load.

Granular test specimens were prepared with a G2 limestone acquired from Cape Lime Quarry in Vredendal. This is the same material that was used in the SANRAL project, NRA R.027-080-2011/1. The grading of the test specimens followed the COLTO specification (Table 3.4), but the aggregate fractions greater than 13.2 mm were excluded from the mix to reduce the risk of aggregate breakage, lateral material displacement and increase the certainty that embedment is represented with the initial blow.

Table 3.4: Limestone (G2) grading.

Sieve size [mm]	COLTO lower limit. Passing [%]	Limestone samples. Passing [%]	COLTO upper limit. Passing [%]
37.5	100	100	100
26.5	84	89	94
19.0	71	76	84
13.2	59	66	75
4.75	36	46	53
2.0	23	34	40
0.425	11	21	24
0.075	4	8	12

Specimens were compacted inside the steel mould at four different levels of compaction effort. Compaction was done with the Bosch vibratory compaction hammer at the material's optimum moisture content (OMC). The final specimen height ranged between 68 mm and 75 mm depending on the level of compaction. Thereafter, specimens were cured inside the mould, following one of two protocols as presented in Table 3.5. The first protocol aimed at reducing the moisture content inside the specimen, by exposing the specimen to the oven conditions at 30°C. This accelerated the hydration process from the surface downward. The second protocol allowed moisture to be retained inside the specimen while the intrinsic material properties stabilised. This was done by insulating the specimen with plastic before exposing it to the oven conditions. The later protocol created favourable embedment conditions. A summary of all the specimens is presented in Table 3.5. Three BPTs and three RBPTs were conducted per set.

Table 3.5: Limestone specimen preparation.

Set	Quantity	Compaction effort	Curing
1	6	35 seconds	40 hours @ 30°C exposed
2	6	17 seconds	40 hours @ 30°C exposed
3	6	10 seconds	40 hours @ 30°C exposed
4	7	5 seconds	40 hours @ 30°C exposed
5	7	5 seconds	12 hours @ 30°C insulated

Data interpretation of the BPT and RBPT were divided into two categories: the response characteristics of the granular layer's upper 30 mm and the embedment potential thereof, which is in principle the permanent deformation potential.
Response characteristics include the Young's modulus E and Poisson's ratio ν of the material. These properties were back calculated by replicating the initial load cycle of the RBPT with a FE model. The linear elastic FE model assumed symmetry and therefore represented only a quarter of the test as illustrated in Figure 3.6. The base and radial edges were fully constrained, while a frictionless contact condition was specified between the steel ball and specimen surface. This mechanistic-empirical approach resulted in the relation of the model response properties (E, ν) and elastic deflection u_e to the total deflection of the initial RBPT load cycle (Figure 3.6).

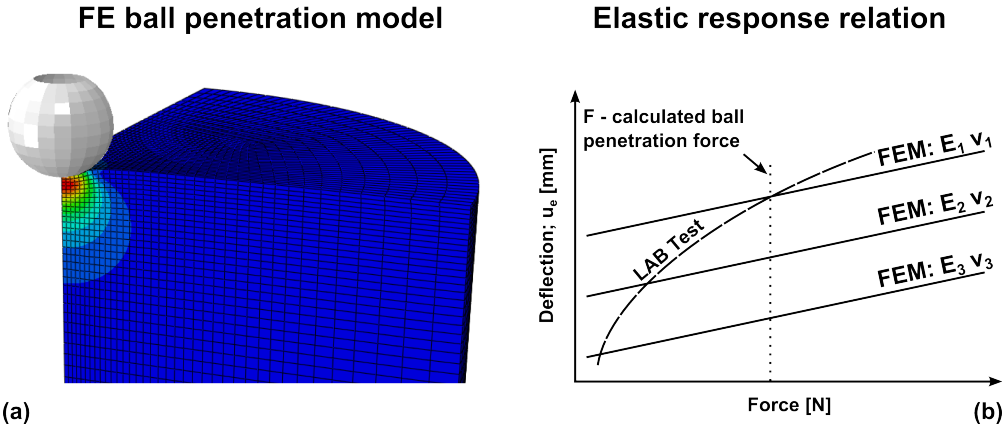

Figure 3.6: (a) FE ball penetration model, (b) Elastic response back calculation.

Response properties can be determined for each material condition at a certain applied force. Since the ball penetration test determines the embedment potential, the force generated by this test should be applied in determining the elastic properties of the material. The BPT force is derived as defined in Equations 3.21 to 3.24.

$$PE = KE \tag{3.21}$$

$$mgh = \frac{1}{2}mv^2 \tag{3.22}$$

where:

PE = potential energy
KE = kinetic energy
m = mass of the Marshall hammer (4.53 kg)
g = gravity (9.81 $m.s^{-2}$)
h = hammer free fall height (457 mm)
v = hammer velocity just before impact (2.944 $m.s^{-1}$)

Applying the linear impulse-momentum principle and assuming that the hammer-ball impulse F is represented by a half sine wave form results in:

$$mv = \int_0^{t_c} F dt \tag{3.23}$$

$$F = k_1 \sin(k_2 t) \tag{3.24}$$

where:

k_1 = peak force
$k_2 = \pi / t_c$
t_c = elastic collision contact time

Analysis of the permanent deformation potential consisted of four phases. During the first phase a linear relation was established between the magnitude of the permanent deformation u_p and the total plunger displacement u_e of the initial RBPT cycle (Equation 3.25). Here, the term *total displacement* comprised the permanent deformation plus the resilient deformation per load cycle.

$$u_p = a_1 u_e + b_1 \tag{3.25}$$

where:

$u_p,\ u_e$ = magnitude of the permanent deformation and total deflection
$a_1,\ b_1$ = material parameters

$$b_1 = a_2 F + b_2 \tag{3.26}$$

where:

F = applied load
$a_2,\ b_2$ = modelling parameters

Deformation ratios (DR) used for normalisation of the permanent deformation trends per load magnitude and material condition were established during the second phase. The fraction of embedment during the initial cycle, where $PD_{N=1}$ is equal to u_p, in comparison to the average ball penetration value comprise the DR as defined in Equation 3.27.

$$DR = \frac{PD_{N=1}}{ball\ pen.\ value} \times 100 \tag{3.27}$$

During the second phase the cumulative deformation trends were established. These trends have a natural logarithmic form as presented in Equation 3.28.

$$PD = a_3 ln(N) + b_3 \tag{3.28}$$

where:

N = load cycles

$a_3,\ b_3$ = material parameters

$$a_3 = a_4 e^{b_4 DR} \tag{3.29}$$

$$b_3 = a_5 DR + b_5 \tag{3.30}$$

where:

DR = deformation ratio

$a_4,\ b_4$ = model parameters

$a_5,\ b_5$ = model parameters

A relation between the deformation ratios and the rate of deformation was established in the fourth phase as illustrated in Figure 3.7. This relation indicates the contribution of the deformation ratios to the permanent deformation or otherwise stated, the embedment phenomenon. The application of the PD models with reference to the FE seal model is addressed Section 3.2.4.

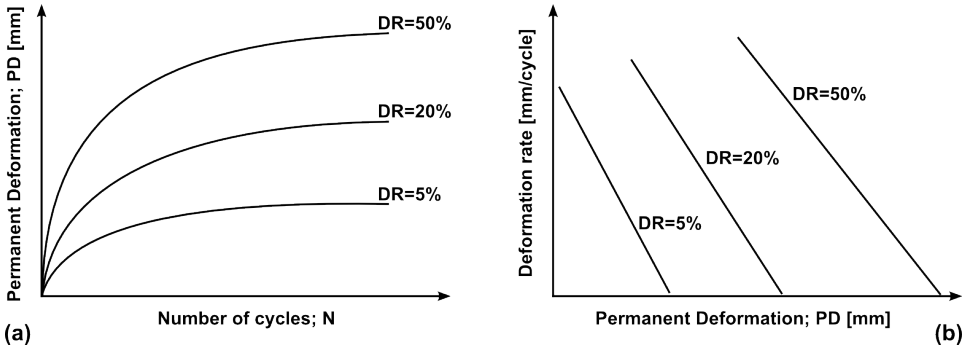

Figure 3.7: (a) Permanent deformation per DR, (b) Deformation rate per DR

3.2.2 FE seal model development

From the onset of the integrated research project, it was predetermined that the structural seal modelling aspect should have a simple approach. The simple approach should result in quick structural insights with various material characteristics subject to preselected traffic loads. Numerous variables were considered and investigated. A comprehensive layout of all the investigated variables is presented in the research limitations, Section 3.3. Emanating from the comprehensive list, the major variables as presented in Table 3.6 were selected. These variables were included in the development of a meso-scale, 2D plain strain FE seal response model.

Table 3.6: Variables included in the seal model development.

Seal structures	Components	Variations	Description of variation with reference to modelling
Single seal	Aggregate	1	Fixed nominal sizes: 6.7 mm, 9.5 mm, 13.2 mm & 19.0 mm with varying ALD. Elliptical idealised shapes. Adjustable horizontal spacing.
	Adhesive zone	N/A	Fixed thickness of 100 μm. Response dependant on the binder criteria.
Double seal	Binder	2	Binder conditions: virgin, virgin + water, PAV, PAV + water & 6 field recovered binders. Response characteristics for 0 $°C$, 10 $°C$, 25 $°C$ & 50 $°C$. Type of coat: tack, penetration & fog spray coat. Varying final binder height i.e. surface texture.
Cape seal	Base	1	Vary with elastic modulus and Poisson's ratio.
	Traffic	2^{i}	Vary with tyre inflation pressure vertical load, speed and free rolling and acceleration.

[i] Heavy Vehicle and Light Vehicle wheel loads

The FEM approach on meso-scale was selected over the DEM on meso-scale, because the material response characteristics (stress and strain) of seal models were of interest. The FEM package, Abaqus, was already available at the research institution of this study. Abaqus was successfully used in the LOT project by Huurman (2008). Another FEM package namely CAPA3D was considered, but in the light of resource economy and previous success, Abaqus was the selected FEM platform. The 2D developmental domain was selected over the 3D domain. Firstly, it was computationally less demanding and secondly, it resulted in a simplified modelling approach which was the objective. However, Tehrani *et al.* (2013) indicated that discrepancies arise in modelling whether in 3D or 2D in comparison to measured data. Therefore, calibration of the modelling trends were conducted and is discussed in Section 3.2.4 during seal model verification and validation process.

Within the Abaqus 2D continuum, either a plane stress or plane strain environment must be selected. Plane strain was selected over plane stress, though neither option accurately described the modelling problem. Plane strain is generally preferred in combination with cohesive interface properties (da Silva and Campilho, 2012) as is the case with the seal models. Trial simulations were conducted for both constraints

and the plane strain option yielded more conservative results than plane stress. The outcome of the seal models are material responses i.e. stress and strain for specific seal structures. Actual seal structures were related to simplistic idealised structures. During this process insights into the geometrical properties such air void positions and 2D aggregate spacings of seal structures were obtained with the computer tomography imaging technique. This resulted in the development of a meso-scale idealised seal model generator (Figure 3.8), which is discussed in greater detail in Appendix B. In this section the development of each component as pertaining to the idealised seal structure is discussed. Illustrations of the positions where data were collected from the FE models are also presented.

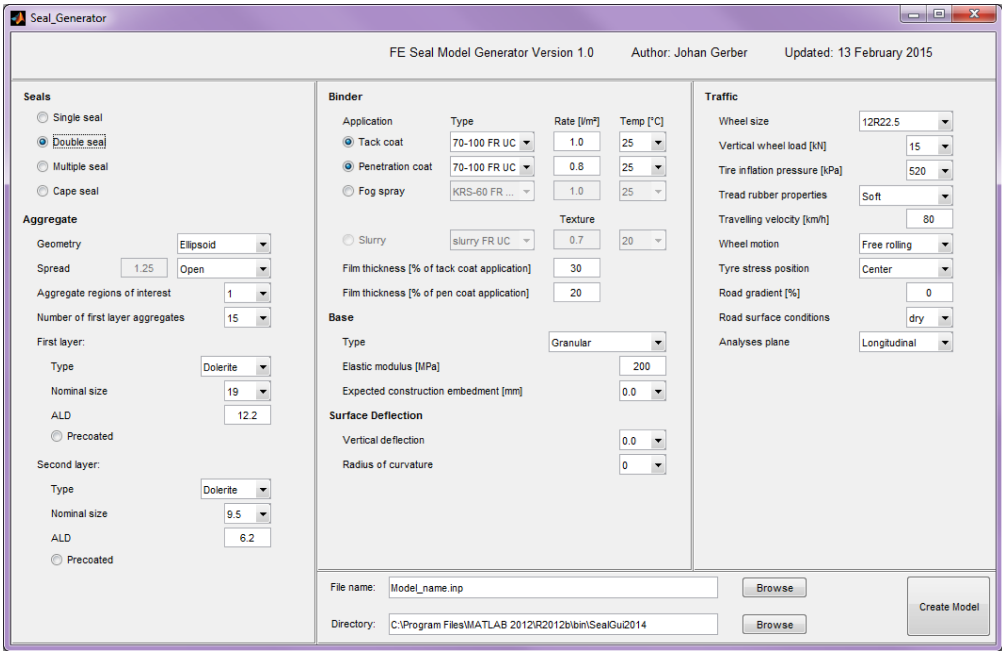

Figure 3.8: Idealised seal model generator front end.

Aggregates

Aggregates were modelled with idealised related geometries. An ellipse was selected to represent the shape of the idealised aggregates, where the nominal aggregate size defined the length of the major axis and the ALD determined the length of the minor axis. The aggregates were modelled as isotropic solids with linear elastic properties. The representation of single and cape seals comprised a single layer of equivalent size aggregates. Double seals were represented by two layers of aggregates. The first layer being similar to the single and cape seal and the second layer consisted of a smaller pair of unequal vertical dimensions. The number of first layer aggregates

determines the length of the seal model. A model can have a minimum of five first layer aggregates and a maximum of 99. For the various aggregate nominal sizes, different numbers of aggregates were selected to represent the seal. For nominal sizes of 6.7 mm, 9.5 mm, 13.2 mm and 19.0 mm the corresponding number of aggregates were 27, 21, 19 and 15 respectively. The reason for this type of selection was to allow at least five intervals, excluding the first and last aggregate, that measured approximately 127 mm from aggregate centre to aggregate centre. These intervals are equal to the distance needed for Dehlen's radius of curvature (ROC) as illustrated in Figure 3.9 (Horak, 1987). The ROC was used in the model validation and verification process.

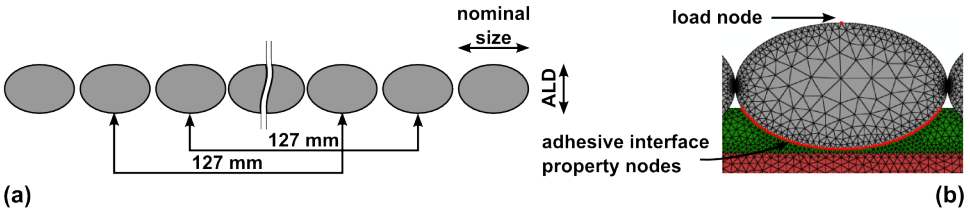

Figure 3.9: (a) Idealised aggregate packing and ROC intervals, (b) Adhesive interface property nodes and load node.

Closely packed aggregates of the single seal structures were allowed to make aggregate to aggregate contact when subjected to loading, simulating aggregate interlock. Wheel loads were applied to the node situated at the pinnacle of the aggregates and in the case of elliptical aggregates the position was on the minor axis. The surfaces of the aggregates were smooth and exhibited no micro texture. The micro texture effect was therefore included in assigning an adhesive zone which represented the aggregate-binder bond strength.

Adhesive zone

The adhesive zone is a set of nodes that define the binder-aggregate bond strength (Figure 3.9). These nodes are assigned with properties which represent the bond strength for a combination of factors such as: the aggregate type, the aggregate micro surface texture, the bitumen type and operating temperature. The bond strength of precoated aggregates can also be included in the adhesive zone properties, however, precoated aggregates do not form part of this study.
Adhesive zones are assigned to the regions of interest. The region of interest is mainly the response at the centre of the model and therefore an adhesive zone is assigned only to the aggregate at the centre of the seal model. It is however possible to assign adhesive zones to the remaining aggregates, but this would increase computational

time. It should be noted that the response characteristics of the adhesive zone differ to the response characteristics of the binder, although nodes are shared at the binder-aggregate interface.

Binder

Binders are modelled as linear viscoelastic, homogeneous layers. The seal model generator allows binders to be selected according to type, age and operating temperature. Similar to seal construction the tack coat application rate is in litres per square meters which translate to a binder layer height for a 2D model. The final tack coat layer height i.e. aggregated wetted height, depends on the aggregate size and spread rate or in the 2D case, the aggregate spacing. Tack coats (Figure 3.10) are fully bound to the substrate and the assumption is made that a thin film of binder always exists between the substrate and seal aggregates. The thickness of this film is a fraction of the application rate and can be adjusted according to the phenomenon investigated.
In the case of double seals, a penetration coat is applied to the top of the first layer off aggregates and serves as the tack coat for the second layer of smaller aggregates. By manipulating the tack coat and penetration coat application rates, air voids can be created between the first and the second aggregate layers. The final binder height of the double seal is thus dependent on the application rates of the two coats and the spacing of the first layer of seal aggregates.
Within specific restrictions, fog sprays can be included in the simulation of single and double seals. Only a cationic fog spray can be selected which results in shoulder bonds of the seal aggregates. Fog sprays are not allowed in the case of aggregate to aggregate contact, this is due to a FE contact restriction where nodes sharing are not allowed. Therefore, it is not a practical restriction, but a simulation restriction. In the case of a single seal it is possible to obtain air voids between the tack coat and fog spray by manipulating the application rates. Similar for double seals, obtaining voids between the penetration coat and fog spray are possible by manipulating the respective application rates.

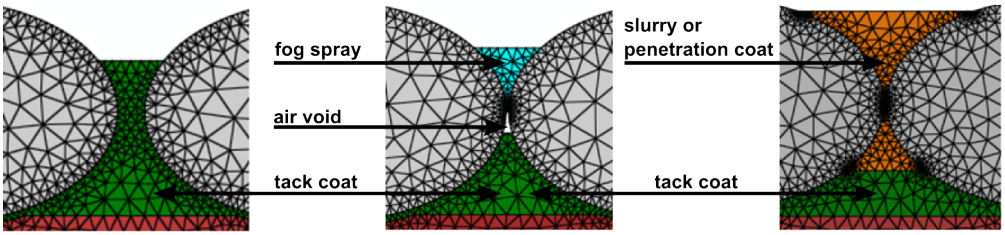

Figure 3.10: Binder applications: tack coat, fog spray, penetration coat and slurry.

Fog sprays are not included in the cape seal setup since early stone loss is not a major concern with this type of seal structure and similar to binders, the slurry is modelled as a linear viscoelastic, homogeneous layer. The study assumes that the slurry mixture penetrates all the available volumetric vacancies within the aggregate matrix, therefore no air voids are included in a cape seal simulation. The study also assumes that spreading of slurry with squeegees results in a thin film of slurry between closely spaced aggregates and therefore no aggregate to aggregate contact is possible within a cape seal model. The stiffness of the layer depends thus on the characteristics of the slurry and not aggregate interlock. It should be noted that this study does not consider the application and effects of a prime coats on an existing or newly constructed base.

Base

The base layer provides structural support for the seal and is modelled as a linear elastic homogeneous layer. Boundary conditions are assigned to the nodes located at the exterior of the base and to the vertical edges of the binder layers. The base layer is furthermore utilised for the investigation of embedment which is a surface phenomenon, therefore only the upper 30 mm of the base is included in the structural models. An initial state of embedment can be specified, thus the model can consider embedment at various stages of the seal's service life. Near the region of embedment interest a refined mesh is generated.

Mesh

Although models are termed *idealised*, geometries that need to be meshed remain complex. A first order, randomly generated, triangular mesh was consequently selected. The unstructured, randomly generated mesh is able to create a quality mesh within the specific tolerances. The size of the mesh i.e. the representative volume element (RVE) per seal type depends on the size of the aggregates and a greater volume is obtained with smaller aggregates in comparison to larger aggregates. The models are meshed in such a manner that nodes at the material interfaces of the seal structures are shared, minimising stress distortion from one material type to another.

Seal structures

Three basic seal structures were developed, each structure allowing specific variations of itself. The single seal structure (Figure 3.11) is the most basic structure of the three and allows the nominal aggregate size to vary among three sizes; 6.7 mm,

9.5 *mm* and 13.2 *mm*. The ALD can vary between 45% and 70% of the corresponding nominal size. Aggregates can be spaced apart (open spread) or be allowed to make contact (aggregate interlock). All single seals include a tack coat, however fog sprays are optional.

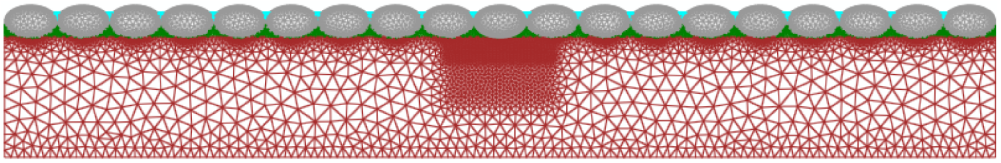

Figure 3.11: Single seal structure including a fog spray.

The double seal structure (Figure 3.12) is the most complex of the three structures and allows the nominal aggregate size of first layer to vary between two sizes: 19.0 *mm* and 13.2 *mm*. The first layer has an open spread and an adjustable ALD, similar to the single seal. The size of the second layer of aggregates however, depends on the nominal size of the first layer. A second layer nominal size of 9.5 *mm* correspond with a first layer nominal size of 19.0 *mm*. Similarly does a 6.7 *mm* second layer nominal size corresponds to a 13.2 *mm* first layer nominal size. The two systems represent the traditional 19.0 *mm* + 9.5 *mm* and 13.2 *mm* + 6.7 *mm* double seals. The vertical dimensions for the pair of second layer of aggregates are not identical but the height is controlled with the ALD.

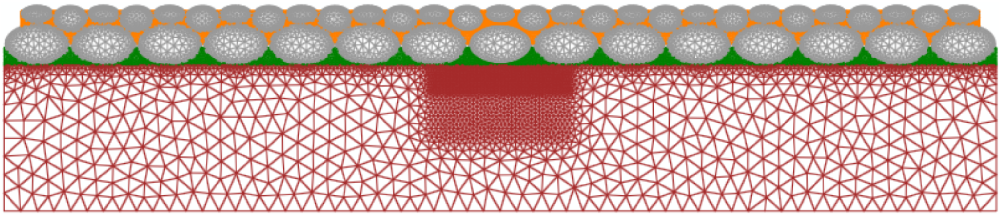

Figure 3.12: Traditional double seal structure.

There is, however, a variation of the traditional double seal and is termed *multiple seal*. The multiple seal consists of a 19.0 *mm* + 6.7 *mm* + 6.7 *mm* aggregate combination of which a portion of the 6.7 *mm* aggregates are spread prior to the application of the penetration coat (Figure 3.13). The multiple seal model however allows only for an open aggregate spread with an adjustable ALD. A multiple seal and the traditional double seal models are required to have a tack coat and a penetration coat, but fog sprays are optional.

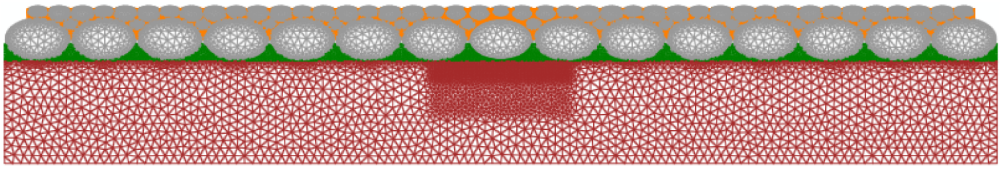

Figure 3.13: Multiple seal structure.

The cape seal structure completes the three structures developed in this study. This structure is in many ways similar to the single seal structure, but the nominal sizes of the aggregate can either be 19.0 mm or 13.2 mm with an adjustable ALD (Figure 3.14). Aggregate interlock and fog sprays are not included in this structure and the structure requires a tack coat and slurry application.

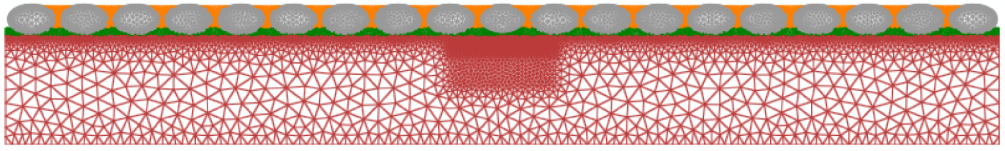

Figure 3.14: Cape seal structure with slurry.

One major difference of the cape seal structure in comparison to the other seal structures is the distribution of the wheel load across the whole surface of the cape seal i.e. across the aggregate load nodes and the nodes at the upper edge of the slurry layer, according to an assumption based on the load-penetration function (Equation 3.31) for asperities as developed by Cesbron *et al.* (2008).

$$P = CE^*\delta^\gamma \tag{3.31}$$

where:

P = vertical load

δ = rubber penetration

E^* = rubber stiffness

$C,\ \gamma$ = asperity shape constants

The percentage of the load applied to the aggregate was estimated by computing the fraction of the asperity hight h_a across the asperity tread-rubber penetration δ value ($\frac{h_a}{\delta} \times 100$), while the remainder of the total load was applied to the slurry surface. The variation of each seal structure is summarised in Table 3.7.

Table 3.7: Summary of the seal structure variations.

	Single seal	Double seal	Cape seal
nominal size	6.7 mm 9.5 mm 13.2 mm	19.0 $mm + 9.5$ mm 13.2 $mm + 6.7$ mm 19.0 $mm + 6.7$ $mm + 6.7$ mm	13.2 mm 19.0 mm
ALD variation[i]	✓	✓	✓
open spread	✓	✓	✓
interlock	✓	x	x
tack coat	✓	✓	✓
penetration coat	x	✓	x
fog spray	✓	✓	x
slurry	x	x	✓
load position	aggregate	aggregate	aggregate and slurry nodes

[i] all aggregates: $0.45 \times nominal\ size \leq ALD \leq 0.7 \times nominal\ size$

Seal model output and data positions

The type of output data and its acquisition points depend on the failure mechanism of interest. The three mechanisms which the model accounts for are: adhesive failure, cohesive failure and embedment. Adhesive failure emanates from tensile and shear stress, therefore the peak stress conditions situated in the adhesive zone are of interest. Trial models indicated that combinations of peak shear and tensile stress form around the edges of the aggregates at the interface nodes situated on or near the major axis as illustrated in Figure 3.15.

The peak values alone do not fully represent the stress conditions obtained in the adhesive zone. Obtaining a representative stress was approached with a normal distribution of the entire adhesive interface (all the nodes). Selecting the stress value at two standard deviations to the right as the representative value is conservative, but includes the distribution properties such as the spread and variance. Values exceeding three standard deviations were adjudicated as outliers and excluded from the analysis.

Cohesive failure refers to fatigue damage within the binder material itself. Similar to adhesive damage, cohesive damage also emanates from tensile and shear stress, therefore the peak tensile and shear stress within the binder layer is of interest. A combination of the peak stress situation is obtained in the binder elements situated on or near the aggregate major axis. However, similar to the adhesion interface, the individual peak stresses do not fully portray the stress condition obtained in the binder and therefore all the binder elements at the region of interest between the two aggregates (Figure 3.15) were selected for a similar statistical analysis as discussed for the adhesive zone.

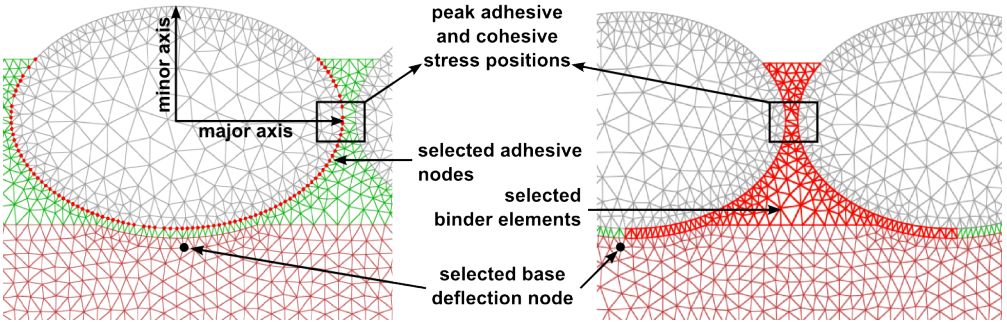

Figure 3.15: Data acquisition locations for the three failure mechanisms.

Embedment is a function of the applied load and the base strength which results in vertical deformation of the base when subjected to loads. The vertical deflection of the base directly underneath the seal aggregate is therefore of interest and obtained from such a node as illustrated in Figure 3.15.

3.2.3 Traffic model formulation

Traffic load data was obtained from Tyre Stress Seal, a software package developed by the Council for Scientific and Industrial Research (CSIR) of South Africa. Tyre Stress Seal was compiled from research conducted on different wheel loads with the stress in motion (SIM) system. The inter-active software allows user defined functions such as:

a) Selection of desired wheel size.

b) Specifying the vertical load and tyre inflation pressure (TiP) of selected wheel.

c) Defining the output display format (block mode, contours or interpolated data).

d) Exporting the 3D stress distributions to an output file.

Five different wheel sizes at various vertical loads and TiPs (Table 3.8) were exported from Tyre Stress Seal and formed the bases of the traffic formulation for the FE seal models. Two of the five wheel sizes were heavy vehicle (HV) wheel loads and the

Table 3.8: Wheel size and load combination as derived from Tyre Stress Seal.

Size	Class	Vertical load [kN]	TiP [kPa]
12R22.5	HV	15 20 35 40 50	520 620 720 800 950 1000
315-80R22.5	HV	20 35 40 50 75 100	520 620 720 800 950 1000
265-65R17	LV	5.4	190
245-70R16C	LV	5.4	190
195R15C	LV	6.0	360

remainder were passenger vehicles, also referred to as light vehicle (LV) wheel loads. The traffic model therefore makes provision to address the discrepancies in damage which arise in applying different wheel loads to the seal structure. Tyre Stress Seal provides only one vertical load and one corresponding TiP for the three LVs. Each vertical load and TiP combination as presented in Table 3.8, was related from its 3D macro-scale output to a 2D meso-scale load function. The procedure is illustrated in Figure 3.16 and summarised as follows:

a) Export Tyre Stress Seal data in block format (raw data format).

b) Select the two centre blocks (Pin 11 & Pin 12) to represent the contact stress at centre of the tyre and select the two edge blocks (Pin 7 & Pin 16) to represent the contact stress underneath the side-wall of the tyre.

c) Adjust the measured pin stress data to satisfy pneumatic tyre theory and convert the stress signals into 2D force functions.

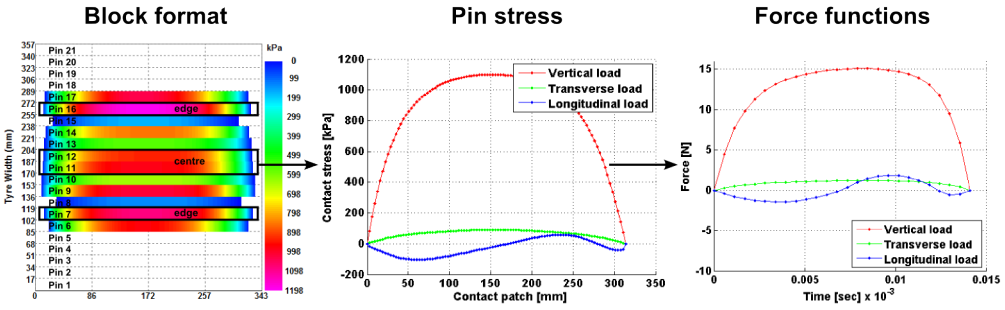

Figure 3.16: Typical SIM output and 2D force functions adjustment procedure.

The latter process resulted in losing the effect of the third dimension, therefore, emphasis was placed on translating the 3D stress situation to a 2D force system for the longitudinal direction i.e. the direction of travel. Forces which are present in the longitudinal direction are the vertical force and the longitudinal forces. From the onset of the traffic model formulation it was decided to limit the longitudinal influencing factors to: free rolling, acceleration and braking wheels, axle speed variation and vertical inclines. No other factors such as wheel turn, wheel spin, wheel lock or any damping effects were considered. Although cognisant of the effects which these influencing factors introduce, especially the contribution of the tread rubber properties to the longitudinal shear force, the objective was to obtain general structural seal responses with various classes of traffic in the 2D domain.
Transforming the complex pin stress signals to simplified functions, while adhering to pneumatic tyre theory in the longitudinal direction, encompassed the adjustment

process. During this process the pin stress signals were converted to 2D force functions as defined in Equation 3.32.

$$F_{z,y,x} = \sigma_{z,y,x} \times aggregate\ nominal\ size \times unit\ width \tag{3.32}$$

where:

$F_{z,y,x}$ = force functions
$\sigma_{z,y,x}$ = pin stress
$unit\ width = 1\ mm$

The shape of longitudinal force function F_x was replaced with parabola segments. The number of segments varied between two and three and depended on the original pin stress function. The roots of each segment were inherited from the original F_x and the integral of the newly segmented F_x resulted in the rolling resistance F_r. In some cases the parabola peak values were slightly adjusted and the vertical force F_z was skewed with an iterative process to satisfy Equation 3.33. Although the transverse force F_y had no effect in a vertical-longitudinal 2D simulation, it followed a similar transformation procedure than F_z.

$$F_r = \frac{F_z(\Delta x)}{R_s} \tag{3.33}$$

where:

R_s = undeflected tyre radius
Δx = horizontal offset of the vertical resultant for a free rolling wheel

In general the longitudinal force is of little importance on thicker surface layers such as asphalt or concrete, but in the case of a thin seal surfaces it has a significant effect on the response of the layer. Longitudinal forces were therefore further adjusted for driven (acceleration) and brake wheels. Based on the work of Moore (1975), an assumption was made that the brake force coefficient and relative traction increased linear towards peak values of 1.0 at a slip ratio of 0.2. According to Miller *et al.* (2001) general wheel slip ranges between 0% and 3%, therefore a slip value of 3% was selected to account for the braking force F_b or traction force F_d as presented in Equation 3.34. These forces were superimposed on the existing longitudinal force, adjusting the overall F_x.

$$\frac{F_{b,d}}{F_z} = ms_{b,d} \tag{3.34}$$

where:

m = linear increase rate
$s_{b,d}$ = brake or drive slip ratio

In the case of an incline (ϕ) the horizontal component of the translated vertical force ($F_z \sin(\phi)$) was included to account for the total relative traction or brake force coefficient as defined in Equation 3.35.

$$\frac{F_{total}}{F_z} = \frac{F_{b,d}}{F_z} + \frac{F_z \sin(\phi)}{F_z \cos(\phi)} \tag{3.35}$$

It is acknowledged that the tyre road contact stress is a complex scenario and the approach followed in this study is a simple relation thereof. However, the quality of the SIM data provided satisfactory results during the model verification process. A summary of the peak vertical and longitudinal forces per wheel size and load combination is presented in Appendix B.

3.2.4 Seal model verification and validation

Seal model verification is defined as the process for establishing the model validity via empirical means. The very reason for constructing a FE seal model is to obtain insights into the model's structural response, yet the model outputs need to be converted into formats that are comparable with measured or observed data. The accuracies of these comparisons are synonymous for the data validation process. Discrepancies between modelled and field obtained data, result in the application of calibration factors. Model verification and validation were conducted for the three failure mechanisms which include: cohesive failure, adhesive failure and embedment.

Cohesive failure

The ability of the model to predict cohesive damage and ultimately fatigue cracking is the phenomenon that was validated. Element stress and deflection data were therefore reworked for comparison with empirical data as obtained by van Zyl (2015). Van Zyl devised a method of illustrating fatigue cracking by expanding three basic components which included: the radius of curvature (ROC), traffic counts and the time of crack observation. The difference in the D_0 and D_{127} Benkelman Beam measurements, which is used to determine the ROC utilising Dehlen's method, describes the deflection of the seal. Multiplying the deflection with the yearly traffic count, results in a cumulative deflection with time for the respective seal type as illustrated in Figure 3.17. Van Zyl categorised the findings and calculations into single, double and cape seal structures and indicated the stages (years) at which cracking was initially observed. A philosophy was therefore developed that repeated deflection under traffic yields fatigue cracking.

A constant deflection per seal sample was assumed and van Zyl further differentiated each seal structure into aggregate nominal sizes, binder type and climatic regions.

The empirical data does however not differentiate between aggregate shape or spread rate. Neither does it indicate whether aggregates were precoated nor does it reference the binder application rates. There is no clarity on the use of fog sprays or rejuvenators and some case traffic counts were recorded only in equivalent 80 kN axles (E80s), thus no distinction is made between light vehicles and heavy vehicles.

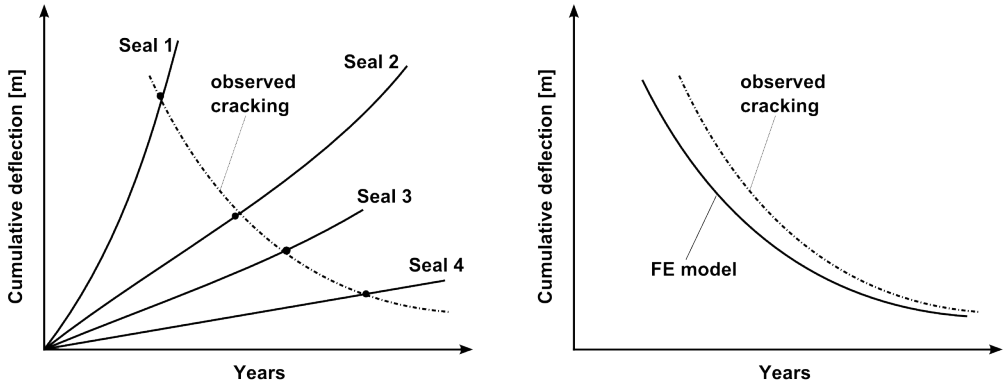

Figure 3.17: Schematic layout of the verification process for seal fatigue cracking as developed by van Zyl (2015) per seal type.

Relating the model ouput to the format of van Zyl (2015) consisted of a dual process. During the first process the ROC obtained with the model was translated to cumulative deflection over time by utilising the same traffic counts n_i and growth rates as van Zyl. The second process consisted of calculating the number of load simulations to crack initiation N_i. This was done by implementing the binder's shear stress response obtained at the 2^{nd} standard deviation, into Mukandila's (2015) cohesion transfer functions (Equation 3.16). Subsequent the data transformation, Miner's rule was implemented to determine the fraction of damage D generated by the annual traffic count as defined in Equation 3.36. A total damage fraction that is greater or equal to one indicates the existence of crack initiation. The simulated cracks were compared to the empirical observed cracks with reference to time (years) and calibrated accordingly. Figure 3.18 illustrates this process.

$$D = \frac{n_1}{N_1} + \frac{n_2}{N_2} + \ldots + \frac{n_n}{N_n} \tag{3.36}$$

where:

$_n$ = number of years
n = observed number of load repetitions per year
N = maximum calculated number of load repetitions per year
D = fraction of damage

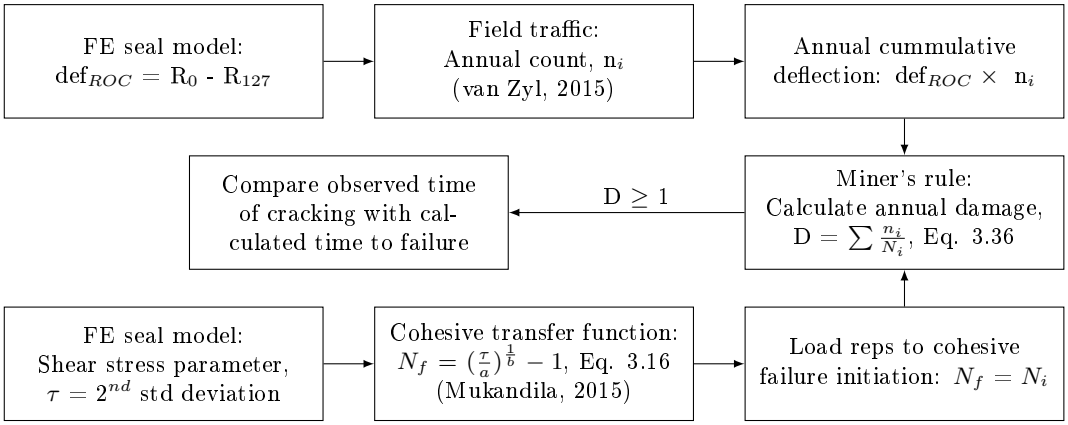

Figure 3.18: Module integration during the cohesive validation process.

Each N_i as defined in Equation 3.36 was further expanded to accommodate the primary variations that are encountered in road seals. These variations consist of structural variables, time related variables and traffic loads as presented and described in Table 3.9. Depending on the observed traffic data, Equation 3.36 is expanded to Equation 3.37 which includes the time related variables and traffic variations of a defined structural seal setup.

Table 3.9: Primary variables included in the verification process.

Structural variables	**Quantity**	**Description**
Seal type	3	Single, double and cape seal
Seal size	8	Full description presented in Table 3.7
Aggregate type	1	Dolerite
Aggregates spread	2	Open spread or interlocked
Binder type	1	70-100 penetration grade
Binder volume and structural position	3	Minimum, maximum and fog spray
Time related variables	**Quantity**	**Description**
Base stiffness	3	Weak, average and strong
Binder temperature	2	$10°C$ and $25°C$
Binder age	6	Virgin, PAV, 3yr, 5yr, 6yr and 10yr
Traffic load variables	**Quantity**	**Description**
Light vehicles	3	Full description presented in Table 3.8
Heavy vehicles	2	Load and TiP reduced to a 3×3 matrix
HV matrix	9	Vertical load = 15 kN, 20 kN, 35 kN TiP = 520 kPa, 800 kPa, 1000 kPa
Travelling speed	2	20 km/h and 80 km/h
Rolling conditions	2	Free rolling and traction wheels

$$D = \frac{n_{(1,°C,E,lc)}}{N_{(1,°C,E,lc)}} + \frac{n_{(2,°C,E,lc)}}{N_{(2,°C,E,lc)}} + \ldots + \frac{n_{(n,°C,E,lc)}}{N_{(n,°C,E,lc)}} \tag{3.37}$$

where:

$°C$ = binder temperature

E = base stiffness (elastic modulus)

lc = load case

Multiple terms were utilised in describing the annual damage accumulation and the possible combinations of variables are summarised in Table 3.9. A schematic layout of the hierarchy between the structural variables, time related variables and traffic loads are illustrated in Figure 3.19.

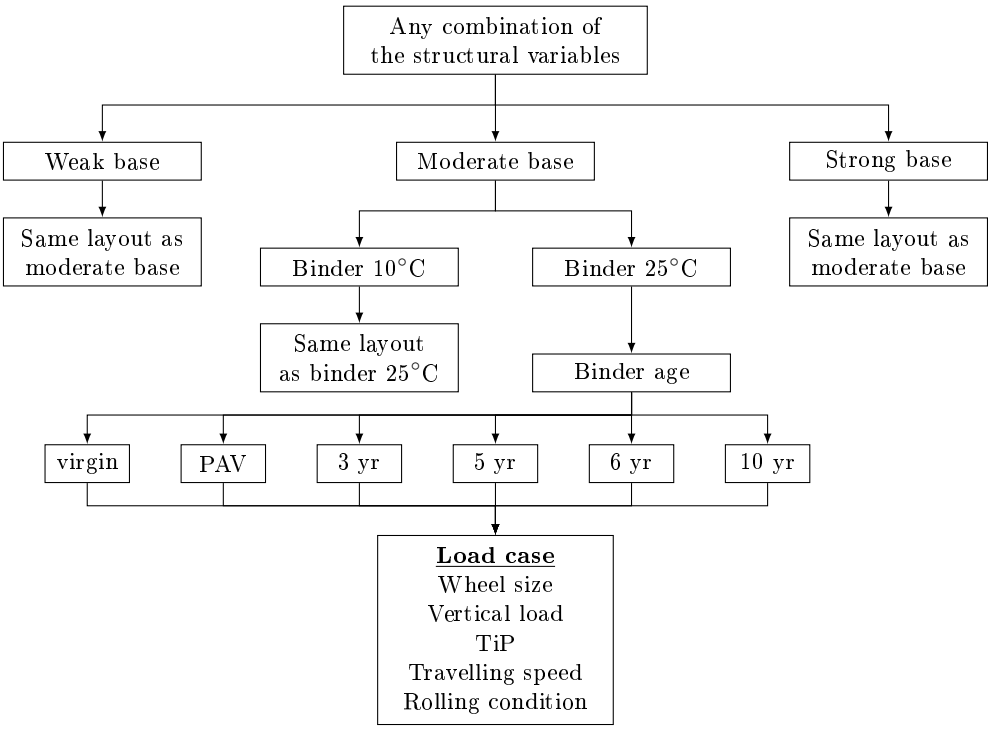

Figure 3.19: Schematic layout of the hierarchy between the structural variables, time related variables and traffic load cases.

Adhesive failure

The ability of the seal model to predict short term adhesive fatigue failure, which results in aggregate loss, was the phenomenon being validated. Aggregate ALD, binder application rates and adhesive zone stress data were therefore reworked and compared with empirical data as obtained by van Zyl (2015).

The empirical data, containing years of practical experience, calculations and observations, indicated that short term aggregate loss depends on the combination of four factors as documented in the TRH3 (2007). These factors include: the minimum

binder application rate, aggregate ALD, embedment potential and the daily traffic count. Combinations of these factors result in the critical minimum binder application rate to successfully hold the aggregate and is commonly referred to as the *red line* due to its colour in the TRH3 as illustrated in Figure 3.20.

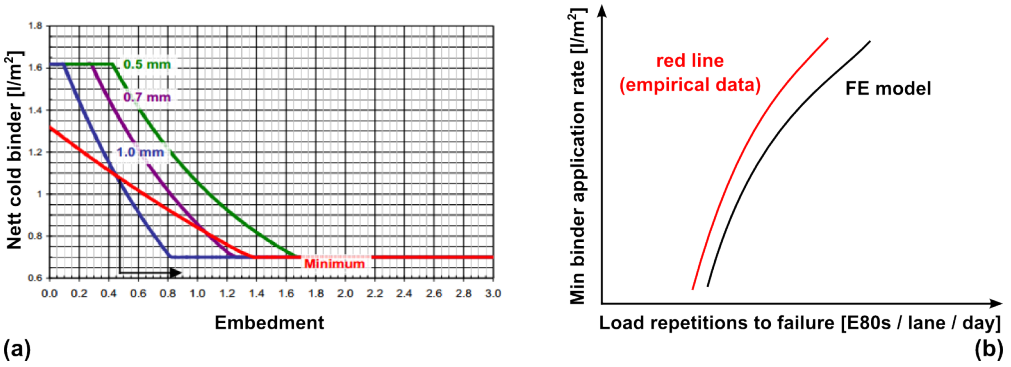

Figure 3.20: Adhesive fatigue verification: (a) Minimum binder application rate, the red line (TRH3, 2007), (b) Schematic illustration of early aggregate loss verification.

Design combinations falling below the red line result in early aggregate loss. The red line does not clearly differentiate between the binder and aggregate type, but the TRH3 (2007) indicates that the red line was designed for conventional binders and should be adjusted in the case of modified binders.

Van Zyl (2015) established relationships between the HV, LV, E80s and ELVs from a number of traffic monitoring sites in South Africa. The E80s were subsequently related to the critical minimum binder application rates for a certain ball penetration value (embedment potential) and aggregate ALD as illustrated in Figure 3.20. These relationships served as the comparisons for the FE seal model adhesive analyses.

Similar to the cohesive analysis, the 2^{nd} standard deviation of the adhesive zone shear stress was implemented into Mukandila's (2015) adhesive transfer functions (Equation 3.20). This resulted in the number of load repetitions to aggregate loss, which were used in the validation process. Figure 3.21 illustrates this process, where

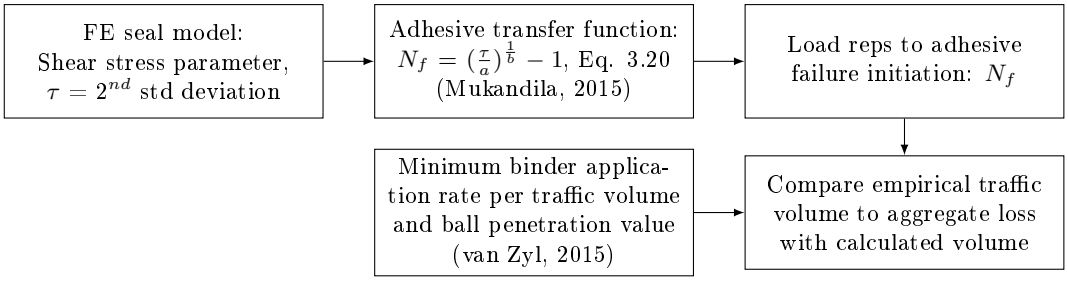

Figure 3.21: Module integration during the adhesive validation process.

FE seal model data was obtained according to outline as presented in Table 3.9 and Figure 3.19.

Embedment

The ability of the seal model to predict embedment was the phenomenon being validated. Therefore, the elastic deflection of the base directly underneath the seal aggregate in the FE model was reworked and compared with empirical data as obtained by van Zyl (2015). Van Zyl's data related the percentage of retained surface texture depth i.e. texture loss to the number of ELVs for each seal structure. ELVs were determined with an equivalent damage factor of 10, since the TRH3 factor of 40 was considered to be too excessive (Figure 3.22).

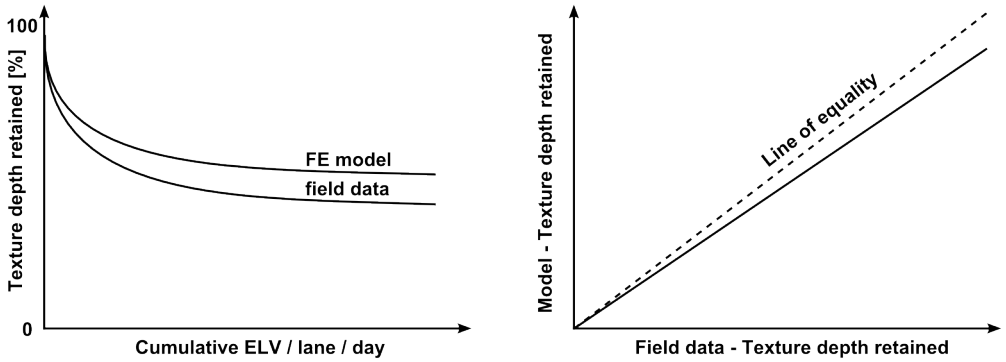

Figure 3.22: Schematic illustration of embedment verification.

To briefly reiterate, texture loss consists out of four components, namely, stone orientation, embedment, binder rise and aggregate wear. Out of the four components, stone orientation and embedment are the major contributors towards texture loss. Van Zyl's data did not indicate the contribution of each component, but it did indicate on which type of base the texture loss occurred with a corresponding ball penetration value. Since the seal model was developed to include only the embedment component of texture loss the trends resulting from the validation process is of greater relevance than the absolute values obtained.

The process of seal model data transformation for purpose of empirical comparisons consisted of two steps. The first step related the vertical base deflection u_e of the FE seal model to the permanent deformation u_p obtained during the repeated ball penetration tests and ultimately a permanent deformation trend PD as described and defined in Equation 3.25 to Equation 3.30. In the second step the embedment depth was transformed to the remaining surface texture T_r, by subtracting the embedded texture fraction T_{em}, from the existing surface texture T_{ex}. This resulted in comparing the observed and calculated texture loss developments as illustrated in

Figure 3.23. FE seal model data were obtained according to outline as presented in Table 3.9 and Figure 3.19, where a weak base refers to a low Young's modulus and a strong base denotes a high Young's modulus. A low modulus was in the region of 10 MPa to 50 MPa and a high modulus ranged from 300 MPa to 500 MPa, while a moderate modulus was in the region of 100 MPa to 200 MPa for this study. Traffic load cases included HV and LV wheel loads, thereby lending insight into the equivalence factors utilised in determining ELVs and other wheel load relations such as fatigue during the seal model comparative analyses.

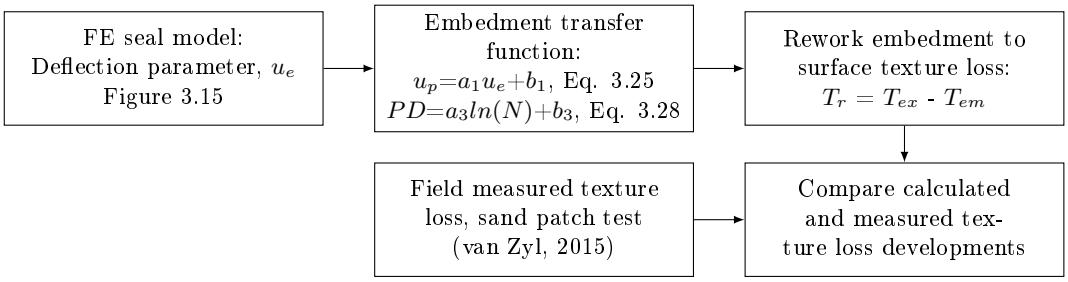

Figure 3.23: Module integration during the embedment validation process.

3.2.5 Seal model comparative analysis

A comparative analysis revealed the relative difference in seal performance with changes to specific variables. Performance in this context refers to the number of load repetitions to failure and failure constitutes of adhesive failure, cohesive failure and embedment. The variables comprised the structural variables, time related variables and traffic load variables as presented in Table 3.9. The relative difference in seal performance was obtained by changing one of the variables at a time.

The comparative analysis consisted out of four categories of which the first three categories were populated with the three seal types. The fourth category consisted of an inter seal type comparison. Each of the first three categories followed a factorial approach in comparing the seal performances with changes to the relevant structural, time related and traffic variables, whereas the fourth category was used to conduct comparisons among the three different seal types.

A factorial approach simply indicates that only a selected number of model variations are compared within a greater matrix of possible variations. Such an approach results in an attainable time frame by significantly reducing the number of FE simulations needed to accomplish the research objectives. Thus, the factorial approach forms indirectly part of the research limitations.

3.3 Research limitations

Perfection is seldom, if ever, obtainable. This is mainly due to either known or unforeseen limitations. This section delineates the limitations of this study by addressing the limitations within the model development, material characterisation, traffic loads formulation and the model verification and validation processes.

3.3.1 Seal model limitations

A comprehensive list of variables, from which the the seal models were developed, is presented in Table 3.10. The number of possible variable combinations without limitations is simply too great to achieve a successful outcome. The seal model was therefore confined to a 2D FE approach, which consisted of idealised geometries representing three seal types. The seal types are: single seals, double seals and cape seals. Each model was designed to lend insight into the responses of three failure mechanisms which were: adhesive failure of seal aggregates, cohesive failure of seal binder and embedment of seal aggregates.
The model applied only mechanical loading and no environmental loading. Therefore, the model did not simulate lengthy durations of surface exposure to sunlight. This component and other environmental related components were included in the material characterisation process.

3.3.2 Material characterisation limits

Typical seal aggregate types were selected for investigation. These aggregate types included dolerite, quartzite and granite. Quartzite is an acidic metamorphic rock which is hydrophilic, while granite is an acidic crystalline rock with a low degree of hydrophobicity. Dolerite is a basic igneous rock which is hydrophobic. Therefore, the three aggregate types: quartzite, granite and dolerite represent electronegativity, electroneutrality and electropositivity respectively.
Aggregates were limited to linear elastic properties which were deduced from literature. Aggregates could therefore not exhibit wear or be crushed. Although provisions were made for the three different aggregate types within the architecture of the seal model generator, only dolerite section was populated with properties. Financial and time constraints disallowed expansive stone-column testing by Mukandila (2015). Adhesive fatigue testing was, therefore, limited to dolerite columns with 70-100 penetration grade binder.
The binder response characteristics were limited to the 70-100 penetration grade binder for virgin, PAV and field recovered ages and a virgin cationic rapid set emulsion 60% spray grade (CRS-60). Cohesive fatigue properties were limited to the

Table 3.10: Comprehensive list of the investigated seal model variables.

Component	Variable	Description of the variables
Aggregate	Shape	Idealised, arbitrary and X-ray deduced.
	Size	Identical ALD and nominal sizes or graded sieve fraction ALD and nominal sizes.
	Type	Dolerite.
	Spread rate	Open and interlocked.
	Micro texture	On surface exterior.
	Hardness	Material property.
	Precoated	Influences binder bond.
Adhesive zone	Thickness	$10\mu m$ to $100\mu m$.
	Temperature	$0°C$, $10°C$, $25°C$ and $50°C$.
	Bond condition	Clean, dusty or moisture (wet).
Binder	Type	70-100 penetration grade, CRS-60, and slurries.
	Temperature	$0°C$, $10°C$, $25°C$ and $50°C$.
	Age	0 years (virgin) to 20 years.
	Application rate	Minimum to maximum in litre/m^2.
	Coating	Tack coat, penetration coat or fog spray.
Base	Geometry	Homogeneous or discrete particles.
	Type	Granular, cement stabilised, bitumen treated, asphalt or an old seal (reseal).
	Temperature	$0°C$, $10°C$, $25°C$ and $50°C$ (viscoelastic bases).
	Strength	Affects the embedment potential.
	Adhesive zone	Binder-base bond.
	Initial embedment	Embedment ascribed to construction.
Seal	Type	Summarised and illustrated in Figure 2.1.
	Dimension	3D, 2D vertical-longitudinal plane or 2D vertical-transverse plane.
	Size	Depends on the aggregate nominal size.
Traffic	Load case	Summarised in Table 3.8.
	Positions	Below the tyre wall and at the centre of the contact patch.
	Rolling conditions	Free rolling, acceleration, deceleration, wheel lock, wheel spin and traction on inclines.
	Speed	5 km/h to 120 km/h.
	Surface texture	Affects the longitudinal force.
	Tread rubber	Rubber properties affects the longitudinal force.

70-100 penetration grade binder. With the termination of slurry testing during trial tests, slurry characteristics were substituted with mortar characteristics from literature (Huurman, 2008). Although not exactly similar in composition and response, it was assumed that the mortar characteristics were representative of the slurry characteristics. Slurry characteristics were therefore limited to the latter assumption. Base response and permanent deformation characteristics were limited to a mechanistic-empirical approach which included ball penetration tests, repeated ball penetration

tests and FE models thereof. The material was restricted to a single G2 limestone sample which was sufficient in providing prove of concept.

3.3.3 Traffic load formulation constraints

Traffic load formulations consisted of SIM data and literature. Though an abundance adequate data exists, it is limited to slow, free rolling wheel speeds and an artificial surface texture. It is acknowledged in this study that travelling speed, existing surface texture and tread rubber properties influence the magnitude of the longitudinal contact force. In the context of the seal failure mechanisms, the longitudinal force has a significant effect on aggregate loss.
SIM data conversion from 3D to 2D was restricted to the vertical-longitudinal plane. Free rolling wheel conditions were adjusted for cases which included acceleration, deceleration and traction on inclines. No wheel-lock, wheel-spin or out of plane motion was considered.

3.3.4 Seal model verification and validation restrictions

Adhesive failure, cohesive failure and embedment are the phenomena which were verified and validated. This study was limited to the damage characteristics of virgin 70-100 penetration grade binder for cohesive and adhesive failure. The validation processes were therefore restricted to these conditions. The embedment potential was restricted to a conceptual permanent deformation model derived from a G2 limestone base.

3.4 Closure

The remainder of this document is structured as follows (Figure 1.1): Chapter 4 presents a summary of the binder characterisation process as conducted by Mukandila (2015). Chapter 5 presents the conceptual embedment testing and model characteristics, while a summary of the field data observations and analyses as conducted by van Zyl (2015) is presented in Chapter 6. By altering the variable combinations as presented in Table 3.9 and illustrated in Figure 3.19, Chapter 7 to Chapter 10 populates the comparative analysis categories where; Chapter 7 presents the single seal analysis, Chapter 8 presents the double seal analysis, Chapter 9 presents the cape seal analysis, and Chapter 10 presents the comparative seal analysis. This study concludes with Chapter 11 which presents the conclusions of this study and recommendations towards further research.

4. Binder characterisation

Materials exhibit response and damage properties when subjected to loads. Analysis and interpretation of these properties define the characteristics of the materials. This chapter presents a summary on the analysis and interpretation of the binder testing program as conducted by Mukandila (2015). Additional information on slurries, required to populate the bituminous material characteristic section within the architecture of the finite element (FE) seal model generator, is also discussed.

4.1 DSR binder analysis

The DSR binder testing and analysis program consisted of three categories. These categories included binder response testing, binder fatigue testing and binder-aggregate bond (adhesive zone) fatigue testing. This section addresses the test data and the analysis thereof for each of the three categories.

4.1.1 Parallel plate response data

Mukandila (2015) translated the viscoelastic response properties of the binders to the Prony series format. The Prony series consist of four parameters: the instantaneous shear modulus G_0, Poisson's ratio ν and a number of Prony series elements, which includes the normalised stiffness reduction α_i and the relaxation rate τ_i. The Prony series parameters for the virgin 70-100 penetration grade binder at $25°C$ are presented in Table 4.1. A complete summary of all the Prony series parameters for each binder and condition as pertaining to this study is presented in Appendix C. The Prony series parameters emanate from the complex shear modulus data i.e. the master curve, as obtained with DSR testing. A comparison of Mukandila's (2015) Prony series as presented in Table 4.1 and the corresponding master curve, obtained by applying Equation 3.11, Equation 3.12 and Equation 3.5, is illustrated in Figure 4.1. This Prony series compares closely with its corresponding master curve between the 10^{-1} and 10^{3} frequency range. Outside of this range the Prony series deviates from the complex shear modulus of the master curve.

Table 4.1: Prony series, virgin 70-100 penetration grade binder tested at 25°C (Mukandila, 2015).

α_i	τ_i
0.61	0.000519
0.258	0.00186
0.0692	0.00399
0.00147	0.0161
0.0591	0.0307
2.9e-05	0.0883
0.00147	0.366
0.000173	3.41
6.75e-05	7.9
3.67e-05	50.1

$G_0 = 23\ MPa,\ \nu = 0.5$

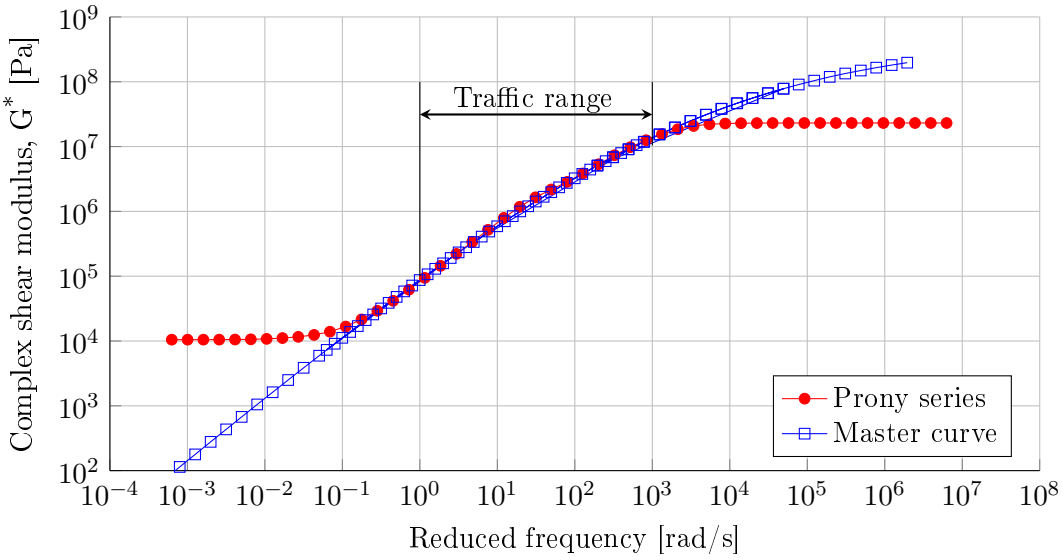

Figure 4.1: Comparison between the DSR master curve and the Prony series for virgin 70-100 penetration grade binder at 25°C (Mukandila, 2015).

Traffic loading times of rolling wheels are calculated to be 0.003 seconds at 120 km/h and 0.15 seconds at 5 km/h. This results in a loading frequency range of approximately 6 Hz to 333 Hz, where 1 Hz is equal to 2π rad/s which is within the range of the Prony series (Figure 4.1). The Prony series is implemented as the constitutive material model for binders in the finite element (FE) seal model analyses. The shear stress responses obtained with the FE models serve as the input to the binder column fatigue data analysis (Figure 3.18).

Initial FE shear stress results indicated that the FE seal model response is within the linear viscoelastic (LVE) range for penetration grade binders (Figure 4.2). The LVE shear stress limits were developed by Petersen *et al.* (1994) during the Strate-

gic Highway Research Program (SHRP) as defined in Equation 4.1. The LVE shear limits of 40 aged and virgin penetration grade binders were found to be a function of the complex shear modulus G*. Researchers (Airey *et al.*, 2002) have criticised the conservative nature of Equation 4.1, therefore, providing additional support that the FE seal model outputs are within the LVE for the 70-100 penetration grade binder.

$$\tau = 0.12(G^*)^{0.71} \tag{4.1}$$

where:

τ = DSR shear stress [kPa]

G^* = Complex shear modulus [kPa]

Figure 4.2 illustrates the SHRP LVE limit and shear stress results from the FE seal model simulations for a virgin 70-100 penetration grade binder at 25°C. The LVE stress limits were determined at the point beyond which shear complex modulus G* has reduced to 95% of its initial value. All the initial results are below the SHRP LVE limit, indicating consent for LVE conditions. The LVE conditions are influenced by temperature and loading time. A reduction in temperature results in an increase in the allowable shear stress magnitude. The opposite is true for a reduction in loading time, which results in a reduction in the allowable shear stress magnitude. A summary of the traffic loads displayed in Figure 4.2 is presented in Table 4.2.

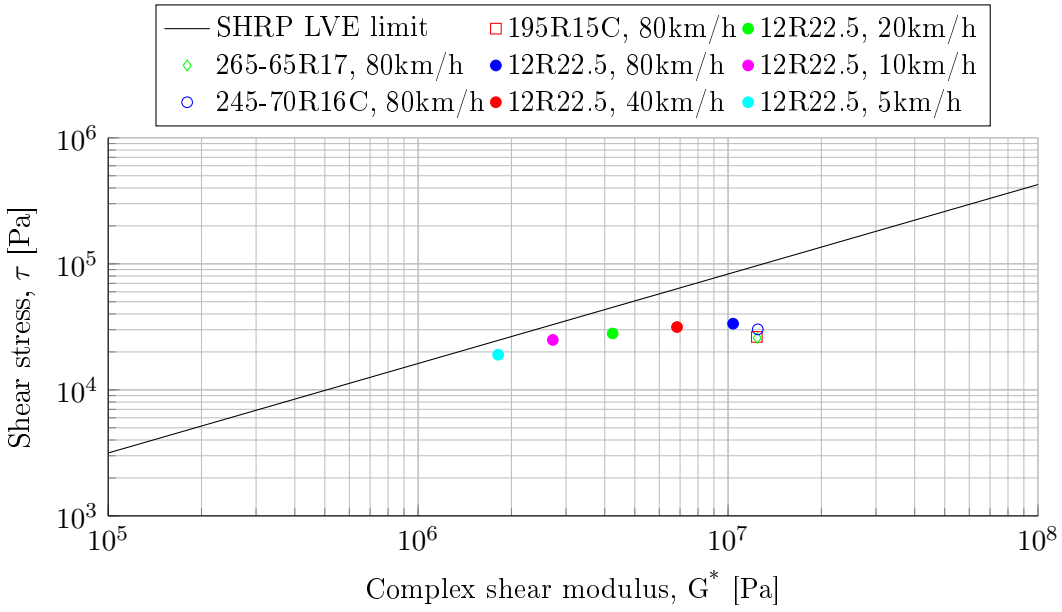

Figure 4.2: FE seal model results and linear viscoelastic (LVE) stress limits for penetration grade binders.

Table 4.2: Traffic loads for FE seal model LVE limit validation.

Wheel size	Load [kN]	Velocity [km/h]
195R15C	6.0	80
265-65R17	5.4	80
245-70R16C	5.4	80
12R22.5	20	5 - 80

According to Rowe (2015), parameters emanating from LVE measurements are able to lend insight into durability cracking of binders. The Glover-Rowe parameter (G-R) as defined in Equation 4.2, relates the stiffness (G^*) and viscosity (δ) parameters of the DSR master curves to stress performance and subsequent relations to cracking at intermediate temperatures. The original criteria for the onset of cracking and significant crack observation were determined for $G\text{-}R = 180\ kPa$ and $G\text{-}R = 450\ kPa$ and are base on the performance of materials in limited climatic conditions (Rowe, 2015).

$$G\text{-}R = \frac{G^*(\cos\delta)^2}{\sin\delta} \tag{4.2}$$

Since aged binders are more prone to fatigue cracking than virgin binders, Mukandila (2015) utilised the $G\text{-}R$ parameter at the prescribed conditions of 15°C and 0.005 rad/s to describe the ages of the various 70-100 penetration grade binders according to durability as illustrated in Figure 4.3. The $G\text{-}R$ parameters thus indicate that the field recovered binders are less durable and more susceptible to cracking than the virgin and PAV binders.

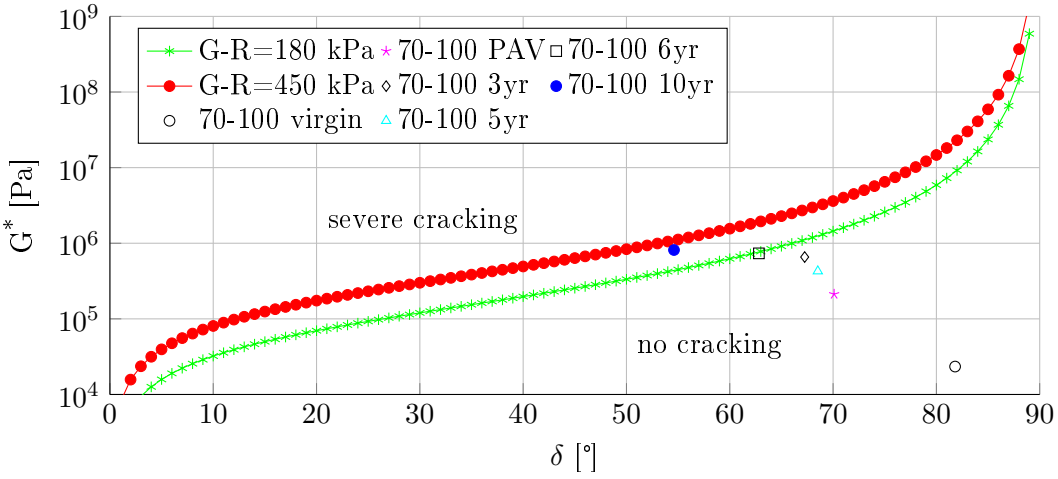

Figure 4.3: Glover-Rowe parameter applied to virgin, PAV and field recovered 70-100 binder data (Mukandila, 2015).

4.1.2 Binder column fatigue data

Mukandila (2015) conducted stress controlled bitumen column fatigue tests at 10 Hz. A summary of the applied loads (torque) and testing temperatures are presented in Table 4.3. According to Shan *et al.* (2010), the introduction of rest periods followed by retesting of the specimens significantly improves the binder's response to fatigue. This phenomenon is termed *self-healing* and was not included in Mukandila's binder column fatigue tests.

Table 4.3: Experimental plan of the binder column fatigue tests (Mukandila, 2015).

Torque[i] [Nmm]	Temp. [°C]	Binder[ii]
5 to 40	10	70/100 pen. grade
5 to 40	25	70/100 pen. grade

[i] $frequency = 10\ Hz$ [ii] virgin binder

An end of life transfer function, developed by Mukandila (2015), relates the magnitude of the applied shear stress τ to the number of load applications to cohesive failure N_f as illustrated in Figure 4.4. The transfer function as defined in Equation 4.3, was rearranged with τ as the independent variable and N_f the dependent variable (Equation 4.4). The material parameter values of Equation 4.4 are summarised in Table 4.4.

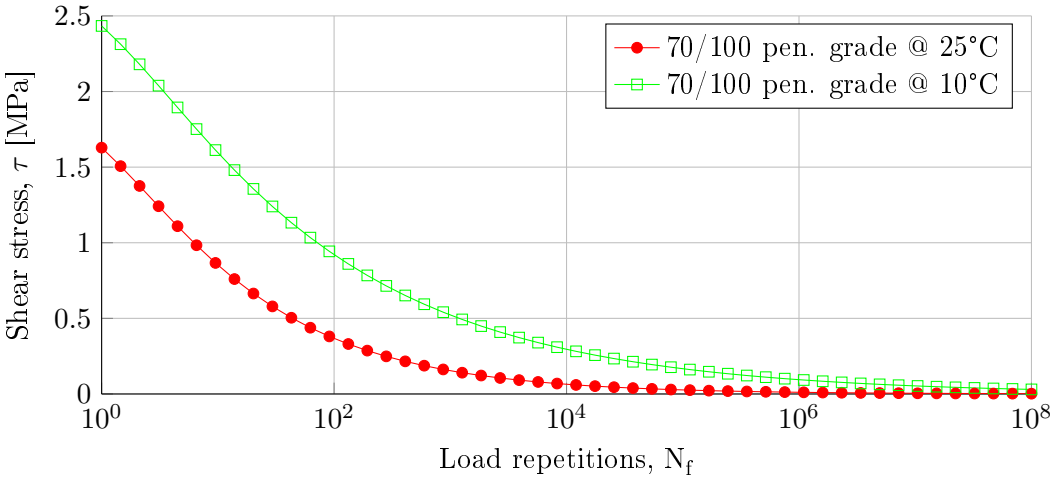

Figure 4.4: Cohesive fatigue transfer functions for virgin 70-100 penetration grade binder (Mukandila, 2015).

$$\tau = a(1 + N_f)^b \tag{4.3}$$

$$N_f = (\frac{\tau}{a})^{\frac{1}{b}} - 1 \tag{4.4}$$

where:

τ = constant shear stress [MPa]

N_f = number of load cycles to failure [-]

$a,\ b$ = material parameters [-]

Table 4.4: Material parameter values of the cohesive fatigue transfer functions used in Equation 4.4 (Mukandila, 2015).

Temp. [°C]	a	b
10	2.889	−0.2476
25	2.119	−0.3797

Although the fatigue trends (Figure 4.4) correspond to the asphalt fatigue trends as described by Read and Whiteoak (2003) in the Shell bitumen handbook and by Rowe and Brown (1997) where more load repetitions are observed for lower temperatures, the number of load repetitions to failure is very conservative. Equation 4.4 does not include a binder endurance limit i.e. an asymptote parallel to the load cycle axis representing a stress level below which failure will never occur, thus resulting in unlimited fatigue life. The latter is a source of concern, since an infinitesimal stress will result in a definite number of load repetitions to failure at 25°C and 10°C.
The Shell bitumen handbook further indicates that constant stress controlled tests exhibit a greater fatigue rate than constant strain controlled tests. Hintz (2012) explains that as fatigue sets in around the periphery of the test specimen, a reduction of the intact radius occur due to the formation of cracks. Applying a constant torque load over a diminishing effective area increases the fatigue rate. According to Huang (1993), the stress controlled test is applicable for thicker layers (>150 mm) whereas the strain controlled test is applicable for thinner layers (<50 mm). Calculations using the FE seal model results are dependent on the transfer functions and will in this case result in fewer repetitions to failure in comparison to strain controlled transfer functions.

4.1.3 Stone column fatigue data

Mukandila (2015) conducted stress controlled stone column fatigue tests at 10 Hz. No rest periods were included and the experimental test program as pertaining to this study is summarised in Table 4.5. Similar to the binder column fatigue formulations, Mukandila (2015) developed end of life transfer functions for adhesive fatigue as illustrated in Figure 4.5. The material parameters are summarised in Table 4.6.

Table 4.5: Experimental plan of the stone column fatigue tests (Mukandila, 2015).

Torque[i] [Nmm]	Temp. [°C]	Binder[ii]	Aggregate
50 to 200	10	70/100 pen. grade	Dolerite
50 to 200	25	70/100 pen. grade	Dolerite

[i] $frequency = 10\ Hz$ [ii] virgin binder

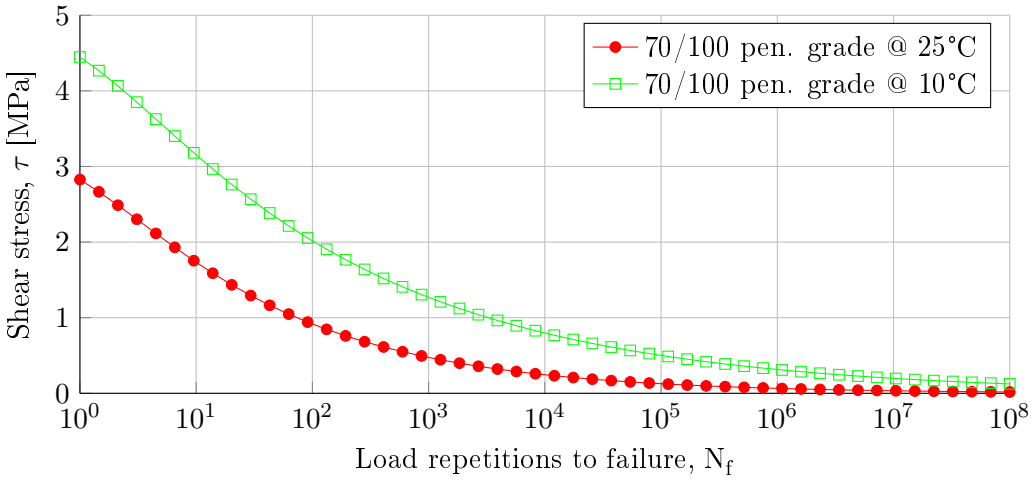

Figure 4.5: Adhesive fatigue transfer functions for virgin 70-100 penetration grade binder (Mukandila, 2015).

The surface roughness of the stone column tests were neither recorded nor altered subsequent sample preparation. Aggregate cores of proximately 11 *mm* were drilled from parent rock and cut to size, thereby creating an artificial surface roughness. Mo (2010) indicates that a rough surface texture dramatically increases the shear stress within the adhesive zone. Surface roughness is therefore an important parameter to consider when conduction stone column tests. Mukandila's adhesive fatigue trends, however, correlate with Mo's (2010). In both cases the cooler specimens exhibit greater resistance to adhesive fatigue, though Mo's tests were conducted on smaller aggregate columns and with a different binder.

Table 4.6: Material parameter values of the adhesive fatigue transfer functions used in Equation 4.4 (Mukandila, 2015).

Temp. [°C]	a	b
10	5.116	−0.2018
25	3.448	−0.2871

According to Little and Jones (2003), the dominant failure mechanism within the adhesive zone has a strong relationship with the binder type and film thickness.

Adhesive failure dominates in films with thickness $< 200\ \mu m$, while cohesive failure dominates in films $> 250\ \mu m$. Although Mukandila's 100 μm film thickness falls within the adhesive range as discussed by Little and Jones (2003), it borders on the transition phase from dominant adhesive failure to dominant cohesive failure.

4.2 DSR mortar analysis

During the LOT program (Huurman, 2008), it was established that ravelling can be ascribed to damage which occurs within the fine material of a Porous Asphalt Concrete mix. A mortar mixture consisting of 34% Cariphalt XS, SBS modified bitumen, 29.9% sand with a maximum grain size of 500 μm and 36.1% Wigro 60k filler which includes 25% chalk hydrate, was prepared from which various test specimens were produced. The percentages are in terms of component mass to the total mixture mass.

The DSR mortar testing followed a similar approach to the binder testing, consisting of mortar response testing, mortar fatigue testing and mortar-aggregate bond (adhesive zone) fatigue testing. As previously mentioned, the difficulties obtained with initial slurry testing and the consequent discontinuation thereof, resulted in the assumption that mortar characteristics can represent fine slurry.

A typical slurry mixture consists of: 100 parts fine aggregate, 20 parts of 60% stable grade emulsion, 1 to 2 parts of cement or hydrated lime (filler) and 15 parts water. With subsequent water evaporation it is estimated that the slurry layer consists of, $10\% - 12\%$ residual binder, $1\% - 2\%$ filler and $87\% - 89\%$ fine aggregates by mass (uncompacted). This study acknowledges the difference in composition of slurry with comparison to mortar, yet mortar remains a close alternative for the types of phenomenological insights desired with the simulation of the cape seal FE model. This section, therefore, presents the DSR mortar results from the LOT program (Huurman, 2008), as pertaining to this study.

4.2.1 Parallel plate response data

The viscoelastic response properties of virgin and aged mortar were translated into a two term Prony series. The mortar Prony series selected for this study are summarised in Appendix C and an example is presented in Table 4.7. Virgin mortar was subjected to short term aging by placing mortar slabs with a thickness of 2 mm inside an oven at $175°C$ for 90 minutes. This simulated the aging effect of heating during road construction.

Aged mortar samples included additional aging by placing the mortar slabs inside a weatherometer. The conditions inside the weatherometer were as follows: UV light

Table 4.7: Prony series of virgin mortar at 25°C (Huurman and Woldekidan, 2007).

α_i	τ_i
0.7456	0.0192
0.1771	0.3693

$G_0 = 1873\ MPa$, $\nu = 0.45$

of 60 W/m^2 in the range of 300 nm to 400 nm, relative humidity of 70% and a room temperature of 40°C, resulting in a surface temperature of 70°C (Huurman, 2008). The mortar was subjected to these conditions for a 1000 hours, simulating the field aging effect of seven years. The mortar Prony series were implemented as the constitutive material models for slurries in the cape seal FE model analyses. The dissipated energy responses W_{in} obtained with the FE model serve as an input to the mortar column fatigue data analysis.

4.2.2 Mortar column fatigue data

Mortar column fatigue tests were conducted at two different frequencies, two different temperatures and a range of stress controlled i.e torque controlled conditions as presented in Table 4.8. Regression analyses of the test data resulted in the development of cohesive fatigue transfer functions based on the dissipated energy principle as presented in Equation 4.5. The transfer function relates the dissipated energy ratio of the initial cycle W_0/W_{in} to the number of load repetitions N_f that will result in cohesive failure.

Table 4.8: Mortar column fatigue test program (Huurman, 2008).

Frequency [Hz]	Temp. [°C]	Torque range [Nmm]
10	0 & 10	35 to 140
40	0 & 10	35 to 140

$$N_f = \left[\frac{W_0}{W_{in}}\right]^n \tag{4.5}$$

where:

W_0 = reference energy [MPa]

W_{in} = dissipated energy of initial cycle [MPa]

n = material constant [-]

where:

$$n = a_3 + b_3 T \tag{4.6}$$

$$W_0 = a_4 + b_4 T \tag{4.7}$$

where:

T = temperature

The model parameters emanating from the regression analyses for the reference energy W_0 and material constant n are presented in Table 4.9. The regression analyses have linear relationships and account for temperature effects within the material. A similar regression approach was adopted for the stone column fatigue data analysis of the mortar-aggregate bond.

Table 4.9: Model parameters for dissipated energy fatigue model (Huurman, 2008).

Mortar	a_3	b_3	a_4	b_4
virgin	1.522	0.057	13.144	-1.179
aged	1.817	0.063	5.222	-0.459

4.2.3 Stone column fatigue data

Huurman (2008) hypothesised that the bitumen component in the mortar mix and the surface morphology of the corresponding aggregates are responsible for the mortar-aggregate bond strength. Bitumen that had undergone the same aging protocols was therefore utilised in the stone column testing. Aggregates consisted of bestone and greywacke. Though both aggregate types are different in composition to dolerite, only the results of the greywacke will be presented for the purpose of this study. Cores, with a diameter of 6.7 mm, were drilled from parent rock of which the surfaces were prepared by sand blasting. The micro texture of the sandblasted greywacke columns was approximately 50 μm to 60 μm. Virgin and aged stone column specimens were prepared, having a minimum binder film thickness of 15 μm.
The test routine was similar to the mortar column testing, though less torque was generally required. All tests were stress controlled and a summary of the stone column fatigue test program is presented in Table 4.10.
Regression analyses of the test data resulted in the development of adhesive fatigue transfer functions based on an equivalent tensile stress approach as defined in Equation 4.10. The transfer function relates the tensile stress ratio of the initial cycle σ_e/σ_0 to an accumulative damage rate $\dot{D}$. This damage rate was subsequently related to the number of load repetitions N_f that resulted in adhesive failure (Equation 4.8). The parameters for σ_e are obtained in the adhesive zone of the FE seal model simulations, while σ_0 are determined with the stone column tests.

$$N_f = \frac{1}{D_1} \tag{4.8}$$

Table 4.10: Stone column fatigue test program (Huurman, 2008).

Binder	Temp. [°C]	Torque range[i] [Nmm]
virgin	0 to 20	20 to 125
aged	0 to 20	20 to 125

[i] All tests conducted at 10 Hz

where:

N_f = number of cycles to fatigue failure

D_1 = damage accumulation of the initial cycle

$$D(t) = \int_0^t \dot{D}(\sigma)dt \tag{4.9}$$

where:

D = damage accumulation of the cycle

$\dot{D}$ = damage accumulation rate

$$\dot{D}(\sigma_e) = \left(\frac{\sigma_e}{\sigma_0}\right)^{n_0} \tag{4.10}$$

where:

σ_e = equivalent tensile stress [MPa]

$\sigma_e > 0$, otherwise $\dot{D}(\sigma_e) = 0$ if $\sigma_e \leq 0$

σ_0 = reference tensile stress [MPa]

n_0 = material parameter

$$\sigma_e = \sigma_n + \frac{\tau}{\tan\phi} \tag{4.11}$$

where:

σ_n = normal stress [MPa] (positive for tension)

ϕ = angle of internal material friction [°]

τ = shear stress [MPa]

$$n_0 = a_5 + b_5 T \tag{4.12}$$

$$\sigma_0 = a_6 + b_6 T \tag{4.13}$$

$$\phi = a_7 + b_7 T \tag{4.14}$$

where:

T = temperature

The model parameters emanating from the linear regression analyses for the reference tensile stress σ_0, internal friction angle ϕ and material constant n_0 are presented in Table 4.11. The regression analyses account for temperature effects within the material.

Table 4.11: Model parameters for adhesive fatigue model (Huurman, 2008).

Mortar	a_5	b_5	a_6	b_6	a_7	b_7
virgin	4.808	-0.102	12.642	-0.235	24.257	0.784
aged	5.169	-0.082	10.478	-0.199	29.203	0.487

4.3 Closure

This chapter discussed the origins and analysis methods of the binder and mortar material data that are implemented in this study. The binder and mortar response properties, serve as input parameters to the FE seal model. Fatigue data in the form of transfer functions are applied during model post processing of which the results are validated with the empirical field data. In some cases field data is unable to isolate and address a specific mechanism of interest. In such cases new laboratory tests are developed to address the issue. The following chapter introduces a new laboratory concept for seal aggregate embedment testing.

5. Embedment characterisation

For years practitioners made use of the ball penetration test (BPT) to estimate the embedment potential of the underlying substructure before sealing. This chapter presents the results and the interpretation of the BPT in the context of a newly developed repeated ball penetration tests (RBPT). The RBPT lends insight into the deformation potential of a base structure with reference to load magnitudes.

5.1 Base embedment analysis

A limestone base was selected for this investigation as discussed in Section 3.2.1. The results of the specimen preparations, ball penetration values and repeated ball penetration tests are presented in this section.

5.1.1 Specimen preparation results

Standard modified AASHTO compaction tests were conducted on G2 limestone material, establishing the optimum moisture content (OMC) for the specific grading as presented in Figure 5.1. The OMC of 5.0% is slightly greater than an OMC of 4.4% obtained by van den Berg (2014) on the same material. The increase in OMC is ascribed to the exclusion of the aggregate fractions greater than 13.2 mm.

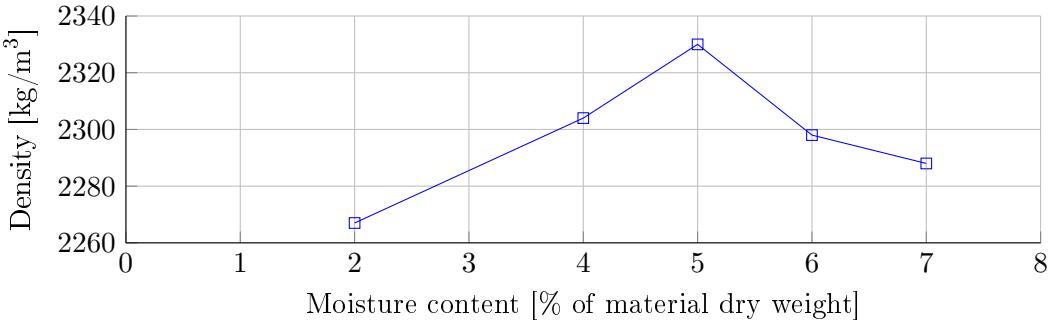

Figure 5.1: Modified AASHTO density test for OMC.

Five sets, each containing six to seven specimens, were compacted with the Bosch vibratory hammer at various compaction efforts at OMC. A summary of the resulting maximum dry density (MDD) and the moisture content (MC) of the upper 20 mm per specimen is presented in Table 5.1. Over compaction resulted in slushing, where some fines and moisture were lost resulting in a variation of MC obtained after the curing process. Commencement of sealing is prohibited if the MC in the base exceed 50% of OMC (TRH3, 2007). It is apparent that the density of the first three sets exceed the MDD (2330 kg/m^2) of the modified AASHTO compaction tests, while the density of the final two sets were below 2330 kg/m^2. The fifth set was thus prepared to ensure great embedment potential and high ball penetration test values.

Table 5.1: Specimen compaction and moisture content results.

Set	Compaction effort	MDD [kg/m^3]	MC^i of upper 20 mm
1	35 seconds	2425	12% of OMC
2	17 seconds	2380	12% of OMC
3	10 seconds	2342	17% of OMC
4	5 seconds	2272	29% of OMC
5	5 seconds	2269	95% of OMC

[i] subsequent curing

5.1.2 Ball penetration test results

Three ball penetration tests per density set were conducted. The average ball penetration values for set 1 to set 5 are, 2.8 mm, 2.8 mm, 3.6 mm, 3.9 mm and 6.3 mm respectively. These values are illustrated in Figure 5.2 with the corresponding specimen density and post curing MC.

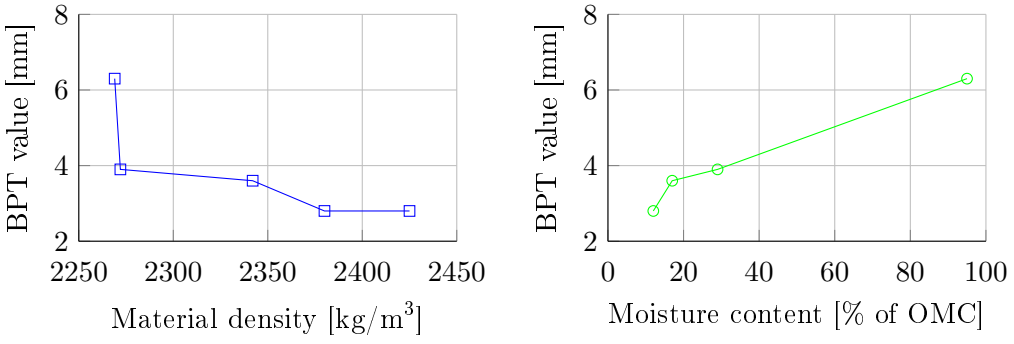

Figure 5.2: Ball penetration test values as a function of density and MC.

Definite trends were observed in both cases. The BPT values increase as material density decrease, but the moisture content relation results in a clearer depiction of dependency. The increases in BPT values are almost linearly in relation to the increases in the MC.

5.1.3 Repeated ball penetration test results

Repeated ball penetration tests were conducted on the five sets at three different constant load settings which included: 0.5 kN, 1.0 kN and 5.0 kN. An exception was made for set 5, where the 5.0 kN test was replaced with a 2.5 kN test due to difficulties obtained with major deformation in the specimen. LVDTs recorded the cumulative deformation process at a frequency of 1024 Hz, while a load cell monitored the applied load at the same frequency as presented in Figure 5.3. High data acquisition frequency results in an accurate depiction of the load cycle, but significantly increases data file sizes. Data were therefore acquired at three intervals: 0-100 cycles, 990-1000 cycles and 9990-10000 cycles. Although a seating load of 0.1 kN was applied to all the tests, Figure 5.3 illustrates that the target force was only reached subsequent the initial load cycles. This was the case for all the tests.

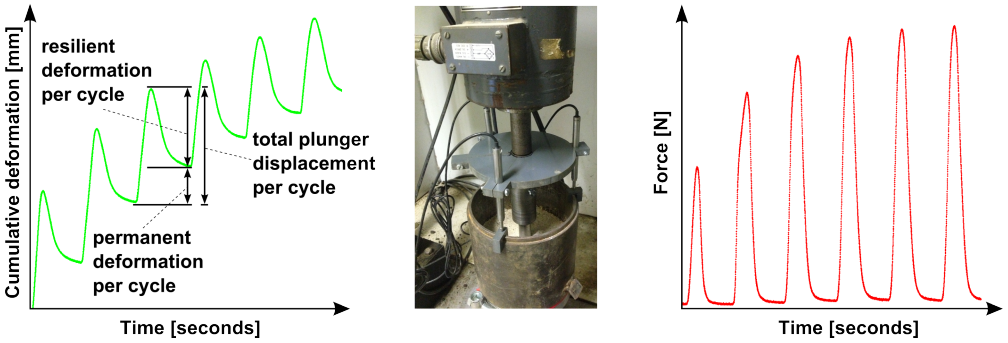

Figure 5.3: Data acquisition process for repeated ball penetration tests.

The overall outcome of the RBPTs was the relation between the cumulative deformation and the constant applied load as illustrated for Set 1 in Figure 5.4. The shape of the cumulative deformation i.e. embedment has a prevailing natural logarithmic trend. The majority of the embedment occurs within the initial 100 cycles, which is similar to the trends obtained by Araya *et al.* (2010) with repeated load CBR testing on unbound granular base materials. This is not surprising considering that the methods of load application are comparable with the primary difference being the shape of the loading foot.

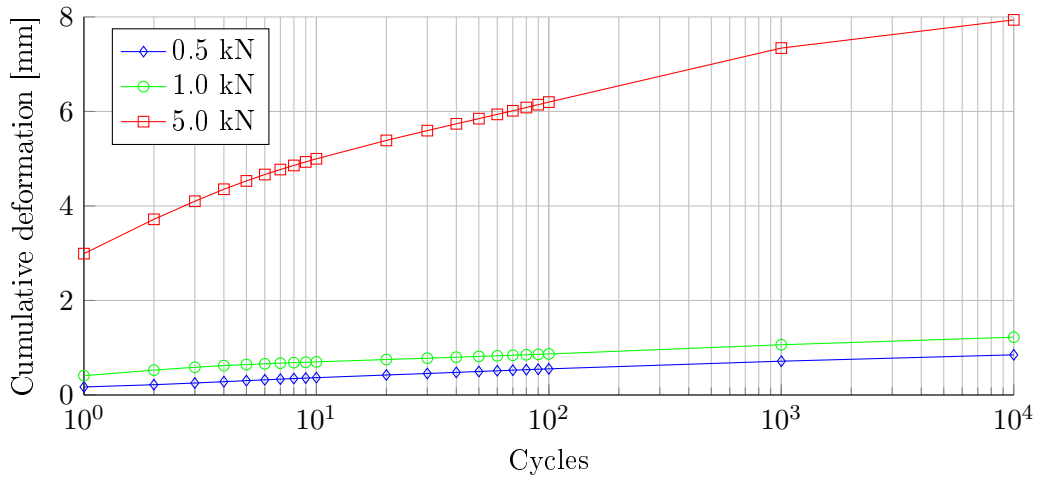

Figure 5.4: Cumulative deformation RBPT results for Set 1.

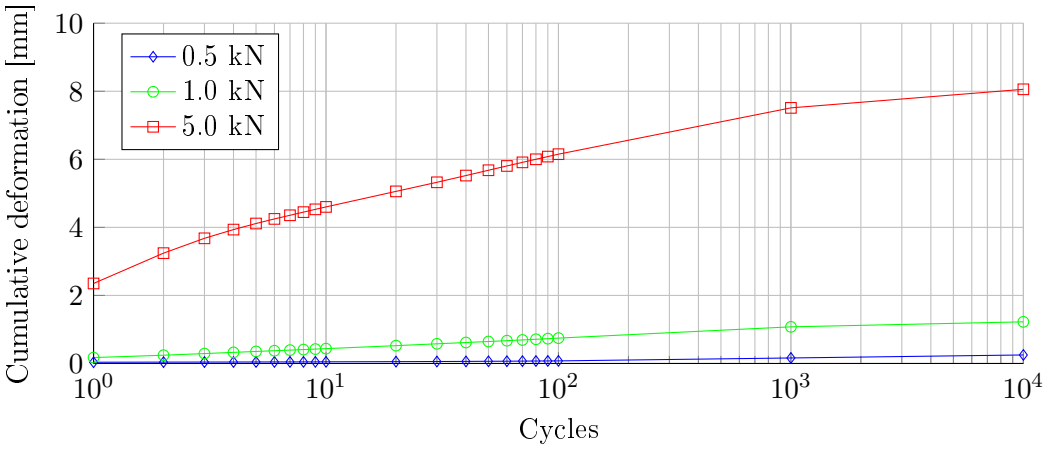

Figure 5.5: Cumulative deformation RBPT results for Set 2.

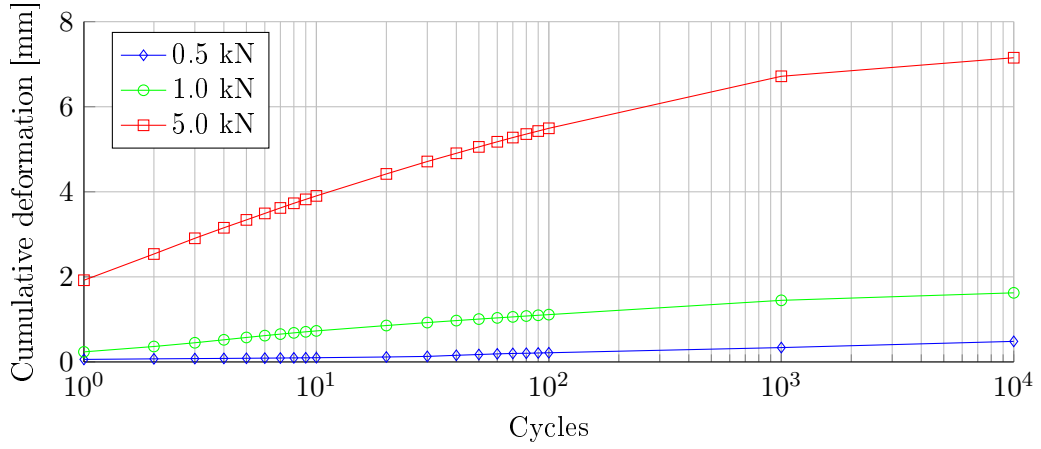

Figure 5.6: Cumulative deformation RBPT results for Set 3.

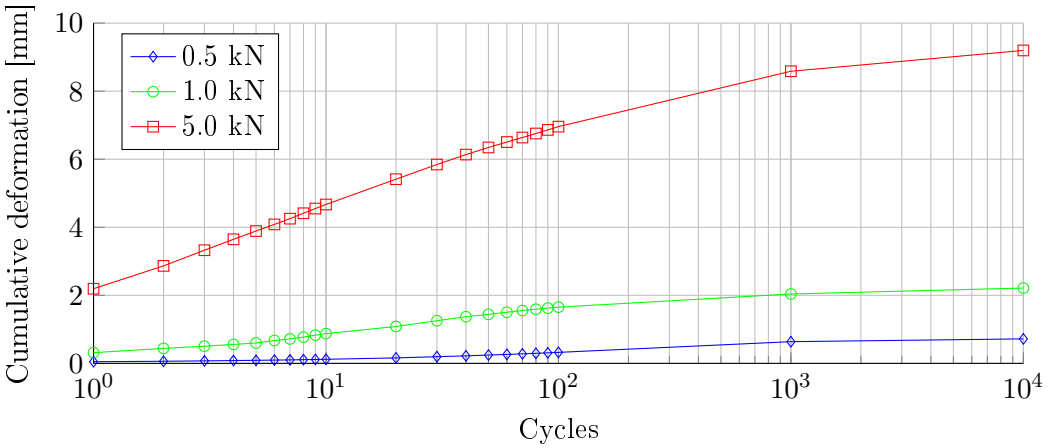

Figure 5.7: Cumulative deformation RBPT results for Set 4.

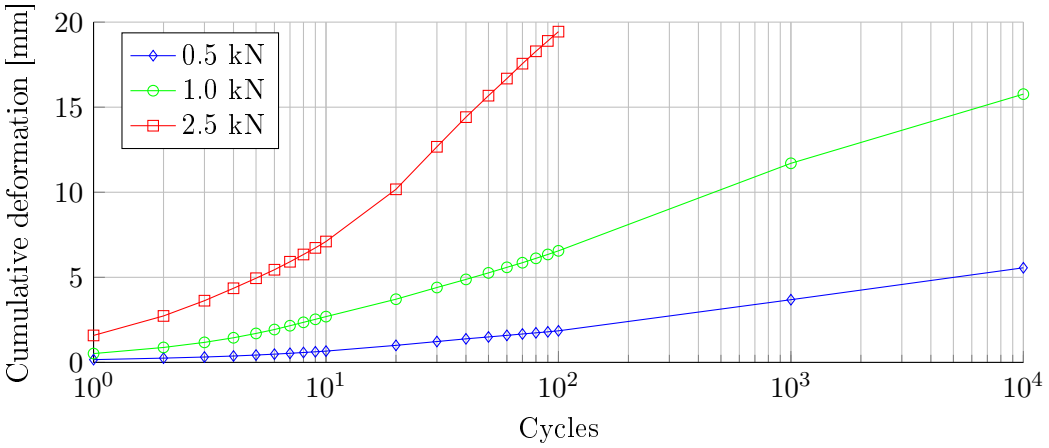

Figure 5.8: Cumulative deformation RBPT results for Set 5.

5.2 Conceptual embedment model

The FE seal model includes an elastic base component that requires elastic model parameters. An elastic response is therefore obtained from the seal model that is included in an embedment model. This model describes the embedment development of the seal aggregate subject to traffic. The elastic parameters and embedment model were derived from the embedment test analyses as discussed in this section.

5.2.1 Base material response analysis

A finite element RBPT model was developed to back calculate the base response parameters. These parameters include the Young's Modulus E and Poisson's ratio ν. The elastic deformation from RBPT FE model's initial cycle was superimposed

on the laboratory RBPT's permanent deformation component as derived from the initial load cycle (Figure 5.3). The elastic deformation trends obtained with the FE RBPT model for various base stiffness and applied forces are illustrated in Figure 5.9. The permanent deformation trends of the total plunger displacement for the initial cycle of the laboratory RBPTs are superimposed on the elastic deformations. Even though there were differences in the total deformation of the various RBPT sets, the major influence was not the different compaction efforts, but the high percentage of moisture present in Set 5. This was however the intent and the RBPT results were divided into two categories: strong bases and weak bases, which served as the upper and lower limits for this research. The model parameters for the base response analyses are summarised and presented in Table 5.2.

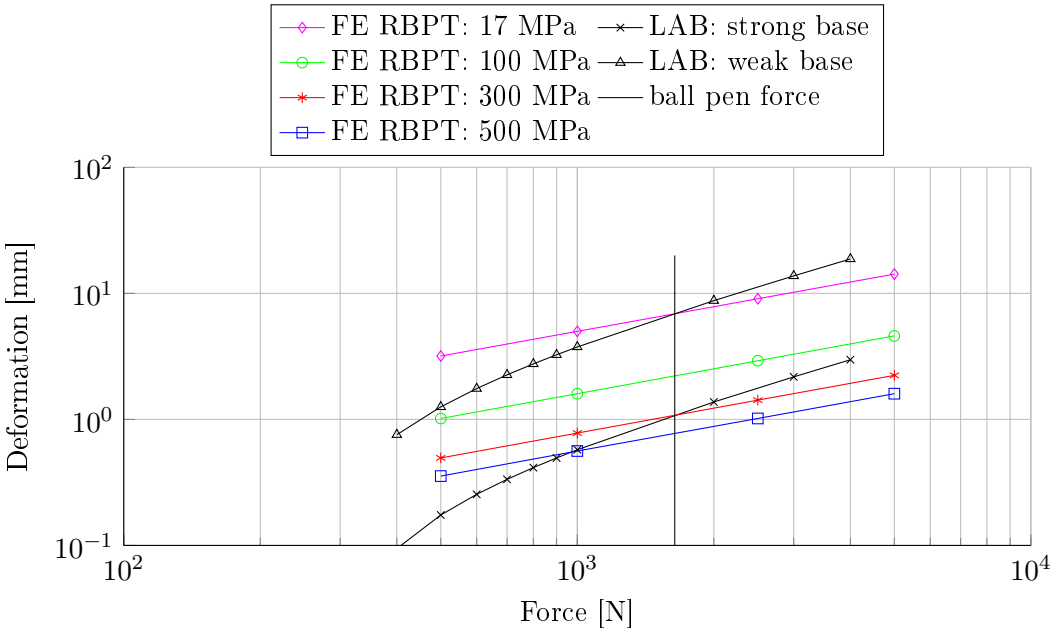

Figure 5.9: Response analysis of the RBPTs.

$$u_{el\ def} = a_1 F^{b_1} \tag{5.1}$$

where:

$u_{el\ def}$ = elastic deflection from FE models

F = applied force

$a_1,\ b_1$ = model parameters

$$a_1 = a_2 E^{-b_2} \tag{5.2}$$

where:

$a_2,\ b_2$ = model parameters

E = Young's modulus

$$u_{p_{n=1}} = a_3 F + b_3 \tag{5.3}$$

where:

$u_{p_{n=1}}$ = permanent deformation of initial cycle
$a_3,\ b_3$ = model parameters

Table 5.2: Model parameters for the base response analysis.

Base strength	b_1	a_2	b_2	a_3	b_3
weak (17 MPa)	0.65	0.3616	-0.658	0.005	-1.2435
strong (300 MPa)	0.65	0.3616	-0.658	0.0008	-0.2257

Application of the calculated ball penetration force (1640 N), indicated the position where the FE model trends should intersect with the RBPT data. Iterative adjustments to the Young's modulus E in Equation 5.2 resulted in a vertical shift of the FE model trend until the desired position was obtained. Moduli values of 300 MPa and 17 MPa were obtained for the strong and weak bases respectively as summarised in Table 5.3. Although a change in the Poisson's ratios ν made slight changes to the FE model trends, it was negligible and a ν of 0.35 was assumed for all relations. The E and ν response properties were implemented in the FE seal model and were, for this case, associated with the permanent deformation potential of the base.

Table 5.3: Back calculated base stiffness values for the corresponding ball penetration values (BPV).

Base stiffness [MPa]	BPV [mm]
17	6.3
50	5.9
100	5.3
200	4.0
300	2.8
450	1.0[i]

[i] Extrapolated value

5.2.2 Base material permanent deformation analysis

The scope of the permanent deformation analysis consisted of four sequential phases as discussed in Section 3.2.1. A quick summary follows:

a) Establish the relationship between the magnitude of permanent deformation u_p and the corresponding total plunger displacement u_e of the RBPTs. Here, total displacement comprises the permanent deformation plus the resilient deformation.

b) Create deformation ratios DR with the associated average BPT value. The DR will be used to normalise the PD trends.

c) Define the cumulative permanent deformation trends PD per load magnitude and material condition.

d) Establish the relationship between the cumulative permanent deformation PD and the cumulative permanent deformation rate $\dot{PD}$.

The embedment potential is represented by the cumulative permanent deformation PD trends as defined in Equation 3.28 and illustrated in Figure 5.10. These trends were developed from the cumulative deformation data (Figure 5.4) and comprised a natural logarithmic format. Normalisation of these trends with reference to the initial load cycle and the corresponding ball penetration value resulted in the deformation ratios DR, thereby associating any initial deformation to an embedment potential as defined in Equation 3.27. The corresponding material and modelling parameters are presented in Table 5.4.

Table 5.4: Material and model parameters for the base embedment analysis.

Base strength	$\mathbf{a_1}$	$\mathbf{a_2}$	$\mathbf{b_2}$	$\mathbf{a_4}$	$\mathbf{b_4}$	$\mathbf{a_5}$	$\mathbf{b_5}$
weak (17 MPa)	0.999	$-3e^{-5}$	-0.007	0.6805	0.0121	-0.0212	-0.7059
strong (300 MPa)	0.999	$-3e^{-5}$	-0.007	0.0707	0.0148	0.0286	-0.2065

The stress fields inside granular materials are subject to the stress history, therefore the permanent deformation is related to the stress history. A relationship between the cumulative permanent deformation rate $\dot{PD}$ and cumulative permanent deformation PD was established for each DR. This relation, as illustrated in Figure 5.11, indicates the contribution of the DR to permanent deformation, thereby taking into consideration the loading history with reference to embedment. A single load at a DR equal to 50%, exceed the entire contribution of a 20% DR load.

5.3 Closure

This chapter addressed a conceptual approach for the development of a base embedment model, utilising a mechanistic-empirical approach. A new laboratory developed

repeated ball penetration tests was used to observe the embedment development. Much debate amongst practitioners exist regarding the notion that approximately 50% of seal aggregate embedment occurs during construction. The FE seal model lends insight to this discussion by ascertaining the degree of embedment associated to traffic (pneumatic roller) loads. Field data is however required to validate the seal model and is discussed in the following chapter.

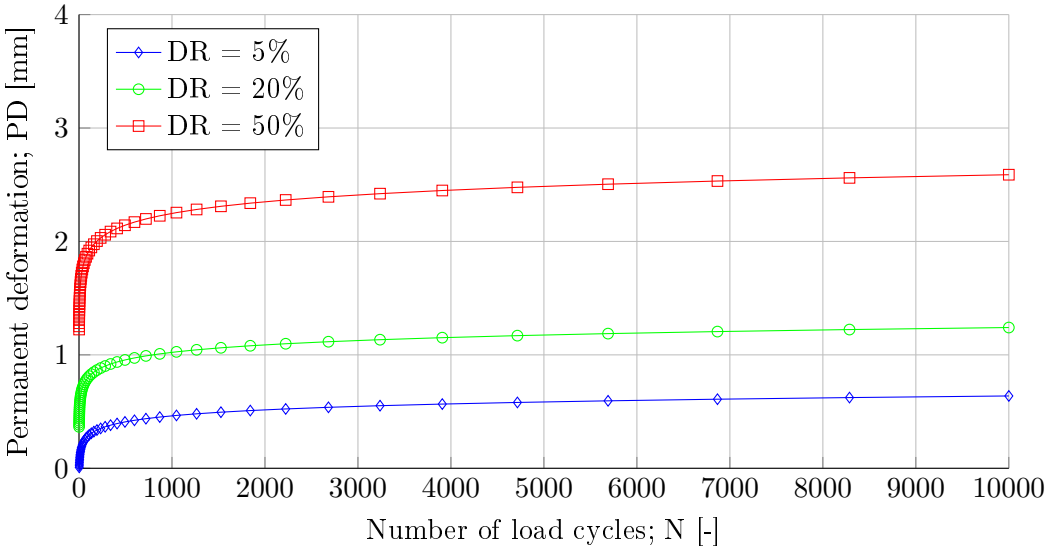

Figure 5.10: Permanent deformation (PD) trends and deformation ratios (DR) of the 300 MPa base.

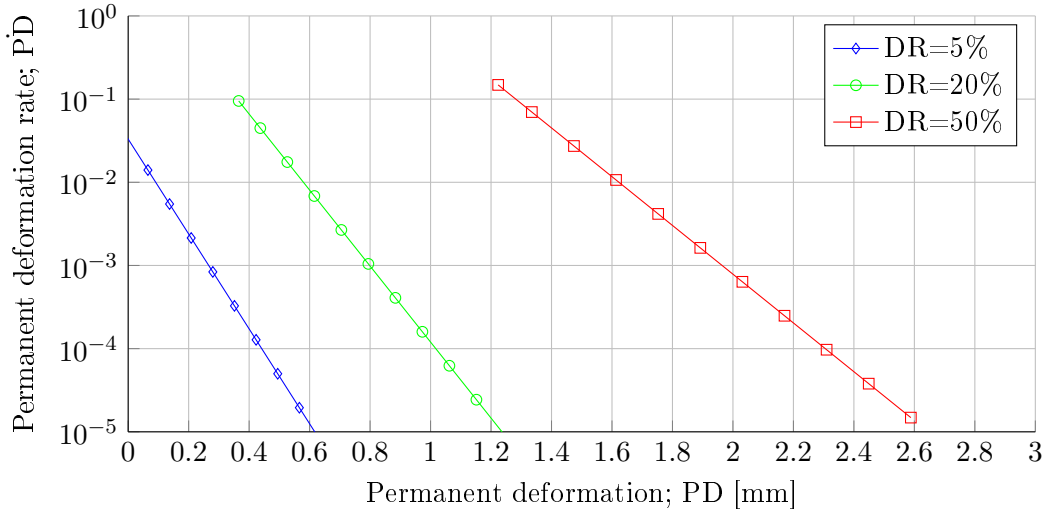

Figure 5.11: Relationship between the permanent deformation and permanent deformation rate in mm/cycle.

6. Field data analyses

Field data is required for the validation process of the FE seal model results. This chapter presents a summary on the field and empirical data analyses and the interpretations thereof as conducted by van Zyl (2015) and Burger and van Zyl (2004) for the purpose of FE seal modelling verification. Data was obtained for aggregate loss, fatigue cracking and surface texture loss. Table 6.1 serves as input parameters for the average South African road section in the case of HDM-4 deterioration models. These parameters describe the state of a newly constructed pavements.

Table 6.1: Assumptions and values assigned to different parameters for pavement deterioration models (Burger and van Zyl, 2004).

Traffic	**Value**	**Description**
AADT	3000	Annual average daily traffic
% Heavy	15	Percentage trucks in the traffic spectrum
E80-factor	1.2	The equivalence factor for heavy vehicles
% Growth	4	Rate of increase in the AADT annually
ELANES	2	Effective number of lanes
YE4	0.098	Calculated from the AADT (millions per year)
YAX	1.17	Calculated from the AADT (millions per year)
Structure	**Value**	**Description**
Base type	-	Granular
Deflection 1	0.4 mm	Two deflections were used to determine the sensitivity of
Deflection 2	0.8 mm	the cracking model to pavement strength (through SNP)
General	**Value**	**Description**
CDS	1	Construction defects indicator for the surfacing layer
COMP %	100	Indicator for compaction compliance
CDB	1	Construction defects indicator for the base layer
CRT	0	Retardation time for cracking due to maintenance
RRF	1	Retardation time for ravelling due to maintenance
MMP	66.67	Monthly mean precipitation (66.67 = 800 mm/year)
HS	20	Thickness of all bituminous surfacings
CW	7.2	Carriageway width (m)

6.1 Aggregate loss

Early aggregate loss is a phenomenon primarily observed on single and doubles seals, therefore no data on cape seals is presented in this section. Disregarding poor construction and incompatible material selections, aggregate loss is a result of inapt bonding for the corresponding traffic conditions. As previously mentioned, practitioners identified empirical relations between four components, able to indicate the boundary between adequate and inadequate bonding conditions. These components include: the annual average daily traffic (AADT) per lane per day, the ball penetration value (embedment potential), aggregate ALD and the minimum binder application rate.

6.1.1 TRH3 empirical data

A standard seal design is based on the equivalent light vehicle (ELV) passes per lane per day as the traffic component. AADT is converted to ELVs, assuming a heavy vehicle (HV) to light vehicle (LV) equivalent damage factor of 1 to 40. Van Zyl (2015) established relationships among the AADT, HV, LV, E80s and ELVs from a number of traffic monitoring sites in South Africa. These relations for single seals are presented in Table 6.2 to Table 6.4 and include the associated ball penetration values, aggregate ALDs and minimum binder application rates.
An illustration of the minimum binder application rates, related to the number of E80s as obtained from Table 6.2, is presented in Figure 6.1. As the traffic volume increases lower critical minimum binder application rates are required to avoid bleeding. Any combination of the relevant components below or outside the limits of the respective trends in Figure 6.1, results in aggregate loss. This was the format in which FE seal model validation comparisons were conducted.

Table 6.2: Critical minimum binder application rates for a ball penetration value of 1.0 mm (van Zyl, 2015).

Traffic analysis per lane per day					Average least dimension (ALD)				
AADT	**HV**	**LV**	**E80s**	**ELVs**	**4**	**6**	**8**	**10**	**12**
5848	20	5828	13	6628	0.57[i]	0.87	1.16	1.45	1.73
4501	50	4451	49	6451	-	0.72	1.01	1.3	1.58
3692	100	3592	121	7592	-	0.63	0.92	1.21	1.49
3028	200	2828	288	10828	-	0.56	0.85	1.13	1.41
2697	300	2397	472	14397	-	0.52	0.8	1.08	1.36
2330	500	1830	873	21830	-	-	0.74	1.02	1.29
2037	800	1237	1522	33237	-	-	-	0.94	1.22

[i] minimum application rate $[l/m^2]$

Table 6.3: Critical minimum binder application rates for a ball penetration value of 2.0 mm (van Zyl, 2015).

Traffic analysis per lane per day					Average least dimension (ALD)				
AADT	**HV**	**LV**	**E80s**	**ELVs**	**4**	**6**	**8**	**10**	**12**
5848	20	5828	13	6628	-	0.69[i]	0.98	1.26	1.54
4501	50	4451	49	6451	-	0.52	0.8	1.08	1.36
3692	100	3592	121	7592	-	-	0.7	0.97	1.25
3028	200	2828	288	10828	-	-	-	-	1.16
2697	300	2397	472	14397	-	-	-	-	1.11
2330	500	1830	873	21830	-	-	-	-	1.03
2037	800	1237	1522	33237	-	-	-	-	-

[i] minimum application rate $[l/m^2]$

Table 6.4: Critical minimum binder application rates for a ball penetration value of 3.0 mm (van Zyl, 2015).

Traffic analysis per lane per day					Average least dimension (ALD)				
AADT	**HV**	**LV**	**E80s**	**ELVs**	**4**	**6**	**8**	**10**	**12**
5848	20	5828	13	6628	-	0.59[i]	0.88	1.16	1.44
4501	50	4451	49	6451	-	-	-	0.96	1.24
3692	100	3592	121	7592	-	-	-	-	1.12
3028	200	2828	288	10828	-	-	-	-	1.03
2697	300	2397	472	14397	-	-	-	-	-
2330	500	1830	873	21830	-	-	-	-	-
2037	800	1237	1522	33237	-	-	-	-	-

[i] minimum application rate $[l/m^2]$

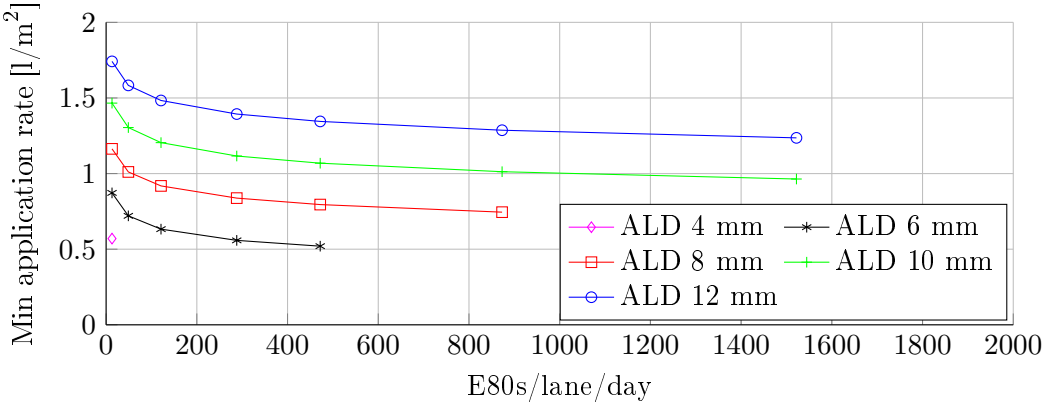

Figure 6.1: The relationship between the critical minimum binder application rates, E80s and ALD in mm for a ball penetration value of 1.0 mm (van Zyl, 2015).

The relative damage exponent n with which the load equivalency factor is determined was unknown for the various E80 estimations, therefore a value of 4 was assumed. Alternatively, ELVs can replace the E80s on the independent axis in Figure 6.1, by applying the relation as obtained from Table 6.2 and defined in Equation 6.1.

$$ELVs = aE80s + b \tag{6.1}$$

where:

$a = 18.09$

$b = 5797.3$

6.1.2 HDM-4 ravelling initiation

The HDM-4 ravelling initiation model simulates the initiation of aggregate loss due to bond fatigue and is therefore different to the critical minimum binder criteria which is associated with early aggregate loss. Two important parameters in the ravelling initiation model are the CDS and RRF. A CDS value = 1 indicates that the surface dressing is at optimum binder content, while a RRF = 1 indicates that no retardation is applied due to maintenance (Burger and van Zyl, 2004). The HDM-4 ravelling initiation model differentiates between surfacing types and suggests that on a typical newly constructed South African road section, single and double seals would ravel prior to cape seals as indicated in Table 6.5.

Table 6.5: HDM-4 ravelling initiation model results on the average South African sealed surface road section (Burger and van Zyl, 2004).

Surface material	Ravelling initiation
All (excluding CAPE, SL)	8.7 years
CAPE, SL	11.7 years

6.2 Fatigue cracking

Empirical and modelling data are presented in this section. Empirical field observations were conducted by Van Zyl (2015), while HDM-4 crack initiation data was obtained from Burger and van Zyl (2004).

6.2.1 Observed field cracking

Van Zyl (2015) developed the philosophy that repeated surface deflection results in fatigue cracking of seals. In order to verify this hypothesis, van Zyl obtained empirical

data from 34 sites throughout South Africa. This section presents the interpretation of the field data. The data consisted of three components: the Benkelman Beam deflection data subjected to a standard 80 kN axle load with which the radius of curvature (ROC) calculated according to Dehlen's method, the annual traffic count for the year of data collection with the corresponding traffic growth rate for each site and the time in years when fatigue cracking was first observed.

An assumption was made that the surface layer accounts only for the difference in the D_0 and D_{127} deflection measurements. If the surface layer is therefore viewed as a bending beam the magnitude of vertical displacement would be equal to D_0 - D_{127}. The surface deflection was further assumed to have remained constant throughout the service life of the seal. Interpretation of the deflection data is presented in Figure 6.2. Here, the cumulative surface deflection data resulting from the annual traffic count (Figure 3.18) is illustrated for the double seals. The annual traffic count was adjusted according the growth rate, converted to E80s and back calculated to the initial year following construction.

Data points representing initial fatigue cracking were superimposed on the cumulative deflection results at the respective times of observation. The resulting trend was termed the *trigger* line and defined in Equation 6.2. The trigger line indicated that seals which were exposed to constant high surface deflections i.e. low ROC, exhibit fatigue cracking at an earlier stage than the seals which were exposed to higher ROCs. A summary of the trigger line parameters as pertaining to this study is presented in Table 6.6.

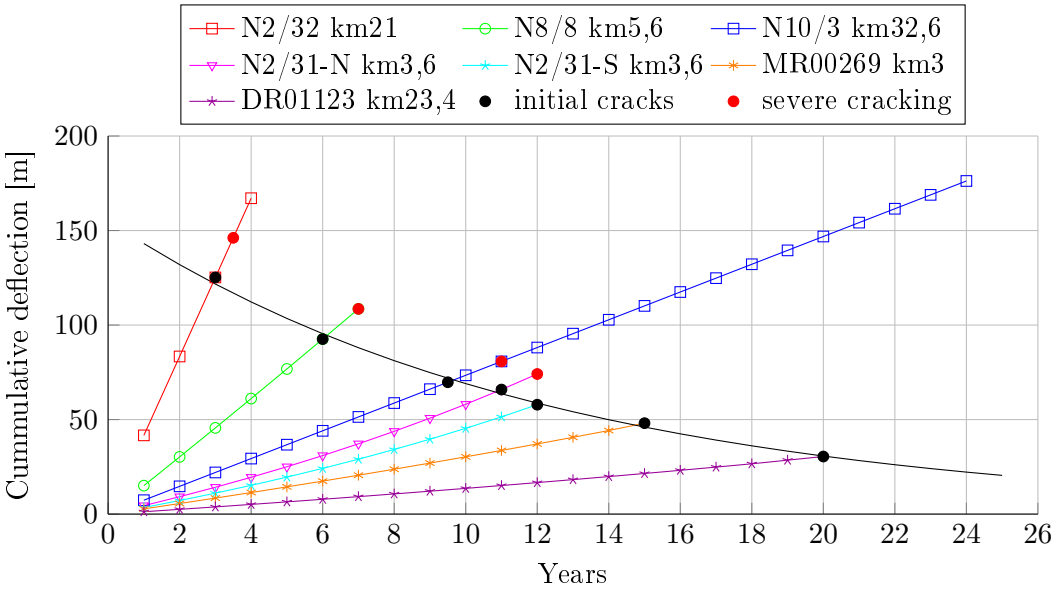

Figure 6.2: Double seal trigger line (van Zyl, 2015).

$$u_{cum\_def} = ae^{b \times Age} \tag{6.2}$$

where:

u_{cum_def} = cumulative deflection
Age = time in years
$a,\ b$ = model parameters

Table 6.6: Trigger line model parameters utilised in Equation 6.2 (van Zyl, 2015).

Seal type	a	b
Single seal	155.17	−0.081
Double seal	155.17	−0.081
Cape seal	155.17	−0.083

Since the FE seal model was developed to include only the upper 30 mm of the base structure, the model was used to verify van Zyl's assumption that the seal layer accounts only for the difference of the D_0 and D_{127} deflection measurements. A comparison between the modelled and field measured values for the ROC and D_0 - D_{127} surface deflections is illustrated in Figure 6.3. The modelled and field measured results are close in comparison and thus verifies the deflection assumption.

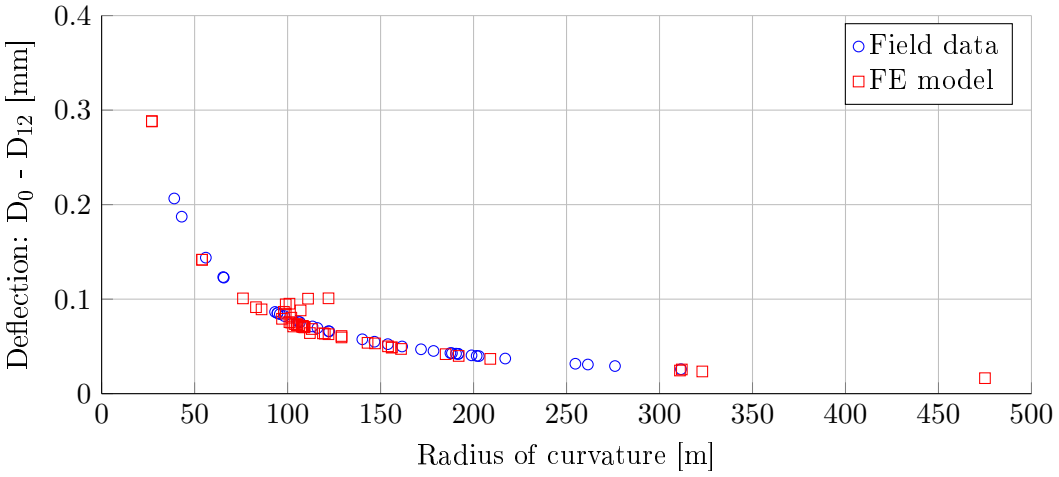

Figure 6.3: Field measured and FE seal model radius of curvature results.

6.2.2 HDM-4 crack initiation values

Two important parameters used to calculate the initial crack initiation for all cracks are SNP and YE4. SNP is the average adjusted pavement structural number and

can be determined from falling weight deflectometer (FWD) deflections. YE4 is the annual number of equivalent standard axles, calculated from AADT. Based on the parameters presented in Table 6.1, calculations were made to determine the crack initiation periods for two deflection levels and at one traffic level. The results are summarised in Table 6.7 and indicates that on the average South African road section, initial cracks would occur from 11 years to 13 years if the that section is not maintained (Burger and van Zyl, 2004). The HDM-4 crack initiation model also suggests that it is not particularly sensitive to an increase in the surface deflection.

Table 6.7: HDM-4 crack initiation periods for all cracks on the average South African sealed surface road section (Burger and van Zyl, 2004).

Deflection [mm]	Period [years]
0.4	12.4
0.8	11.4

6.3 Surface texture loss

Surface texture is defined as the air volume per area confined on the surface of a seal, between the upper bound at the aggregate asperities and the lower bound at the air-bitumen interface. Surface texture loss is a reduction of the air volume and a result of the simultaneous occurrence of aggregate orientation, aggregate wear, embedment and binder rise. This is a phenomenon which mainly results in problems on single and double seals.

Van Zyl (2015) obtained texture data using the sand patch test for single and double seals. The data consisted of the retained surface texture and calculated cumulative ELVs for a certain ball penetration value and base structure as illustrated in Figure 6.4. The underlying base structures included old seals, crushed stone bases and bitumen stabilised material (BSM) bases.

Van Zyl also developed a conceptual model with which to determine the retained texture depth (RTD) as a function of ELVs. Instead of the specified HV to LV equivalent damage factor of 40, the model obtained adequate results with a factor of 10 and is presented alongside the HDM-4 surface texture depth model (Figure 6.4). Van Zyl's model is defined in Equation 6.3 while the model parameters are presented in Table 6.8. The HDM-4 surface texture depth models over predicts the loss of surface texture when compared to the field data as illustrated in Figure 6.4 and Figure 6.5.

$$RTD = a_1 ln(x) + a_2 ln(x)^2 + a_3 ln(x)^3 + a_4 ln(x)^4 + a_5 ln(x)^5 + a_6 BP \qquad (6.3)$$

where:

RTD = retained texture depth

BP = ball penetration value

x = associated traffic count in ELVs

Table 6.8: Model parameters for van Zyl's (2015) conceptual RTD model.

a_1	a_2	a_3	a_4	a_5	a_6
1213	15.34	-33.22	2.89	-0.07	-9.42

6.4 Closure

This chapter discussed the field data and the analysis thereof as conducted by van Zyl (2015) and Burger and van Zyl (2004) for the purpose of FE seal model validation. Data capturing was dived into three categories: ravelling, surface cracking and surface texture loss. A fundamental difference in the risk to ravelling was highlighted by indicating that empirical knowledge (TRH3, 2007) considers ravelling as a single load rip-off effect, whereas the HDM-4 model simulates ravelling as a bond fatigue mechanism. Surface cracking was related to a fatigue mechanism consisting of a cumulative surface deflection approach, while the discrepancies between observed and HDM-4 modelled surface texture loss approaches were illustrated. The hypothesis of this study states that FE model of seals can be used to bridge the disconnect that exists between field data and current deterioration models. The following chapter deals with single seal analysis.

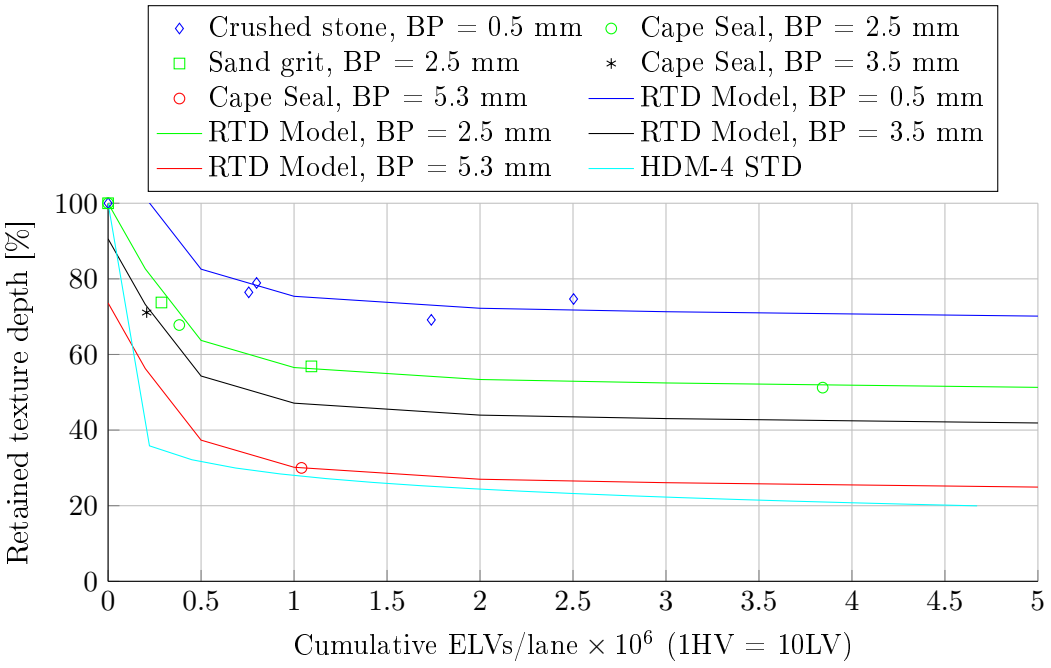

Figure 6.4: Retained texture depths (RTD) of single seals for various substructures and ball penetration (BP) values (van Zyl, 2015).

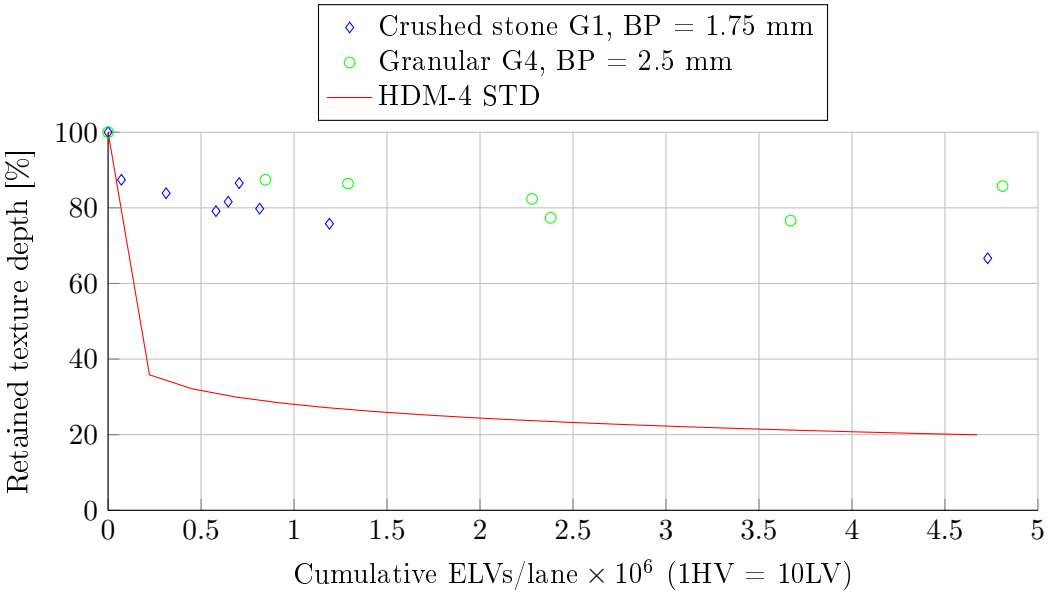

Figure 6.5: Retained surface texture depth of Double Seals for granular bases and associated ball penetration (BP) values (van Zyl, 2015).

7. Single seal analysis

A single seal is mainly constructed as a reseal on an existing substrate. There are, however, cases where newly constructed bases are sealed with single seals. This chapter illustrates and addresses the response and corresponding fatigue behaviour of the simulated single seal models on newly constructed bases with reference to the three failure mechanisms as defined by this study.

7.1 Adhesive failure

The adhesive failure analysis presents the shear stress response (Figure 7.1) and corresponding fatigue life calculations of the single seal models according to the primary variations as presented in Table 3.9. The primary variations as defined in this study include the structural variables, time related variable and traffic load variables. These variables are used to verify and validate the seal model's ability to simulate adhesive failure.

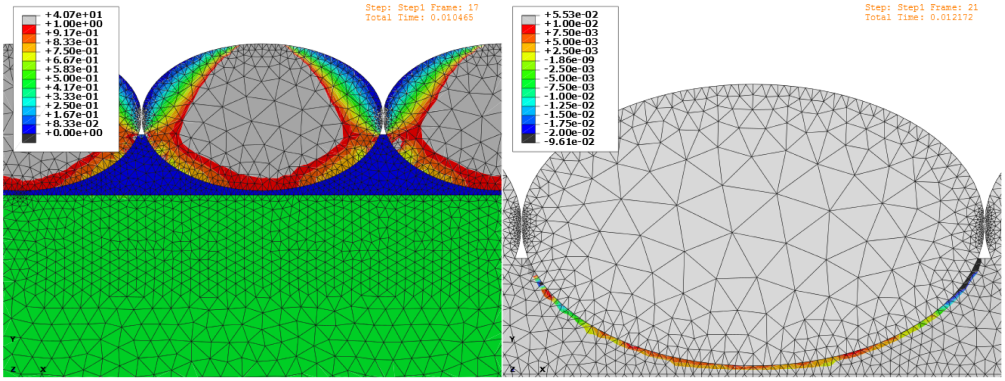

Figure 7.1: Screen grabs of aggregate interlock FE single seal contact simulations (MPa): von Mises stress (left) and adhesive zone shear stress (right).

7.1.1 Analysis of the structural variables

The structural variables are selected prior to seal construction and remain constant throughout the service life of a seal. These variables define the geometry and material selection of the seal. Typical structural variables include: the seal size and aggregate type, binder type and application rate, aggregate spread rate and substrate type.
Each structural component has an influence on the adhesive shear stress response and the fatigue life as presented in Figure 7.2, which illustrates the response variations for three different seal sizes at four aggregate spread rates. Aggregate spread rate is quantified in m^3/m^2, but in the case of the 2D model it is presented in terms the adjacent edge to edge spacing in mm. This study makes no formal correlation between the TRH3 (2007) m^3/m^2 spread rates and edge to edge spacings.
The trends in Figure 7.2 indicate that the shear stress responses increase as the spacing is increased from 0 mm to 2 mm. The 0 mm spacing represents aggregate interlock, while the 2 mm spacing signifies an open spread. These trends are consistent for all three seal sizes at similar time related and traffic load variables. It is noteworthy to mention that 6.7 mm seal exhibits less stress than the 9.5 mm and 13.2 mm seals, due to an increased number of contact points at the tyre road surface interface.
When evaluating the load repetitions to failure of the 13.2 mm seal, a 115% stress increase form 0 mm to 2 mm spacing results in a 90% reduction in load repetitions. The reduction in load repetitions is directly attributed to the implementation of the adhesive end of life transfer function as developed by Mukandila (2015). A detailed evaluation on the load repetitions to failure is addressed in Section 7.1.4.
In comparison to the spread rate, the ALD of the aggregate has less of an influence on the shear stress response as illustrated in Figure 7.3. The trend in Figure 7.3 indicates a 45% stress increase from a 6 mm ALD to a 9 mm ALD for the 13.2 mm seal. An elongated aggregate offers a greater binder contact area, which results in a reduction of bond stress when subject to traffic loads. The ALD stress differences is not as significant as the stress obtained with various binder application rates as illustrated in Figure 7.4.
The shear stress reduces by approximately 45% as the binder application rate increases from 0.8 l/m^2 to 1.6 l/m^2. The model simulation, therefore, supports the common perception that an increase in the binder application rate reduces the risk of aggregate loss. This phenomenon is further emphasised in Figure 7.4 with the application of an additional fog spray (FS) coating, which further reduces the risk of aggregate loss. The Fog Spay creates shoulder bonds on the aggregates reducing the adhesive shear stress obtained at the interface between the tack coat and the aggregate.

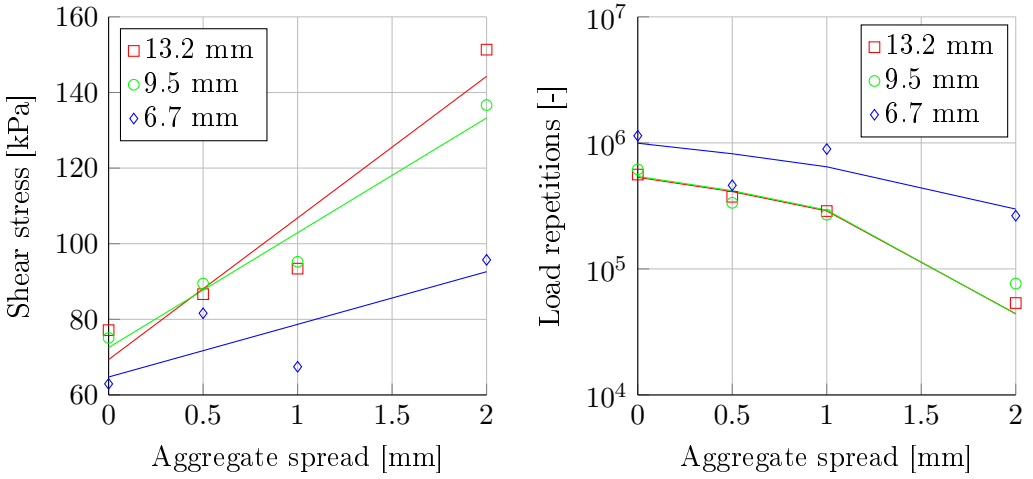

Figure 7.2: Shear stress and corresponding load repetitions to failure for the 6.7, 9.5 & 13.2 mm single seals and virgin 70-100 pen. grade binder at 40% wetted height. Temperature: 25°C, base stiffness: 200 MPa, traffic load: 20 kN-800 kPa at 80 km/h.

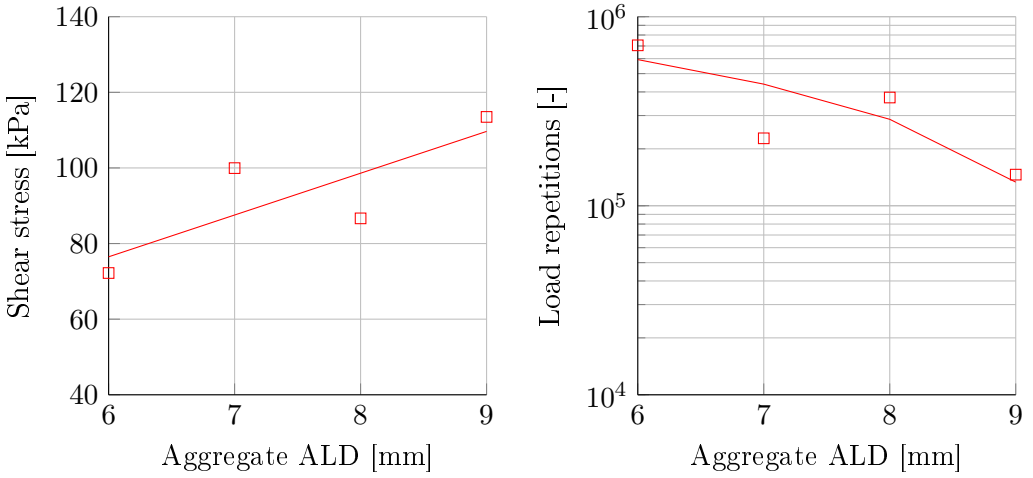

Figure 7.3: Shear stress and corresponding load repetitions to failure for the ALD of the 13.2 mm single seal and virgin 70-100 pen. grade binder at 40% wetted height. Temperature: 25°C, base stiffness: 200 MPa, traffic load: 20 kN-800 kPa at 80 km/h.

An increase in the binder application rate results in an increase in the aggregate wetted height. Similarly does the existence of construction embedment increase the wetted height as illustrated in Figure 7.4. The single seal models at 1.0 l/m^2 application rates, were subjected to 0.5 mm and 1.0 mm construction embedment depths, which resulted in aggregate wetted heights of 72% and 85% respectively. These wetted heights are similar to the wetted heights obtained at application rates of 1.4 l/m^2 and 1.6 l/m^2 without any construction embedment. It is therefore not surprising that the results are comparable, since conclusions are formed that the wetted height

i.e. binder application rate and aggregate spread rate are the two major structural components that affect aggregate loss.
The shear stress obtained with a variation in the structural variables ranges between 60 kPa and 160 kPa. This is comparable with the 3D seal models of Huurman (2010), having used similar material characteristics, load cases and temperatures. Huurman obtained an adhesive zone shear stress range of 115 kPa to 130 kPa for the maximum critical value.

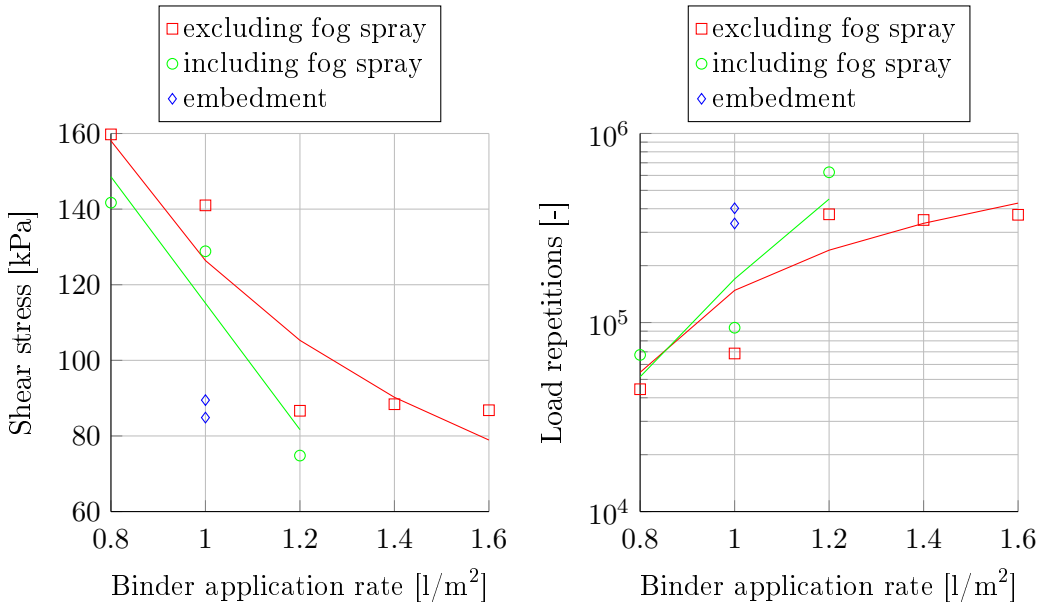

Figure 7.4: Shear stress and corresponding load repetitions to failure for virgin 70-100 pen. grade binder application rates and a 8 mm ALD, 13.2 mm single seal. Temperature: 25°C, base stiffness: 200 MPa, traffic load: 20 kN-800 kPa at 80 km/h.

7.1.2 Analysis of the time related variables

A time related variable refers to the change in condition of that variable over time. Material property change is a typical example of a time related variable, therefore simulations were conducted with changes to the base stiffness as illustrated in Figure 7.5. A reduction in the base stiffness resulted in an exponential increase of the shear stress. The increase in shear stress again results in a reduction in the number of load repetitions to failure. This is the case for the virgin 70-100 pen. grade binder at both $10°C$ and $25°C$. The adhesive bond at $10°C$ proves to be more resilient than a bond at $25°C$, resulting in a greater number of load repetitions to failure at $10°C$ than at $25°C$.

Similar trends in the bond strength with temperature difference were observed by Lombard (2015) during bitumen bond strength (BBS) tests. Lombard's tests were conducted with the same 70-100 pen. grade binder on dolerite cores drilled from the parent rock utilised in Mukandila's (2015) stone column tests.
Further analysis of the influence in binder temperature is presented in Figure 7.6, which reveals the rapid decrease in the shear stress as the binder temperature increases. Although adhesive fatigue parameters were only obtained at $10°C$ and $25°C$ it was assumed, based on Figure 7.5, that the number of load repetitions to failure at $50°C$ will be less than the case at $25°C$.

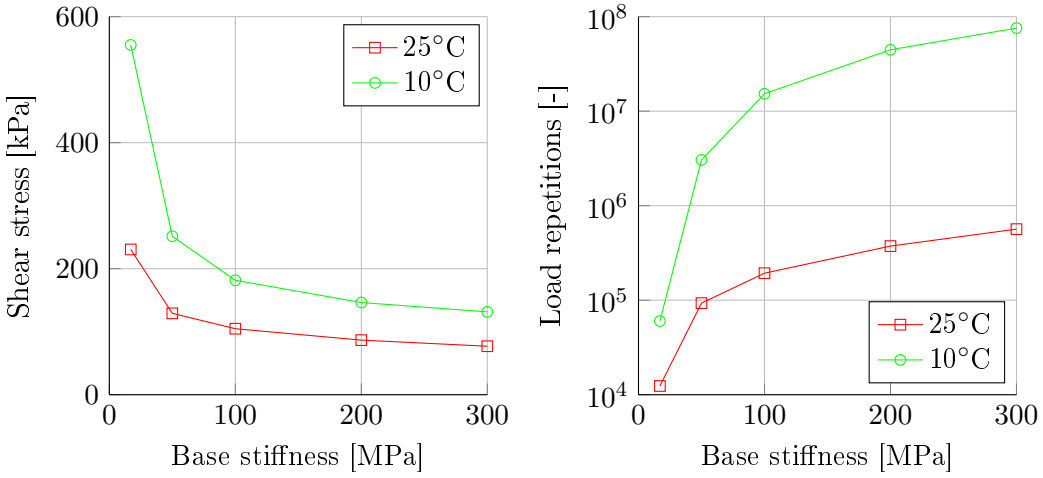

Figure 7.5: Shear stress and corresponding load repetitions to failure for a 1.2 l/m^2 app. rate, 8 mm ALD , 13.2 mm single seal. Traffic load: 20 kN-800 kPa at 80 km/h.

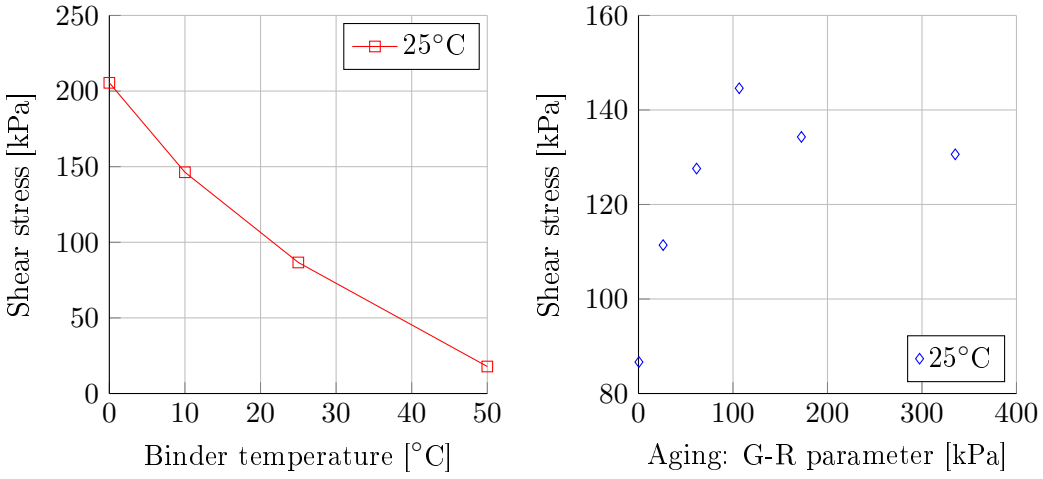

Figure 7.6: Shear stress for a 1.2 l/m^2 app. rate, 8 mm ALD, 13.2 mm single seal. Base stiffness: 200 MPa, traffic load: 20 kN-800 kPa at 80 km/h.

Insights into the binder response due to aging are also presented in Figure 7.6 for temperatures at $25°C$. Here, aging is defined by the Glower-Rowe (G-R) parameter as discussed in Section 4.1.1, Figure 4.3. An increase in G-R, reflects an increase in the binder age. The limited sample of G-R parameters indicate an initial increase in the shears stress response which reaches a peak value, followed by a reduction with time.
Although the binder age is a significant parameter which accounts for an increase of approximately 50% in the bond stress during a 10 year (G-R = 340) service life, the two major time related components remain the strength of the substrate support i.e. the base stiffness and binder temperature. These two components dictate the bond strength with reference to time.

7.1.3 Analysis of the traffic load variables

Traffic load variables are defined as the variation of traffic loads to which the road is subject. It is intuitive to expect heavier loads to cause greater damage, but the type of damage should properly be defined. In the case of adhesive damage, Figure 7.7 indicates that wheel loads of 15 kN to 35 kN at tyre inflation pressures (TiP) of 800 kPa to 1000 kPa, induce similar shear stress magnitudes at the bond interface. This indicates that not only the vertical load, but rather the corresponding contact stress is representative for the expected extent of adhesive damage. An exception to the latter was observed for a case where an overloaded and under inflated wheel (35 kN at 520 kPa) developed excessive longitudinal forces at the edge (E) of the tyre underneath the tyre walls (Table B.3, Appendix B). These tyres are known as *M-shapes* due to the distribution shape of the load and cause more damage than evenly distributed loads. The evenly distributed loads are encircled in Figure 7.7 and serve as a reference for typical heavy vehicles (HV) of which the 20 kN-800 kPa wheel load represents an equivalent 80 kN dual wheel axle (E80).
A popular assumption in seal design is the notion that one heavy HV causes the equivalent damage of 40 light vehicles (LV). As previously stated, damage should accurately be defined and in the case of adhesive fatigue, Figure 7.8 indicates that an equivalent LV:HV wheel load damage ratio ranges from 1.2:1 to 9.3:1 as summarised in Table 7.1. In this study an E80 is used as the reference load, thereby, resulting in an equivalent LV:HV wheel load damage ratio of approximately 4:1. Tyre contact stress is thus an insightful parameter to establish equivalent damage factors for vehicle classes.
It is common practice to reduce the allowable travelling speed on newly sealed sections. This reduces the risk of aggregate loss while the new surface settles in terms of aggregate orientation and adhesive bond development. Figure 7.9 substantiates

this practice by illustrating an increase of shear stress obtained at the adhesive bond due to an increase in travelling speed. The shear stress increases logarithmically by approximately 92% as the speed is increased linearly from 5 km/h to 80 km/h. This results in a reduction in the number of load repetitions to failure.

Figure 7.10 illustrates the increase in shear stress as the rolling motion of the wheel changes. The shear stress of a free rolling (FR) wheel on a horizontal road and a road with a 10% gradient (FR+G) is virtually similar at 86 kPa. This stress increases with approximately 35% for driven wheels (D) on horizontal roads and by almost 87% for driven wheels on a 10% gradient (D+G). A driven wheel on a steep incline and an overloaded under inflated tyre are therefore the major traffic related variables that poses a risk to adhesive failure. The risk of adhesive failure is quantified in the verification and validation process.

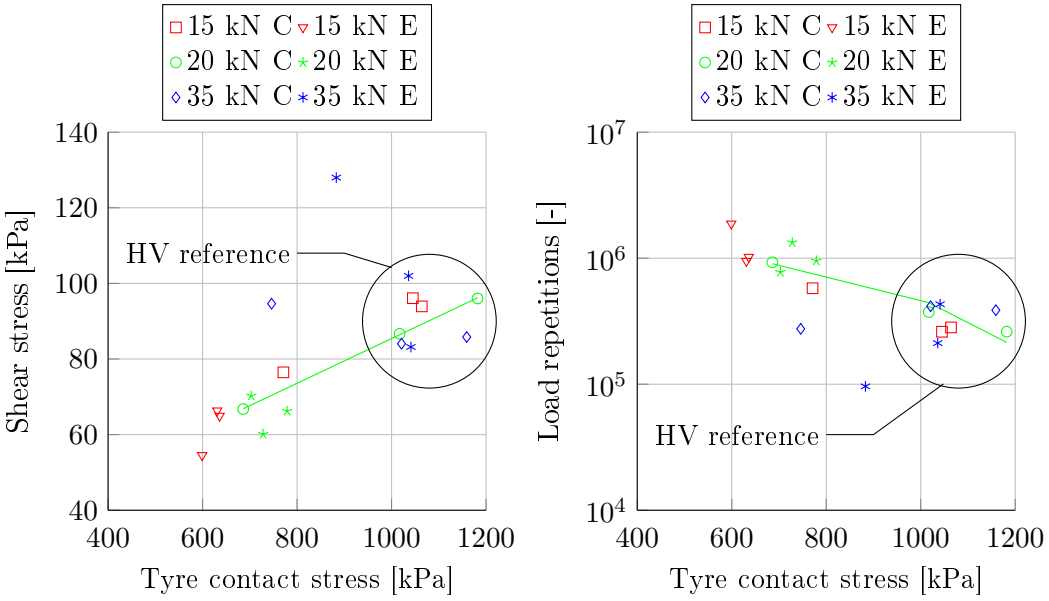

Figure 7.7: Shear stress and corresponding load repetitions to failure for a 1.2 l/m^2 app. rate, 8 mm ALD , 13.2 mm single seal with tyre edge (E) and centre (C) loads. Temperature: 25°C, base stiffness: 200 MPa, travelling speed at 80 km/h.

Table 7.1: Equivalent LV:HV damage ratios as illustrated in Figure 7.8.

Load case description	LV load reps. to failure	HV load reps. to failure	LV:HV ratio
Maximum LVs and minimum HVs	2428823	261553	9.3 : 1
Minimum LVs and maximum HVs	1110437	927311	1.2 : 1
Average LVs and E80 ref HVs	1548220	373678	4.1 : 1

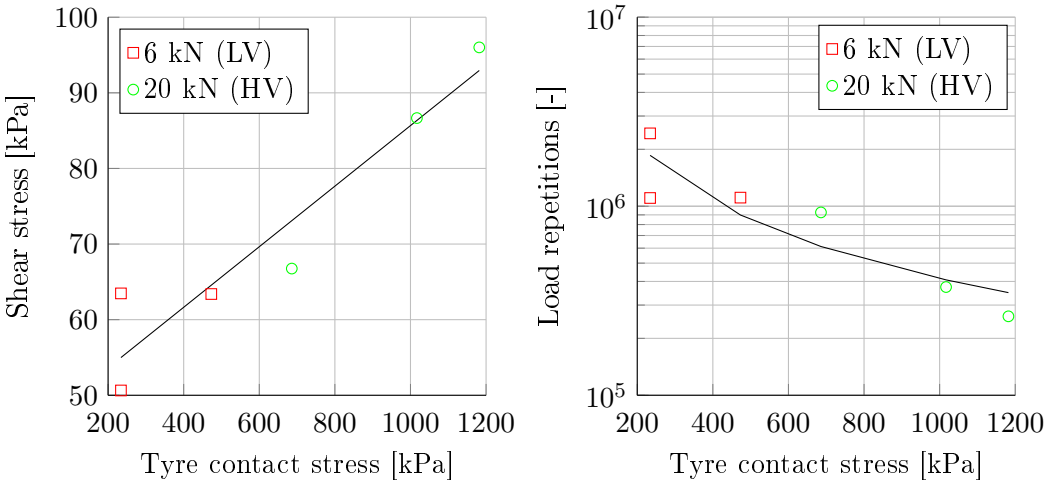

Figure 7.8: Shear stress and corresponding load repetitions to failure for a 1.2 l/m^2 app. rate, 8 mm ALD , 13.2 mm single seal with LV and HV wheel loads. Temperature: 25°C, base stiffness: 200 MPa, travelling speed at 80 km/h.

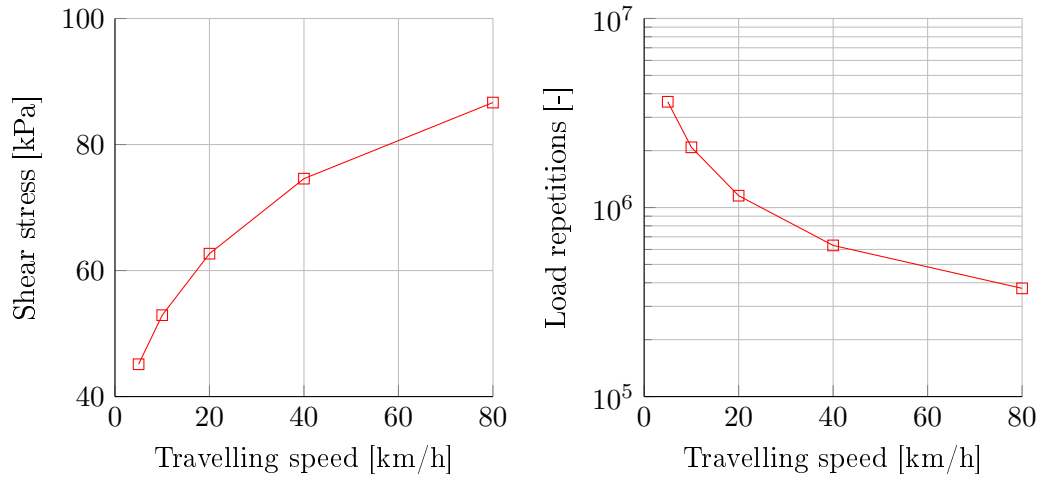

Figure 7.9: Shear stress and corresponding load repetitions to failure for a 1.2 l/m^2 app. rate, 8 mm ALD , 13.2 mm single seal for different travelling speeds. Temperature: 25°C, base stiffness: 200 MPa, traffic load: 20 kN-800 kPa

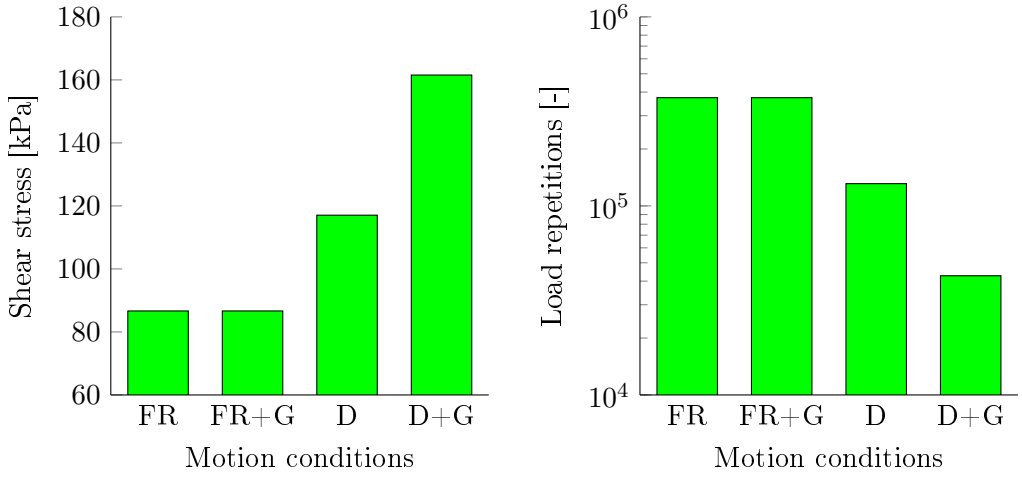

Figure 7.10: Shear stress and corresponding load repetitions to failure for a 1.2 l/m^2 app. rate, 8 mm ALD , 13.2 mm single seal for free rolling (FR) and driven (D) wheels including a 10% gradient (G). Temperature: 25°C, base stiffness: 200 MPa.

7.1.4 Adhesive failure verification and validation

A number of 13.2 *mm* single seal (8 *mm* ALD) and 9.5 *mm* single seal (6 *mm* ALD) models were constructed with various binder application rates according to the empirical *red-line* data as presented in Table 6.2. For the purpose of verification and validation the number of models was expanded to include variations with reference to the binder temperature and aggregate spread rate. Table 6.2 was empirically developed for substrates with a 1.0 *mm* ball penetration value, therefore the corresponding base modulus of the models was selected at 450 MPa.

The model results are presented in Figure 7.11 and indicate, as expected, a reduction in the shear stress as the binder application rate increases. The general trends of this phenomenon are summarised in Table 7.2 and were used in generating data, comparable with the empirical documented, red-line data of Table 6.2. The models were subjected to 20 kN wheel loads i.e E80s at 80 km/h, while the red-line data was developed for average annual daily traffic (AADT). The red-line traffic data were therefore adjusted to the total number of E80s ($E80_{Tot}$). This was done by adjusting the LVs with the equivalency factor of 4 as obtained in this study and adding the results to the existing number of E80s: $E80_{Tot}$=$E80s$+$LVs \times 4$. The $E80_{Tot}$ was further adjusted to incorporate the effect of lateral wandering according to Huurman's (1997) description (Appendix D).

Comparisons between the empirical red-line data and the number of load repetitions to failure for the models are presented in Figure 7.12. Both instances, 8 *mm* ALD and 6 *mm* ALD modelled data, indicate a significant dependence on the aggregate

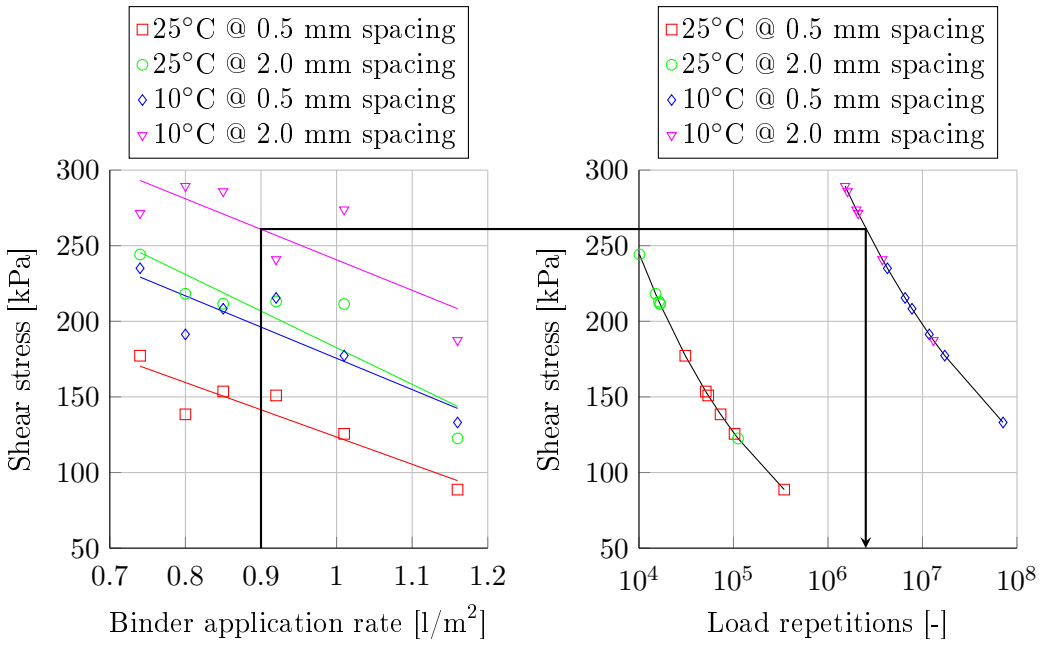

Figure 7.11: Shear stress and binder application rate trends with the corresponding number of load repetitions to failure for the 8 mm ALD, 13.2 mm single seal models. Base stiffness: 450 MPa, traffic load: 20 kN-800 kPa at 80 km/h.

Table 7.2: Summary of the trend formulations as depicted in Figure 7.11.

Description of variables	Stdev[i]	Trend formulation	R^2
Binder application rate (x) and shear stress (y) for $25°C$ @ 0.5 mm	2^{nd}	$y = -180.27x + 303.74$	0.84
Binder application rate (x) and shear stress (y) for $25°C$ @ 2.0 mm	2^{nd}	$y = -242.24x + 424.77$	0.80
Binder application rate (x) and shear stress (y) for $10°C$ @ 0.5 mm	2^{nd}	$y = -206.75x + 382.25$	0.79
Binder application rate (x) and shear stress (y) for $10°C$ @ 2.0 mm	2^{nd}	$y = -201.87x + 442.52$	0.64
Load repetitions (x) and shear stress (y) at $25°C$	2^{nd}	$y = 3448.7x^{-0.287}$	1.0
Load repetitions (x) and shear stress (y) at $10°C$	2^{nd}	$y = 5116x^{-0.202}$	1.0

[i] Standard deviation towards the right

spacing and binder temperature. According to these results a seal with an open spread and "warmer" binder is the more likely structure to exhibit early aggregate loss, which is intuitive. The load repetitions to failure of the seal with a spread rate of 2.0 mm and binder temperature of $25°C$ was therefore directly compared to the empirical data as illustrated in Figure 7.13, where lines of equality indicate the time

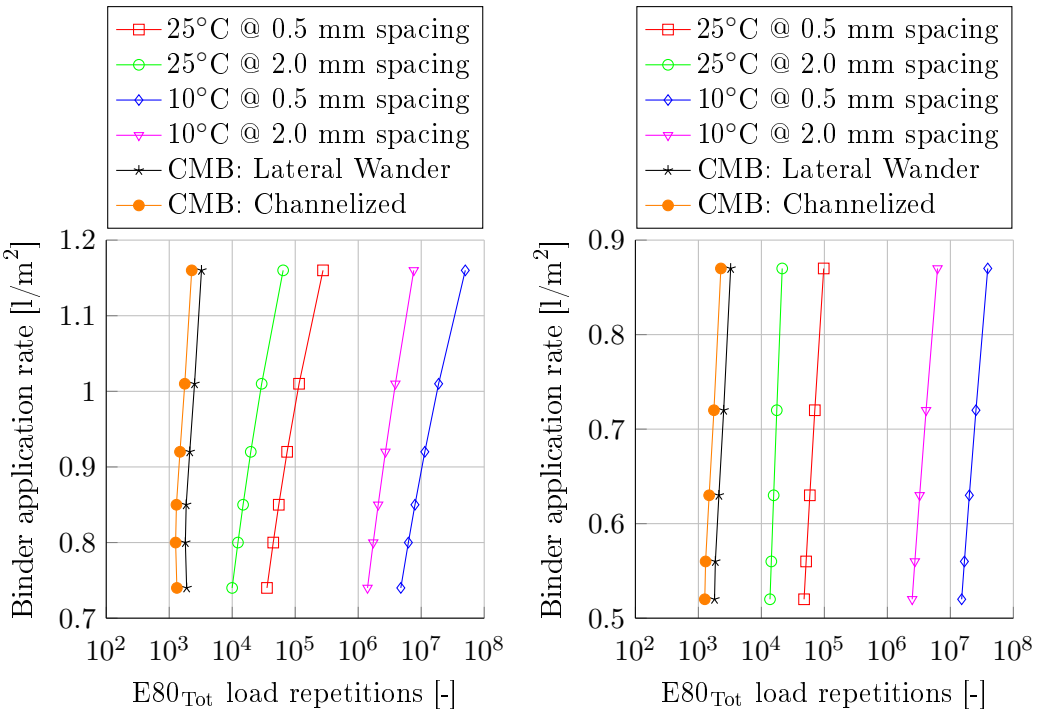

Figure 7.12: Comparisons between the critical minimum binder (CMB) application data (Table 6.2) and FE models thereof: 8 mm ALD (left) and 6 mm ALD (right).

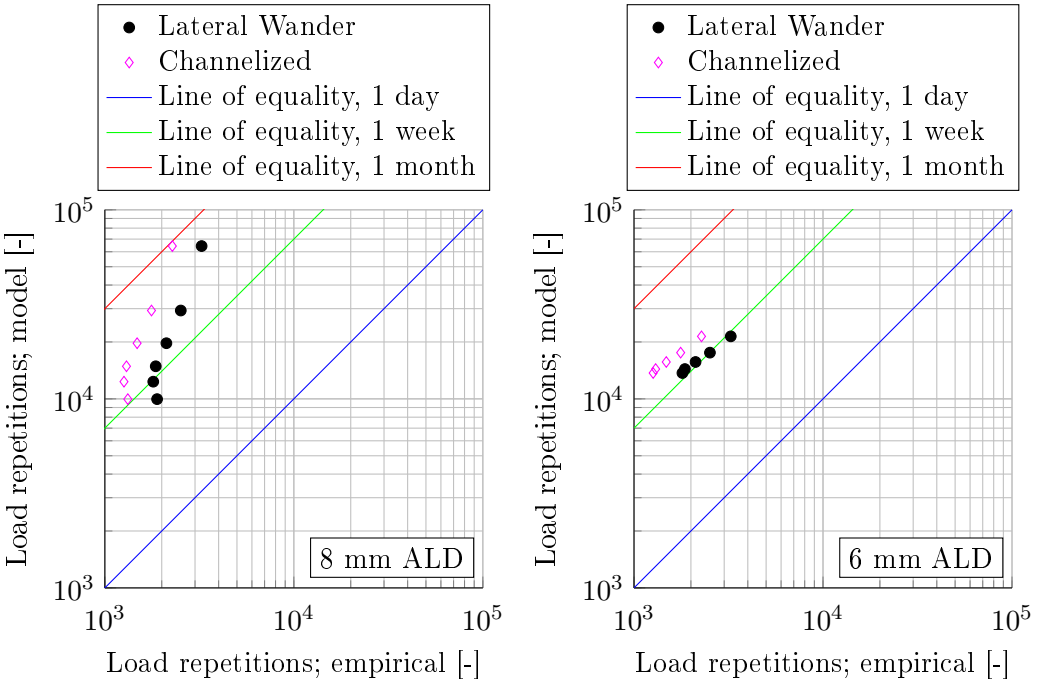

Figure 7.13: Empirical (Table 6.2) and modelled number of E80 load repetitions to failure for 8 mm ALD (left) and 6 mm ALD (right) single seals.

of failure. Considering that the FE seal models are constructed with the aggregate orientation already in ALD, the results in Figure 7.13 indicate that no catastrophic failure i.e. single load rip-off or aggregate loss occur within one day. This can be attributed to the measure of shear stress obtained within the adhesive bond. Lombard (2015) recorded tensile fracture stresses during bitumen bond strength (BBS) testing on the same materials. The BBS results indicated single load fracture stresses ranging from 2000 kPa to 2500 kPa for tests conducted at 15°C and 400 kPa to 1200 kPa for tests conducted at 35°C with a load rate of 700 kPa/s. The maximum shear stress in this instance is approximately 250 kPa (Figure 7.13) at 80 km/h and although shear stress cannot directly be compared to tensile stress, Lombard's results give valuable insight.

The model does however indicate an adhesive bond fatigue and therefore stone loss after one week's traffic for both the 13.2 mm (8 mm ALD) and 9.5 mm (6 mm ALD) seals. The fatigue rate is solely dependent on Mukandila's (2015) transfer function and is far more conservative than 8.7 years obtained with the HDM-4 ravelling initiation model. An interesting observation made by Lombard was that all the virgin 70-100 penetration grade BBS tests exhibited cohesive failure during post testing analysis.

7.2 Cohesive failure

The outline of the cohesive failure analysis is very similar to the adhesive failure analysis. The shear stress responses (Figure 7.14) of the binder and corresponding load repetitions to cohesive failure are presented and discussed according to the primary seal model variations as defined in this study.

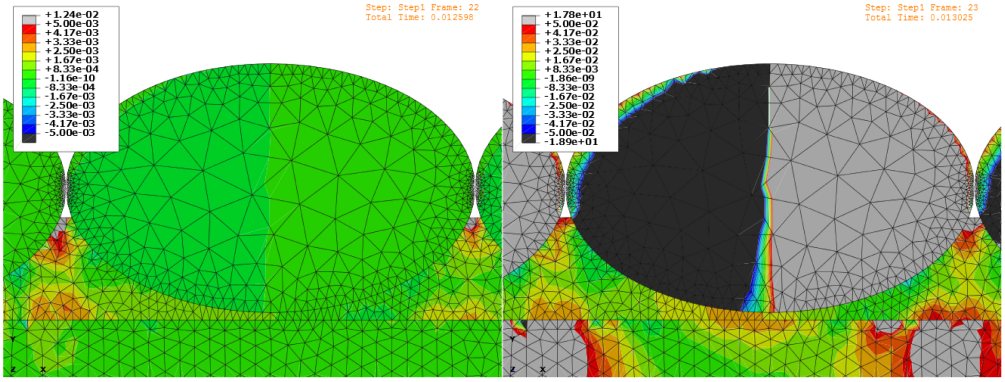

Figure 7.14: Screen grabs of aggregate interlock FE single seal contact simulations: shear strain ϵ_{12} (left) and shear stress σ_{12} in MPa (right).

7.2.1 Analysis of the structural variables

As previously mentioned, the structural variables refer to the geometry and material types of the seal model. With the consideration of aggregate sizes and spread rates, Figure 7.15 illustrates that seals constructed with aggregate interlock, exhibit slightly higher stresses in the binder than seals constructed with a small aggregate edge to edge spacing of 0.5 *mm*. From here on, the general trend indicates that a reduction in the spread rate i.e. an increase in the aggregate spacing, results in a significant increase in binder shear stress. Higher shear stresses correspond to lower load repetitions to cohesive failure. The number of load repetitions to failure will be discussed in detail in Section 7.2.4.

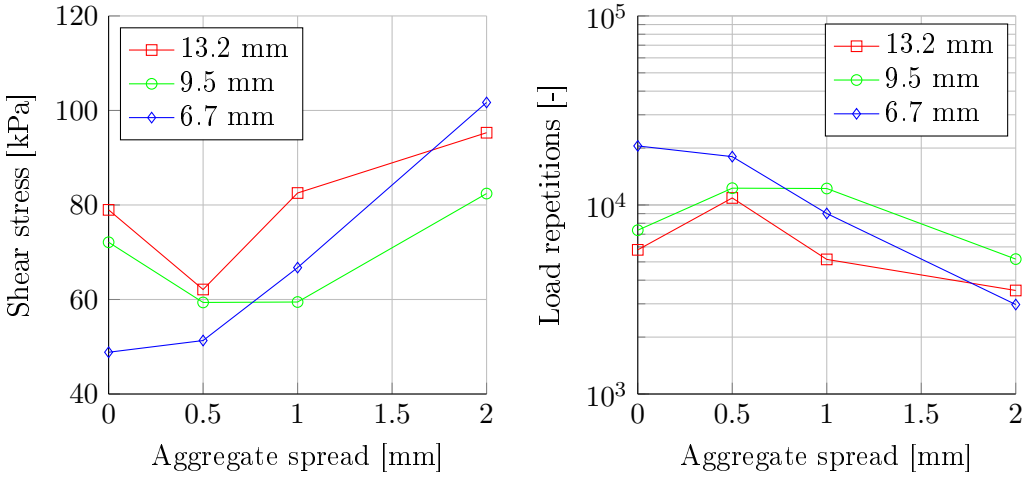

Figure 7.15: Shear stress and corresponding load repetitions to failure for the 6.7, 9.5 & 13.2 mm single seals. Virgin 70-100 pen. grade binder at 40% wetted height. Temperature: 25°C, base stiffness: 200 MPa, traffic load: 20 kN-800 kPa at 80 km/h.

The ALD of the seal aggregate does not have a substantial influence on the binder shear stress as illustrated in Figure 7.16. The general trend indicates a slight stress reduction as the ALD increases, while the number of load repetition to failure range between 10000 and 20000. The ALD per nominal size is therefore a less significant in the context of binder fatigue.

Contrary to the ALD, the binder application rate does have a significant effect on the shear stress as illustrated in Figure 7.17. Reduction in the stress occurs as the application rate is increased. This is intuitive, since an increase in the binder application rate, increases the column of binder resisting the traffic forces which results in more load repetitions to binder fatigue failure. The general shear stress trend declines by approximately 64% as the binder application rate is linearly increased from 0.8 l/m^2 to 1.6 l/m^2

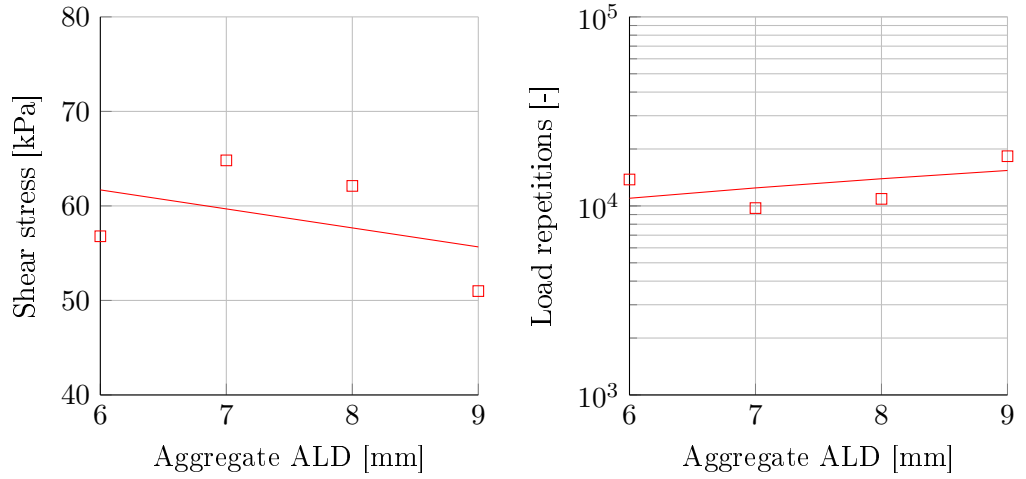

Figure 7.16: Shear stress and corresponding load repetitions to failure for the ALD of the 13.2 mm single seal and virgin 70-100 pen. grade binder at 40% wetted height. Temperature: 25°C, base stiffness: 200 MPa, traffic load: 20 kN-800 kPa at 80 km/h.

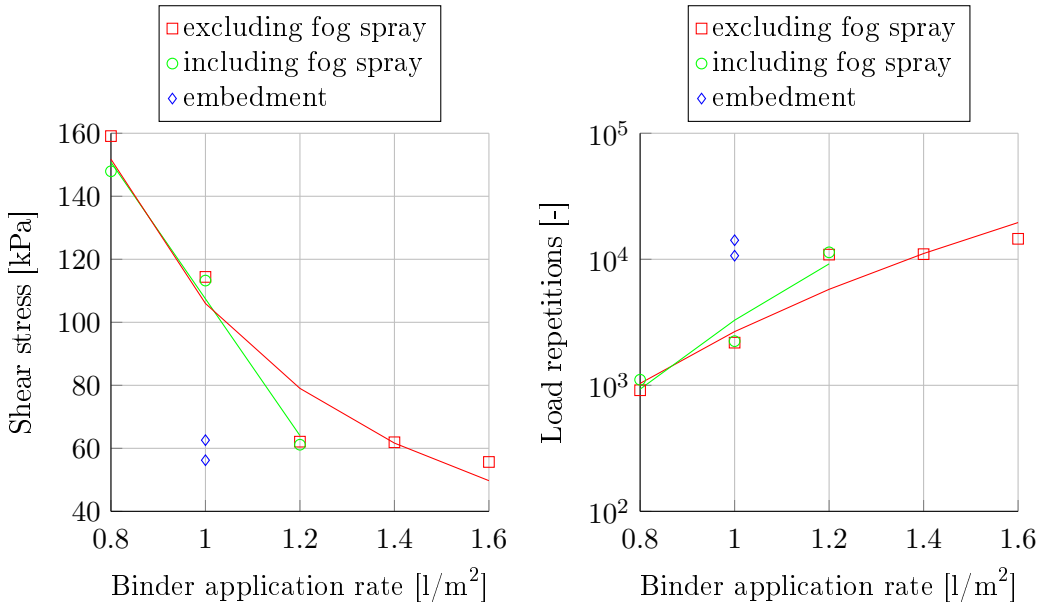

Figure 7.17: Shear stress and corresponding load repetitions to failure for virgin 70-100 pen. grade binder application rates and a 8 mm ALD, 13.2 mm single seal. Temperature: 25°C, base stiffness: 200 MPa, traffic load: 20 kN-800 kPa at 80 km/h.

The application of an additional fog spray (FS) is irrelevant in terms of improving the tack coat fatigue rate. However, construction embedment (0.5 *mm* to 1.0 *mm*) does reduce the shear stress which in turn results in a higher number of load repetitions to failure in comparison to the same seal structure without any construction embedment.

7.2.2 Analysis of the time related variables

A time related variable refers to the change in condition of that variable with reference to time. The same time related variables utilised in the adhesive fatigue analysis are discussed in terms of cohesive fatigue and yields similarities in the trends (Figure 7.18) obtained for a variation of the base stiffness with binder temperatures at $10°C$ and $25°C$. The exponential decrease in binder shear stress, results in an increase in the load repetitions to failure as the base stiffness is increased from 17 MPa to 300 MPa. These stiffness values were discussed in Section 5.2.1. A major difference in load repetitions to failure is obtained between the various temperatures and is ascribed to the material characterisation as observed by Mukandila (2015) while developing the end of life cohesive transfer functions.

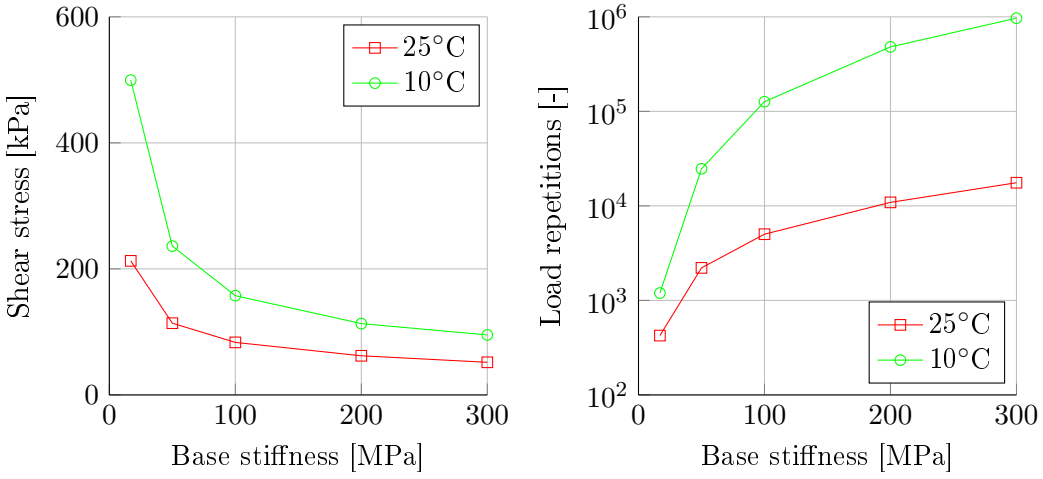

Figure 7.18: Shear stress and corresponding load repetitions to failure for a 1.2 l/m^2 app. rate, 8 mm ALD , 13.2 mm single seal. Traffic load: 20 kN-800 kPa at 80 km/h.

Figure 7.18 also indicates that weaker bases result in earlier fatigue, while lower temperatures provide greater resistance to fatigue than higher temperatures. The latter phenomenon is further analysed in Figure 7.19, which illustrates a significant reduction in the shear stress as the temperature increases from $0°C$ to $50°C$. Since no binder damage parameters were developed for the upper and lower temperature limits, an assumption based on Figure 7.18 is made that the binder fatigue at $50°C$ would occur prior to the same case at $25°C$ and binder fatigue at $0°C$ would occur after the same case at $10°C$. This assumption is consistent with the binder fatigue trends as discussed in The Shell Bitumen Handbook (Read and Whiteoak, 2003).
Figure 7.19 further indicates a general trend of initial shear stress increase followed by a reduction as the binder ages. Aging is represented by the Glower-Rowe (G-R) parameter as discussed in Section 4.1.1, Figure 4.3. According to The Shell Bitumen

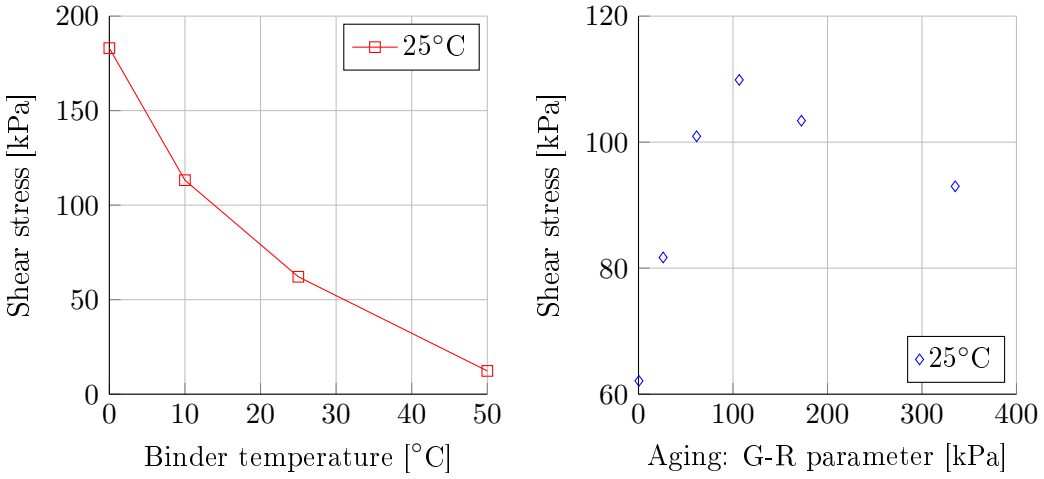

Figure 7.19: Shear stress for a 1.2 l/m^2 app. rate, 8 mm ALD, 13.2 mm single seal. Base stiffness: 200 MPa, traffic load: 20 kN-800 kPa at 80 km/h.

Handbook, the fatigue strength reduces as the load repetitions increase, but simultaneously does an increase in binder stiffness (aging) reduce the effect of repeated loading. However, it remains evident that the binder temperature and base stiffness are the major time related variables that affects the binder fatigue rate.

7.2.3 Analysis of the traffic load variables

The traffic load variables, which refer to the variety of traffic load conditions on the road, were analysed in terms of cohesive fatigue and resulted in similar findings when compared to the adhesive analysis. This is observed in the case where shear stresses are compared for various combinations of vertical wheel loads and tyre inflation pressures as illustrated in Figure 7.20. Similar to the adhesive failure analysis, the overloaded under inflated tyre (35 $kN - 800\ kPa$) induced the highest shear stress and therefore the most damage, while the 20 kN-800 kPa wheel load is shown to be a good HV reference load and is also an E80.

With regard to the TRH3 (2007) LV:HV equivalency factor of 40:1, it is again illustrated in Figure 7.21 that damage should accurately be defined. In the case of cohesive fatigue damage the reference HV wheel load (E80) accounts for approximately 2.3 times the damage of a LV wheel load. A summary of the ranges for equivalent cohesive damage is presented in Table 7.3. The tyre contact stress and not the vertical load dictates the extent of damage to the surface.

Travelling speed not only affects the stress condition in the binder bond, but a linear increase in the travelling speed as illustrated in Figure 7.21, results in a logarithmic increase in the binder shear stress. The binder response is therefore load-rate dependent. This phenomenon was also observed by Lombard (2015) during BBS tests and

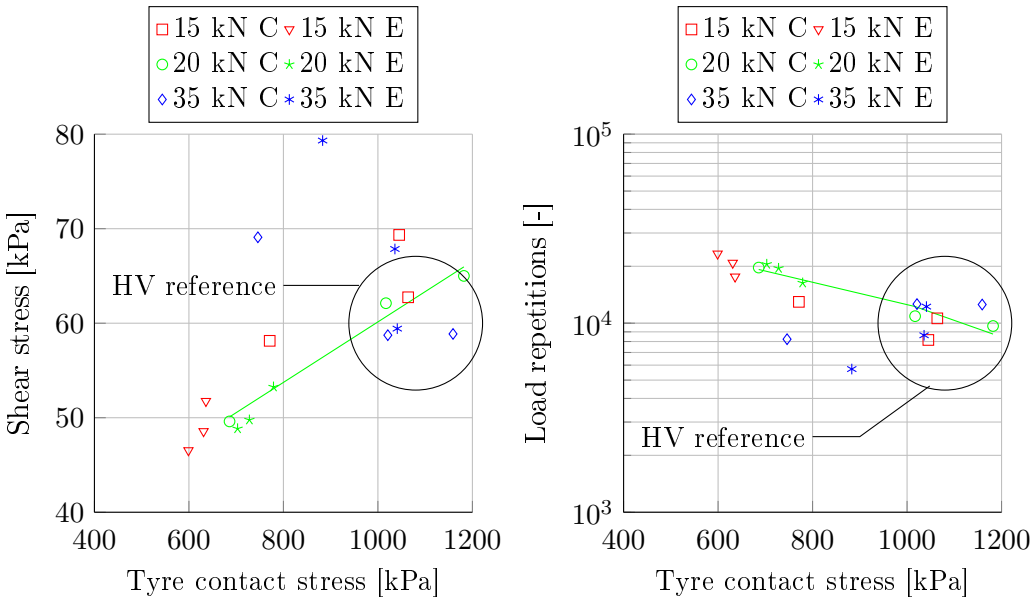

Figure 7.20: Shear stress and corresponding load repetitions to failure for a 1.2 l/m² app. rate, 8 mm ALD , 13.2 mm single seal with tyre edge (E) and centre (C) loads. Temperature: 25°C, base stiffness: 200 MPa, travelling speed at 80 km/h.

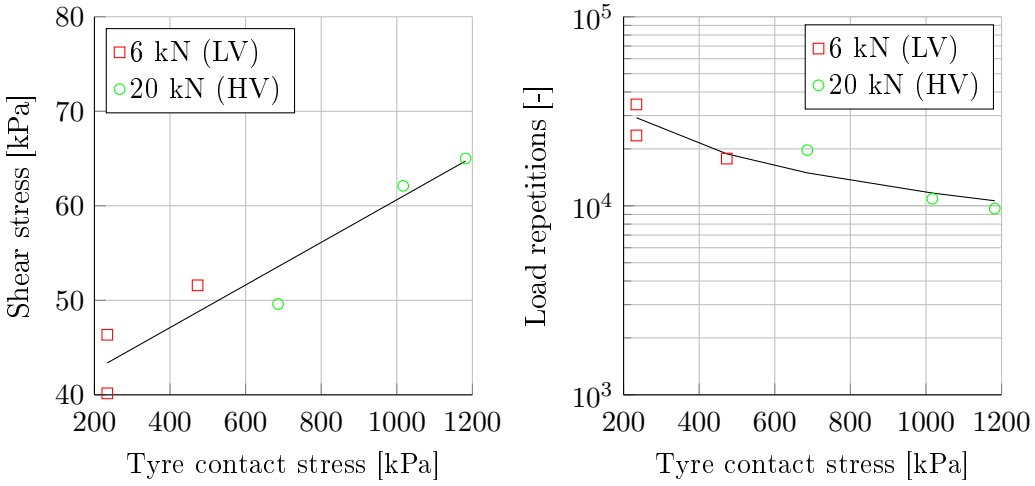

Figure 7.21: Shear stress and corresponding load repetitions to failure for a 1.2 l/m² app. rate, 8 mm ALD , 13.2 mm single seal with LV and HV wheel loads. Temperature: 25°C, base stiffness: 200 MPa, travelling speed at 80 km/h.

Pauli *et al.* (2013) during adherence energy tests via force-displacement atomic force microscopy (FA-AFM). Lombard indicated that the binder tensile stress increased as a result of greater load rates, while Pauli *et al.* (2013) illustrated a deflection increase with an increased load rate.

Table 7.3: Equivalent LV:HV damage ratios as illustrated in Figure 7.21.

Load case description	LV load reps. to failure	HV load reps. to failure	LV:HV ratio
Maximum LVs and minimum HVs	34370	9664	3.6 : 1
Minimum LVs and maximum HVs	17768	19693	1 : 1.1
Average LVs and E80 ref HVs	25228	10893	2.3 : 1

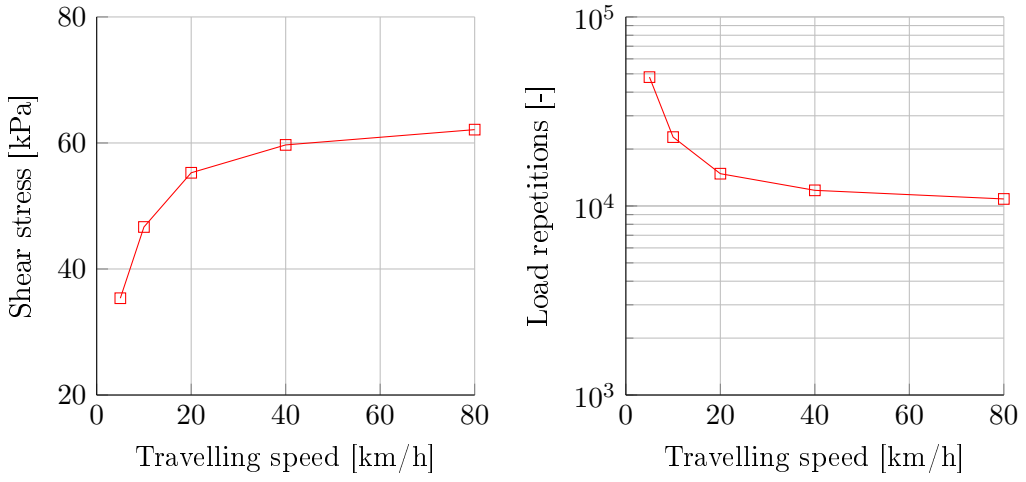

Figure 7.22: Shear stress and corresponding load repetitions to failure for a 1.2 l/m^2 app. rate, 8 mm ALD , 13.2 mm single seal for different travelling speeds. Temperature: 25°C, base stiffness: 200 MPa.

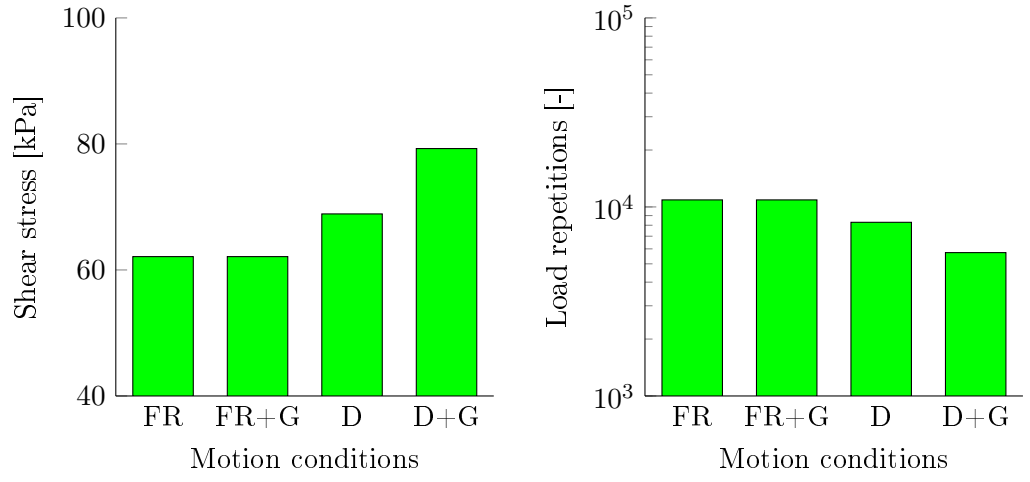

Figure 7.23: Shear stress and corresponding load repetitions to failure for a 1.2 l/m^2 app. rate, 8 mm ALD , 13.2 mm single seal for free rolling (FR) and driven (D) wheels including a 10% gradient (G). Temperature: 25°C, base stiffness: 200 MPa.

With the consideration of the motion conditions, Figure 7.23 illustrates that a rolling wheel has less of an influence on the cohesive binder fatigue rate when compared to the results of the adhesive fatigue analysis. Even though the cohesive results indicate an increase in shear stress of 11% from a free rolling (FR) to a driven (D) wheel and a further increase of 15% for a driven wheel on a 10% gradient (D+G), it is not as dramatic as was observed for the adhesive fatigue analysis. It should be noted that the number of load repetitions under these conditions to cohesive failure ranges between 4000 and 5000 load applications. This is very conservative and is directly related to the cohesive end of life transfer functions of Mukandila (2015).

7.2.4 Cohesive failure verification and validation

Post processing of the cohesive shear stress analyses with Mukandila's (2015) end of life transfer functions, resulted in the load repetitions to failure parameter N_i as discussed in Equation 3.36. The n_i parameter of Equation 3.36 represents the traffic volume and was therefore artificially populated with a wide range of traffic volumes and traffic growth rates to match the volumes and growth rates observed by van Zyl (2015) in the development of the trigger lines for cohesive cracking. The traffic volumes were differentiated into three regions as summarised in Table 7.4.

By calculating the cumulative E80 load repetitions over a 20 year service life span, an estimated time (year) of failure and subsequent cumulative deflection to failure was determined for each seal model. These results are illustrated in Figure 7.24 where it is evident that the majority of the FE model simulations result in failure within the first year. Since the FE seal models respond within the linear viscoelastic range (Figure 4.2) and simulate field observed deflections (Figure 6.3), the transfer function of Mukandila (Equation 4.4) is deemed to experience difficulty in relating the seal response parameters to field performance evaluations. Aspects such as self-healing, loading rates and aged-sample testing were omitted during the development of the end of life transfer functions.

According to Molenaar (2007) the effect of self-healing, lateral wander and the geometrical differences between the test specimen and actual pavement are three critical factors that contribute towards fatigue resistance. Self-healing includes two factors describing the amount of binder in the aggregate matrix and the rest period of consecutive loads on the surface of the road. Factors of 20 and 10 were selected to represent the two cases respectively. The calculation methods of these factors are presented in Appendix D. No factor was included to describe the geometrical differences, since the FE models incorporated and accounted for an idealised geometry, however a lateral wander factor was introduced as described by Huurman (1997).

Table 7.4: Cohesive failure validation traffic volumes and growth rates.

Regions	Traffic volume description	Number of E80s/day/lane	Annual growth rate i [%]
Region 1	High	600-300	1, 3, 5
Region 2	Moderate	300-150	1, 3, 5
Region 3	Low	150-38	1, 3, 5

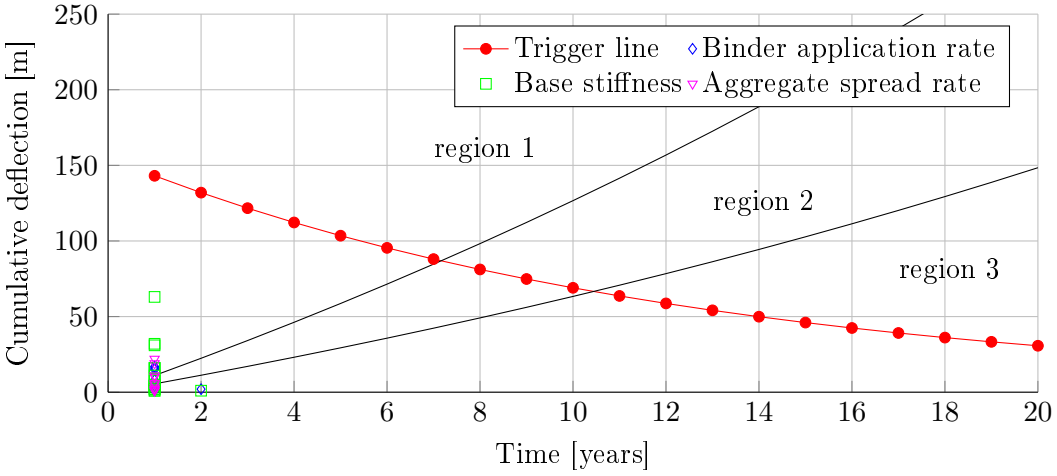

Figure 7.24: Cumulative deflection and time of cohesive fatigue cracking for E80s at 25°C and a 3% growth rate.

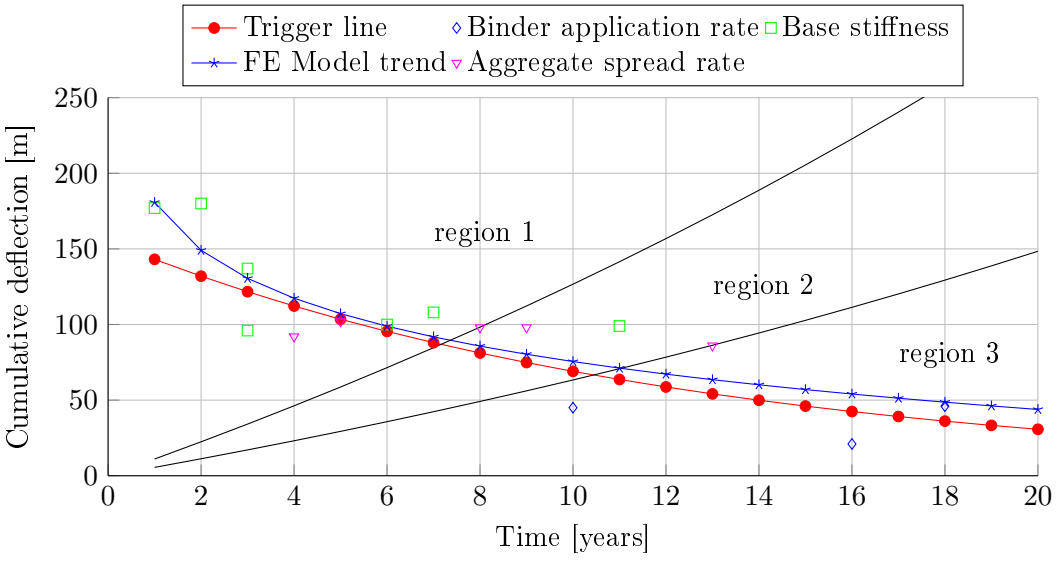

Figure 7.25: Cumulative deflection and adjusted time of cohesive fatigue cracking for E80s at 25°C and a 3% growth rate.

Adjustments to Figure 7.24, which includes self-healing and lateral wander factors, are illustrated in Figure 7.25 and displays a close comparison to van Zyl's trigger line. It should be noted that Molenaar's (2007) laboratory data was obtained from asphalt beams and therefore the magnitude of the factors serve only as an indication to the contribution towards fatigue resistance in seals. These adjustments indicate the importance of the factors in the development of cohesive fatigue transfer functions. Figure 7.25 suggests that early fatigue cracking is dominated by the base stiffness parameter, where week bases have higher cumulative deflections. Other parameters such as the binder application rate and aggregate spread rate also influences the crack initiation time on moderate to strong bases. The HDM-4 crack initiation model predicts that cracking would occur at approximately 12 years after construction.

7.3 Embedment failure

The embedment failure analysis presents the base deflection response (Figure 7.26) and corresponding load repetitions to failure, according to the outline of the primary variations. In this case failure is defined in terms of retained surface texture. The TRH3 (2007) stipulates a minimum surface macro texture of 0.7 mm, but makes provision for cases with remaining surface textures 0.5 mm to 0.3 mm.

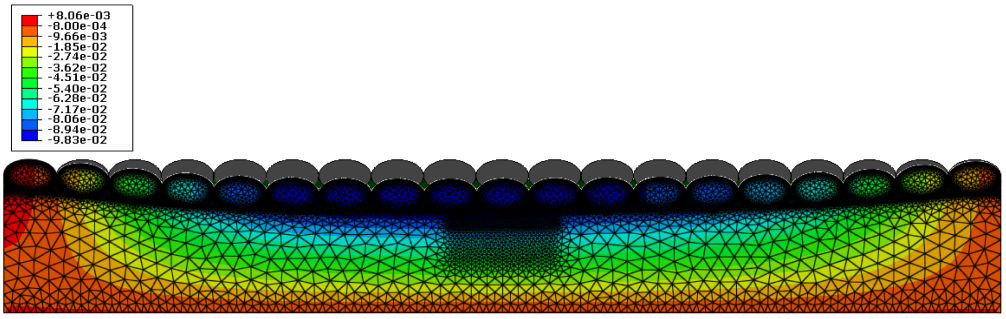

Figure 7.26: Screen grab of the FE single seal simulations: exaggerated vertical deflection (mm) displaying the radius of curvature.

7.3.1 Analysis of the structural variables

In practice, seal sizes and spread rates often vary. Nominal size cases which include 6.7 mm, 9.5 mm and 13.2 mm as presented in Figure 7.27, were analysed at various spread rates to establish the typical embedment trends. The general trend indicates that the vertical deflection response of the base beneath the seal aggregate increase as the aggregate spacing is increased. This observation holds true for all three of the respective seal sizes. However, the spacing does not significantly influence the

number of load repetitions to failure, where a retained surface texture of 0.3 *mm* was selected as the failure criterion. In cases where the minimum surface texture was not exceeded, the remaining surface textures after 10 million load applications are presented.

The aggregate nominal size is a significant factor which dramatically affects the number of load repetitions to failure. This is manly accredited to a decrease in the initial surface macro texture of smaller aggregates, which results in a reduction of load repetitions for a designated failure criterion as illustrated in Figure 7.28.

Although greater spacing results in higher initial embedment rates, the aggregate nominal size in combination with its ALD (Figure 7.29) dictates the final result. A lower ALD has a reduced initial surface texture in comparison to a higher ALD. This ultimately results in fewer load repetitions to failure.

A similar explanation is attributed to the binder application rate, which significantly affects the retained surface texture as illustrated in Figure 7.30. Higher application rates increase the risk of surface texture loss and may lead to bleeding. The application of an additional fog spray (FS) does not result in a substantial reduction of the vertical deflection and therefore, actually contributes to a reduction in load applications to failure, since more voids i.e. available texture are filled. The binder application rate and aggregate nominal size are the two major structural variables that affect surface texture loss as a result of embedment.

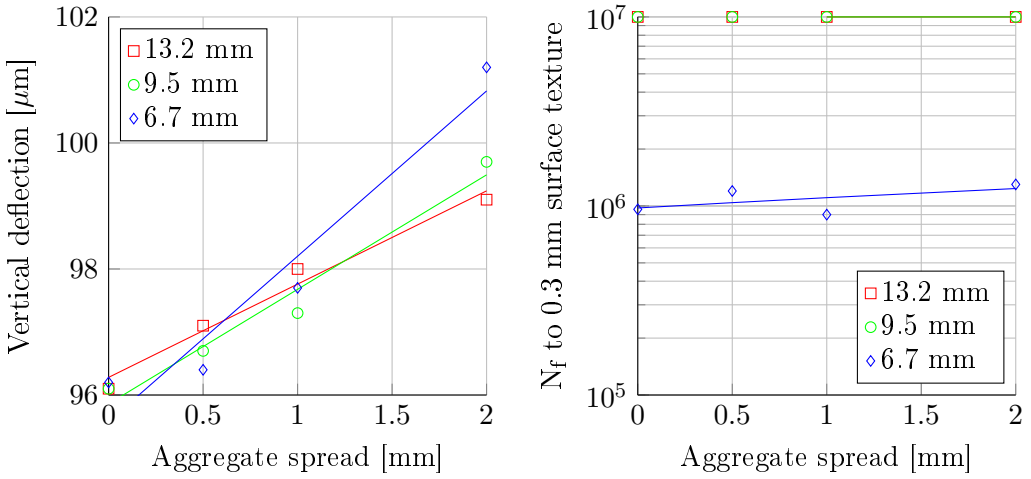

Figure 7.27: Vertical deflection and resulting load repetitions to failure for the 6.7, 9.5 & 13.2 mm single seals. Virgin 70-100 pen. grade binder at 40% wetted height. Temperature: 25°C, base stiffness: 200 MPa, traffic load: 20 kN-800 kPa at 80 km/h.

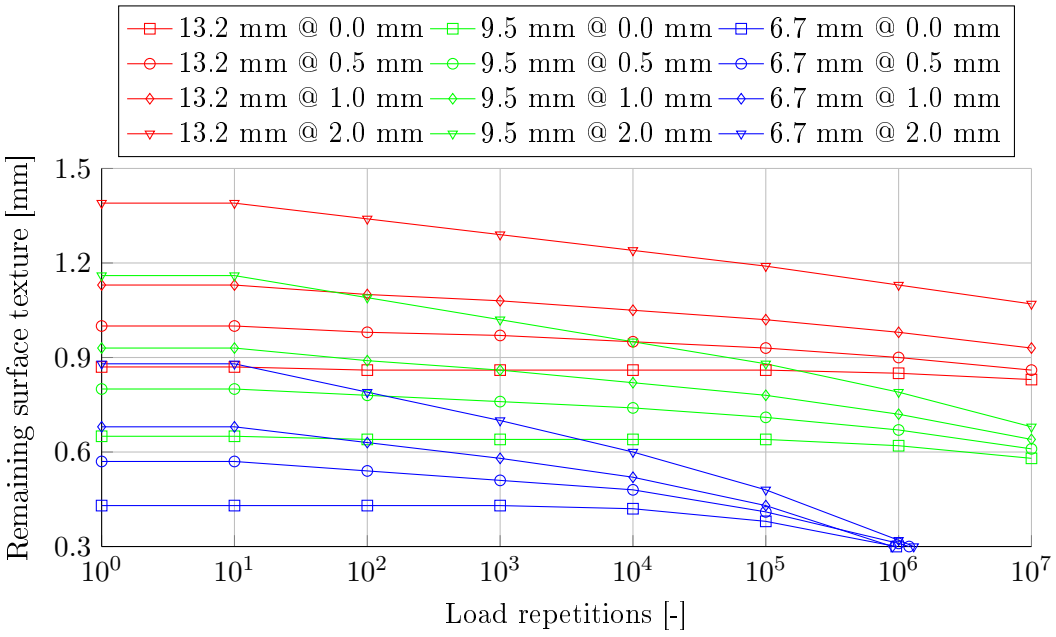

Figure 7.28: Retained surface texture for the 6.7, 9.5 & 13.2 mm single seals @ various spacings (mm). Virgin 70-100 pen. grade binder at 40% wetted height. Temperature: 25°C, base stiffness: 200 MPa, traffic load: 20 kN-800 kPa at 80 km/h.

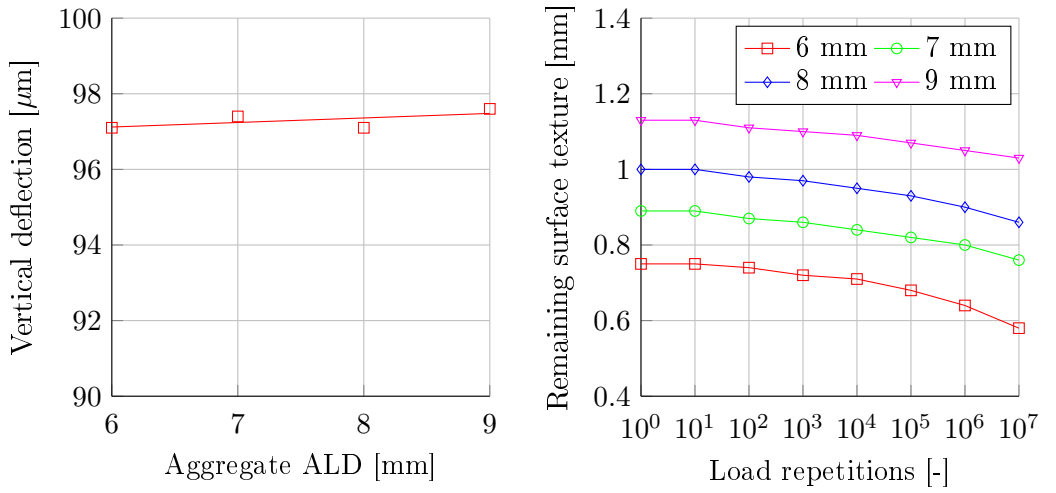

Figure 7.29: Vertical deflection and remaining surface texture for the ALDs of the 13.2 mm single seal and virgin 70-100 pen. grade binder at 40% wetted height. Temperature: 25°C, base stiffness: 200 MPa, traffic load: 20 kN-800 kPa at 80 km/h.

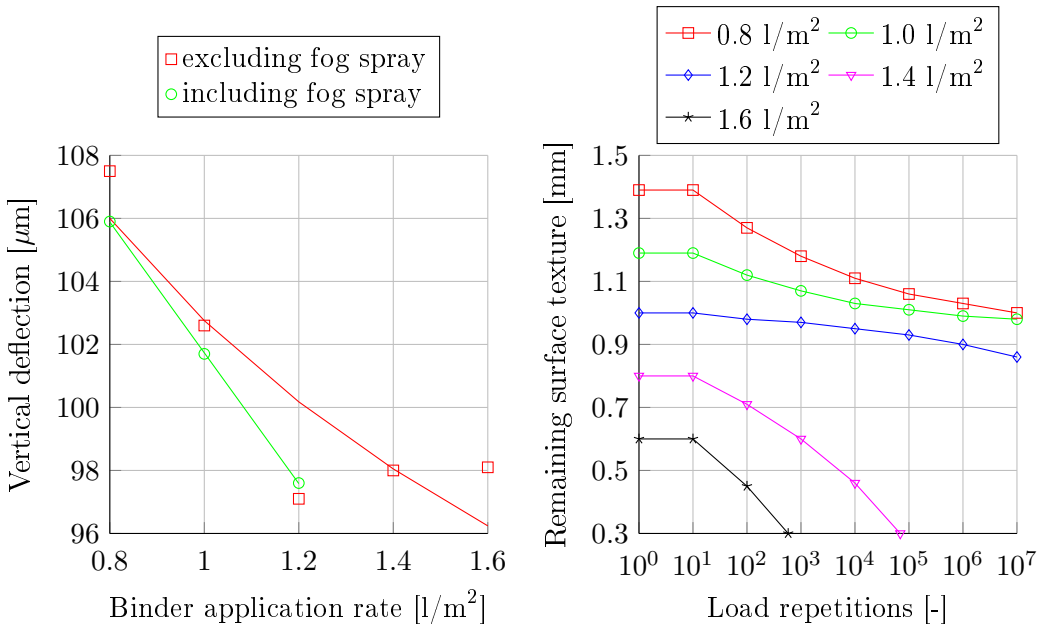

Figure 7.30: Vertical deflection and remaining surface texture for various virgin 70-100 pen. grade binder application rates and a 8 mm ALD, 13.2 mm single seal. Temperature: 25°C, base stiffness: 200 MPa, traffic load: 20 kN-800 kPa at 80 km/h.

7.3.2 Analysis of the time related variables

The analysis of the time related variables was conducted for one geometrical condition i.e. fixed combination of structural variables of which only the material conditions were varied. An embedment failure in terms of remaining surface texture was selected at 0.3 *mm* to accommodate a variety of seal models. In cases where the minimum surface texture were not exceeded, the remaining surface texture after 10 million load applications is presented as illustrated in Figure 7.31.

A reduction in the base stiffness dramatically increased the vertical deflection. This resulted in a vast reduction of load repetitions to failure from approximately 10 million to a 500 as the base stiffness was decreased from 300 MPa to 17 MPa and emphasise the sensitivity of embedment to changes in the base strength. Figure 7.31 further illustrates that a change in the binder temperature from 10°C to 25°C had hardly any influence on the embedment rate and almost similar deflection results were obtained for the different temperatures. This phenomenon was again observed in Figure 7.32 and repeated itself in the analysis of different binder ages.

Even with an increase in the Glower-Rowe (G-R) aging parameter, the vertical deflections are virtually similar, which suggests similar magnitudes of embedment developments. According to Figure 7.32, binder aging does not have a significant affect on aggregate embedment on moderate to strong bases.

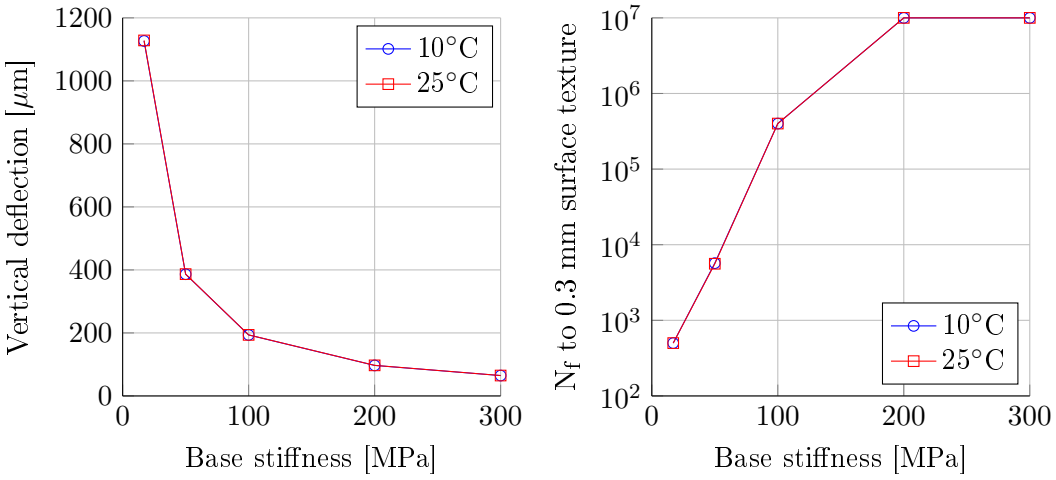

Figure 7.31: Vertical deflection and resulting load reps. to failure for a 1.2 l/m^2 app. rate, 8 mm ALD , 13.2 mm single seal. Traffic load: 20 kN-800 kPa at 80 km/h.

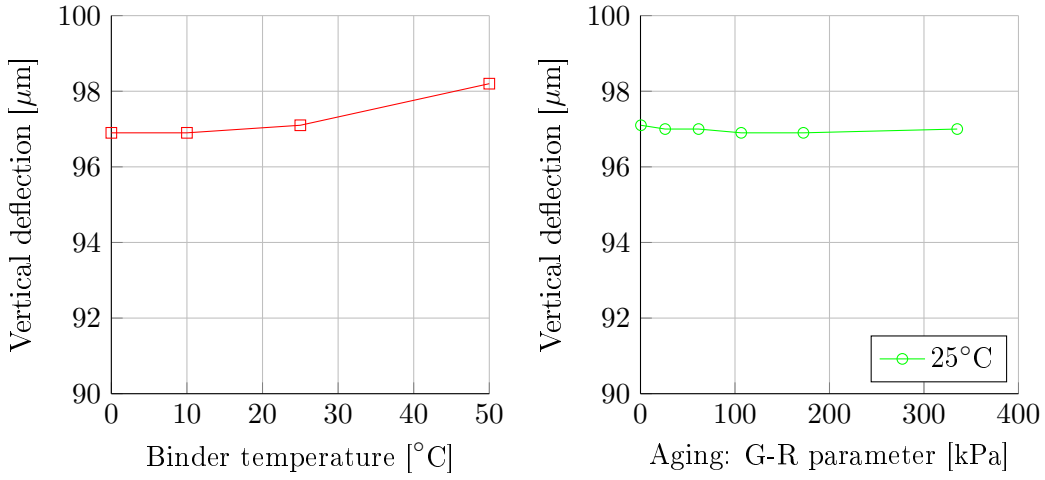

Figure 7.32: Vertical deflection for a 1.2 l/m^2 app. rate, 8 mm ALD, 13.2 mm single seal. Base stiffness: 200 MPa, traffic load: 20 kN-800 kPa at 80 km/h.

7.3.3 Analysis of the traffic load variables

The expectation that heavier loads would result in a fewer number of load repetitions is not met by Figure 7.33 and suggests that the tyre contact stress is a parameter of greater significance. An increase in the tyre contact stress results in a slight decrease in the load repetitions to failure for the 20 kN vertical loads. Symbols C and E indicate the centre and edge positions underneath the tyre respectively.

Figure 7.34 illustrates the vertical deflections of LVs in comparison with the reference HV. The results give valuable insight to the notions that 50% of embedment occurs during construction and that one HV accounts for the damage 40 LV. If a 20 ton

pneumatic roller was used during construction, each of the 10 wheels would roughly be equal to a 20 kN wheel load. According to Figure 7.34, 50% embedment occurs only after approximately 100 000, 20 kN load applications, while an estimated 14% occurs after 100 applications. The LV:HV equivalent damage ratios are summarised in Table 7.5 and suggest no significant differences between the respective vehicle classes on moderate to strong bases.

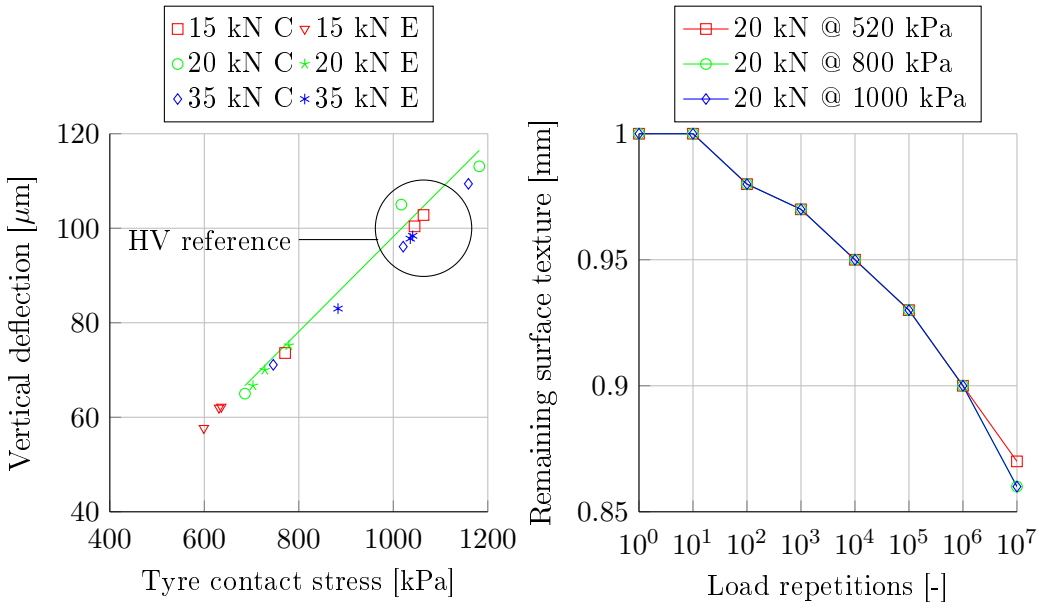

Figure 7.33: Vertical deflection and resulting load reps. to failure for a 1.2 l/m^2 app. rate, 8 mm ALD , 13.2 mm single seal with tyre edge (E) and centre (C) loads. Temperature: 25°C, base stiffness: 200 MPa, travelling speed at 80 km/h.

Table 7.5: Equivalent LV:HV damage ratios after 10^7 load repetitions.

Description	LV: Remaining surface texture	HV: Remaining surface texture	LV:HV ratio
Max LVs and min HVs	87%	87%	1 : 1
Min LVs and max HVs	87%	86%	1 : 1
Average LVs and E80 ref HVs	87%	86%	1 : 1

Other traffic load variables such as the travelling speed and motion conditions as illustrated in Figure 7.35, do not nearly affect the surface texture reduction as much as the major time related variable: the base stiffness. It is emphasised that the base stiffness is the single most significant parameter that determines embedment and thus the remaining surface texture. No other parameter is as significant, not even the variation of the applied loads.

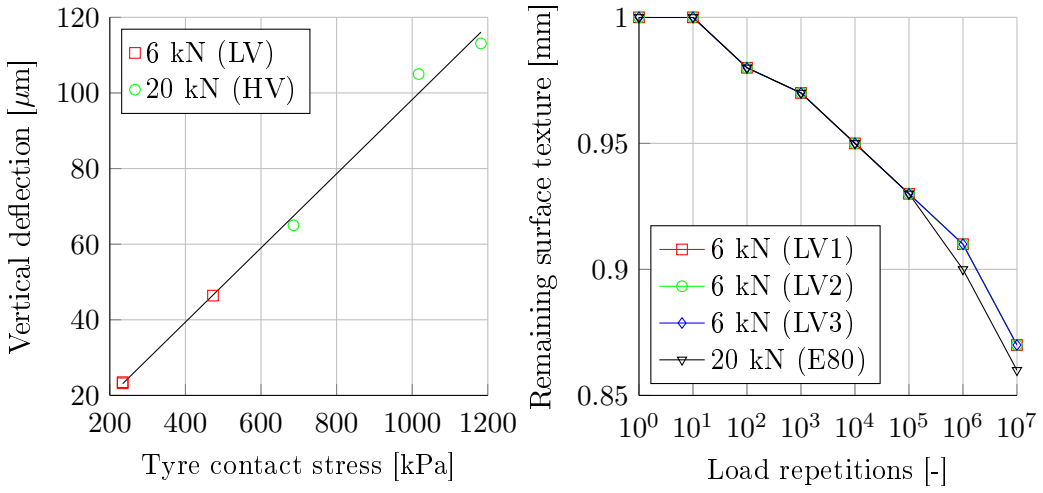

Figure 7.34: Vertical deflection and remaining surface texture for a 1.2 l/m^2 app. rate, 8 mm ALD , 13.2 mm single seal with 3 LVs and E80 HV wheel loads. Temperature: 25°C, base stiffness: 200 MPa, travelling speed at 80 km/h.

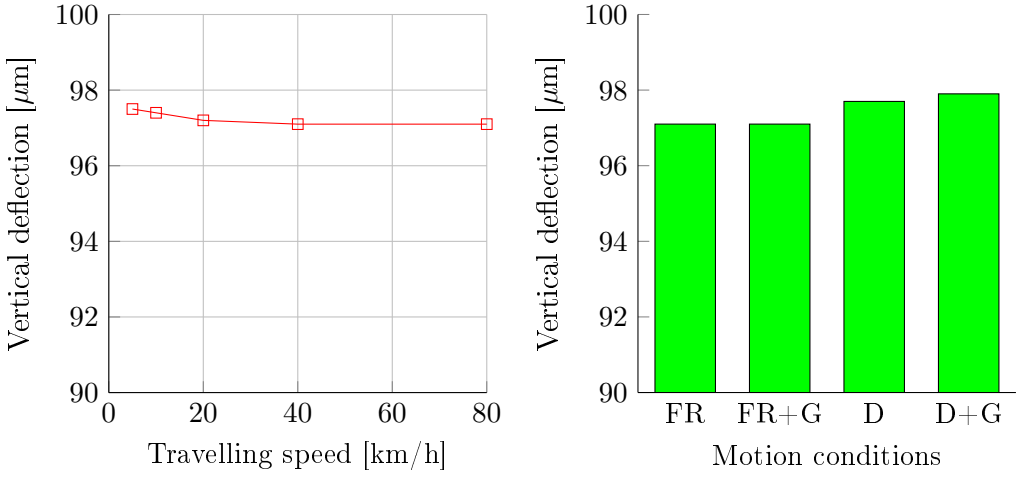

Figure 7.35: Vertical deflection for a 1.2 l/m^2 app. rate, 8 mm ALD , 13.2 mm single seal for various travelling speeds, free rolling (FR) and driven (D) wheels including a 10% gradient (G). Temperature: 25°C, base stiffness: 200 MPa.

7.3.4 Embedment verification and validation

The components of major influence were selected to verify and validate the embedmnet output of the single seal models against field data and interpretations from van Zyl (2015). Three components were included: the seal size, binder application rates and the base stiffness.

The remaining texture depth results were normalised for comparison purposes as illustrated in Figure 7.36 for a 200 MPa base stiffness which corresponds to a 4 mm ball penetration value in this study. Since no field data was obtained for crushed

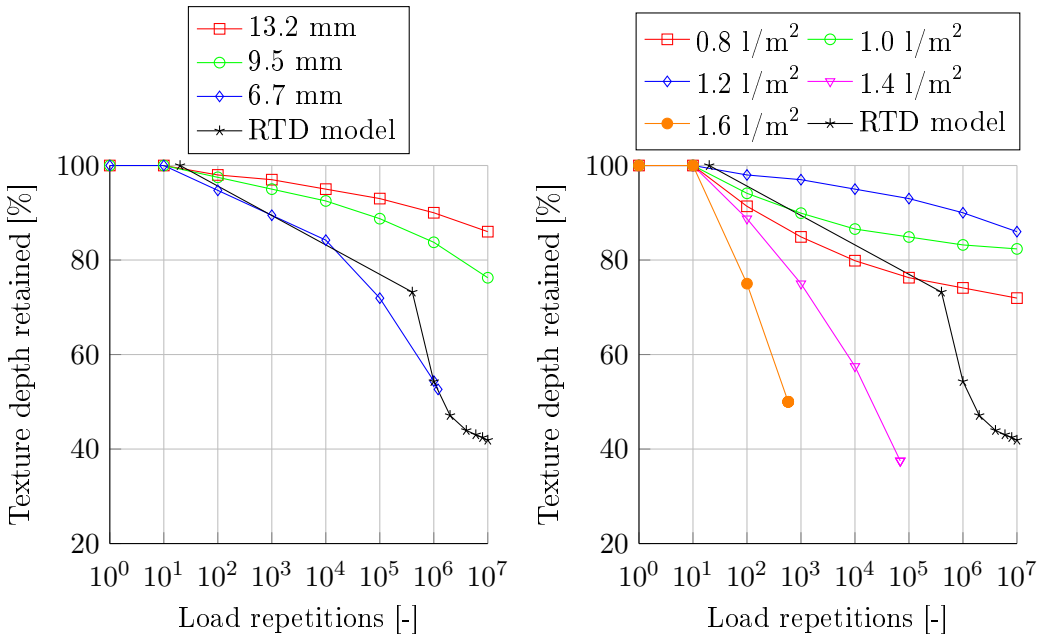

Figure 7.36: Validation of the FE seal model for various seal sizes and binder application rates with the RTD model. Temperature: 25°C, base stiffness: 200 MPa, traffic load: 20 kN-800 kPa at 80 km/h.

stone base with average ball penetration values around 4 mm, van Zyl's (2015) retained texture depth (RTD) model with a ball penetration value of 3.5 mm was selected for comparison.

Van Zyl assumed an equivalent light vehicle (ELVs) damage factor of 10. This means that 10 LVs account for the embedment damage of one HV. In this study the ELVs were therefore reworked to wheel load repetitions and the equivalency factor of 1.1, obtained from the seal model analysis, was applied instead of the assumed factor of 10. The results are illustrated in Figure 7.36, where the RTD model compares closely with the 6.7 mm single seal.

With reference to binder application rate, the RTD model is nested between the 13.2 mm single seals with application rates of 1.2 l/m^2 and 1.4 l/m^2. Calibration of the validation continues to be troublesome due to a lack of field data and proper description thereof.

Although the 200 MPa base stiffness yielded reasonable comparisons with the RTD model, Figure 7.37 illustrates the comparisons in terms of base stiffness variation and includes measured ball penetration field data on a G1 crushed stone base. In this study a base stiffness of 450 MPa equates to a ball penetration value of 1 mm. The difficulty in interpreting the field data is emphasised when attempting to differentiate which portion of the retained surface texture depth can be attributed to embedment and which portion must be accredited to stone orientation. However,

the FE seal model illustrated that it ascertains surface texture values likened to the values obtained in the field.

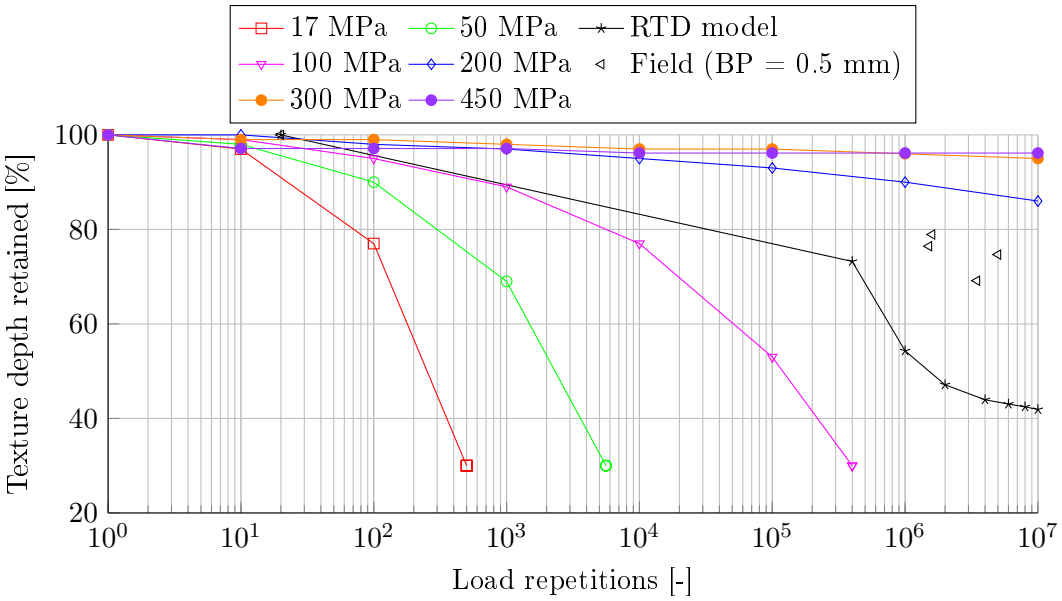

Figure 7.37: Validation of the FE seal model in terms of base stiffness with the RTD model and field data. Temperature: 25°C, traffic load: 20 kN-800 kPa at 80 km/h.

7.4 Closure

Since adhesive damage and cohesive damage occur in close proximity within the seal structure, it is nevertheless surprising that these failure mechanisms display similar failure trends. A smaller magnitude of shear stress response is generally obtained from the cohesive analysis in comparison to the adhesive analysis. In compiling a ranking of importance, both mechanisms indicate that the traffic loads are of lower significance, while the aggregate spread rate and binder application rate are structurally more significant parameters (Figure 7.38). The most significant parameters are the base stiffness in combination with the binder temperature.

Embedment is a phenomenon that is highly dependent on the substrate support strength. No other parameter is as significant, therefore an appropriate selection of structural variables should include a measure of embedment compensation to reduce the effects of surface texture loss and subsequent bleeding. This is more important for single seals than the following chapter which deals with double seals.

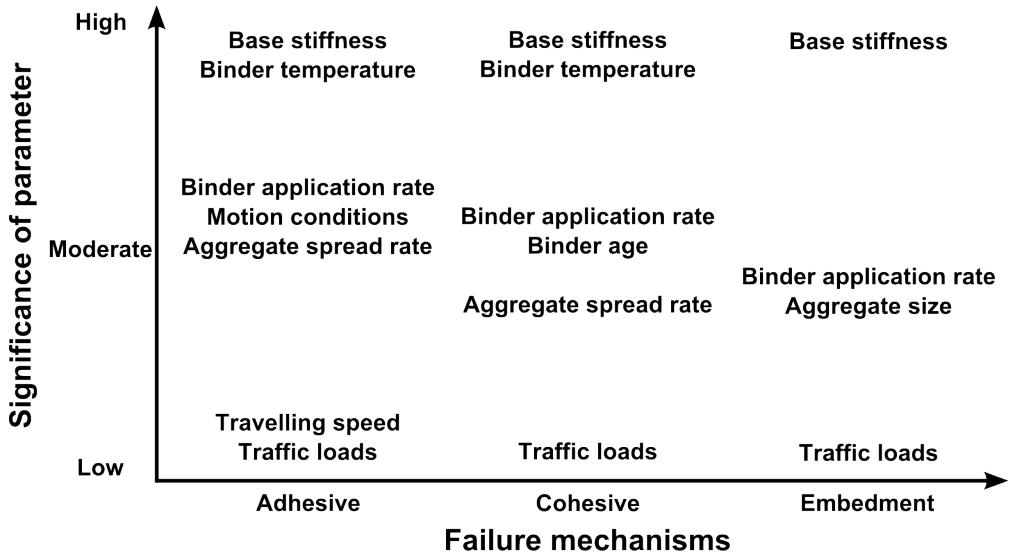

Figure 7.38: Level of parameter significance for single seals.

8. Double seal analysis

The double seal is a popular surface layer within the South African road construction industry. These seals cover vast stretches of the national highway network in mainly rural, but in some cases also urban areas. A double seal is generally constructed on a new or rehabilitated base layer. This chapter illustrates and addresses the response an corresponding fatigue behaviour of the simulated double seal models on homogeneous base structures with reference to the three failure mechanisms as defined in this study.

8.1 Adhesive failure

The adhesive failure analysis presents the shear stress response (Figure 8.1) and corresponding fatigue life calculations of the double seal models according to the primary variations as presented in Table 3.9. The primary variations as defined in this study include the structural variables, time related variable and traffic load variables. These variables are used to verify and validate the seal model's ability to simulate adhesive failure.

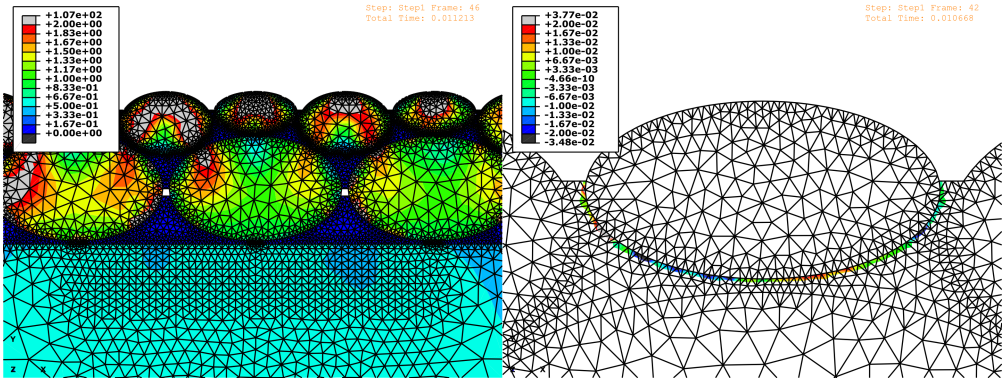

Figure 8.1: Screen grabs of the double seal simulations (MPa): von Mises stress (left) and adhesive zone shear stress (right).

8.1.1 Analysis of the structural variables

The structural variables define the geometry and material selection of the seal. These variables are selected prior to construction and remain constant throughout the service life of the seal. In the double seal scenario, the combination of the aggregate nominal size and spread rate have a significant influence on the shear stress response within the adhesive zone position of the second (top) layer of aggregates (Figure 8.2). It should be noted that the aggregate spread rate is quantified in m^3/m^2, but in the case of the 2D model it is presented in terms of the adjacent edge to edge spacing (mm) of the first (bottom) layer of aggregates.
While there is a general tendency of stress increase for the 19 mm + 9.5 mm and 19 mm + 6.7 mm + 6.7 mm double seals, a slight reduction in stress is observed for the 13.2 mm + 6.7 mm double seal as the spread rate increases from 0.5 mm to 4.0 mm. Most noticeably is the difference in the shear stress magnitudes for the various seal sizes. At a spread of 1 mm there is a 25% stress increase from the 13.2 mm + 6.7 mm seal to the 19 mm + 6.7 mm + 6.7 mm seal and a 120% stress increase from the 13.2 mm + 6.7 mm seal to the 19 mm + 9.5 mm seal. The higher shear stress results in a lower number of load repetitions to failure. A detailed analysis on the number of load repetitions to failure is presented in Section 8.1.4.
Figure 8.3 illustrates the increase in shear stress as the ALD of the 13.2 mm + 6.7 mm seal increases from 9 mm to 14 mm. Here, the ALD is equal to the ALD sum of the first and second layer of aggregates. The general trend indicates an approximate stress increase of 25% and a steady reduction in the number of load repetitions to adhesive failure as the ALD increases from 9 mm to 14 mm.

In comparison to the ALD, a variation in the binder application rate of the 13.2 mm + 6.7 mm seal affect a wider range of shear stress conditions as illustrated in Figure 8.4. An increase in the binder application rate results in a steady decline in the shear stress response. The subsequent effect of the latter trend is a gradual increase in the number of load repetitions to failure. Figure 8.4 also illustrates an unexpected result where an increase in the shear stress is obtained with the application of a fog spray (FS). This suggests that the fog spray shoulder bonds, on the second layer of aggregate, caused an increase in stress and therefore a measure of stress transfer at the interface between the penetration coat and the second layer of aggregate. The difference, however, is small in comparison to stress differences obtained from the various double seal aggregate sizes which, according to this study, remain the major structural component that affects aggregate loss.

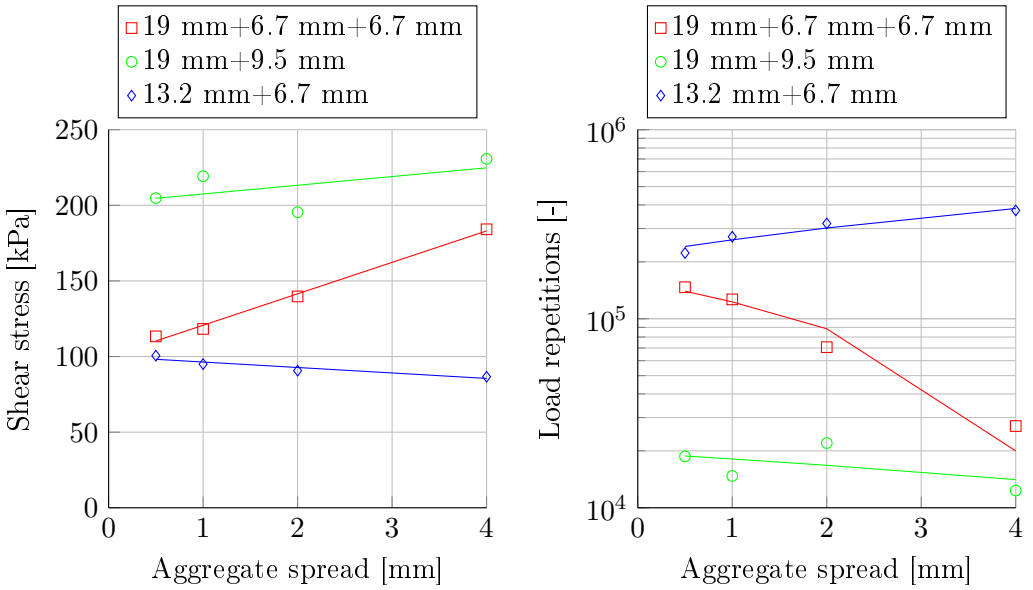

Figure 8.2: Shear stress and corresponding load repetitions to failure for the 13.2+6.7, 19+9.5 & 19+6.7+6.7 mm double seals, virgin 70-100 pen. grade binder. Temperature: 25°C, base stiffness: 200 MPa, traffic load: 20 kN-800 kPa at 80 km/h.

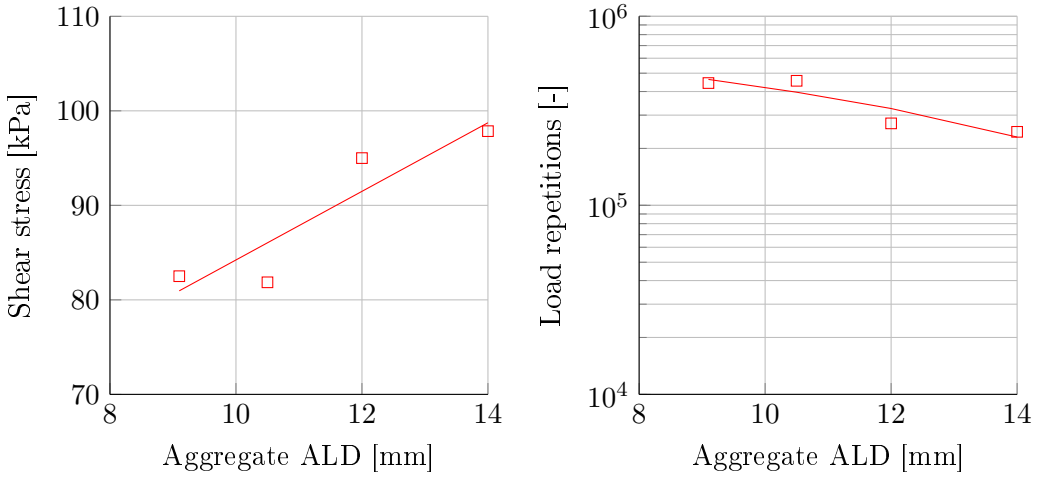

Figure 8.3: Shear stress and corresponding load repetitions to failure for the ALD of the 13.2 mm+6.7 mm double seal with virgin 70-100 pen. grade binder. Temperature: 25°C, base stiffness: 200 MPa, traffic load: 20 kN-800 kPa at 80 km/h.

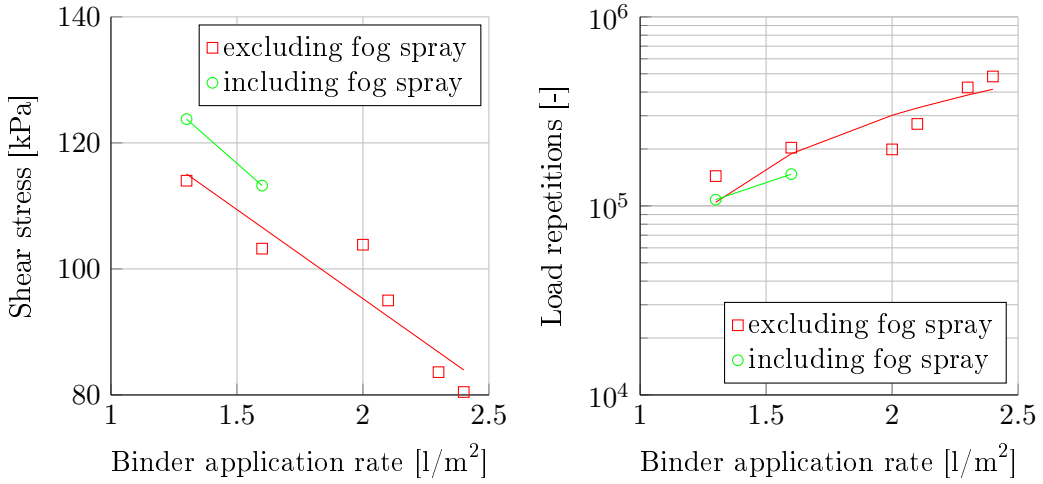

Figure 8.4: Shear stress and corresponding load repetitions to failure for virgin 70-100 pen. grade binder application rates and a 13.2 mm+6.7 mm double seal. Temperature: 25°C, base stiffness: 200 MPa, traffic load: 20 kN-800 kPa at 80 km/h.

8.1.2 Analysis of the time related variables

A time related variable is defined by a change in conditions of that variable over time. Material changes in temperature and strength over time are typical examples of time related variables. Illustrated in Figure 8.5 is the reduction of the adhesive shear stress as a result of an increase in the base stiffness. This phenomenon indicates that stiffer substrates reduce the risk of early aggregate loss.

Figure 8.5 further indicates that greater resistance to adhesive failure is obtained at $10°C$ than at $25°C$. This is somewhat contrary to expectation, while the origin of this phenomenon can be traced to Mukandila's (2015) end of life transfer functions. These functions were developed at 10 rad/s and do therefore not take into consideration the loading time in determining the load repetitions to failure.

More insight into the adhesive response at different temperatures is presented in Figure 8.6, which illustrates the reduction in shear stress with an increase in binder temperature. Figure 8.6 also illustrates the change in adhesive shear stress with an increase in the Glower-Rowe (G-R) aging parameter as discussed in Section 4.1.1, Figure 4.3. The G-R parameters indicate an initial increase in the shears stress response which reaches a peak value, followed by a reduction with time. Quantification in terms of load repetitions to failure was not possible, since no damage parameters for the field recovered binders were developed. It is therefore somewhat speculative to select the two major time related variables which dictate the seal response, but base on the magnitude of shear stress, the base stiffness and binder temperature remains the major factors.

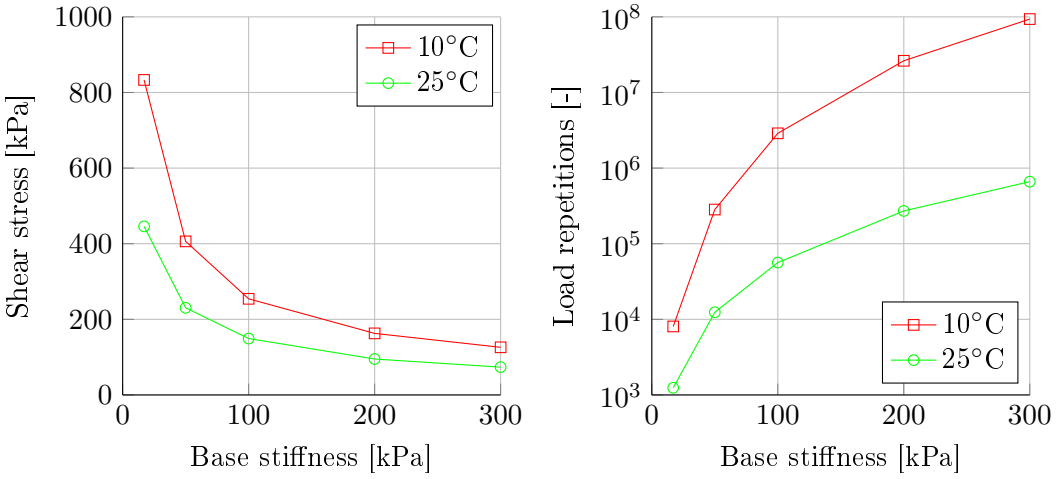

Figure 8.5: Shear stress and corresponding load repetitions to failure for a 2.1 l/m^2 app. rate, 13.2 mm+6.7 mm double seal. Traffic load: 20 kN-800 kPa at 80 km/h.

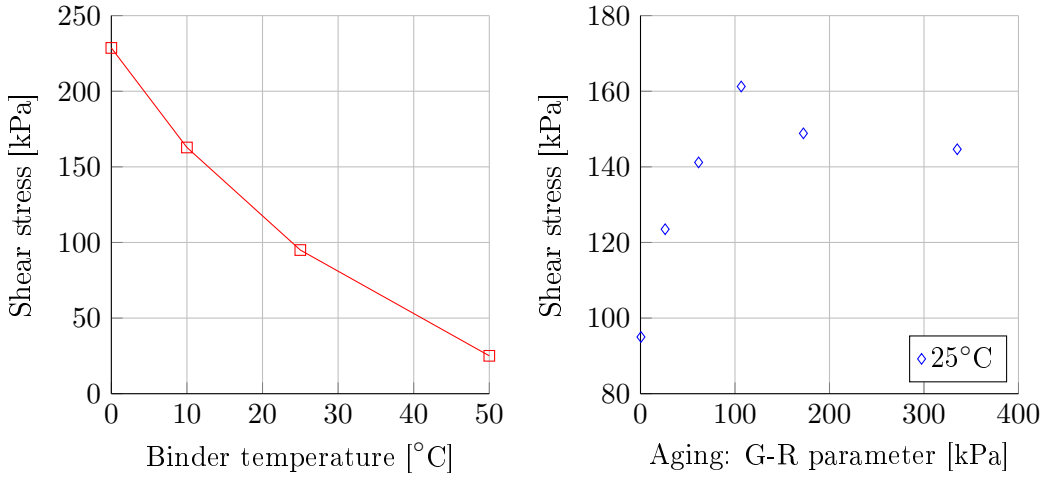

Figure 8.6: Shear stress for a 2.1 l/m^2 app. rate, 12 mm ALD, 13.2 mm+ 6.7 mm double seal. Base stiffness: 200 MPa, traffic load: 20 kN-800 kPa at 80 km/h.

8.1.3 Analysis of the traffic load variables

Traffic load variables define the spectra of design loads that roads are constructed to withstand. Concerning a case for vertical loads and tyre inflation pressures, Figure 8.7 illustrates that a heavier vertical load does not necessarily result in higher adhesive shear stress. It is rather the tyre contact stress that is representative for the measure of adhesive damage. A general increase in shear stress is therefore observed with an increase in tyre contact stress. This phenomenon is followed by a reduction in the load applications to adhesive failure, while the 20 kN-800 kPa load serves as the reference heavy vehicle (HV) load since it is equal to an E80.

In addressing the TRH3 (2007) referenced 40:1 LV:HV equivalency factor, Figure 8.8 illustrates that the average damage of one reference HV wheel load is equal to 14 times the damage of an average light vehicle (LV) wheel load. A summary of the range for LV:HV equivalent damage factors is presented in Table 8.1.

The latter analysis was conducted at 80 km/h and Figure 8.9 illustrates the reduction in shear stress as the travelling speed declines to 5 km/h. This phenomenon therefore justifies the common practice of low speed limits on newly constructed sections to reduce the risk of aggregate loss and results in an increase in the number of load repetitions to failure.

Figure 8.10 illustrates the increase in shear stress as the rolling motion of the wheel changes. The shear stress of a free rolling (FR) wheel on a horizontal road and a road with a 10% gradient (FR+G) is virtually similar at 95 kPa. This stress increases with approximately 4% for driven wheels (D) on horizontal roads and by 11% for driven wheels on a 10% gradient (D+G). A driven wheel on a steep incline and a standard load, over inflated tyre are therefore the major traffic related variables that poses a risk to adhesive failure on double seals. The risk of adhesive failure is quantified in the verification and validation process.

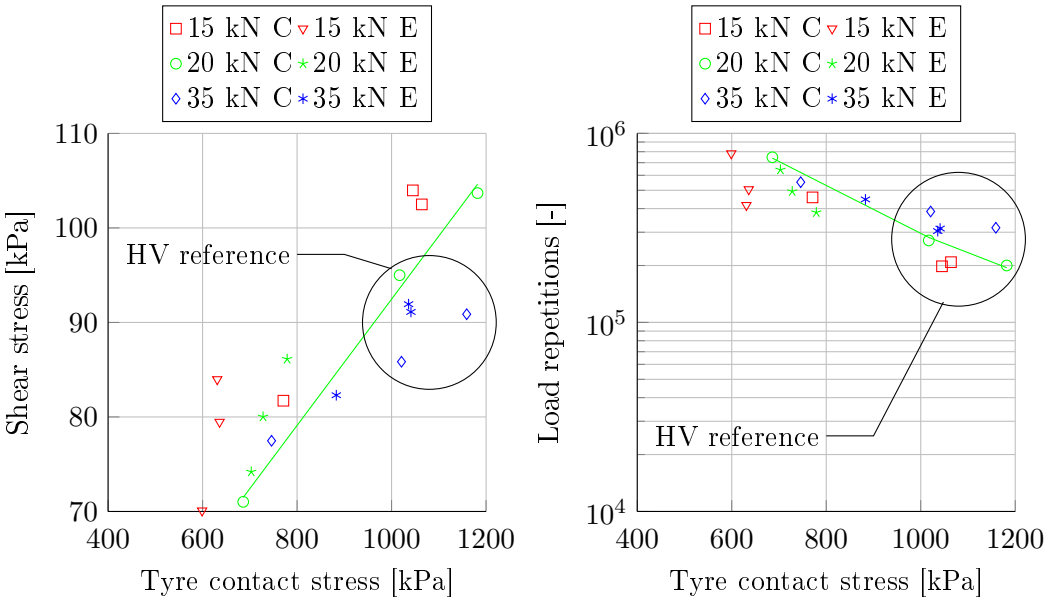

Figure 8.7: Shear stress and corresponding load repetitions to failure for a 2.1 l/m^2 app. rate, 12 mm ALD , 13.2 mm+6.7 mm double seal with tyre edge (E) and centre (C) loads. Temperature: 25°C, base stiffness: 200 MPa, travelling speed at 80 km/h.

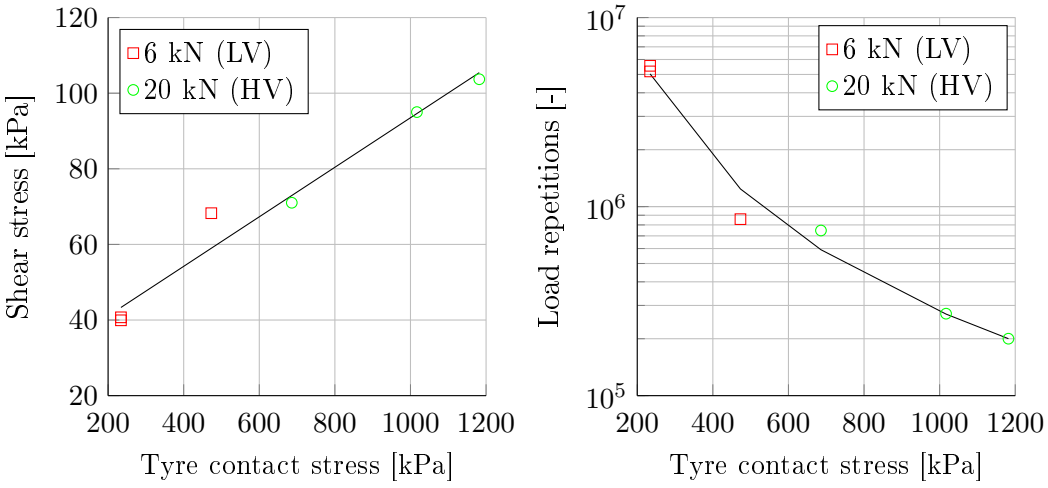

Figure 8.8: Shear stress and corresponding load repetitions to failure for a 2.1 l/m^2 app. rate, 12 mm ALD , 13.2 mm+6.7 mm double seal with LV and HV wheel loads. Temperature: 25°C, base stiffness: 200 MPa, travelling speed at 80 km/h.

Table 8.1: Equivalent LV:HV damage ratios as illustrated in Figure 8.8.

Load case description	LV load reps. to failure	HV load reps. to failure	LV:HV ratio
Maximum LVs and minimum HVs	5555604	200070	28 : 1
Minimum LVs and maximum HVs	858168	747465	1.1 : 1
Average LVs and E80 ref HVs	3867470	271358	14 : 1

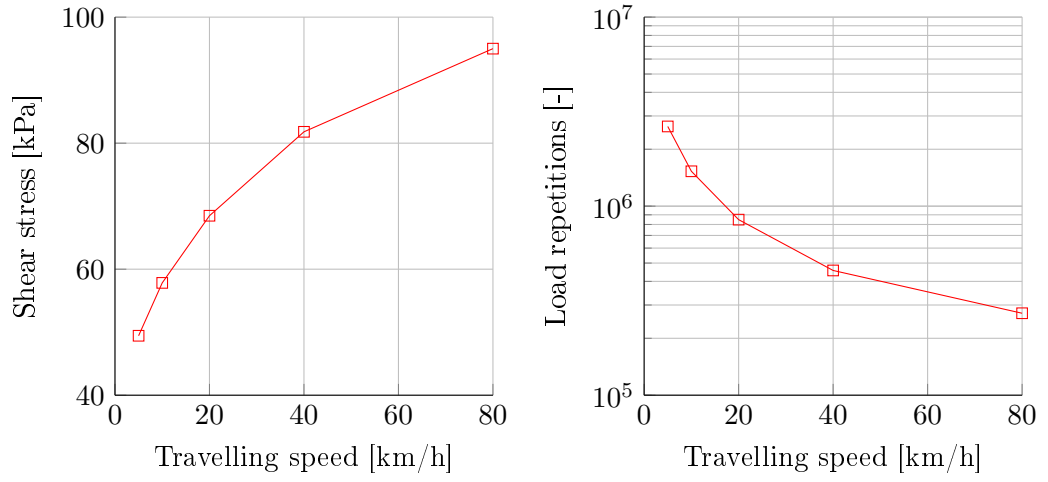

Figure 8.9: Shear stress and corresponding load repetitions to failure for a 2.1 l/m^2 app. rate, 12 mm ALD , 13.2 mm+6.7 mm double seal for different travelling speeds. Temperature: 25°C, base stiffness: 200 MPa, traffic load: 20 kN-800 kPa.

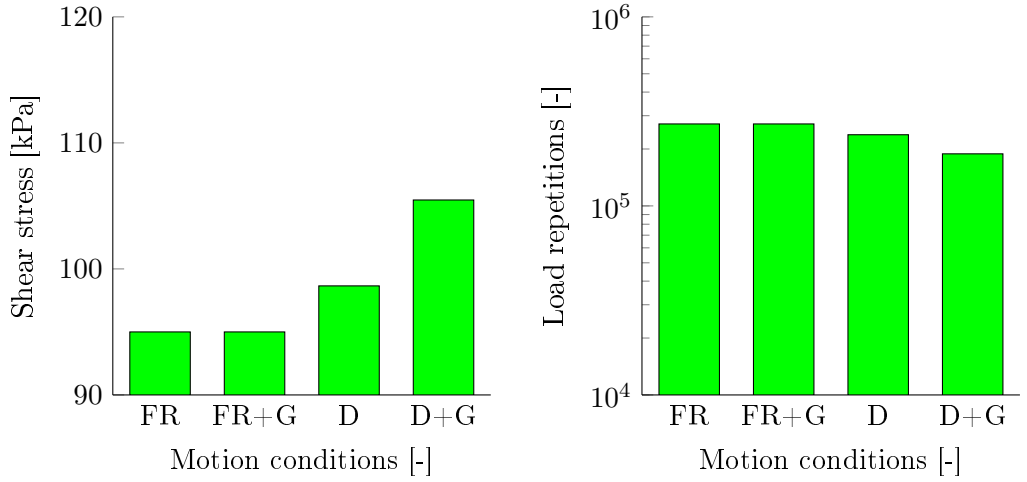

Figure 8.10: Shear stress and corresponding load repetitions to failure for a 2.1 l/m^2 app. rate, 13.2 mm+6.7 mm double seal for free rolling (FR) and driven (D) wheels including a 10% gradient (G). Temperature: 25°C, base stiffness: 200 MPa.

8.1.4 Adhesive failure verification and validation

Similar to the single seal analysis, a number of double seal FE models were simulated according to the empirical red-line data of Table 6.2 for a 12 mm ALD (13.2 mm + 6.7 mm) double seal. Insight obtained in the previous chapter dictated the variable selection of this verification process. The aggregate spread rate was selected at 1 mm, with a binder temperature at 25°C and a substrate stiffness of 450 kPa. The FE simulation results are presented in Figure 8.11 and indicate a decline in shear stress as the binder application rate increases.

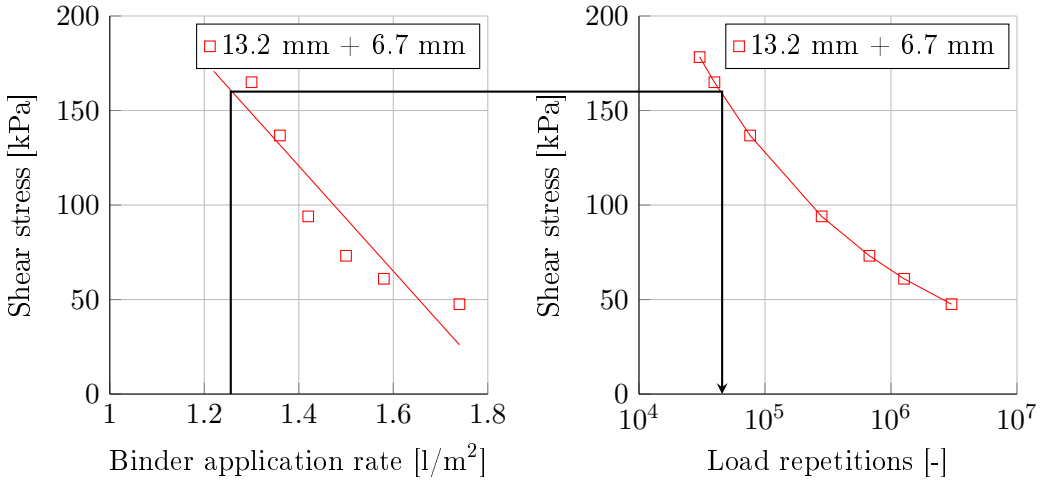

Figure 8.11: Shear stress and binder application rate trends with the corresponding number of load repetitions to failure for the 12 mm ALD, 13.2 mm+6.7 mm double seal models. Base stiffness: 450 MPa, traffic load: 20 kN-800 kPa at 80 km/h.

The trend is as expected and Figure 8.11 further illustrates the relationship between the binder application rate, shear stress and load repetitions to failure. The general relationships are summarised in Table 8.2. It should be noted that these simulations were subjected to 20 kN wheel loads i.e E80s at 80 km/h, while the red-line data was developed for average annual daily traffic (AADT). The red-line traffic data was therefore adjusted to 20 kN wheel loads by utilising the equivalency factor of 14 obtained in this study. The traffic data was further adjusted to incorporate the effect of later wandering according to Huurman's (1997) description as summarised in Appendix D.

Table 8.2: Summary of the trend formulations as depicted in Figure 8.11.

Description of variables	Stdev[i]	Trend formulation	R^2
Binder application rate (x) and shear stress (y) for 25°C @ 1.0 mm	2^{nd}	$y = -278.32x + 510.33$	0.89
Load repetitions (x) and shear stress (y) at 25°C	2^{nd}	$y = 3448.9x^{-0.287}$	1.0

[i] Standard deviation towards the right

Comparisons between the empirical critical minimum binder (CMB) application rate data (Table 6.2) and the E80 load repetitions to failure of the corresponding FE seal models are presented in Figure 8.12. Similar to the single seal analysis, the double seal models exhibit a greater number of load repetitions to failure in comparison to the empirical data. Where the empirical data of the TRH3 (2007) suggests immediate failure i.e. failure within one day, the FE model indicates that initial failure would only occur within one month of traffic.

The FE model results, which is dependent on Mukandila's (2015) transfer function, finds itself between the CMB data and the HDM-4 ravelling initiation result of 8.7 years. The lines of equality indicate that no catastrophic failure i.e. single load rip-off occurs within the first day and that very low levels of binder application rates are more likely to exhibit adhesive fatigue failure within the first month. It is further emphasised that the FE seal models were constructed with aggregate orientation already in ALD which contributes to the magnitude of stress obtained in the adhesive zone. This phenomenon was discussed in Section 7.1.4 and will therefore not be repeated in this section.

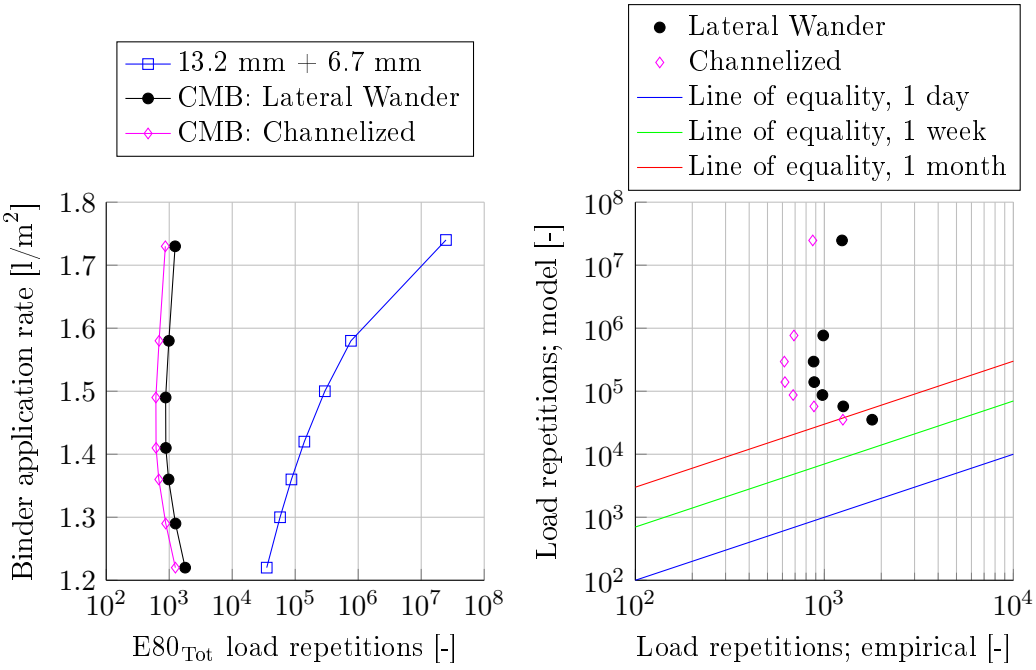

Figure 8.12: Comparisons between the critical minimum binder (CMB) application data (Table 6.2) and FE model results of a 12 mm ALD, 13.2 mm+6.7 mm double seal (left); Empirical and modelled number of E80 load repetitions to failure (right).

8.2 Cohesive failure

The outline of the cohesive failure analysis is identical to the adhesive failure analysis. The shear stress response (Figure 8.13) in the binder and corresponding load repetitions to cohesive failure are presented and discussed according to the primary seal model variations as defined in this study.

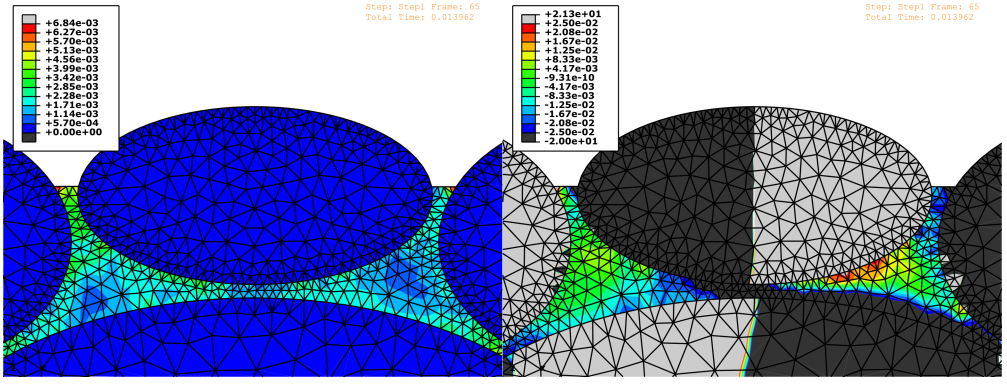

Figure 8.13: Screen grabs of the FE double seal simulations: maximum principle strain ϵ_1 (left) and shear stress σ_{12} in MPa (right).

8.2.1 Analysis of the structural variables

As previously mentioned, the structural variables refer to the geometry and material selection of the seal models. When considering the aggregate sizes and spread rates, Figure 8.14 illustrates a general stress decline for all three seal sizes as the spread rates are increased from 0.5 *mm* to 4.0 *mm*.

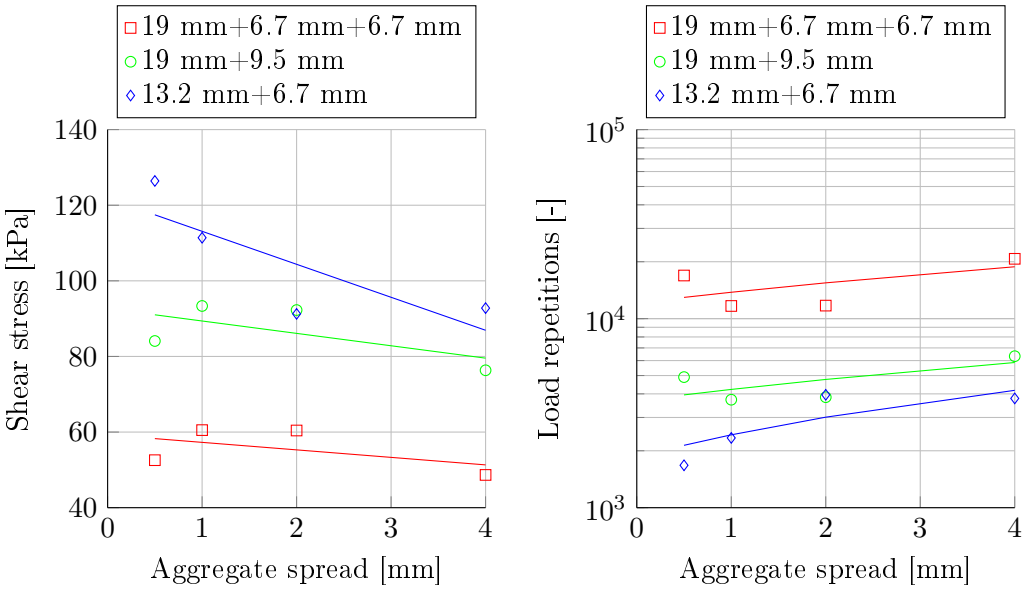

Figure 8.14: Shear stress and corresponding load repetitions to failure for the 13.2+6.7, 19+9.5 & 19+6.7+6.7 mm double seals, virgin 70-100 pen. grade binder. Temperature: 25°C, base stiffness: 200 MPa, traffic load: 20 kN-800 kPa at 80 km/h.

It is interesting to note that the 19 *mm* + 6.7 *mm* + 6.7 *mm* double seal with the twin application of the 6.7 *mm* aggregate for the second layer, exhibit a 35% to 45% reduction in shear stress in comparison to the traditional 19 *mm* + 9.5 *mm* and 13.2 *mm* + 6.7 *mm* double seals. The phenomenon suggests that this type of construction reduces the risk of cohesive fatigue in comparison with the other two as illustrated in the number of load repetitions to failure. A detailed discussion on the load repetitions to failure follows in Section 8.2.4.

The ALD of the 13.2 *mm* + 6.7 *mm* double seal does not have a substantial influence on the stress response, although a general increase in the shear stress (Figure 8.16) is observed as the ALD increases from 9 *mm* to 14 *mm*. This results in a slight reduction in the number of load repetitions to failure with an increase in ALD.

The binder application rate however, has a substantial influence on the shear stress response as illustrated in Figure 8.16. An increase in the binder application rate results in a decrease in the binder shear stress. The opposite effect is therefore observed in the load repetitions to failure. The application of a fog spray (FS) stabilises the

shear stress response of the respected models at approximately 120 kPa, but does not contribute a significant resistance to cohesive fatigue as illustrated by the load repetitions to failure trend.

According to the shear stress magnitudes the binder application rate, followed by the combination of the aggregate spread rate and size are the major structural components that affect cohesive fatigue cracking.

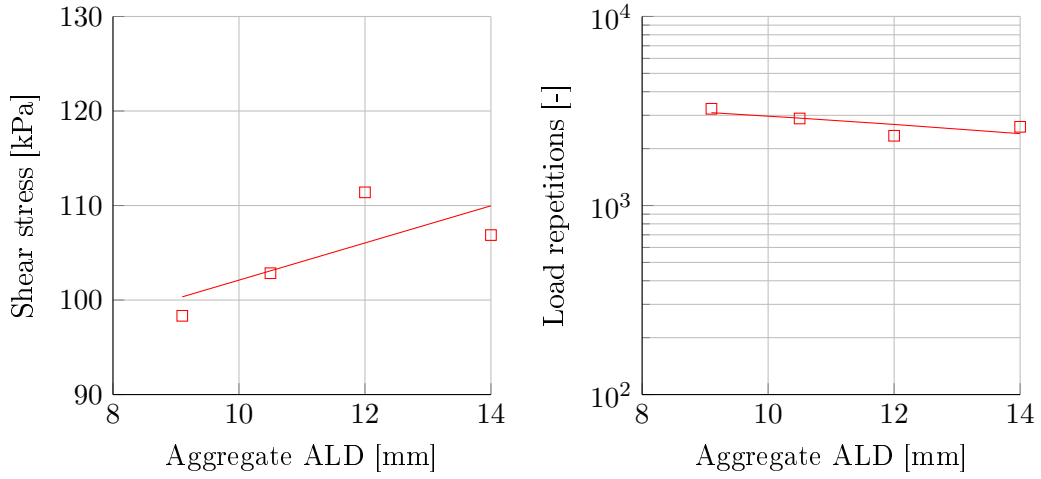

Figure 8.15: Shear stress and corresponding load repetitions to failure for the ALD of the 13.2 mm+6.7 mm double seal with virgin 70-100 pen. grade binder. Temperature: 25°C, base stiffness: 200 MPa, traffic load: 20 kN-800 kPa at 80 km/h.

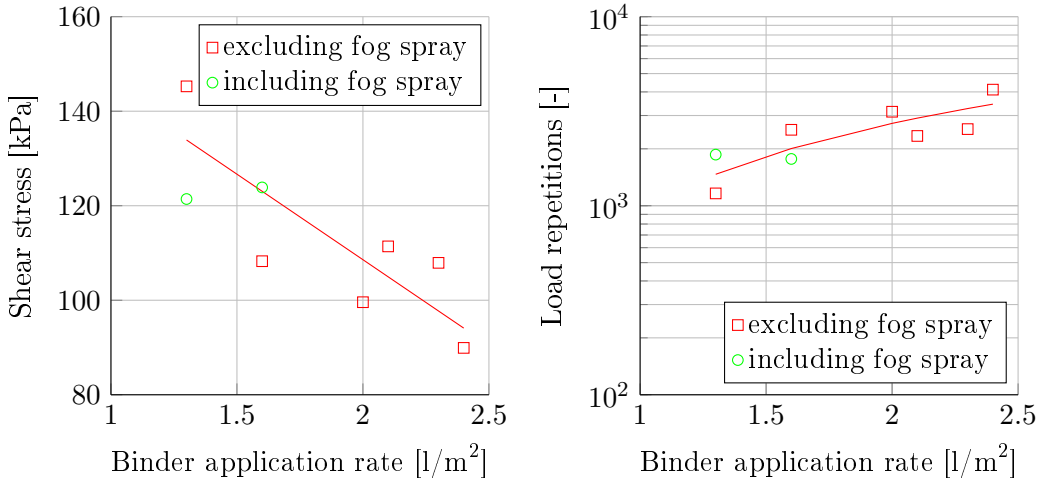

Figure 8.16: Shear stress and corresponding load repetitions to failure for virgin 70-100 pen. grade binder application rates and a 13.2 mm+6.7 mm double seal. Temperature: 25°C, base stiffness: 200 MPa, traffic load: 20 kN-800 kPa at 80 km/h.

8.2.2 Analysis of the time related variables

As previously mentioned, a time related variable refers to the change in condition of that variable over time. Figure 8.17 illustrates the stress responses obtained with changes made to the base stiffness and binder temperature, which results in a reduction of the shear stress as the base stiffness increases.

A greater resilience to cohesive fatigue is observed for $10°C$ than at $25°C$. As mentioned in the previous chapter, this trend relates to the material characterisation as observed by Mukandila (2015) while developing the end of life cohesive fatigue transfer functions. The trend is however consistent with the binder fatigue trends as discussed in the Shell Bitumen Handbook (Read and Whiteoak, 2003), although the common perception in practice advocates that fatigue cracking is more likely to occur during colder periods than warmer periods.

Figure 8.18 further emphasises the reduction in binder shear stress as the temperature increases from $0°C$ to $50°C$. Quantification in terms of load repetitions to failure is however restricted to cases at $10°C$ and $25°C$, since no other damages parameters were developed. Similarly, Figure 8.18 indicates the relationship between the shear stress and binder age without quantification in terms of load repetitions to failure. The general trend indicates an initial shear stress increase followed by a reduction as the binder ages. Aging is represented by the Glower-Rowe (G-R) parameter as discussed in Section 4.1.1. A similar trend was observed during the single seal analysis.

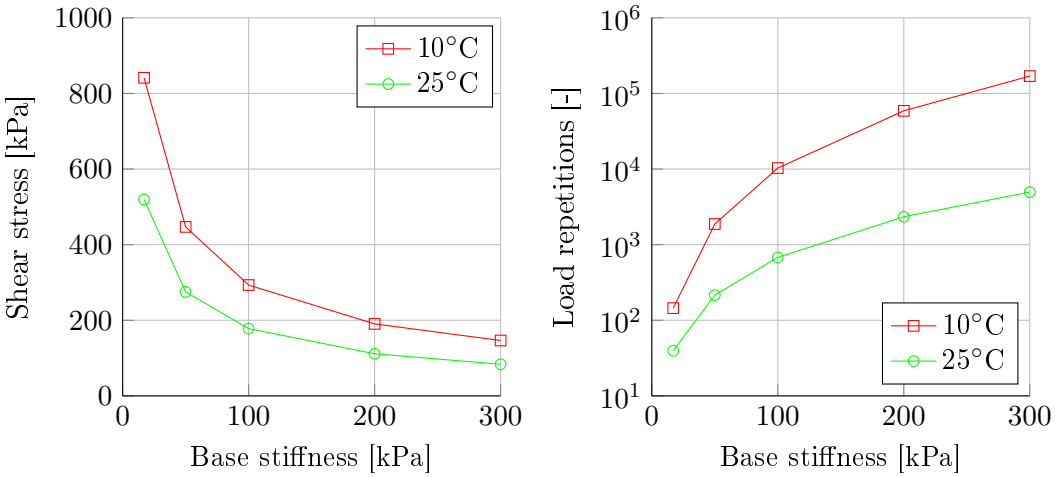

Figure 8.17: Shear stress and corresponding load repetitions to failure for a 2.1 l/m^2 app. rate, 13.2 mm+6.7 mm double seal. Traffic load: 20 kN-800 kPa at 80 km/h.

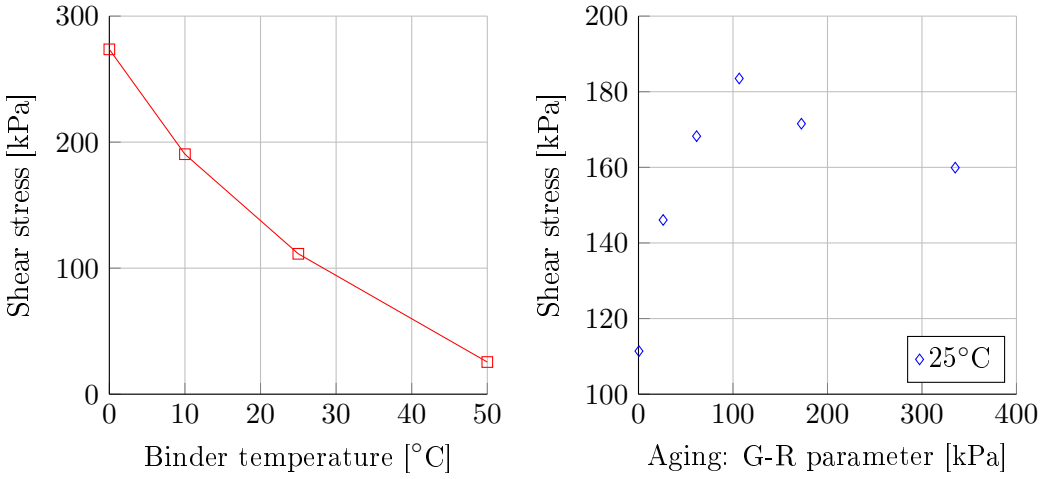

Figure 8.18: Shear stress for a 2.1 l/m^2 app. rate, 12 mm ALD, 13.2 mm+ 6.7 mm double seal. Base stiffness: 200 MPa, traffic load: 20 kN-800 kPa at 80 km/h.

8.2.3 Analysis of the traffic load variables

The traffic load variables are defined as the variety of traffic loads to which a road is subject as shown previously. Variables such as the vertical load and tyre inflation pressure were analysed and presented in Figure 8.19. Binder shear stress response trends obtained at the edge (E) and centre (C) positions beneath the tyre, indicate an increase in the shear stress response as the tyre contact stress increases. The overloading condition at 35 kN does not affect the double seal as much as was observed with the single seal, but reinforces previous sentiments that the tyre contact stress and not only the magnitude of the vertical load is indicative to measure of cohesive fatigue.

Figure 8.20 supports the previous statement and simultaneously addresses the TRH3 (2007) referenced 40:1 light vehicle (LV) to heavy vehicle (HV) damage ratio. The reference HV wheel load (E80) generates approximately 8.5 times more damage than the average LV wheel load. A summary of the range for LV:HV equivalent damage factors is presented in Table 8.3. The number of load repetitions to failure is very conservative and is a direct result of applying Mukandila's (2015) end of life cohesive transfer function.

The binder response is load-rate dependent, where an increase in the travelling speed results in an increase in the shear stress (Figure 8.21). A similar phenomenon was observed by Lombard (2015) while conducting bitumen bond strength testing. This was discussed in Section 7.2.3 and indicated that increased loading rates resulted in higher shear stress magnitudes at failure. Accordingly, an increase in the travelling speed results in a reduction in the number of load repetitions to failure.

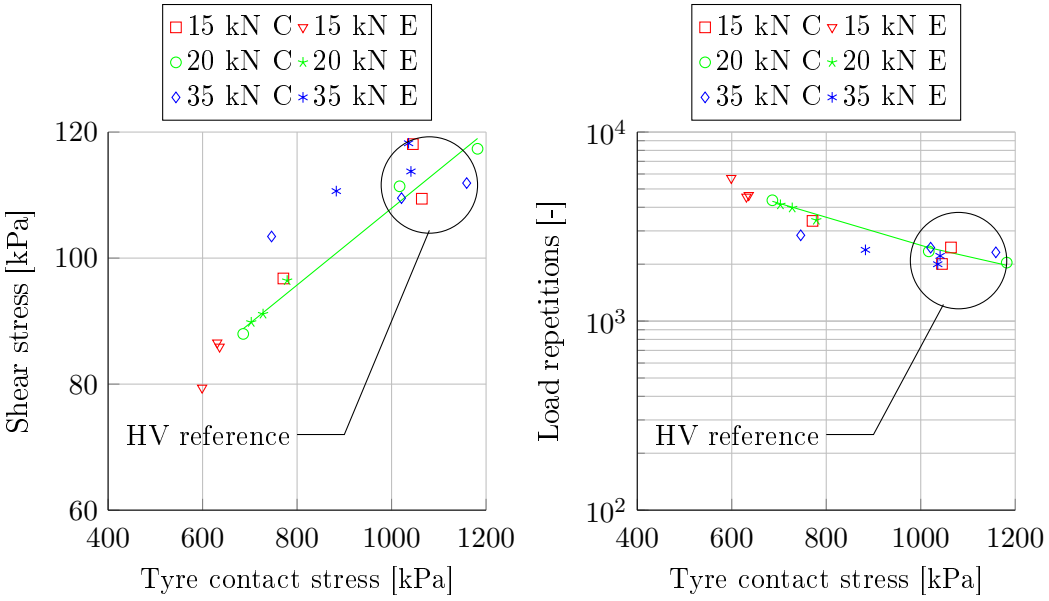

Figure 8.19: Shear stress and corresponding load repetitions to failure for a 2.1 l/m^2 app. rate, 12 mm ALD , 13.2 mm+6.7 mm double seal with tyre edge (E) and centre (C) loads. Temperature: 25°C, base stiffness: 200 MPa, travelling speed at 80 km/h.

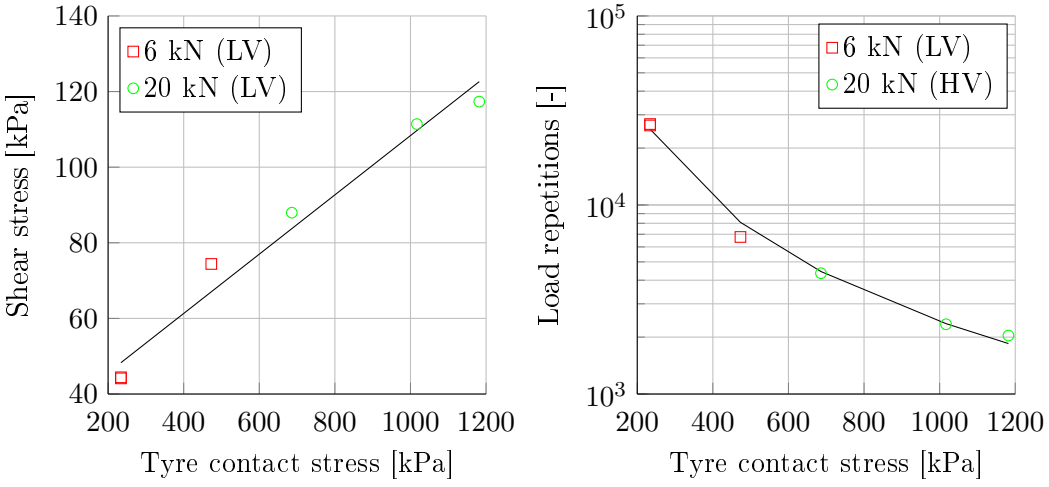

Figure 8.20: Shear stress and corresponding load repetitions to failure for a 2.1 l/m^2 app. rate, 12 mm ALD , 13.2 mm+6.7 mm double seal with LV and HV wheel loads. Temperature: 25°C, base stiffness: 200 MPa, travelling speed at 80 km/h.

Table 8.3: Equivalent LV:HV damage ratios as illustrated in Figure 8.20.

Load case description	LV load reps. to failure	HV load reps. to failure	LV:HV ratio
Maximum LVs and minimum HVs	26793	2038	13 : 1
Minimum LVs and maximum HVs	6772	4356	1.6 : 1
Average LVs and E80 ref HVs	19969	2338	8.5 : 1

In considering the effects of wheel motion, Figure 8.22 illustrates that little difference is observed between free rolling (FR) and driven wheels (D) on a horizontal surface or surfaces with a 10% gradient. It should be noted that the number of load repetitions to failure is approximately 20000 for al four motion condition and is related to the cohesive end of life transfer functions.

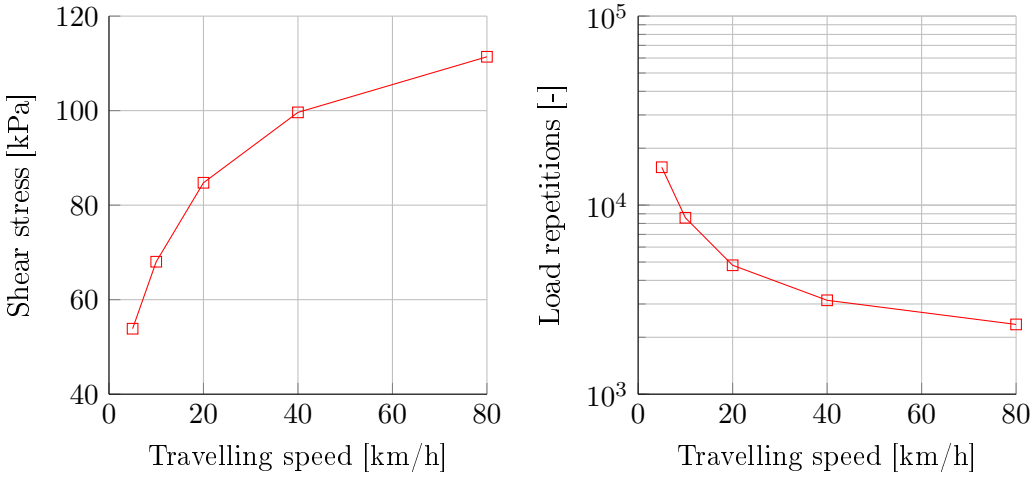

Figure 8.21: Shear stress and corresponding load repetitions to failure for a 2.1 l/m² app. rate, 12 mm ALD , 13.2 mm+6.7 mm double seal for different travelling speeds. Temperature: 25°C, base stiffness: 200 MPa, traffic load: 20 kN-800 kPa.

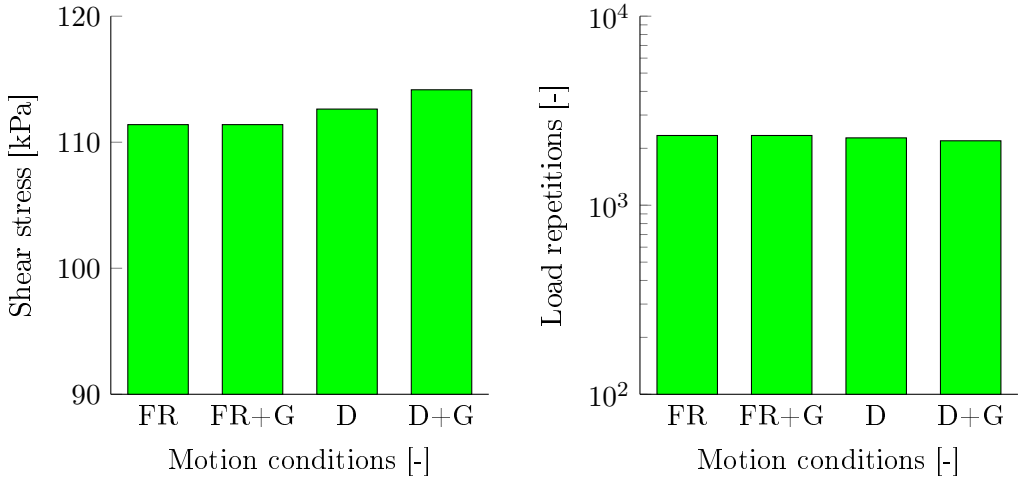

Figure 8.22: Shear stress and corresponding load repetitions to failure for a 2.1 l/m² app. rate, 13.2 mm+6.7 mm double seal for free rolling (FR) and driven (D) wheels including a 10% gradient (G). Temperature: 25°C, base stiffness: 200 MPa.

8.2.4 Cohesive failure verification and validation

Similar to the previous chapter, post processing of the cohesive shear stress analyses with Mukandila's (2015) end of life transfer functions, resulted in the load repetitions to failure parameter N_i as discussed in Equation 3.36. The n_i parameter in Equation 3.36 represents the traffic volume and was therefore artificially populated with the same table of traffic volumes and growth rates used in the previous chapter to match the volumes and growth rates as observed by van Zyl (2015) in the development of the trigger lines for cohesive cracking.

A replica of the traffic volumes and growth rates are presented in Table 8.4, while a complete discussion on factors that influence cohesive fatigue and subsequent adjustments of the cohesive results are presented in Section 7.2.4. The discussion will not be repeated in this section, but in summation:

By calculating the cumulative E80 load repetitions over a 20 year service life span, a time estimate (years) and subsequent cumulative deflection to failure were determined for each seal model simulation (Figure 8.23). The time to failure was adjusted with shift factors to included omitted aspects such as healing and lateral wander. This resulted in the development of a FE model trend as illustrated in Figure 8.24. The trend serve only as a projected result for comparison to van Zyl's (2015) trigger line, since the shift factors were developed for asphalt mixtures. The adjusted trend line indicates the strong influence that a variation in the base stiffness parameter contributes by dictating the seal's cumulative deflection to failure. Other noticeable influences are the aggregate spread rates and binder application rates.

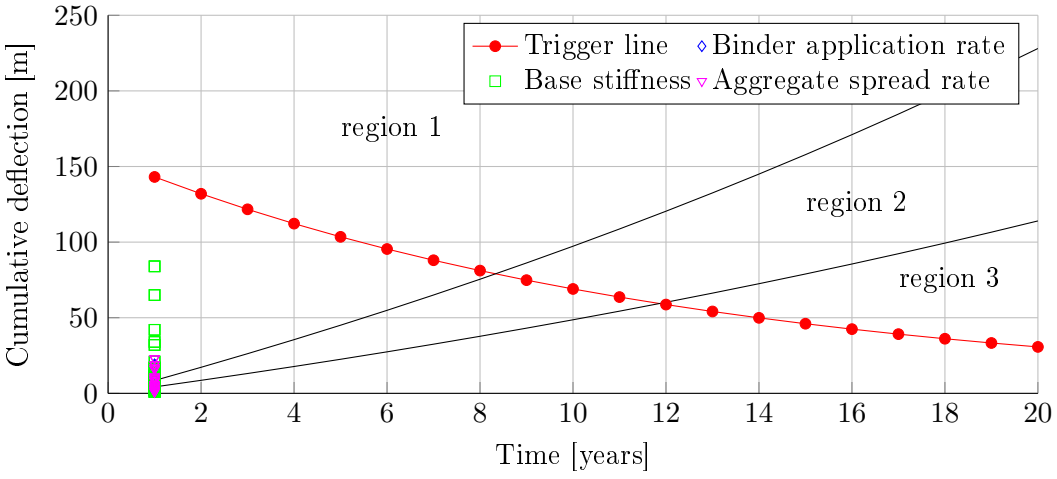

Figure 8.23: Cumulative deflection and time of cohesive fatigue cracking for E80s at 25°C and a 3% growth rate.

Table 8.4: Cohesive failure validation traffic volumes and growth rates.

Regions	Traffic volume description	Number of E80s/day/lane	Annual growth rate i [%]
Region 1	High	600-300	1, 3, 5
Region 2	Moderate	300-150	1, 3, 5
Region 3	Low	150-38	1, 3, 5

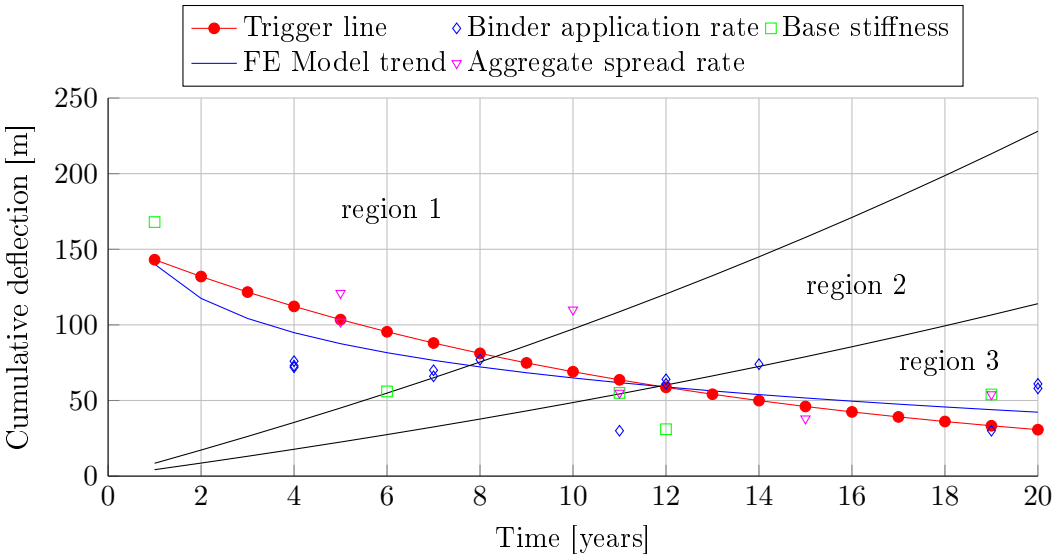

Figure 8.24: Cumulative deflection and adjusted time of cohesive fatigue cracking for E80s at 25°C and a 3% growth rate.

8.3 Embedment failure

The embedment failure analysis presents the base deflection response (Figure 8.25) and corresponding load repetitions to failure, according to the outline of the primary variations. In this case failure is defined in terms of retained surface texture. The

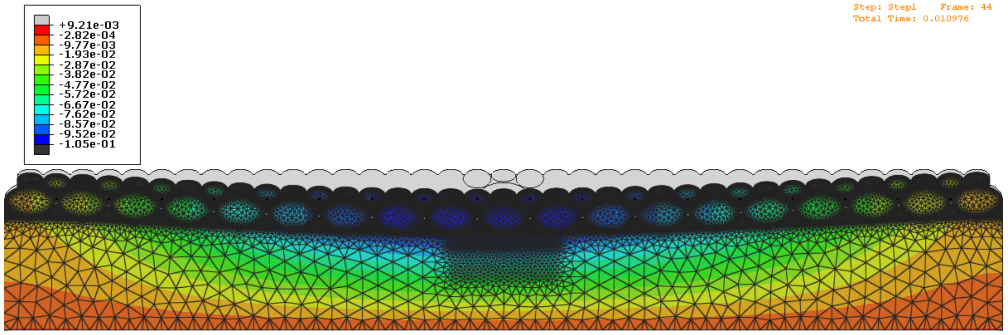

Figure 8.25: Screen grab of the FE double seal simulations: exaggerated vertical deflection (mm) displaying the radius of curvature.

TRH3 (2007) stipulates a minimum surface macro texture of 0.7 mm, but makes provision for cases with remaining surface textures 0.5 mm to 0.3 mm. Some initial surface textures bordered 0.3 mm and to encompass all the relevant models 0.1 mm was selected as the failure criterion.

8.3.1 Analysis of the structural variables

In practice, seal sizes and spread rates often vary, therefore nominal size cases which include the 19 mm + 6.7 mm + 6.7 mm, 19 mm + 9.5 mm and 13.2 mm + 6.7 mm double seals as presented in Figure 8.26, were analysed at various spread rates to establish typical embedmnet trends. The nett binder application rates were distributed at rates of 50/50 to 60/40 between the tack coat and penetration coat respectively. A 40% wetted height (WH) implies therefore that the second layer (top) of aggregates is coated with binder to a height of 40% of that layer's individual ALD.

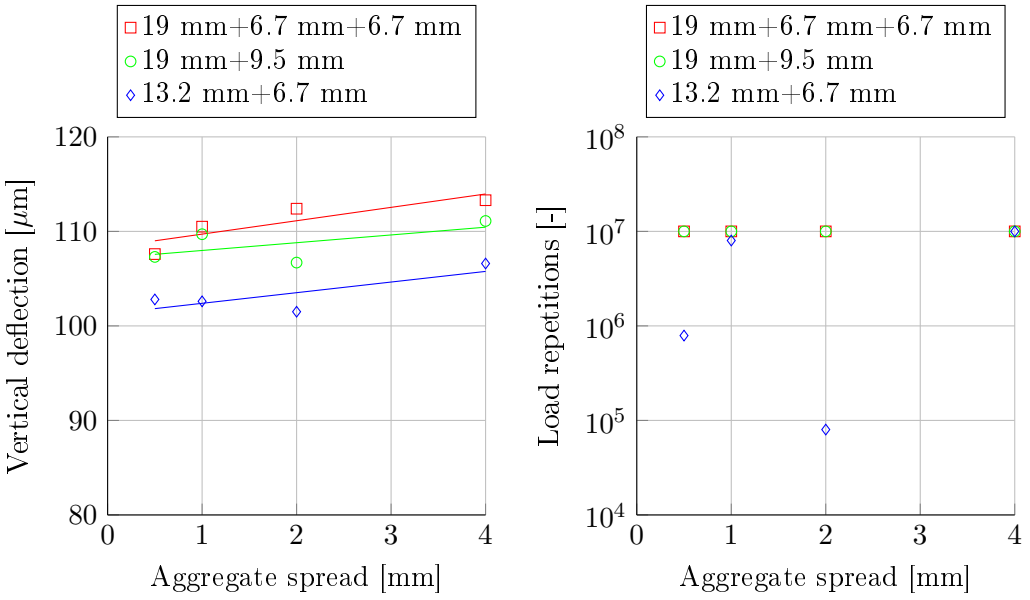

Figure 8.26: Vertical deflection and resulting load repetitions to failure for the 19+6.7+6.7 mm, 19+9.5 mm & 13.2+6.7 mm double seals at 40% wetted height. Temperature: 25°C, base stiffness: 200 MPa, traffic load: 20 kN-800 kPa at 80 km/h.

Figure 8.26 indicates a gradual increase in deflection as the spread rate is increased from 0.5 mm to 4.0 mm. A clear trend in the embedment development is troublesome, hence the re-illustration of the 13.2 mm + 6.7 mm double seals in Figure 8.27 for clarification. Even though embedment occurs during the first 10 to 100 load repetitions, no surface texture is lost due to air voids that had formed between the two aggregate layers during the binder application split. Figure 3.10 illustrates a similar type of air void that had formed in a single seal between the tack coat and a fog

spray. Only after these voids are filled by the up-surging tack coat, a loss in surface texture is observed with the remainder of the embedment development as illustrated in Figure 8.27. In cases such as the 19 mm + 6.7 mm + 6.7 mm and 19 mm + 9.5 mm double seals of Figure 8.26, no loss in surface texture is recorded due to this phenomenon. Figure 8.27 further illustrates that the initial surface texture is a more significant parameter in determining the load repetition to failure than the aggregate spread rate.

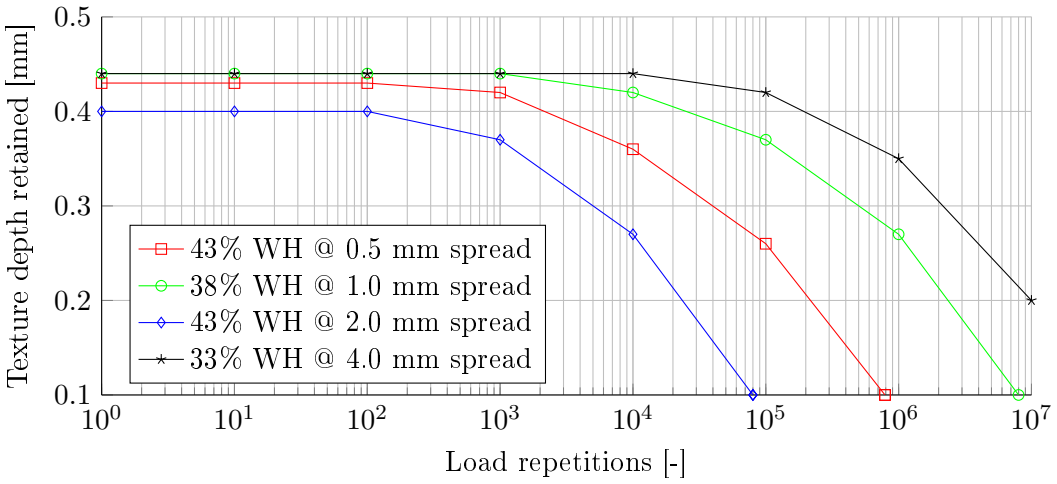

Figure 8.27: Retained surface texture for the 13.2 mm+6.7 mm double seal with virgin 70-100 pen. grade binder at approx. 40% wetted height. Temperature: 25°C, base stiffness: 200 MPa, traffic load: 20 kN-800 kPa at 80 km/h.

Aggregate ALD influences the initial texture depth as illustrated in Figure 8.28 and emphasises that the initial surface texture is a significant parameter with reference to embedment development. However, it is evident that the double seal with a 14 mm ALD exhibits a greater embedment rate than the remaining three. This is due to a slightly higher deformation ratio (DR) as discussed and presented in Equation 3.27. The deformation ratio is thus another significant parameter within the domain of the embedment phenomenon.

Similar to the aggregate ALD, binder application rates affects not only the initial surface texture, but also the air void sizes that form between the first and second layers of aggregate. Figure 8.29 illustrates that the vertical deflection increases at very low application rates, but the combination of voids and available surface texture result in no texture loss. High application rates though, significantly increase the risks of texture loss which can lead to bleeding.

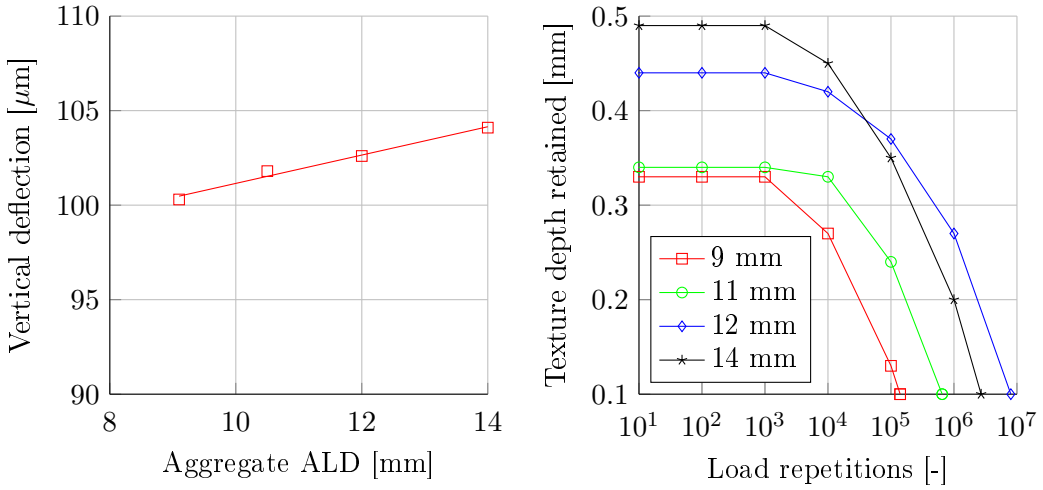

Figure 8.28: Retained surface texture for various ALDs of the 13.2 mm+6.7 mm double seal and virgin 70-100 pen. grade binder at approx. 40% wetted height. Temperature: 25°C, base stiffness: 200 MPa, traffic load: 20 kN-800 kPa at 80 km/h.

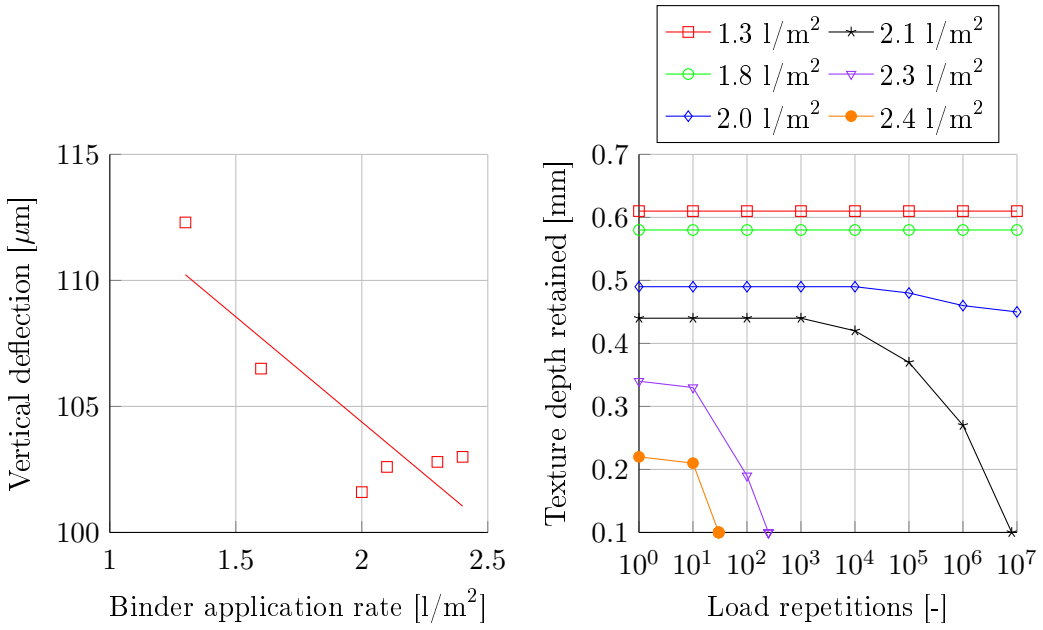

Figure 8.29: Vertical deflection and remaining surface texture for various virgin binder application rates and a 12 mm ALD, 13.2 mm+6.7 mm double seal. Temperature: 25°C, base stiffness: 200 MPa, traffic load: 20 kN-800 kPa at 80 km/h.

8.3.2 Analysis of the time related variables

A single geometrical 13.2 mm + 6.7 mm double seal (12 mm ALD) structure was selected for the time related variable analysis of which the material properties were altered, simulating change with time. Failure in terms of remaining surface texture was selected at 0.1 mm or 10 million load applications, which ever came first, as

illustrated in Figure 8.30 where a reduction in the base stiffness dramatically affects the vertical deflection. The increase in vertical deflection results in a major decline in the number of load repetitions to failure.

A difference in temperature however, has little to no effect on the embedment development and this is further emphasised in Figure 8.31 which indicates a similar degree of deflection for temperatures ranging from $0°C$ to $50°C$. Figure 8.31 also illustrates that binder aging, as represented by the Glower-Rowe (G-R) parameter, does not have a significant influence on the vertical deflection and therefore similar magnitudes of embedment developments are expected.

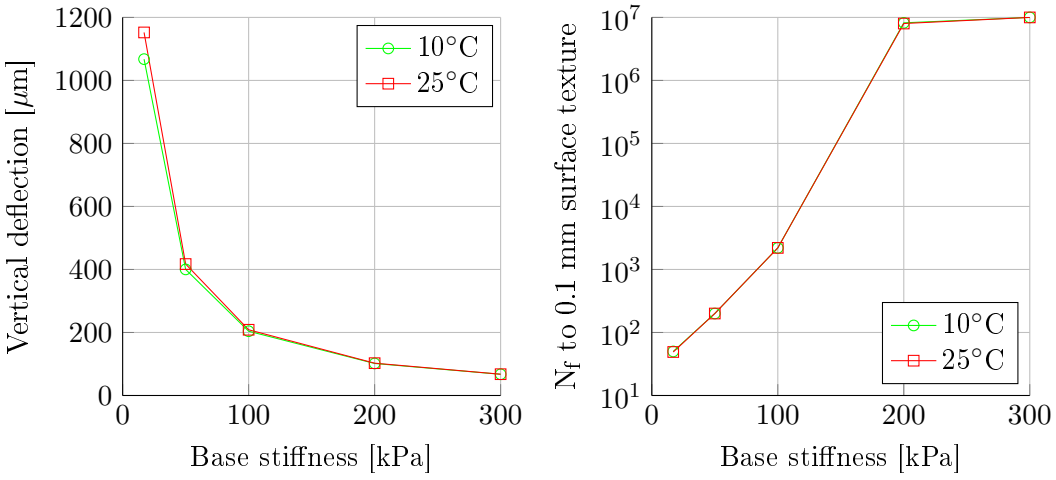

Figure 8.30: Vertical deflection and resulting load reps. to failure for a 2.1 l/m^2 app. rate, 13.2 mm+6.7 mm double seal. Traffic load: 20 kN-800 kPa at 80 km/h.

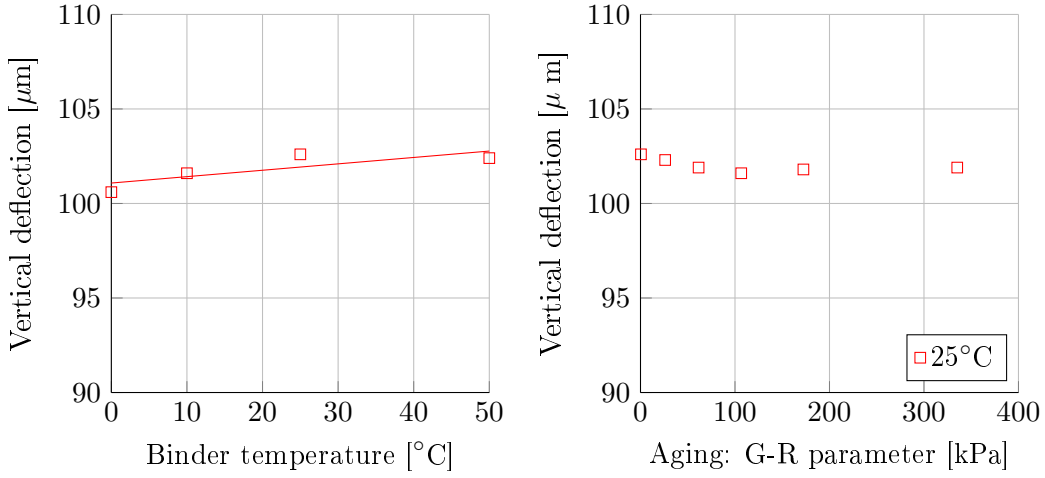

Figure 8.31: Vertical deflection for a 2.1 l/m^2 app. rate, 13.2 mm+6.7 mm double seal. Base stiffness: 200 MPa, traffic load: 20 kN-800 kPa at 80 km/h.

8.3.3 Analysis of the traffic load variables

Similar to the previous chapter, Figure 8.32 illustrates that a difference in the vertical load does not significantly influence the embedment development. Although the vertical deflection increases as the tyre contact stress is increased, the number of load repetitions to failure remains within a narrow band.

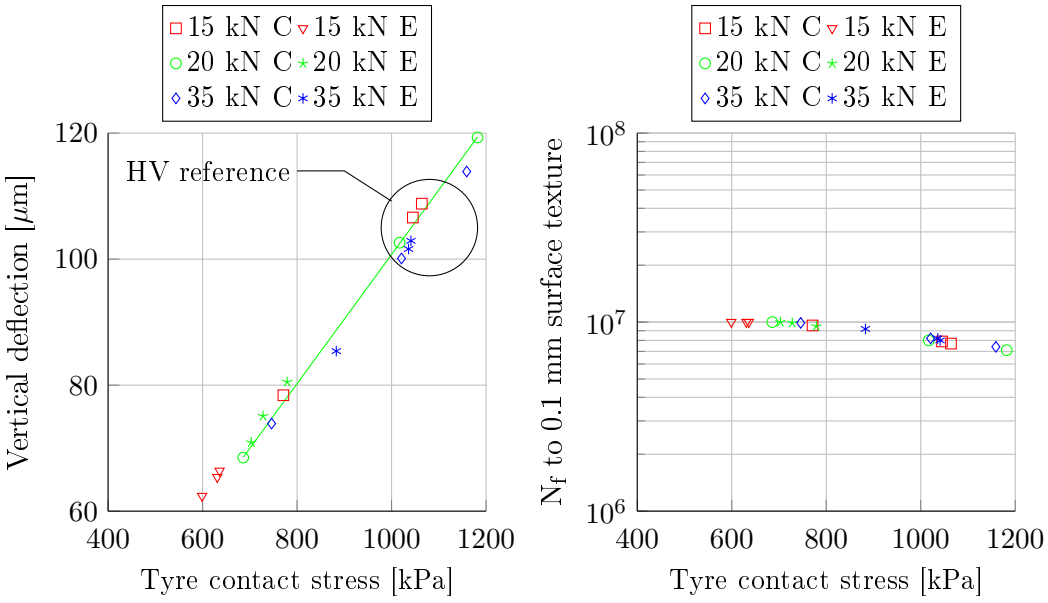

Figure 8.32: Vertical deflection and resulting load reps. to failure for a 2.1 l/m^2 app. rate, 13.2 mm+6.7 mm double seal with tyre edge (E) and centre (C) loads. Temperature: 25°C, base stiffness: 200 MPa, travelling speed at 80 km/h.

The latter phenomenon is further investigated in Figure 8.33, which illustrates the comparison of LVs with HVs including the reference HV (20 kN-800 kPa). Although LV wheel loads result in a reduction of vertical deflection in comparison to the HV wheel loads, the number of load repetitions to failure does not give in-depth insight into equivalent damage factors. A more robust comparison of the LV:HV equivalent damage ratios are presented in Table 8.5. After 10^7 load applications or a failure criterion of 0.1 mm (23%) remaining surface texture, the average LV to reference HV equivalent damage ratio is approximately 6:5 which is much different from the TRH3 (2007) referenced 40:1 ratio.

Other factors such as E80 axle travelling speed and rolling wheel motion conditions are illustrated in Figure 8.34, but indicate vary little difference in the vertical deflection. It is therefore expected that these factors do not have an insignificant contribution to the embedment development in this study.

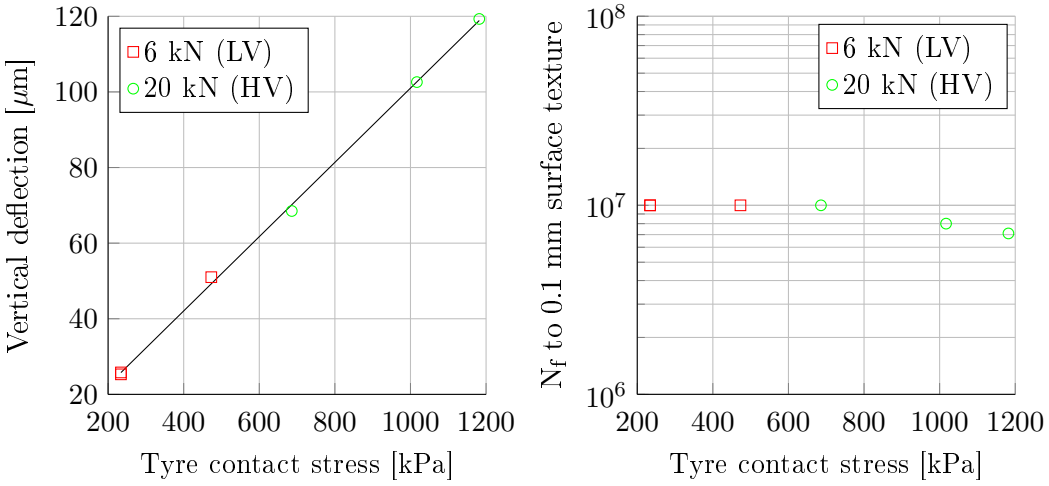

Figure 8.33: Vertical deflection and remaining surface texture for a 2.1 l/m² app. rate, 12 mm ALD, 13.2 mm+6.7 mm double seal, 3 LVs and E80 HV wheel loads. Temperature: 25°C, base stiffness: 200 MPa, travelling speed at 80 km/h.

Table 8.5: Equivalent LV:HV damage ratios as illustrated in Figure 8.33.

Load case description	LV load reps	Remaining LV surf texture	HV load reps	Remaining HV surf texture	LV:HV ratio
Max LVs & min HVs	1.0×10^7	42%	7.1×10^6	23%	1.4 : 1
Min LVs & max HVs	1.0×10^7	27%	1.0×10^7	25%	1.1 : 1
Ave LVs & ref HV	1.0×10^7	30%	8.0×10^6	23%	1.2 : 1

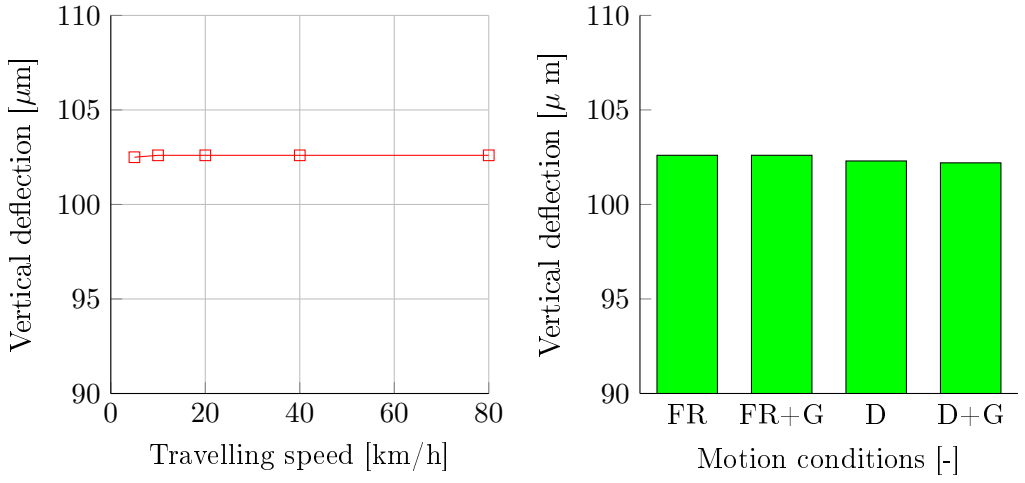

Figure 8.34: Vertical deflection for a 21 l/m² app. rate, 8 mm ALD, 13.2 mm+6.7 mm double seal for various travelling speeds, free rolling (FR) and driven (D) wheels including a 10% gradient (G). Temperature: 25°C, base stiffness: 200 MPa.

8.3.4 Embedment verification and validation

Components of major influence were selected to verify and validate the embedment output of the double seal models, against field data obtained by van Zyl (2015). These components include the seal size, binder application rates and the base stiffness. Texture depth results were normalised for comparison purposes as illustrated in Figure 8.35 for a 200 MPa base stiffness, which corresponds to a 4 mm ball penetration value in this study. Field data of G1 and G4 bases with respected ball penetration values of 1.75 mm and 2.5 mm were available for comparisons.

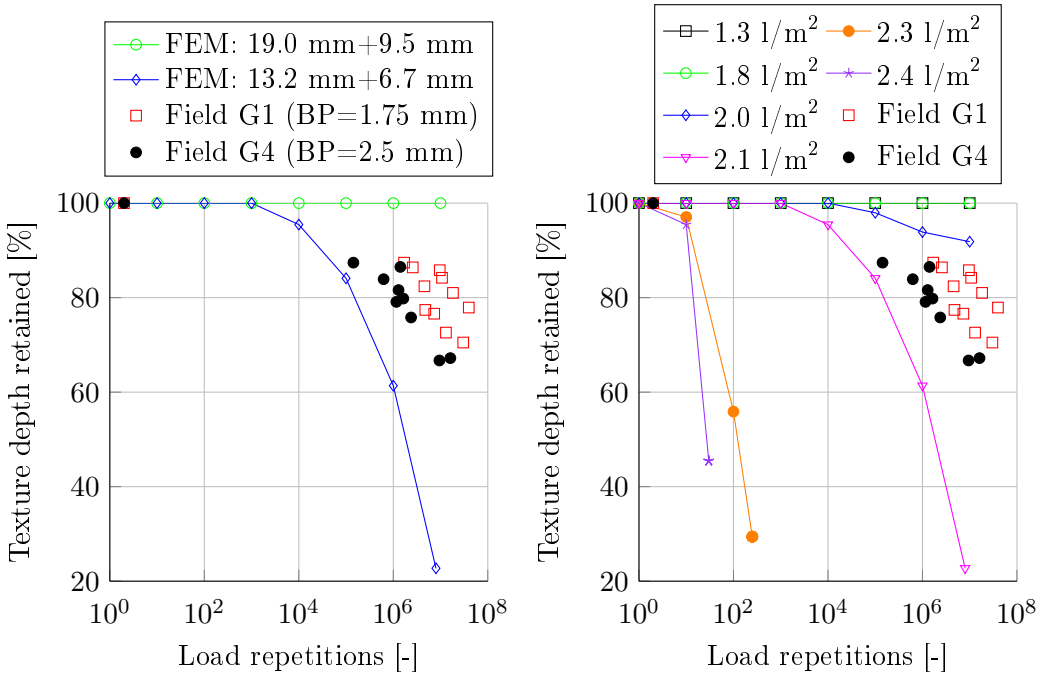

Figure 8.35: Validation of the FE seal model for various seal sizes and binder application rates with field data. Temperature: 25°C, base stiffness: 200 MPa, traffic load: 20 kN-800 kPa at 80 km/h.

A similar adjustment to van Zyl's traffic count was made as discussed in Section 7.3.4, with the exception of a new LV:HV equivalence factor as obtained in Section 8.3.3. The results are illustrated in Figure 8.35 which indicates the comparisons between the field data, seal sizes and binder application rates.

Even with different ball penetration values, the G1 and G2 field data has a close comparison and is nestled between the 13.2 mm + 6.7 mm double seals with binder application rates of 2.0 l/m^2 and 2.1 l/m^2 respectively. Figure 8.35 highlights sensitivity of double seals with respect to binder application rates. A more equitable comparison between the field data and FE model data is illustrated in Figure 8.36,

where the embedment development of models with different base stiffness are presented. Here, the 300 MPa base stiffness is equivalent to a ball penetration value of 2.8 mm, which almost matches the ball penetration value of the G4 material (2.5 mm). However, it is evident that the 300 MPa model in this example predicts less embedment than what was obtained in the field. It remains difficult to assess field data and deducing which portion of the retained surface depth can be attributed to embedment and which should be accredited to stone orientation. Therefore, considering the latter and the sensitivity of embedment to the initial surface texture, the double seal model illustrated that it ascertains surface texture values likened to the values obtained in the field.

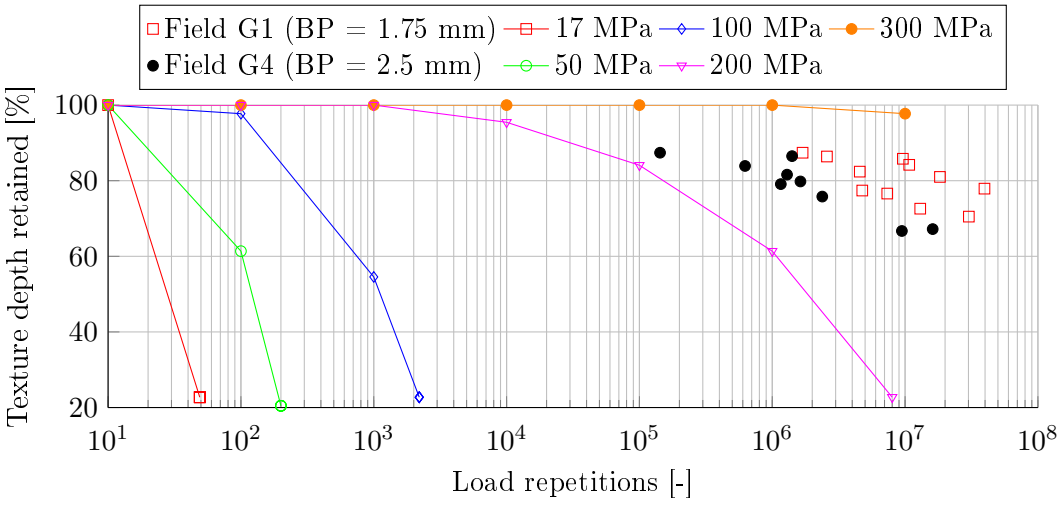

Figure 8.36: Validation of the FE seal model in terms of base stiffness with the field data. Temperature: 25°C, traffic load: 20 kN-800 kPa at 80 km/h.

8.4 Closure

Within the adhesive and cohesive failure trends, the same components significantly influenced the load repetitions to failure and were identified as two structural variables and two time related variables which are: the aggregate size, binder application rate, base stiffness and binder temperature respectively. These four components (Figure 8.37) highly dictates adhesive and cohesive stress responses, although a smaller magnitude of shear stress is generally obtained from the cohesive analysis in comparison to the adhesive analysis.

The embedment development in a double seal does not necessarily influence the surface texture as in the case of a single seal. In some cases a double seal is constructed with voids between the two aggregate layers i.e. tack coat and penetration coat.

During embedment developments these voids have to be filled before a reduction in the remaining surface texture occur. All the structural variables are therefore significant in forming the initial surface texture. The rate of embedment and thus the texture loss rate are highly dependent on the substrate strength and initial surface texture. The latter statement is also true for cape seals which are dealt with in the following chapter.

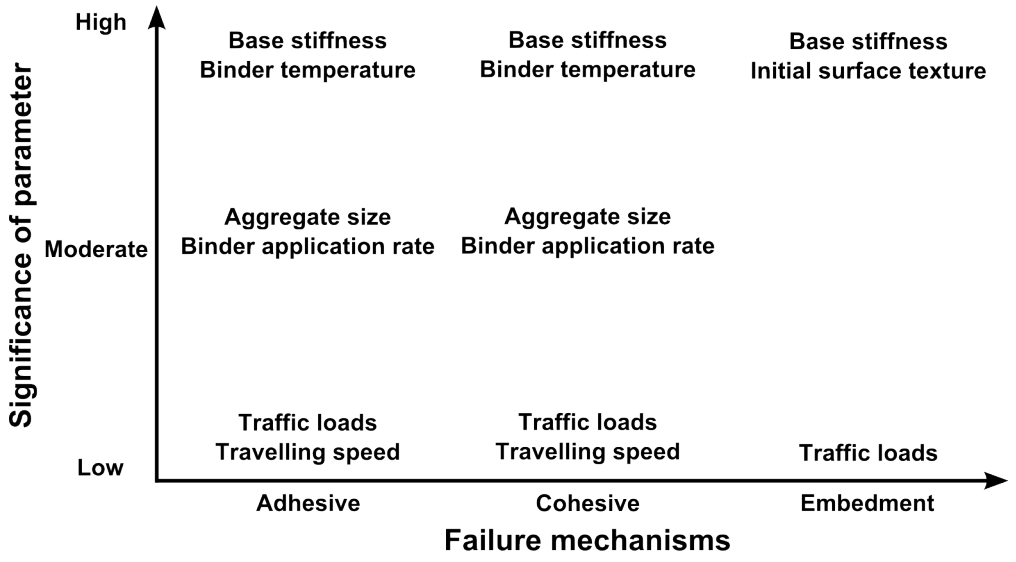

Figure 8.37: Level of parameter significance for double seals.

9. Cape seal analysis

A cape seal is a good alternative to a thin asphalt layer and is the recommended seal to accommodate high traffic volumes. The slurry is spread across the packed aggregates and worked into the voids where it is left to dry, resulting in a solid asphalt-like layer which provides adequate waterproofing to the substrate. This chapter illustrates and addresses the response and corresponding fatigue behaviour of the slurry in the cape seal models with reference to the failure mechanisms as defined in this study. It should be noted that the mortar characteristics as investigated in the Lifetime Optimisation Tool (LOT) project (Huurman, 2008) were assumed to represent the slurry in this study.

9.1 Adhesive failure

The adhesive failure analysis presents the equivalent tensile stress response and corresponding fatigue life calculations for the cape seal models, according to the primary variations as defined in Table 3.9. Here the slurry-aggregate bond strength is of interest and the equivalent tensile stress is the response parameter obtained in contrast to the shear stress (Figure 9.1) responses utilised in the single and double seal analyses. Although the adhesive failure validation was demonstrated for the single

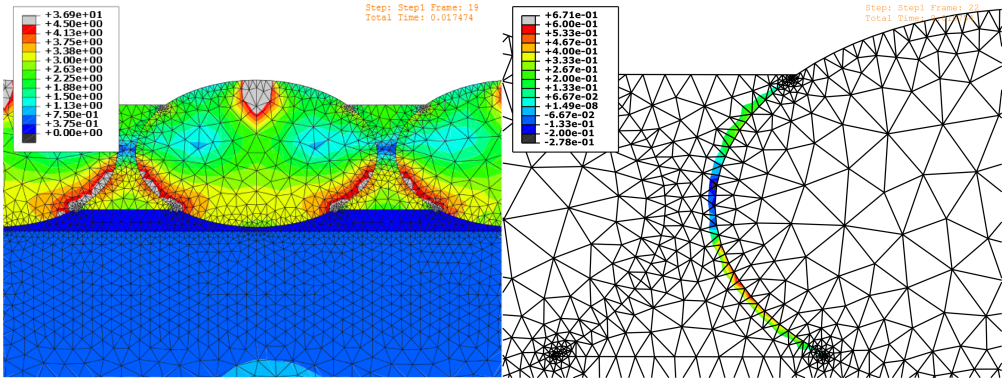

Figure 9.1: Screen grabs of the FE cape seal simulations (MPa): von Mises stress (left) and adhesive zone shear stress (right).

seal models, no field data was obtained for the cape seal analysis whereby it could be validated. Data from the LOT project was therefore utilised for comparisons.

9.1.1 Analysis of the structural variables

The structural variable simulations were all conducted with virgin 70-100 penetration grade tack coats at the corresponding temperatures. Application rates of 0.8 l/m^2 and 1.1 l/m^2 were selected for the 13.2 mm and 19.0 mm seal respectively. A first glance at the structural variations as illustrated in Figure 9.2, indicates that the 19.0 mm cape seal is more sensitive to a change in aggregate spread rate than the 13.2 mm cape seal. With an initial surface texture of 0.7 mm was, it is apparent that the 19.0 mm cape seal is also more prone to adhesive fatigue at spacings of 0.5 mm and 1.0 mm than larger spacings such as 2.0 mm and 4.0 mm. The latter two spacings give approximately similar results compared to the 13.0 mm cape seal analysis.

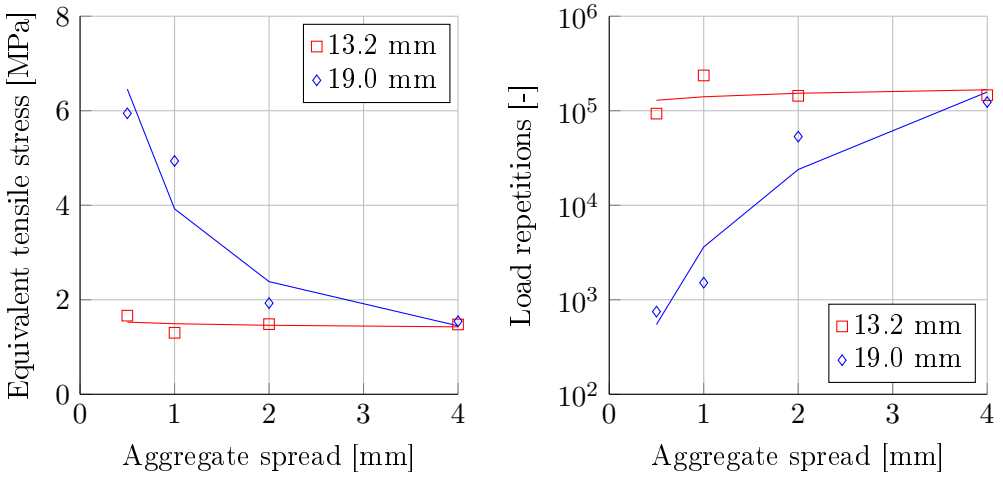

Figure 9.2: Equivalent tensile stress and corresponding load repetitions to failure for the 13.2 mm & 19.0 mm cape seals with virgin slurry and 0.7 mm surface texture. Temperature: 10°C, base stiffness: 200 MPa, traffic load: 20 kN-800 kPa at 80 km/h.

Reasons for the abrupt equivalent stress spikes obtained in Figure 9.2 are assessed in Figure 9.3, which illustrates the model response with changes to the initial surface texture. Distributing the wheel load (d-load) according to the calculations of Cesbron *et al.* (2008), resulted in applying a portion of the load to the aggregates and the remainder to the slurry. The outcome suggests that an over-filled cape seal is more prone to adhesive fatigue than an under-filled cape seal. The opposite however, is true for a concentrated load (c-load) analysis where the load is applied only to the aggregates. In this case the application of more slurry, increases the resistance to

adhesive fatigue. The position of the applied load in combination with the initial surface texture has a significant effect on the outcome of the structural response. In turn, the surface texture is affected by the aggregate spread rate and thus also the portion of load applied to the slurry. Less of an effect is obtained by adjusting the ALD of the aggregate as illustrated in Figure 9.4. The general trend indicates that the cape seal exhibits slightly more resistance to adhesive fatigue failure as the ALD decreases from 9 *mm* to 6 *mm* for a 13.2 *mm* seal.

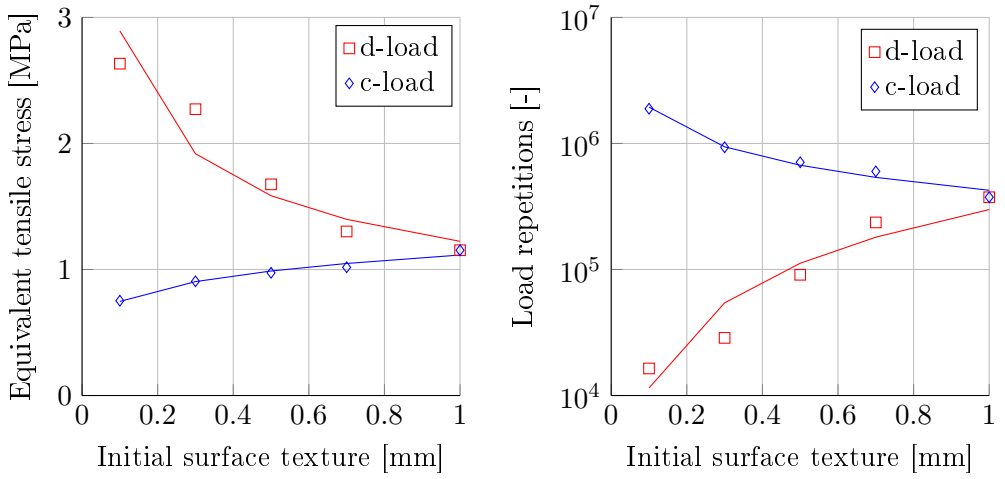

Figure 9.3: Equivalent tensile stress and corresponding load repetitions to failure for the 13.2 mm (8 mm ALD) cape seal with virgin slurry and initial surface textures. Temperature: 10°C, base stiffness: 200 MPa, traffic load: 20 kN-800 kPa at 80 km/h.

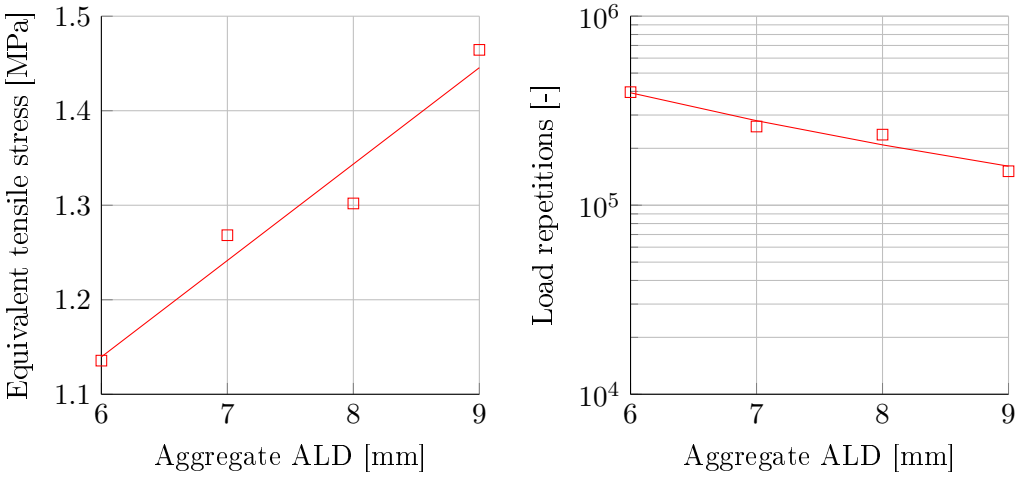

Figure 9.4: Equivalent tensile stress and corresponding load repetitions to failure for the 13.2 mm cape seal with virgin slurry and 0.7 mm surface texture. Temperature: 10°C, base stiffness: 200 MPa, traffic load: 20 kN-800 kPa at 80 km/h.

9.1.2 Analysis of the time related variables

During the LOT project (Huurman, 2008) equivalent tensile stress transfer functions were developed for mortar temperatures ranging from $0°C$ to $20°C$. Application of these transfer functions with respect to the slurry of cape seals is illustrated in Figure 9.5. Increasing temperatures reduce the equivalent tensile stress which is intuitive since, bituminous material exhibits greater stiffness in colder conditions. Greater stiffness results in greater resistance i.e. more load repetitions to adhesive fatigue on moderate to strong bases. However, weak bases result in fewer load repetitions to fatigue at lower temperatures compared to higher temperatures.
Figure 9.5 further indicates the sensitivity of adhesive fatigue with a change in base stiffness. A reduction in the equivalent tensile stress is observed with an increase in base stiffness. This in turn results in an increase of load repetitions to failure. A notable increase in the number of load repetitions to adhesive failure is observed for a slurry at $0°C$ with a base stiffness of 300 MPa.

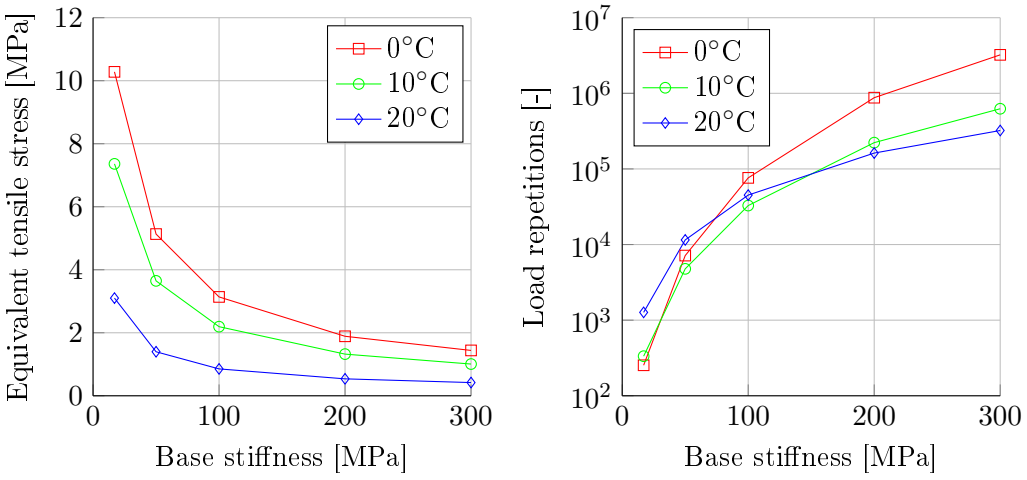

Figure 9.5: Dissipated energy and corresponding load repetitions to failure for the 13.2 mm (8 mm ALD) cape seal with virgin slurry and a 0.7 mm initial surface texture. Traffic load: 20 kN-800 kPa at 80 km/h.

Apart from the temperature, a factor such as the slurry age also affects the bond strength as illustrated in Figure 9.6. The PAV aging protocol exhibits a reduction in the equivalent tensile stress, compared to the virgin slurry. It results therefore in a greater number of load repetitions to failure in comparison to its counterpart, which suggests that the slurry-aggregate bond strengthens with time. This phenomenon is in accordance with the findings of the LOT program, where the adhesive service life span increases with time (Huurman, 2008).

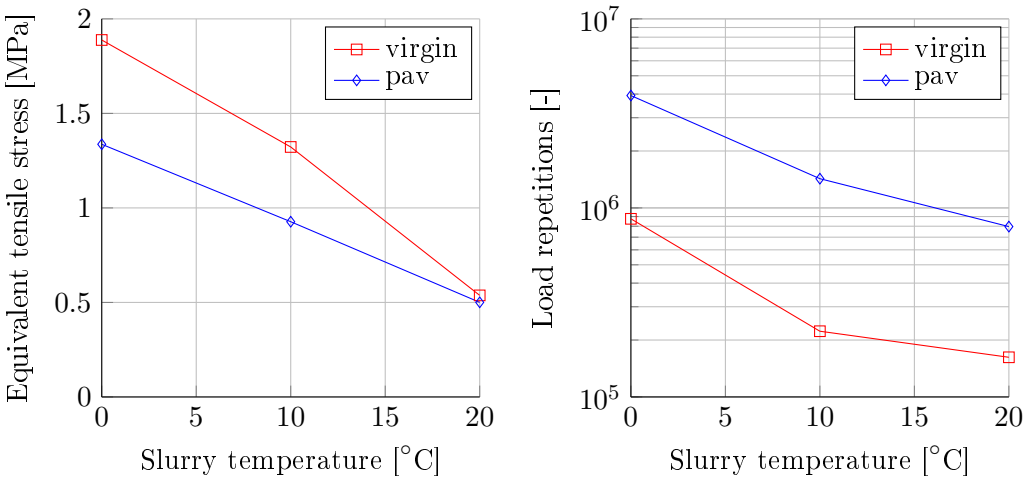

Figure 9.6: Equivalent tensile stress and corresponding load repetitions to failure for the 13.2 mm (8 mm ALD) cape seal with an initial surface texture of 0.7 mm. Base stiffness: 200 MPa, traffic load: 20 kN-800 kPa at 80 km/h.

9.1.3 Analysis of the traffic load variables

The tyre contact patch distributes the vertical load across the asperities of the seal aggregate and surface of the slurry. It is again illustrated in Figure 9.7 that the tyre contact stress rather than the magnitude of the vertical load has greater significance when investigating load-associated influences that result in adhesive fatigue. An increase in tyre contact stress results in a dramatic reduction in the number of load repetitions to failure.

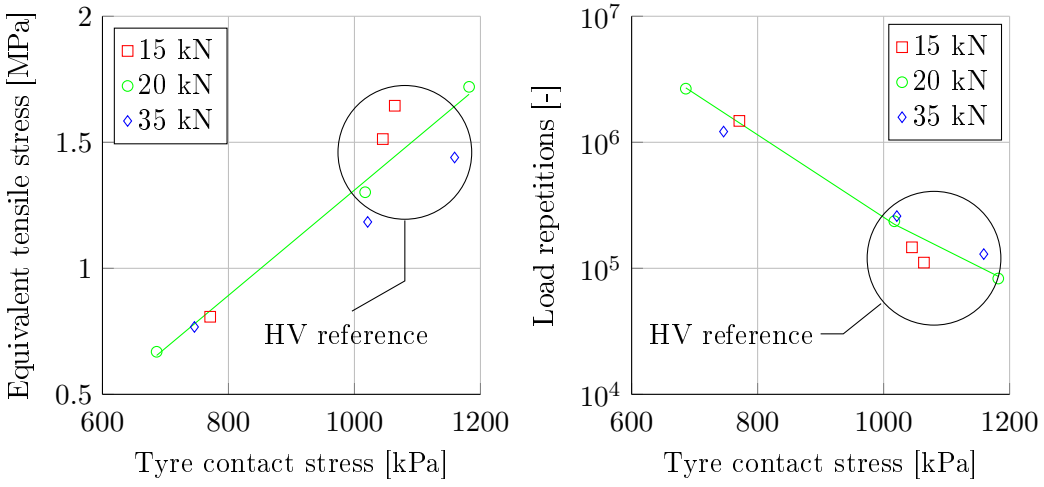

Figure 9.7: Equivalent tensile stress and corresponding load repetitions to failure for the 13.2 mm (8 mm ALD) cape seal with virgin slurry and 0.7 mm surface texture. Temperature: 10°C, base stiffness: 200 MPa.

The number of load repetitions to failure for light vehicle (LV) and heavy vehicle (HV) wheel loads at $10°C$ is illustrated in Figure 9.8. Similar to the previous chapters, the 20 kN-800 kPa HV wheel load represents an E80 and is the reference HV wheel load in this study. The reference HV wheel load induces 160 times more damage than the average LV wheel load. The range of equivalent LV:HV damage ratios is summarised in Table 9.1, and indicates large variance. Table 9.1 suggests that a cape seal is significantly more susceptible to adhesive damage when subjected to high contact stresses, i.e. HV loads.

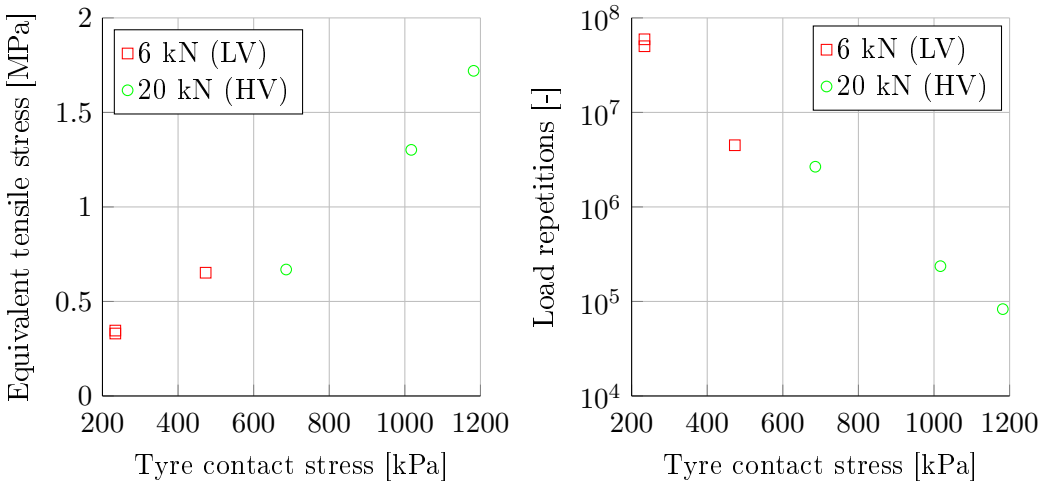

Figure 9.8: Equivalent tensile stress and corresponding load repetitions to failure for the 13.2 mm cape seal, virgin slurry, 0.7 mm surface texture with LV and HV wheel loads. Temperature: 10°C, base stiffness: 200 MPa.

Axle travelling speed has a slight influence on the equivalent tensile stress within the slurry-aggregate bond as illustrated in Figure 9.9. The equivalent tensile stress increased rapidly with increased speeds ranging from 5 km/h to 20 km/h. A further increase in speed results in approximately similar magnitudes of equivalent tensile stress, therefore reaching a plateau. The number of load repetitions to failure continue to increase from 20 km/h to 80 km/h since the loading time has a significant effect on the fatigue calculation. A longer loading time results in greater slurry damage when subject to the same magnitude of load.

A cape seal with 0.7 mm initial surface texture does respond slightly different to various rolling wheel motions as illustrated in Figure 9.10. The equivalent tensile stresses of a free rolling (FR) wheel, free rolling wheel including a 10% gradient (FR+G) and a driven wheel (D) are virtually similar. The exception is a driven wheel on a 10% incline. The latter load case results in a slight increase in the equivalent tensile stress and thus a reduction in the load repetitions to failure.

Table 9.1: Equivalent LV:HV damage ratios as illustrated in Figure 9.8.

Load case description	LV load reps. to failure	HV load reps. to failure	LV:HV ratio
Maximum LVs and minimum HVs	59.37E+06	0.83E+05	715 : 1
Minimum LVs and maximum HVs	4.5E+06	2.66E+06	1.7 : 1
Average LVs and E80 ref HVs	38.0E+06	2.36E+05	160 : 1

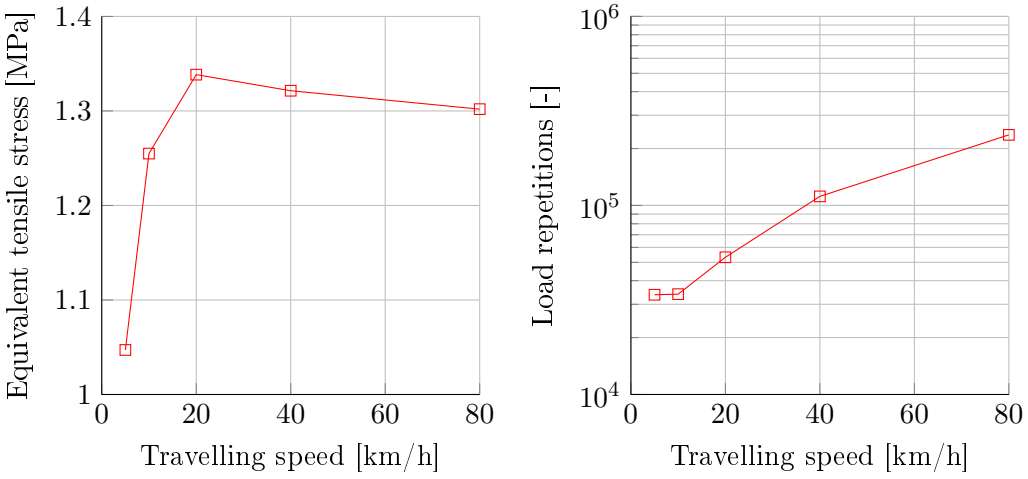

Figure 9.9: Equivalent tensile stress and corresponding load repetitions to failure for the 13.2 mm cape seal, virgin slurry, 0.7 mm initial surface texture. Temperature: 10°C, base stiffness: 200 MPa, traffic load: 20 kN-800 kPa.

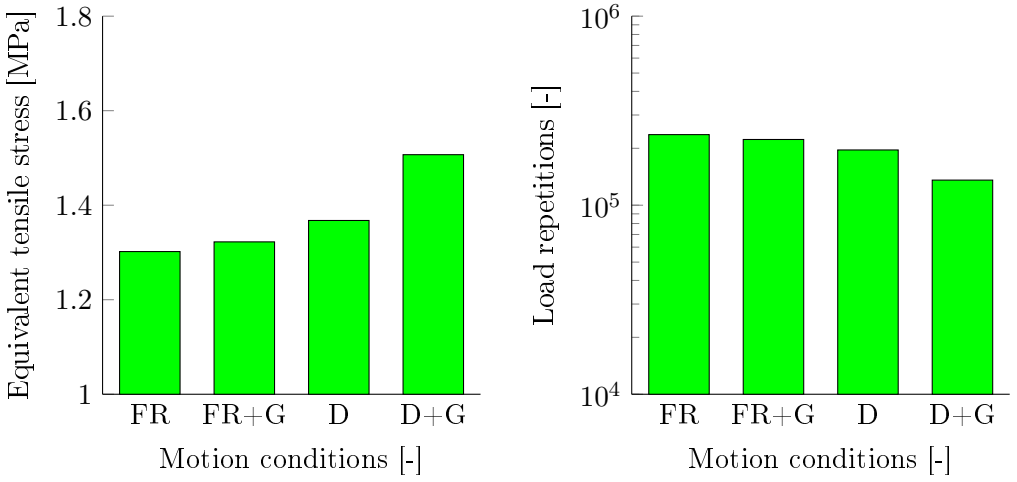

Figure 9.10: Equivalent tensile stress and corresponding load repetitions to failure for the 13.2 mm (8 mm ALD) cape seal, virgin slurry and a 0.7 mm surface texture. Temperature: 10°C, base stiffness: 200 MPa, traffic load: 20 kN-800 kPa at 80 km/h.

9.1.4 Adhesive failure verification and validation

Aggregate loss is not a major concern in practice on cape seals and since no field data was obtained to verify the adhesive fatigue results, the validation process included data emanating from the LOT project. Table 9.2 presents the results of the cape seal and Porous Asphalt Concrete (PAC) models subjected to similar loading conditions.

Table 9.2: Cape seal and LOT (Huurman, 2008) PAC model comparisons at 10°C.

Model type and age	D_1	N_f
Cape seal (13.2 mm) virgin slurry	4.2E-06	2.36E+05
PAC (6.0 mm) virgin mortar	2.4E-08	4.20E+07
Cape seal (13.2 mm) PAV slurry	7.1E-07	1.46E+06
PAC (6.0 mm) PAV mortar	1.5E-08	6.70E+07

Although the structures differ in their meso-scale compositions, base support and size, the exact parameters of the mortar were used in defining the slurry. In both instances the PAV models result in a greater number of load repetitions to failure N_f in comparison to the respected virgin models. The cape seal FE models, consisting of a greater aggregate size, has a higher initial fatigue rate D_1 in comparison to the PAC model which consists of smaller aggregates. A similar trend was observed in Figure 9.2 between the 19.0 mm and 13.2 mm cape seal models.

9.2 Cohesive failure

The layout of the cohesive fatigue analysis is identical to the adhesive fatigue analysis, with the exception that damage parameters for the cohesive analysis are only valid for temperatures ranging from $0°C$ to $10°C$ (Huurman, 2008). The dissipated energy response of the slurry and corresponding load repetitions to cohesive failure are presented and discussed according to the primary seal model variations as defined in this study. Figure 9.11 illustrates the positions of the stress and strain development.

9.2.1 Analysis of the structural variables

In considering the aggregate nominal size and spread rate, Figure 9.12 indicates a reduction in the dissipated energy with an increase in the aggregate spread rate. Higher dissipated energy results are observed for the larger 19.0 mm cape seal in comparison to the 13.2 mm cape seal. The latter seal endures more load applications to failure than the 19.0 mm cape seal and is therefore considered more durable than the 19.0 mm cape seal.

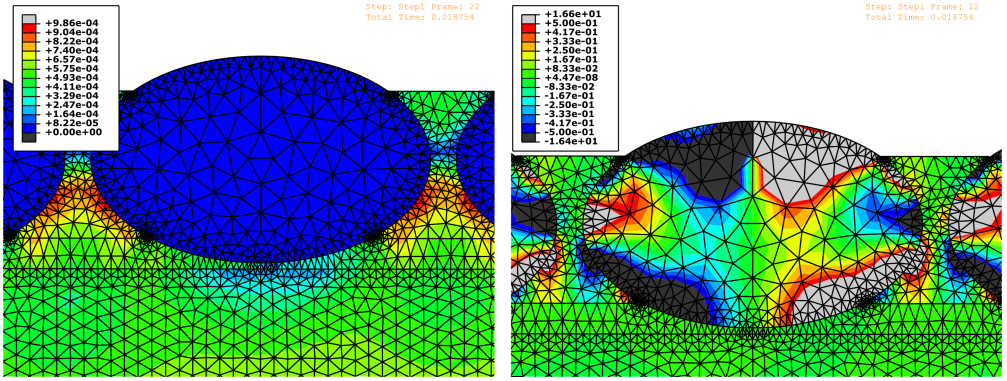

Figure 9.11: Screen grabs of the FE cape seal simulations: maximum principal strain ϵ_1 (left) and shear stress σ_{12} in MPa (right).

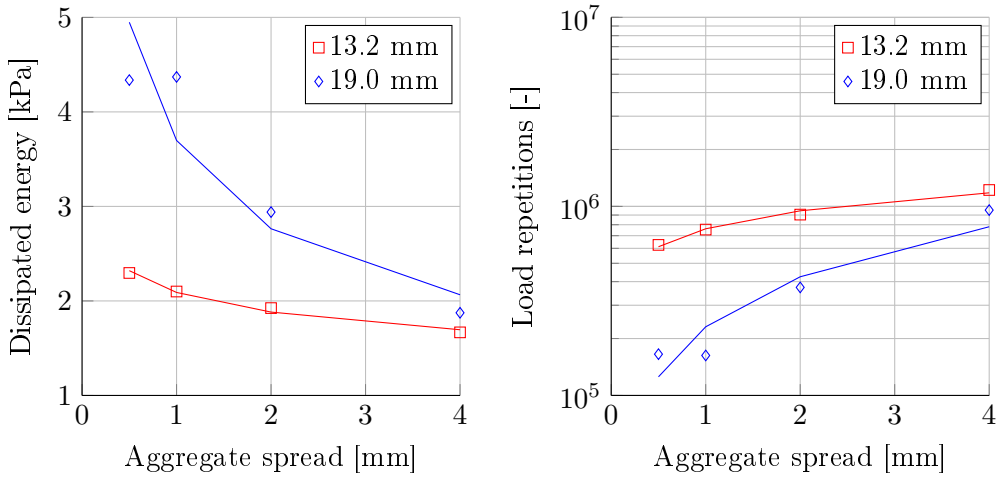

Figure 9.12: Dissipated energy and corresponding load repetitions to failure for the 13.2 mm & 19.0 mm cape seals with virgin slurry and 0.7 mm surface texture. Temperature: 10°C, base stiffness: 200 MPa, traffic load: 20 kN-800 kPa at 80 km/h.

Another aggregate size factor such as the ALD does, to a reasonable extent, influence the load repetitions to failure when the aggregate becomes elongated as illustrated in Figure 9.13. An increase in the dissipated energy is observed for an increase in the aggregate ALD. Larger ALDs i.e. more cubical aggregates, result in a lower number of load repetitions to failure while the number load repetitions to failure increases as the aggregates become more elongated.

When assessing the effect of initial surface texture on the dissipated energy response, Figure 9.14 clearly indicates a difference in results for models that are subjected to a distributed load (d-load) compared to a concentrated load (c-load). The concentrated load has a minimal effect on the dissipated energy response, while the distributed load results in a significant dissipated energy increase with a reduction in initial

surface texture. Since the latter loading case was implemented for the cape seal model simulations, it suggests that an over-filled cape seal has a greater fatigue rate than an under filled cape seal and will result in fewer load repetitions to failure.

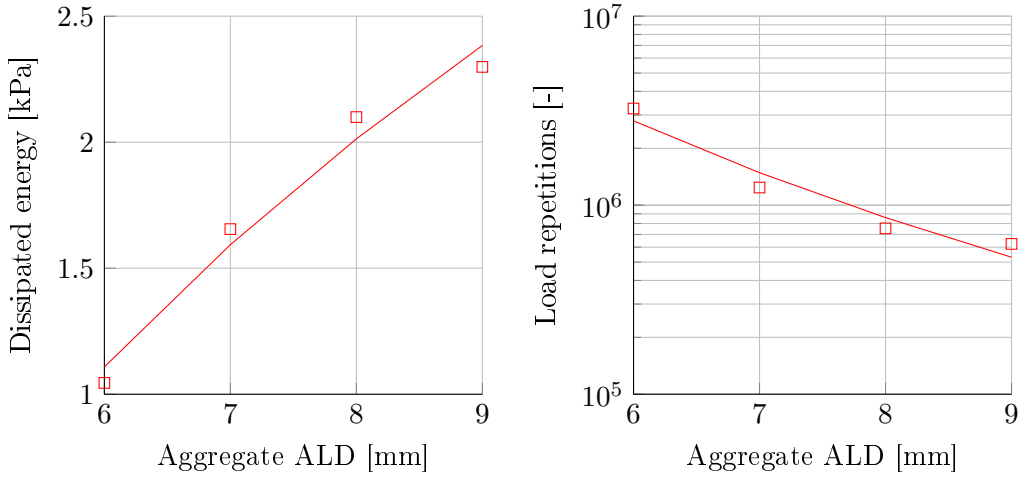

Figure 9.13: Dissipated energy and corresponding load repetitions to failure for the 13.2 mm cape seal with virgin slurry and a 0.7 mm initial surface texture. Temperature: 10°C, base stiffness: 200 MPa, traffic load: 20 kN-800 kPa at 80 km/h.

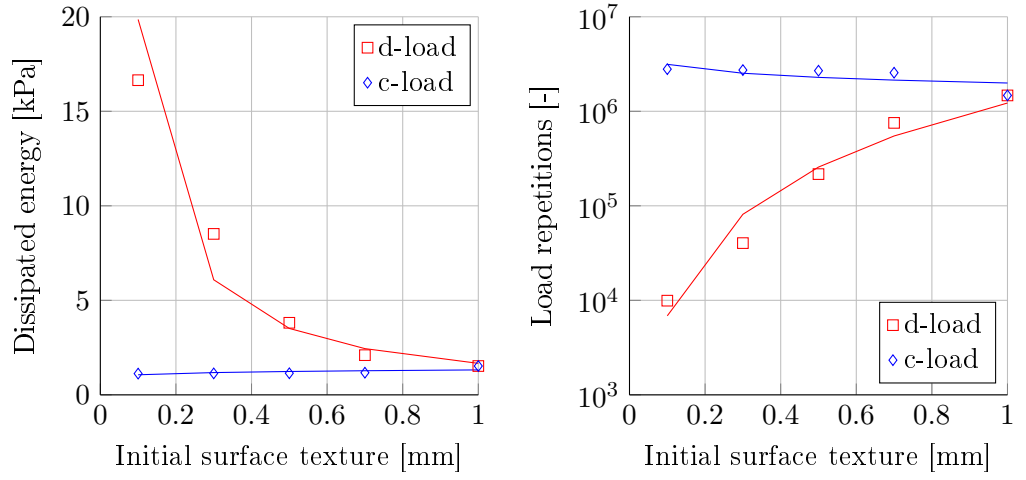

Figure 9.14: Dissipated energy and corresponding load repetitions to failure for the 13.2 mm (8 mm ALD) cape seal with virgin slurry and initial surface textures. Temperature: 10°C, base stiffness: 200 MPa, traffic load: 20 kN-800 kPa at 80 km/h.

9.2.2 Analysis of the time related variables

The base stiffness and material temperature have consistently been amongst the variables in this study that had major effects on the fatigue performances of the seal models. Illustrated in Figure 9.15, it is again evident that the base stiffness significantly influences the dissipated energy response, while the temperature is not as significant, but still noteworthy in comparison to the other structural variables (Figure 9.16).

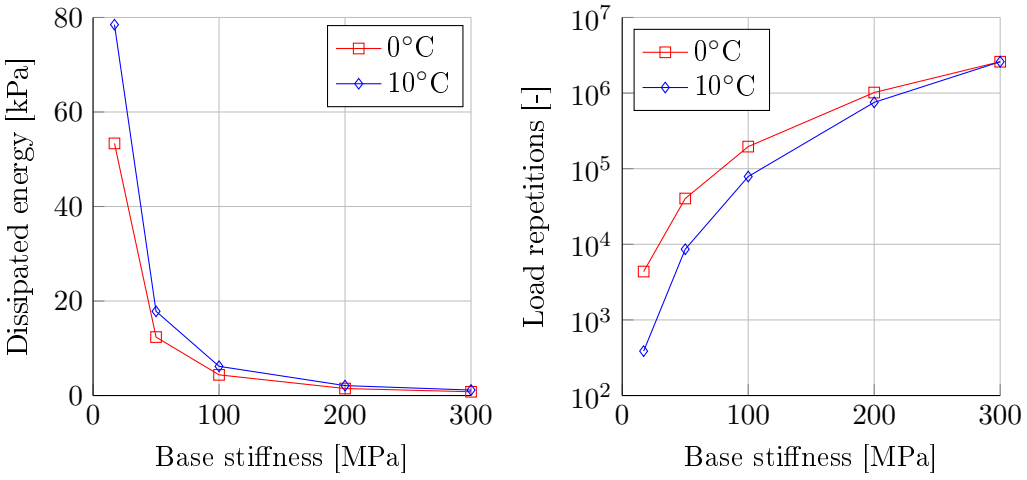

Figure 9.15: Dissipated energy and corresponding load repetitions to failure for the 13.2 mm (8 mm ALD) cape seal with virgin slurry and a 0.7 mm initial surface texture. Traffic load: 20 kN-800 kPa at 80 km/h.

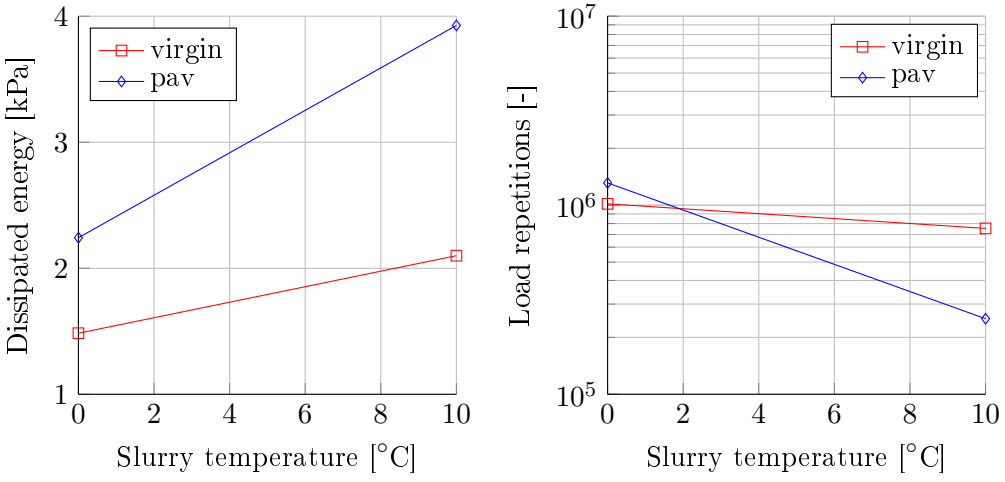

Figure 9.16: Dissipated energy and corresponding load repetitions to failure for the 13.2 mm (8 mm ALD) cape seal with an initial surface texture of 0.7 mm. Base stiffness: 200 MPa, traffic load: 20 kN-800 kPa at 80 km/h.

A reduction in the base stiffness results in a greater fatigue rate and thus a reduction in the number of load repetitions to failure. A reduction in temperature has the opposite effect and results in an increase in the number of load repetitions to cohesive fatigue failure. When the slurry age is considered, Figure 9.16 illustrates that the PAV aged slurry responds with greater dissipated energy results in comparison to the virgin slurry and in both cases an increase in the dissipated energy is observed with an increase in temperature. A similar trend is observed for the PAC models (Huurman, 2008) and suggests that aged slurry exhibits a greater fatigue rate than virgin slurry at $10°C$.

9.2.3 Analysis of the traffic load variables

The traffic load variables are defined as the variety of traffic loads to which a road is subject. Similar to the adhesive fatigue analysis, the cohesive fatigue analysis also indicates that the tyre contact stress dictates the response of the seal structure when compared to the vertical wheel load as illustrated in Figure 9.17. An increase in the tyre contact stress results in an increase in the dissipated energy obtained in the slurry beneath the centre of the tyre contact patch. The increase in dissipated energy results in a reduction in the number of load applications to cohesive fatigue failure.

With the introduction of LVs, Figure 9.18 illustrates that tyre contact stress continues to dictate the dissipated energy response and results in an equivalent LV:HV damage factor of approximately 260:1. Table 9.1 summarises the range of the equivalent damage factors as presented in Figure 9.18. The range in Table 9.3 is approximately

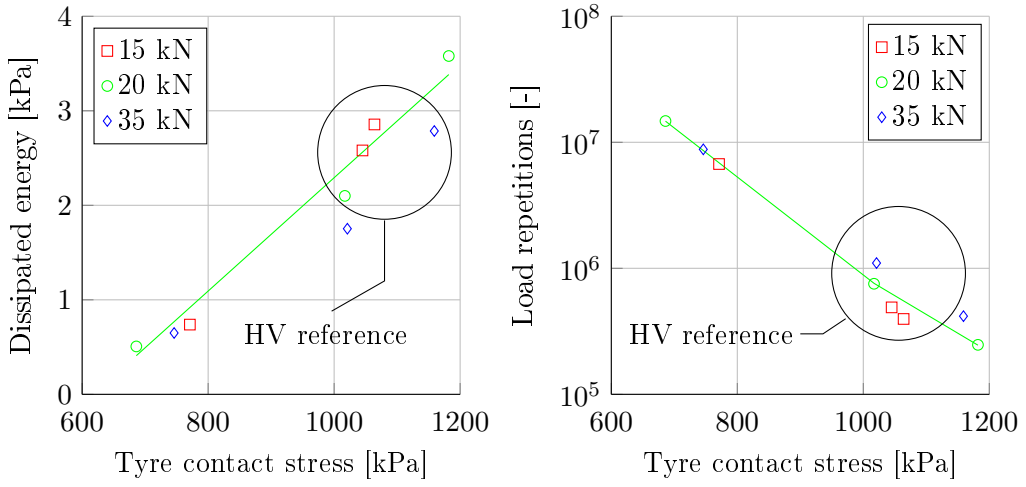

Figure 9.17: Dissipated energy and corresponding load repetitions to failure for the 13.2 mm (8 mm ALD) cape seal with virgin slurry and 0.7 mm surface texture. Temperature: 10°C, base stiffness: 200 MPa.

double in magnitude compared to the range in Table 9.1, while the number of cohesive load repetitions to failure exceed the number of adhesive load repetitions to failure. This suggests that cracks around the aggregate-slurry interface would occur prior to slurry fatigue cracks for the FE modelled cases.

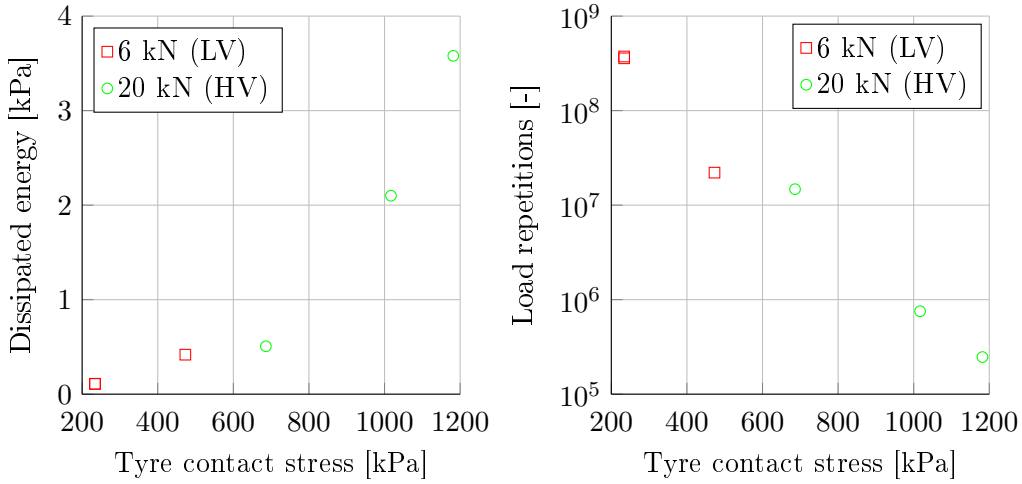

Figure 9.18: Dissipated energy and corresponding load repetitions to failure for the 13.2 mm cape seal, virgin slurry, 0.7 mm surface texture with LV and HV wheel loads. Temperature: 10°C, base stiffness: 200 MPa.

Table 9.3: Equivalent LV:HV damage ratios as illustrated in Figure 9.18.

Load case description	LV load reps. to failure	HV load reps. to failure	LV:HV ratio
Maximum LVs and minimum HVs	37.38E+07	2.47E+05	1500 : 1
Minimum LVs and maximum HVs	2.21E+07	14.75E+06	1.5 : 1
Average LVs and E80 ref HVs	25.12E+07	7.54E+05	330 : 1

Vehicle speed is also a significant traffic load factor as illustrated in Figure 9.19. An increase in travelling speed caused a reduction in the dissipated energy. This was mainly attributed to the viscoelastic response nature of the slurry which resulted in an increase in the load repetitions to failure.

Wheel motion conditions however, do not significantly influence the dissipated energy response in comparison to the travel speed as illustrated in Figure 9.20. A free rolling (FR) wheel, a free rolling wheel on a 10% incline (FR+G) and a driven wheel (D) responded very similarly. A driven wheel on an incline with a gradient of 10% (D+G) indicated a slight increase in the dissipated energy and therefore reflects a reduction in the number of load applications to cohesive fatigue failure.

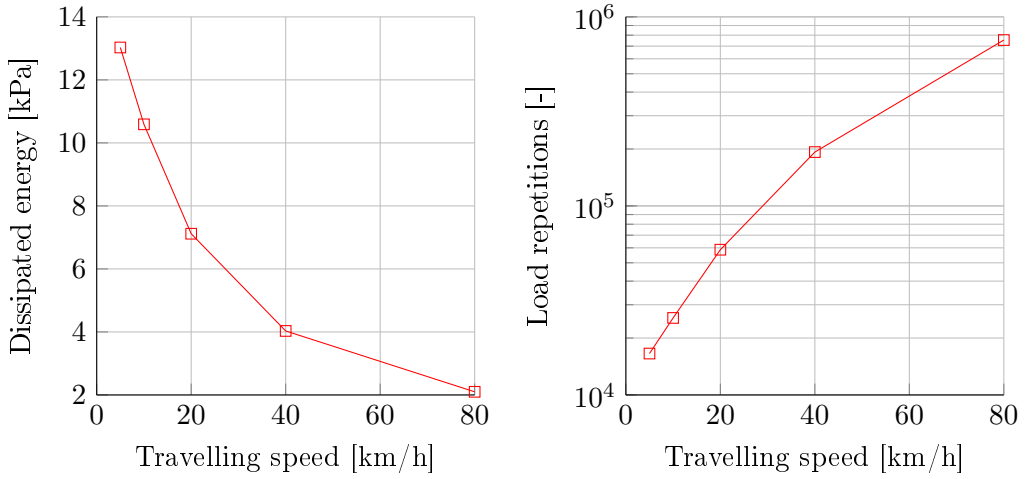

Figure 9.19: Dissipated energy and corresponding load repetitions to failure for the 13.2 mm cape seal, virgin slurry, 0.7 mm surface texture. Temperature: 10°C, base stiffness: 200 MPa, traffic load: 20 kN-800 kPa.

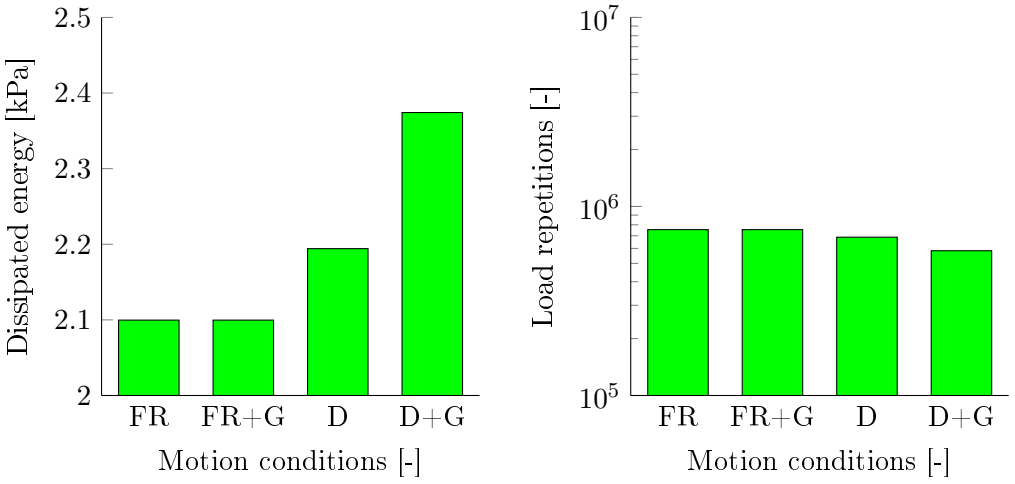

Figure 9.20: Dissipated energy and corresponding load repetitions to failure for the 13.2 mm (8 mm ALD) cape seal, virgin slurry and a 0.7 mm surface texture. Temperature: 10°C, base stiffness: 200 MPa, traffic load: 20 kN-800 kPa at 80 km/h.

9.2.4 Cohesive failure verification and validation

Fatigue cracking is a major concern in practice on cape seals and though van Zyl (2015) developed a cape seal trigger line, healing factor adjustments of the response data is required. The results are at best only an indication and therefore this section includes data emanating from the LOT (Huurman, 2008) project to verify the adhesive fatigue results. Table 9.4 presents the results of the cape seal and Porous Asphalt Concrete (PAC) models subjected to similar loading conditions.

Table 9.4: Cape seal and LOT (Huurman, 2008) PAC model comparisons at 10°C.

Model type and age	W_{in}	N_f
Cape seal (13.2 mm) virgin slurry	2.10	7.54E+05
PAC (6.0 mm) virgin mortar	0.24	7.40E+07
Cape seal (13.2 mm) PAV slurry	3.93	2.51E+05
PAC (6.0 mm) PAV mortar	0.69	1.70E+07

Although the structures differ in their meso-scale compositions, base support and size, the exact parameters of the mortar were used in defining the slurry. In both instances the virgin models result in a greater number of load repetitions to failure N_f when compared to the respected PAV models. The cape seal model consists of greater aggregate sizes and exhibits greater initial dissipated energy W_{in} in comparison to the PAC model which consists of smaller aggregates. A similar trend was observed in Figure 9.12 between the 19.0 mm and 13.2 mm cape seal models.

9.3 Embedment failure

The embedment failure analysis presents the base deflection response (Figure 9.21) and corresponding load repetitions to failure, according to the primary variations as defined in this study. Failure is defined in terms of retained surface texture where the TRH3 (2007) stipulates a minimum surface macro texture of 0.7 mm, but makes provision for cases with surface textures of 0.5 mm to 0.3 mm. No surface texture data was collected by van Zyl (2015) for cape seals, therefore this chapter does not present an embedment verification and validation section.

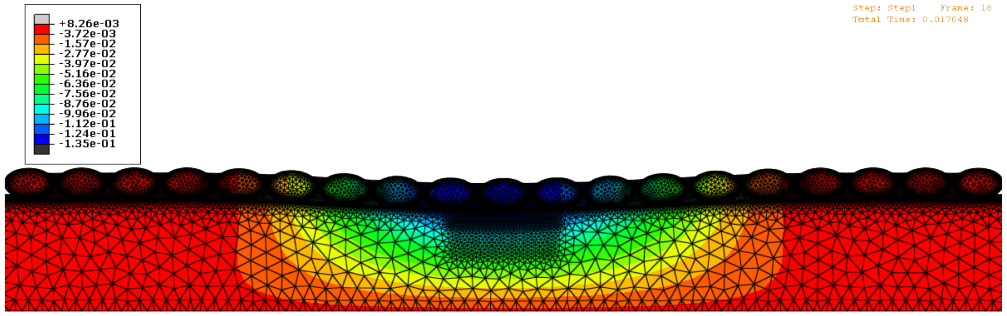

Figure 9.21: Screen grab of the FE cape seal simulation: exaggerated vertical deflection (mm) displaying the radius of curvature.

9.3.1 Analysis of the structural variables

An increase in the aggregate spread rate generally results in an increase in the vertical deflection as illustrated in Figure 9.22 for the 13.2 *mm* cape seal, however the 19.0 *mm* cape seal does not yield a clear trend with an increase in the aggregate spread rate. The response phenomenon is contrary to expectation, but is adequately reflected in the number of load repetitions to embedment failure where a minimum remaining surface 0.1 *mm* was selected as the failure criterion. In the case where this criterion is not reached, the remaining surface texture after 10 million load applications is presented.

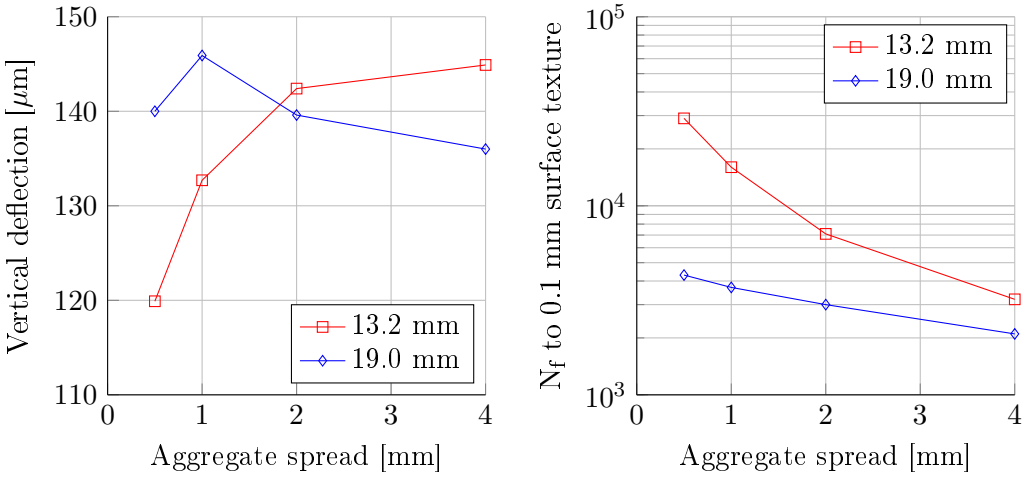

Figure 9.22: Vertical deflection and corresponding load repetitions to failure for the 13.2 mm & 19.0 mm cape seals with virgin slurry and 0.7 mm surface texture. Temperature: 10°C, base stiffness: 200 MPa, traffic load: 20 kN-800 kPa at 80 km/h.

Both seal sizes were constructed with an initial surface texture of 0.7 *mm* and Figure 9.22 indicates that the 19.0 *mm* seal exhibits a greater embedment rate than the 13.2 *mm* seal. A reduction in the number of load repetitions is observed for an increase in the spread rate. This suggests that an open spread seal structure is more susceptible to embedment than an interlocked structure. The shape of the aggregate also affects the embedment rate as illustrated in Figure 9.23. Elongated aggregates i.e. a reduction in the ALD for the same nominal size aggregate, result in a reduction of the vertical deflection which explains the increase in the number of load repetitions to embedment failure.

It is intuitive to expect a greater surface texture to result in an increase in the number of load repetitions to failure, as is the case in Figure 9.24. Although there are major dissimilarities in the vertical deflection, no significant difference in the number of load applications to failure was observed by applying a distributed load (d-load)

in comparison to a concentrated load (c-load). The number of load repetitions to failure increases significantly with an increase in the initial surface texture.

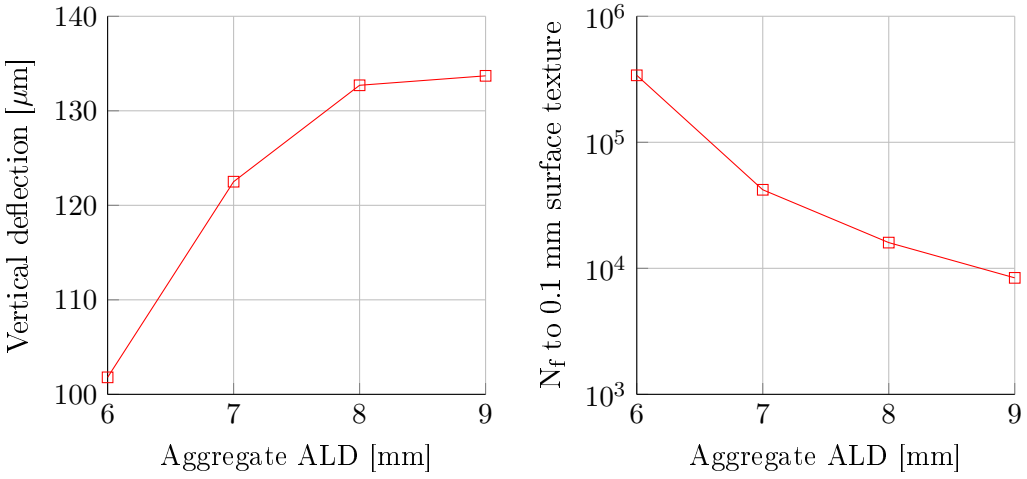

Figure 9.23: Vertical deflection and corresponding load repetitions to failure for the 13.2 mm cape seal with virgin slurry and a 0.7 mm initial surface texture. Temperature: 10°C, base stiffness: 200 MPa, traffic load: 20 kN-800 kPa at 80 km/h.

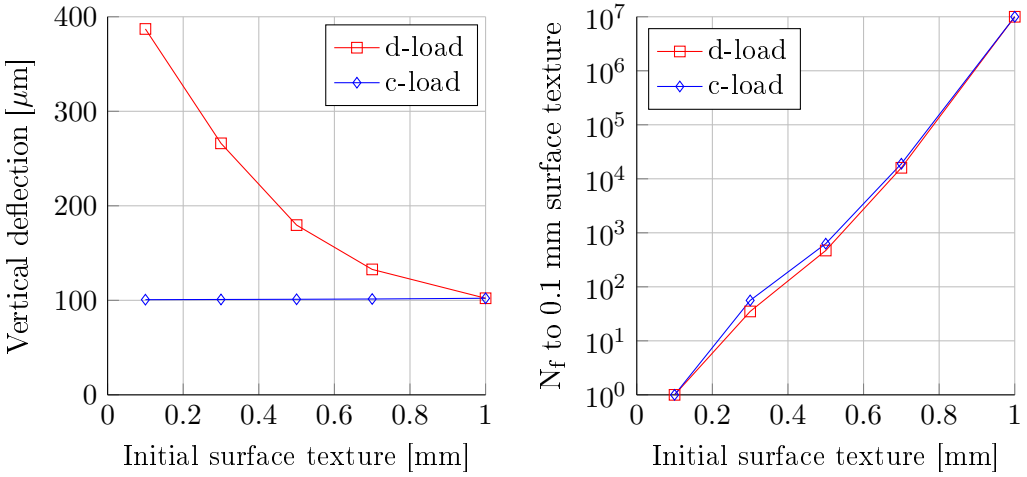

Figure 9.24: Vertical deflection and corresponding load repetitions to failure for the 13.2 mm (8 mm ALD) cape seal with virgin slurry and initial surface textures. Temperature: 10°C, base stiffness: 200 MPa, traffic load: 20 kN-800 kPa at 80 km/h.

9.3.2 Analysis of the time related variables

When considering the effects of time affected variables, the base stiffness of a granular layer and not the slurry temperature dictates the embedment rate as illustrated

in Figure 9.25. Although embedment occurs within a 200 load repetitions for a base stiffness below 100 MPa a dramatic increase in the number of load repetitions to failure is observed for a base stiffness of 200 MPa to 300 MPa. The slurry temperature and age however, has almost no effect on the embedment rate as illustrated in Figure 9.26. Although slight differences are observed in the vertical deflections of the virgin and PAV slurry ages, no variations are observed in the respective number of load repetitions to failure.

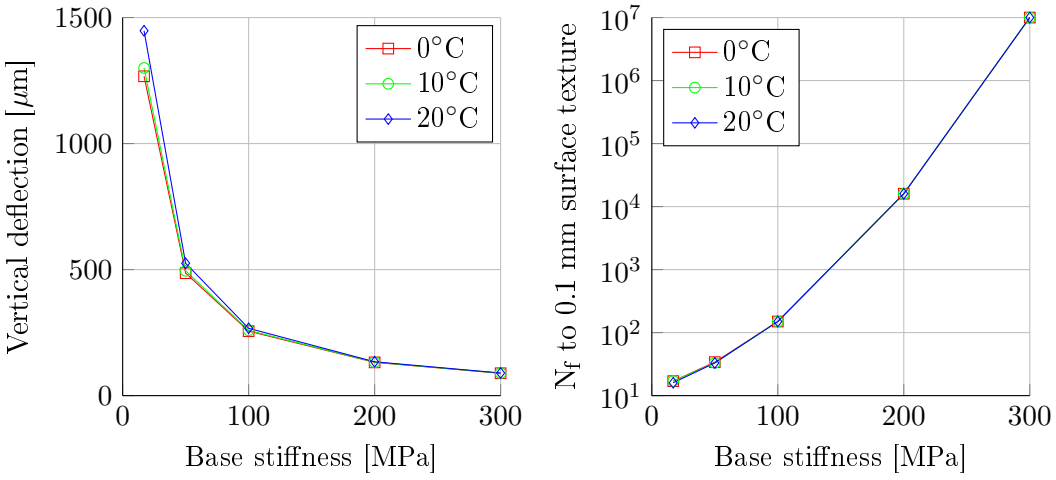

Figure 9.25: Vertical deflection and corresponding load repetitions to failure for the 13.2 mm (8 mm ALD) cape seal with virgin slurry and a 0.7 mm initial surface texture. Traffic load: 20 kN-800 kPa at 80 km/h.

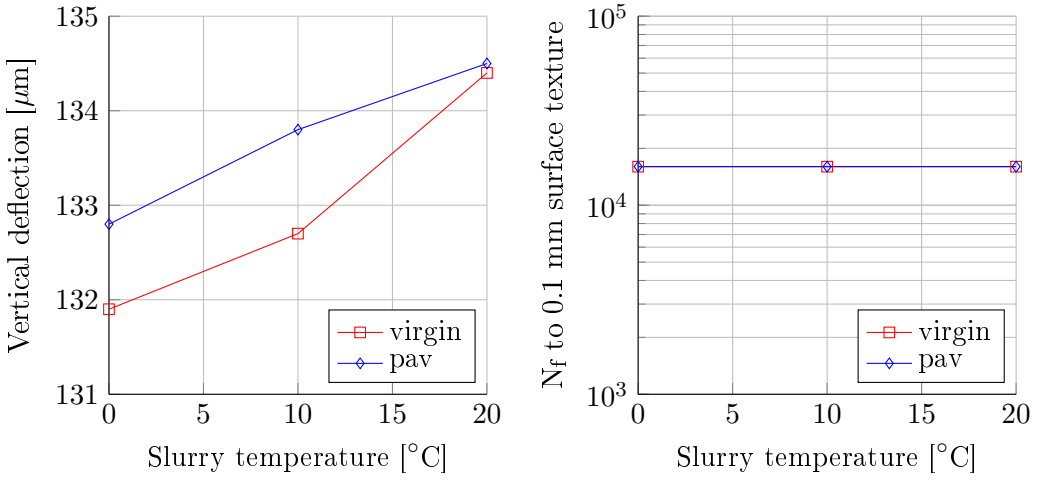

Figure 9.26: Vertical deflection and corresponding load repetitions to failure for the 13.2 mm (8 mm ALD) cape seal with an initial surface texture of 0.7 mm. Base stiffness: 200 MPa, traffic load: 20 kN-800 kPa at 80 km/h.

9.3.3 Analysis of the traffic load variables

The vertical deflection parameter as illustrated in Figure 9.27 is governed by the tyre contact stress rather than the vertical wheel load. Similar observations were made for the adhesive and cohesive analyses. The vertical deflection surges as the tyre inflation pressure increases. This in turn results in a reduction in the number of load repetitions to embedment failure. The reduction however, is not as dramatic as oppose to a change in the base stiffness.

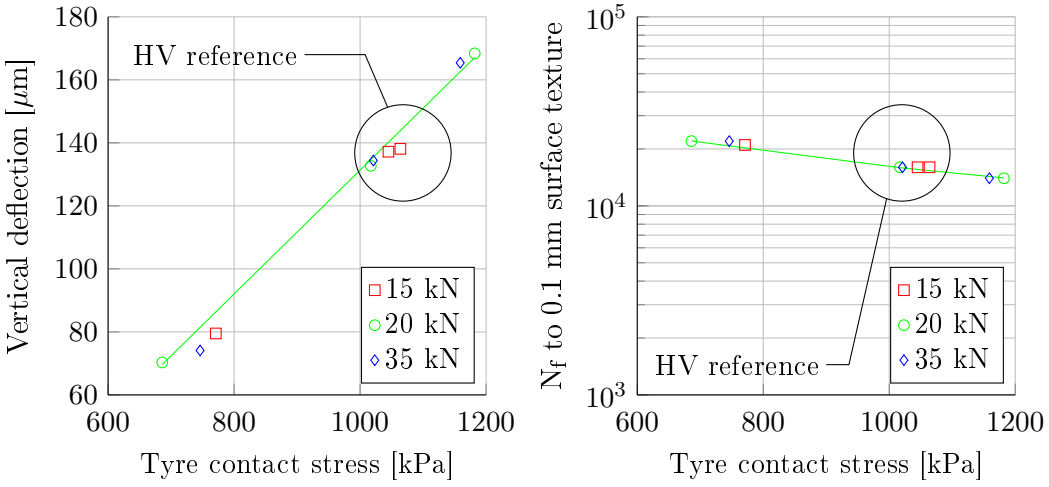

Figure 9.27: Vertical deflection and corresponding load repetitions to failure for the 13.2 mm (8 mm ALD) cape seal with virgin slurry and 0.7 mm surface texture. Temperature: 10°C, base stiffness: 200 MPa.

The difference in the model responses for LV and HV is illustrated in Figure 9.28. Although a LV wheel load results in a reduction of the vertical deflection when compared to HV wheel loads, the difference in the rate of embedment is much smaller than the TRH3 (2007) equivalency factor of 40. Figure 9.28 indicates an equivalent LV:HV wheel load factor of approximately 1.6 and is almost similar to the results obtained for the single and double seal analyses. A summary of the LV:HV equivalent damage factor range is presented in Table 9.5.

The effects of the axle travelling speeds are illustrated in Figure 9.29 and it is clear that there is a slight reduction in the vertical deflection, but this had no impact on the load repetitions to embedment failure. Travelling speed is therefore not a significant parameter with reference to embedment rate.

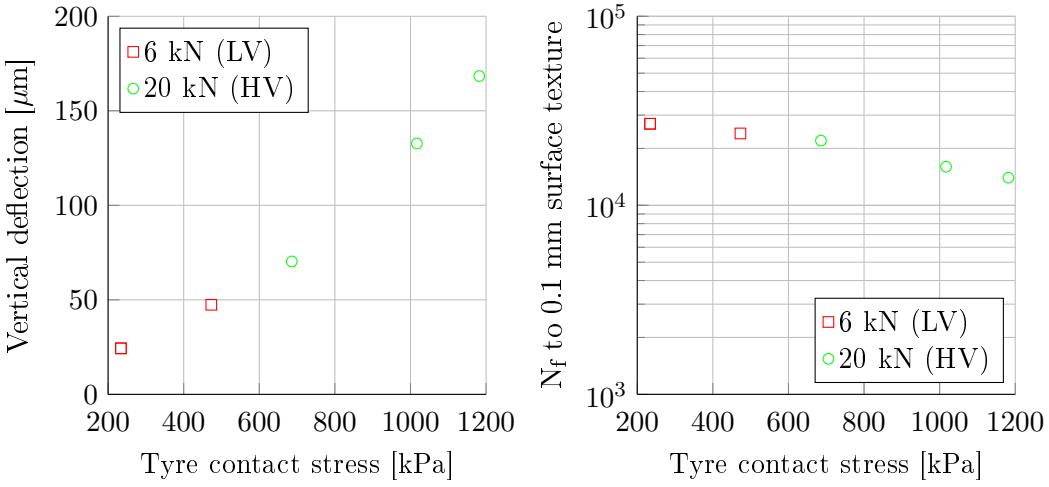

Figure 9.28: Vertical deflection and corresponding load repetitions to failure for the 13.2 mm cape seal, virgin slurry, 0.7 mm surface texture with LV and HV wheel loads. Temperature: 10°C, base stiffness: 200 MPa.

Table 9.5: Equivalent LV:HV damage ratios as illustrated in Figure 9.28.

Load case description	LV load reps	Remaining LV surf texture	HV load reps	Remaining HV surf texture	LV:HV ratio
Max LVs & min HVs	2.7×10^4	14%	1.4×10^4	14%	2 : 1
Min LVs & max HVs	2.4×10^4	14%	2.2×10^4	14%	1.1 : 1
Ave LVs & ref HV	2.6×10^4	14%	1.6×10^4	14%	1.6 : 1

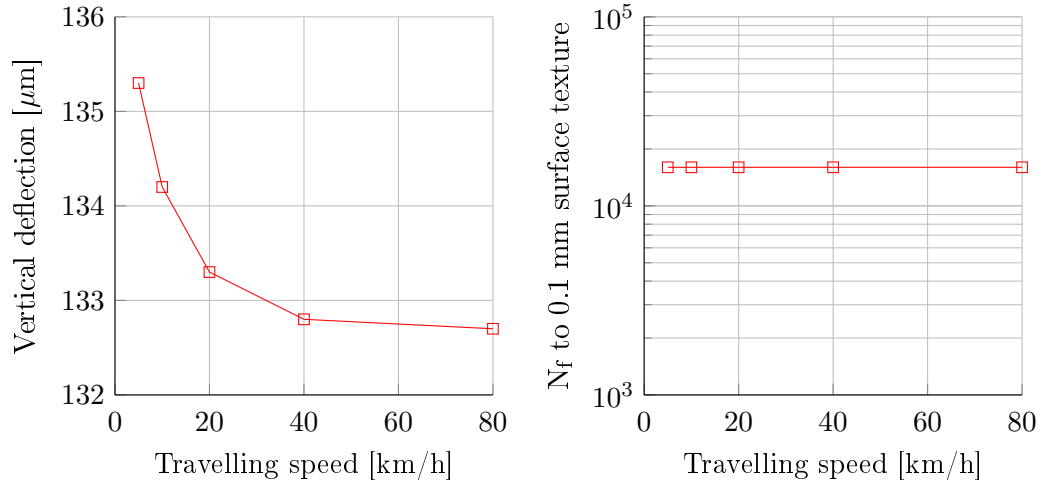

Figure 9.29: Vertical deflection and corresponding load repetitions to failure for the 13.2 mm cape seal, virgin slurry, 0.7 mm surface texture. Temperature: 10°C, base stiffness: 200 MPa, traffic load: 20 kN-800 kPa.

9.4 Closure

Anomalies were observed for the adhesive and cohesive analyses between concentrated and distributed wheel loads with reference to the structural variables. Increases in the response parameters were observed for decreasing surface textures, suggesting that over-filled cape seals are more fatigue prone than under-filled cape seals. Variables therefore that significantly affected the cape seal response, in order of importance, are the base stiffness, surface texture and the tyre contact stress as illustrated in Figure 9.30.

The cape seal includes speed as a variable when translating the response parameters to equivalent load repetitions to failure. An increase in both the adhesive and cohesive load repartitions to failure is observed for an increase in the travelling speed. This suggests that more damage is induced at lower speeds for both failure mechanisms. This phenomenon is extensively discussed in the following chapter where comparative analyses were conducted on all the seal model results.

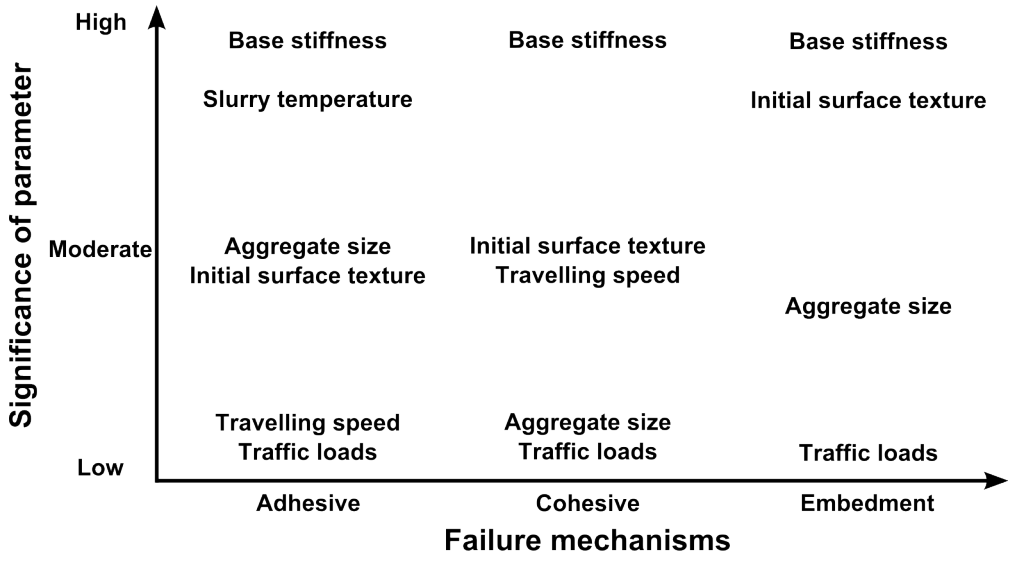

Figure 9.30: Level of parameter significance for cape seals.

10. Comparative analysis

The comparative analysis gives an over-all perspective of the three damage mechanisms with the associated critical response and damage parameters of the respective seal types. The critical response parameters were utilised in the development of a primary seal response model (PSRM). The PSRM consists of nine regression equations, each relating a combination of variables per seal type and damage mechanism to the critical response parameter. This chapter presents the development of these equations for the adhesive, cohesive and embedment failure mechanisms.

10.1 Adhesive failure comparison

An adhesive failure comparison was conducted between the single (S1), double (S2) and cape seal (S4) analyses. This section illustrates and presents the contribution of the primary variables to the response and damage for each respective seal type. The contributions of the primary variables were considered in the development of the primary adhesive response models.

10.1.1 Critical adhesive response parameter analysis

For an objective perspective on the adhesive response comparisons, aggregate nominal sizes were selected at 13.2 mm for single and cape seals and 13.2 mm + 6.7 mm for double seals. The critical response parameter for single (S1) and double (S2) seals is adhesive stress, while an equivalent tensile stress is the critical response parameter for a cape seal (S4). Figure 10.1 illustrates a response comparison for single and double seals and the associated damage of all three seals with reference to the aggregate spread rates.

The single seal response increases with an increase in aggregate spread rate, since the actual contact area decreases, an increase in the shear stress is obtained (Figure 2.13). The opposite is observed for a double seal were an increase in aggregate spacing results in an increase in the actual contact area, since more asperities are in contact with the tread rubber of the tyre. The cape seal, though at a lower temper-

ature ($10°C$), yields a similar performance compared to the single and double seals at 1 mm. It regresses slightly, but to a constant performance, at increased spread rates. A much closer comparison between the cape and single seal is illustrated in Figure 10.2, where a variation in ALD indicates that all three seal types are subject to an escalation in the risks of ravelling with increasing ALD. An escalation of risk, as defined by this situation, constitutes an increase in the critical response parameter which results in a reduction of load repetitions to failure.

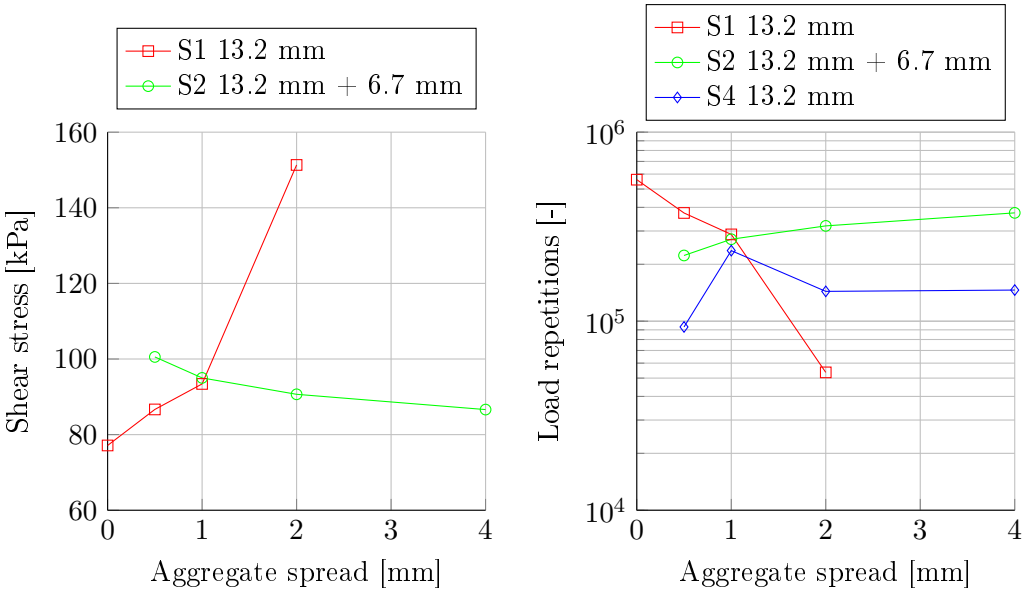

Figure 10.1: Shear stress comparison between S1 and S2 for aggregate spread rates. Load repetitions to failure for all three seal types. Temperature: 25°C (S1,S2) & 10°C (S4). Base stiffness: 200 MPa. Traffic load: 20 kN-800 kPa at 80 km/h.

Applying this definition of risk, Figure 10.3 illustrates that a single seal presents a greater risk to ravelling than a double seal at the respective minimum binder application rates. A reduction in the risk of ravelling is observed for both cases as the binder application rate increases. In the case of the cape seal, the 'binder application rate' is actually the incorrect terminology and should read: 'cured slurry application.' This parameter was estimated from the initial surface texture for comparison purposes (Figure 10.3) and indicates the cape seal's sensitivity to ravelling at low slurry application rates.

It is interesting to note that the binder of the thicker double seal (double aggregate layer) responds with a greater shear stress than the thinner single seal at reduced base support strength, as illustrated in Figure 10.4. There is merit therefore in hypothesising that the radius of curvature (ROC) can be utilised as an indicator for analysing the probability of failure, as will be discussed in Section 10.2.1. The cape

seal ($20°C$) performs very similar to the double seal, though the double seal exhibits slightly improved performance with increased base support strength.

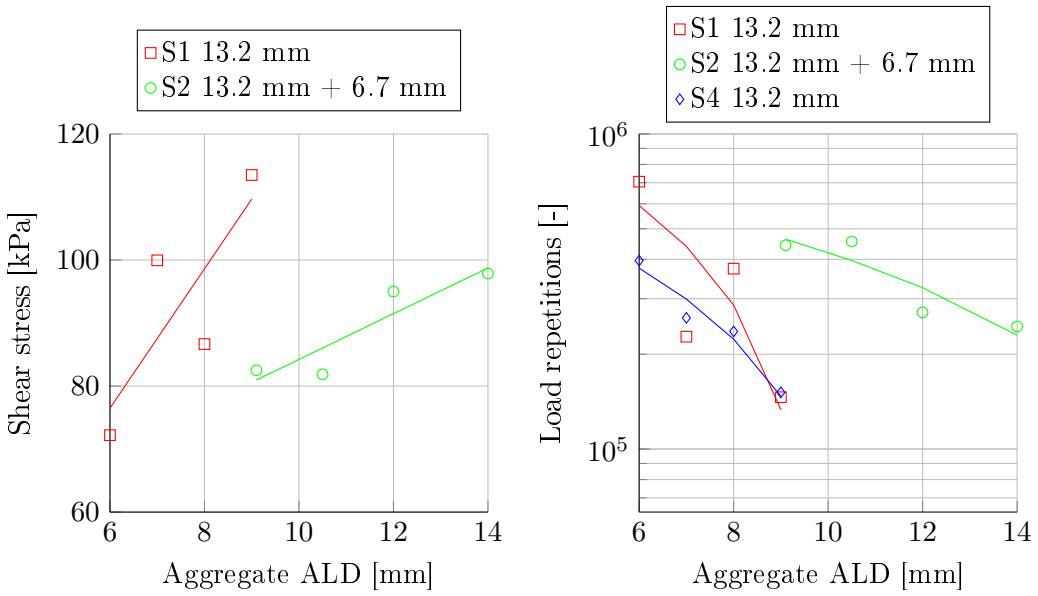

Figure 10.2: Shear stress comparison between S1 and S2 for aggregate ALDs. Load repetitions to failure for all three seal types. Temperature: 25°C (S1,S2) & 10°C (S4). Base stiffness: 200 MPa. Traffic load: 20 kN-800 kPa at 80 km/h.

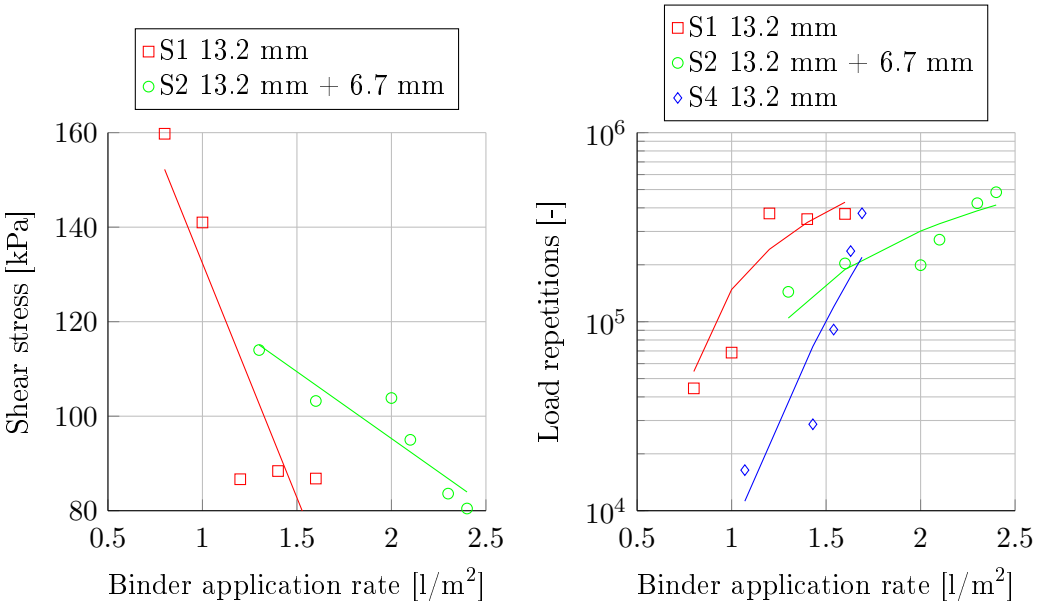

Figure 10.3: Shear stress comparison between S1 and S2 for binder application rates. Load repetitions to failure for all three seal types. Temperature: 25°C (S1,S2) & 10°C (S4). Base stiffness: 200 MPa. Traffic load: 20 kN-800 kPa at 80 km/h.

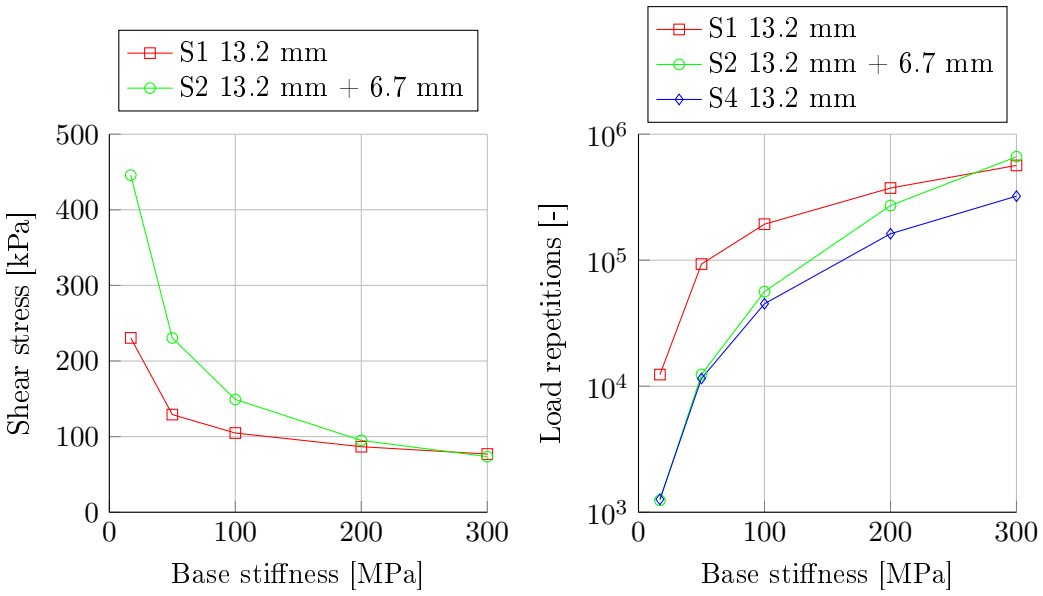

Figure 10.4: Shear stress comparison between S1 and S2 for a variation in base stiffness. Load repetitions to failure for all three seal types. Temperature: 25°C (S1,S2) & 20°C (S4). Traffic load: 20 kN-800 kPa at 80 km/h.

Binder temperature effects are virtually the same for both single and double seals as illustrated in Figure 10.5. This is also reflected in the associated load repetitions to failure, while the cape seal performs significantly worse at colder temperatures. However, the dramatic difference in the latter comparison emanates from the laboratory material parameters of Chapter 4, where Mukandila (2015) obtained significant increases in the end-of-life values for virgin 70-100 bitumen at $10°C$ relative to the values at $25°C$. Huurman (2008) did not obtain such differences for the mortar (slurry) test temperature regime.

Binder aging as represented by the Glower-Rowe parameter (Figure 10.6) indicates a dramatic initial increase in the shear stress response, followed by a decrease. A type of plateau forms, which suggests stable response as the G-R parameter increases from 180 to 350. Stresses obtained from the double seals are slightly higher than the stresses obtained from the single seals. Only virgin binder damage parameters were developed by Mukandila (2015), while virgin and PAV damage parameters were developed for slurries (Huurman, 2008). In comparison, single seals are the better performers under virgin conditions, followed by double seals and then cape seals. The cape seal with its slurry, indicates a reduction in the risk to ravelling at the PAV age and is assumed by Huurman (2008) to be seven years.

A consistent observation throughout this study was the phenomenon that tyre contact stress, rather than the vertical load, is indicative of the expected shear stress response as illustrated in Figure 10.7. Both seals (S1, S2) indicate an increase in

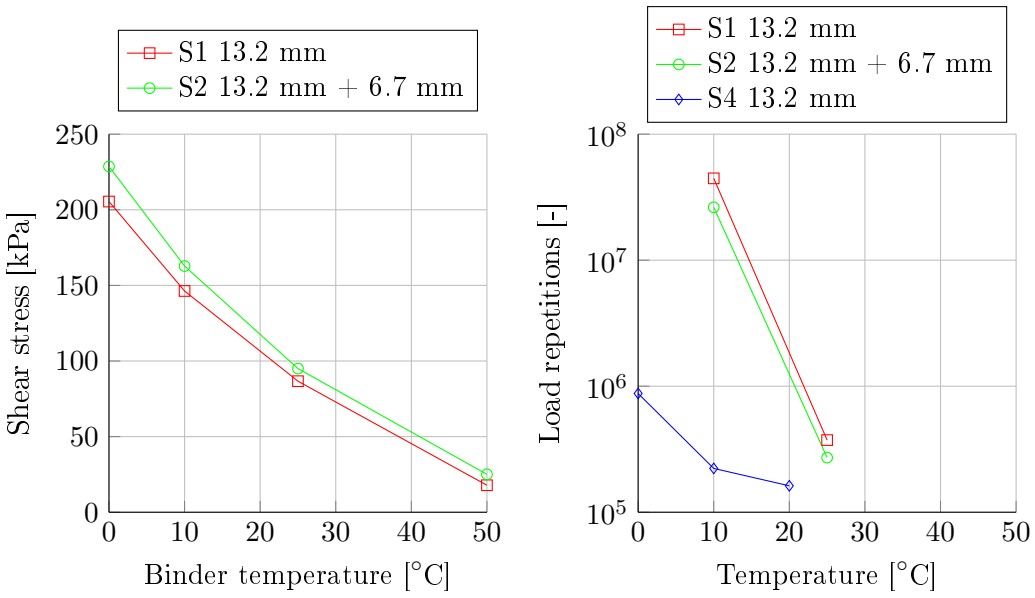

Figure 10.5: Shear stress comparison between S1 and S2 for binder temperatures. Load repetitions to failure for all three seal types. Base stiffness: 200 MPa. Traffic load: 20 kN-800 kPa at 80 km/h.

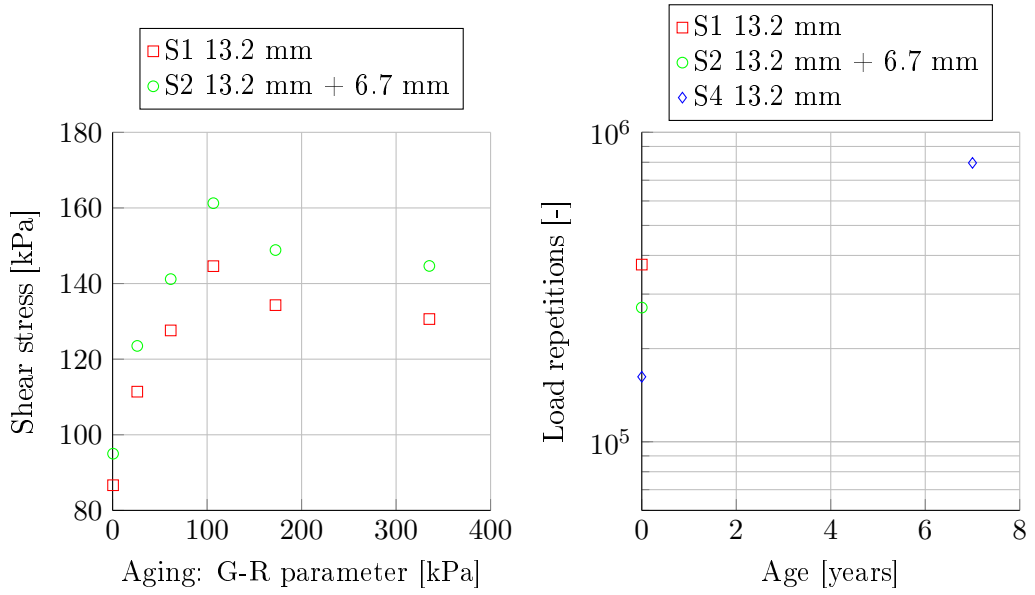

Figure 10.6: Shear stress comparison between S1 and S2 for various binder ages. Load repetitions to failure for all three seal types. Temperature: 25°C (S1,S2) & 20°C (S4). Base stiffness: 200 MPa. Traffic load: 20 kN-800 kPa at 80 km/h.

shear stress response with increasing tyre contact stress, although the double seal increases with a greater rate than the single seal. The cape seal, on the other hand, has even greater response parameter incline as the tyre contact stress increases from 200 kPa to 1200 kPa. This can be deduced from the great number of load repetitions

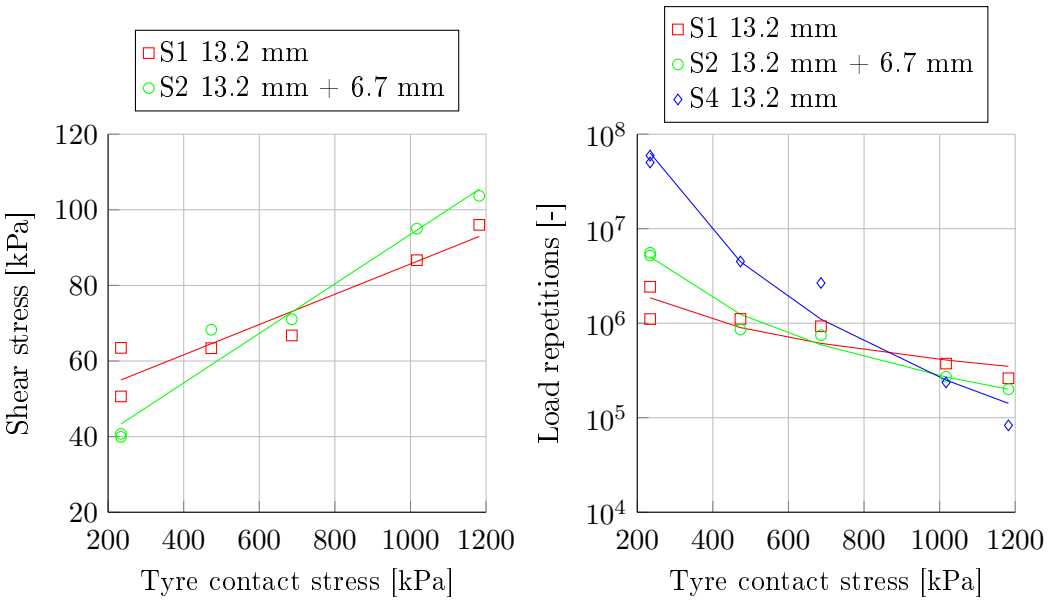

Figure 10.7: Shear stress comparison between S1 and S2 for tyre inflation pressures. Load repetitions to failure for all three seal types. Temperature: 25°C (S1,S2) & 10°C (S4). Base stiffness: 200 MPa. Travelling speed: 80 km/h.

at low contact stresses and the dramatic reduction in load repetitions at higher contact stress. The tyre contact stress is therefore a key variable in analysing ravelling of aggregate on the road's surface. Figure 10.8 illustrates that the single and double

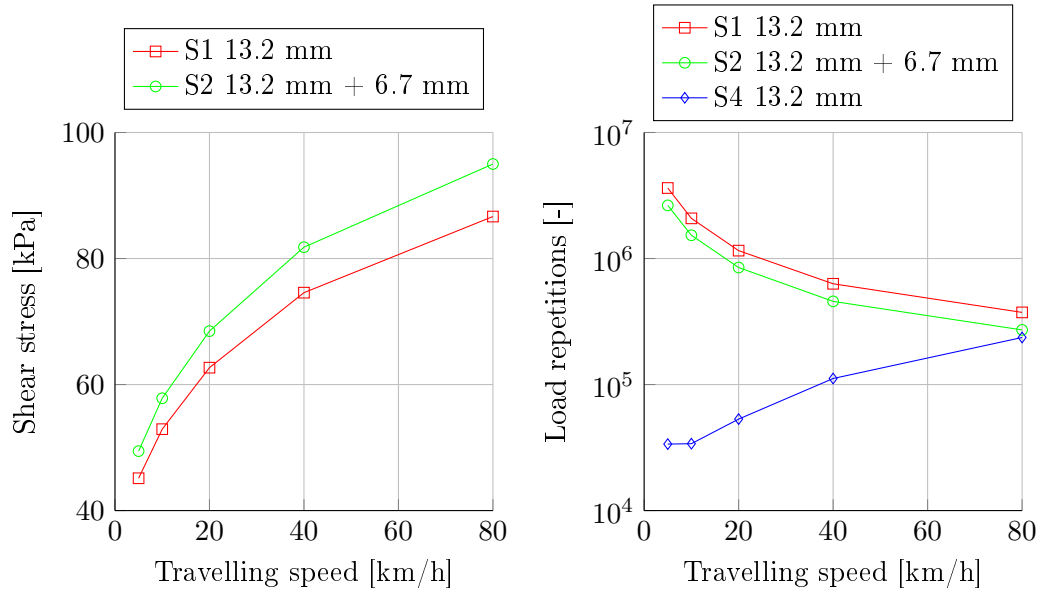

Figure 10.8: Shear stress comparison between S1 and S2 for travelling speeds. Load repetitions to failure for all three seal types. Temperature: 25°C (S1,S2) & 20°C (S4). Base stiffness: 200 MPa. Traffic load: 20 kN-800 kPa.

seals have similar responses to an increase in the travelling speed. Though not displayed in Figure 10.8, the cape seal's equivalent tensile stress response also increases with increasing speeds until reaching a limit at 20 km/h to 40 km/h. The major difference however, is the inclusion of a time parameter in the cape seal's calculation of adhesive fatigue, while the other two seals do not include a time parameter. This leads to a difference in the trend of the number of load repetitions to failure.

10.1.2 Primary adhesive response models

Developing the primary adhesive response models implied the grouping of the critical response variables per seal type within one expression. Typical statistical methods used in developing these types of models and suitable for this case are: multiple linear regression, best subset regression and multivariate adaptive regression splines or commonly known as MARSplines. The latter being a non-parametric model which means that MARSplines make no assumption about the probability distributions of the variables assessed. Multiple linear regression and best subsets regression models are parametric models and therefore the main difference between parametric and non-parametric models is that parametric models have a fixed number of parameters, while non-parametric models grow the number of parameters with a growth in training data.
Initial trial models indicated that the multiple linear regression models obtained a better coefficient of determination R^2 in the dependent variable (DV) accounted for by the independent variables (IV) in comparison to the other models. The aim of the PSRM development is to obtain the simplest model, with acceptable reliability, that can be implemented in the South African Roads Design System (SARDS) simulations and therefore the multiple linear regression approach was selected in this study. The model expression is presented in Equation 10.1 and consists of a single DV with multiple IVs and a residual error term ϵ.

$$Y = \beta_0 + \beta_1 X_1 + \beta_2 X_2 + \ldots + \beta_n X_n + \epsilon \tag{10.1}$$

where:

Y = dependent variable
X_i = independent variable
β_i = variable coefficient
n = number of independent variables
ϵ = residual error term

With multiple regression analyses an assumption is made that the residual error

term is normally distributed and can therefore be neglected from the expression as presented in Equation 10.2.

$$\tilde{Y} = \beta_0 + \beta_1 X_1 + \beta_2 X_2 + \ldots + \beta_n X_n \tag{10.2}$$

Prior to multiple regression analysis the data sets were analysed for multicollinearity. This is when two or more IVs are highly correlated with each other. Such a case was observed between the aggregate nominal size and ALD, thus the aggregate nominal size was rejected as a DV since the ALD had a higher R^2.
The predicted versus observed results for the single, double and cape seal primary adhesive response models with associated distributions of the residual errors are illustrated in Figure 10.9 to Figure 10.11. The respective expressions of the models are defined in Equation 10.3 to Equation 10.5, while the model coefficients are presented in Table 10.2. A description of each variable is addressed in Table 10.1 and the overall model statistics are presented in Table 10.3.

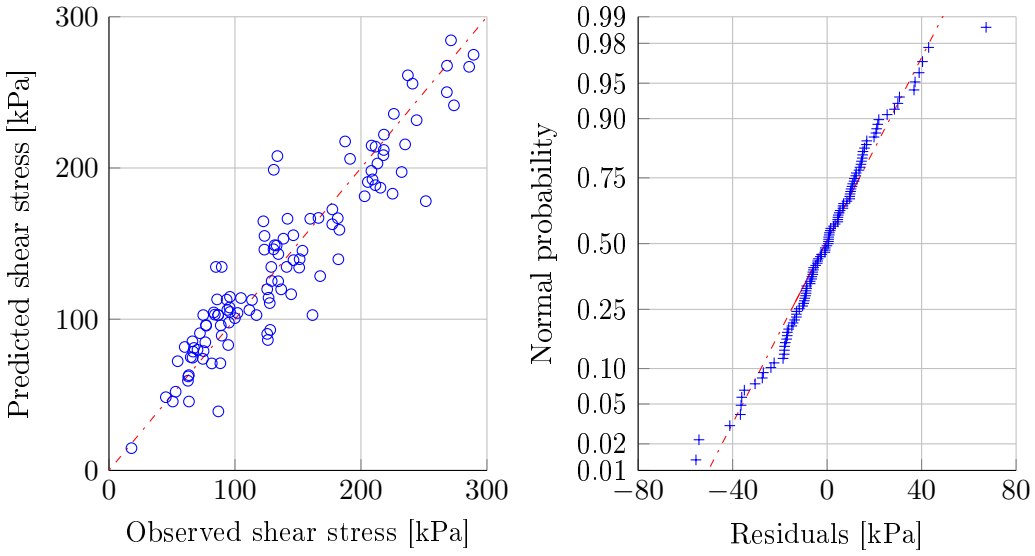

Figure 10.9: Predicted and observed response and residual distribution of the primary adhesive response model for single seals (S1).

$$\tilde{Y}_{S1} = \beta_0 + \beta_1 X_1 + \beta_2 X_2 + \beta_3 X_3 + \beta_4 ln(X_4) + \beta_5 X_5 + \beta_6 X_6 + \beta_7 X_7 + \beta_8 X_8 \tag{10.3}$$

From the comparative analysis it was observed that the base stiffness for all models had a highly non-linear relation to the respective response parameters. The variable X_4 was therefore transformed with the natural logarithmic function prior to its inclusion in the regression analyses. Including all the variables of Table 10.1 in the case of the cape seal regression analysis, resulted in over-fitting. This is when

adding more variables describes the noise i.e. increases R^2, instead of the underlying relationship. The surface texture (X_3) and slurry age (X_6) were therefore excluded in the determination of Equation 10.5.

Table 10.1: Variable description of the multiple linear regression models for the adhesive and cohesive response results.

Variable[i]	Description	S1-range	S2-range	S4-range
X_1	Aggregate spread rate $[mm]$	0 - 2	0.5 - 4	0.5 - 4
X_2	Aggregate ALD $[mm]$	4 - 9	9 - 19	4 - 9
X_3	Binder application rate $[l/m^2]$	0.7 - 1.6	1.1 - 3.2	0.1 - 1.0
X_4	Base stiffness $[MPa]$	50 - 450	50 - 450	50 - 450
X_5	Binder temperature $[°C]$	0 - 50	0 - 50	0 - 10
X_6	Aging: G-R parameter $[kPa]$	0 - 400	0 - 400	–
X_7	Tyre contact stress $[kPa]$	200 - 1200	200 - 1200	200 - 1200
X_8	Travelling speed $[km/h]$	5 - 80	5 - 80	5 - 80

[i] variable X_3 is in terms of surface texture in the case of a cape seal analysis

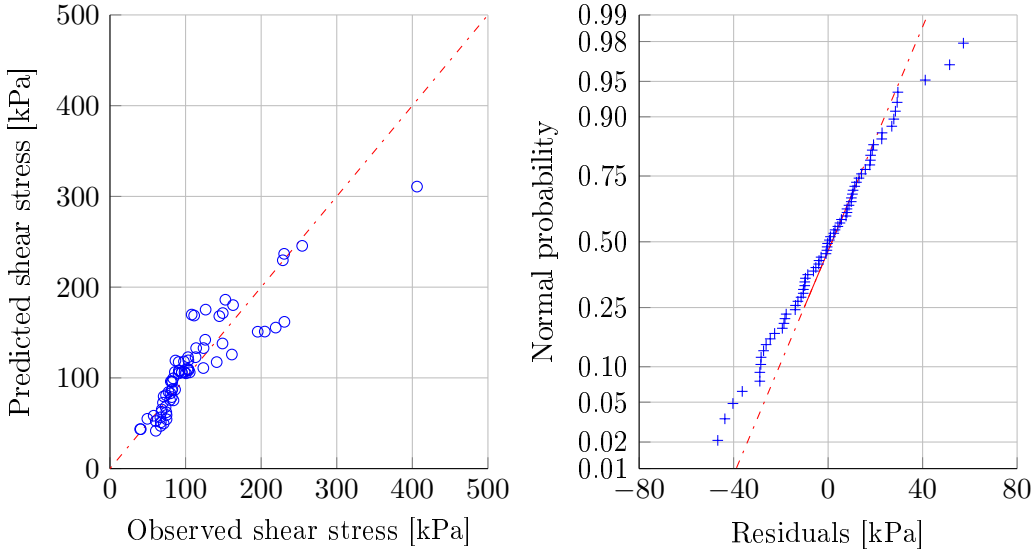

Figure 10.10: Predicted and observed response and residual distribution of the primary adhesive response model for double seals (S2).

$$\tilde{Y}_{S2} = \beta_0 + \beta_1 X_1 + \beta_2 X_2 + \beta_3 X_3 + \beta_4 ln(X_4) + \beta_5 X_5 + \beta_6 X_6 + \beta_7 X_7 + \beta_8 X_8 \quad (10.4)$$

It is clear from the figures but also from the R^2 in Table 10.3 that single and double seal regression models exhibit a closer approximation of the observed to predicted results. All models are statistically significant with P-values < 0.05 which means that the probability of rejecting the null-hypothesis is less than 5%. The root mean

square error (RMSE) for single and double seals are in the same order, though slightly higher for the double seals. The RMSE of the cape seal is slightly larger in terms of the observed equivalent tensile stress. The consequence is a greater distribution between the predicted and observed values, which may result in negative predicted values at very low observed values.

Table 10.2: Model coefficients of the multiple linear regression analyses for the adhesive stress results.

Seal	β_0	β_1	β_2	β_3	β_4	β_5	β_6	β_7	β_8
S1	105.52	45.88	25.9	-159.21	-16.25	-3.52	0.13	0.073	0.724
S2	521.96	8.79	11.0	-33.37	-94.21	-4.94	0.185	0.080	0.683
S4	3.26	-0.486	0.592	–	-1.27	-0.092	–	0.0016	–

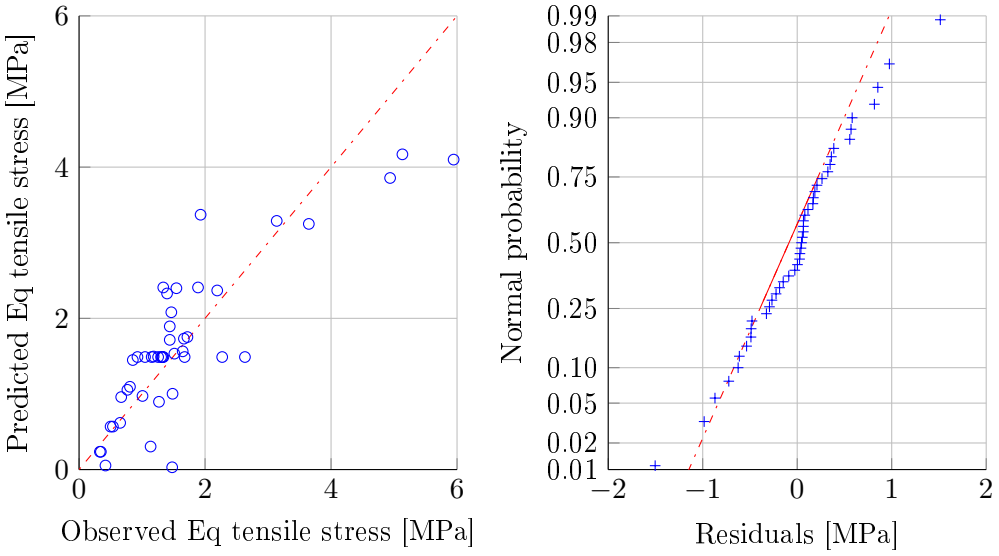

Figure 10.11: Predicted and observed response and residual distribution of the primary adhesive response model for cape seals (S4).

$$\tilde{Y}_{S4} = \beta_0 + \beta_1 X_1 + \beta_2 X_2 + \beta_4 ln(X_4) + \beta_5 X_5 + \beta_7 X_7 \tag{10.5}$$

Table 10.3: Statistical summary of the multiple linear regression models for the adhesive failure stress results.

Seal	R^2	R^2-adjusted	F-value	P-value	RMSE
S1	0.869	0.859	86.59	0.000	24.03
S2	0.789	0.801	34.17	0.000	27.52
S4	0.715	0.679	19.60	0.000	0.684

10.2 Cohesive failure comparison

Similar to the adhesive failure comparison, this section illustrates and presents the cohesive failure comparisons between the single (S1), double (S2) and cape seal (S4) analyses. Critical variables are identified and incorporated, if statistically relevant, in the development of the primary cohesive response models.

10.2.1 Critical cohesive response parameter analysis

Continuing with an objective perspective as discussed in Section 10.1.1, Figure 10.12 illustrates the comparison of the shear stress response between the single and double seals, while including the the cape seal in the load repetitions to failure comparison with reference to the aggregate spread rate. The cohesive response parameter of the cape seal is the dissipated energy parameter, ruling out direct response comparisons with the other seal types.

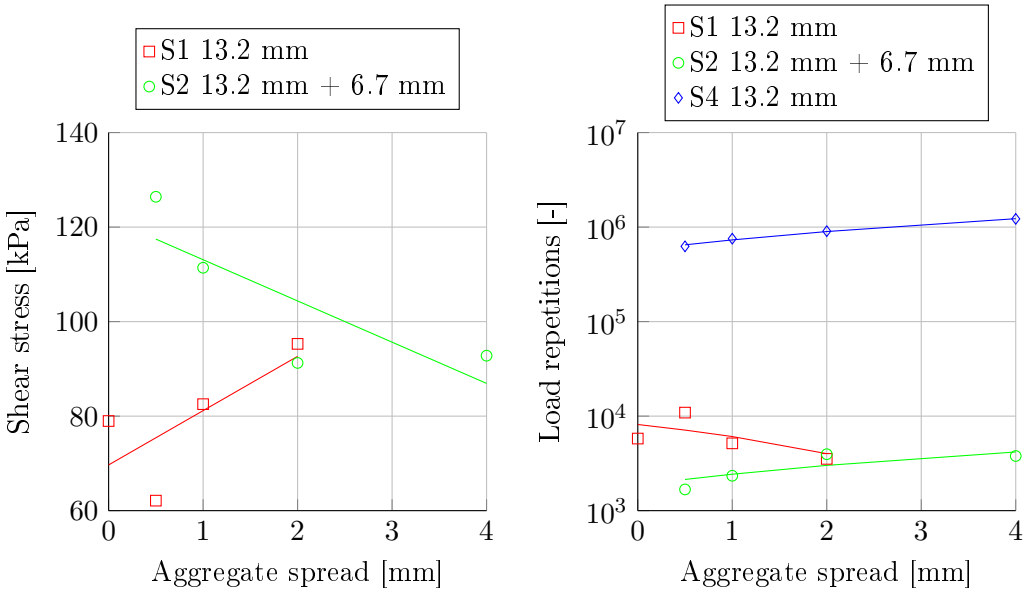

Figure 10.12: Shear stress comparison between S1 and S2 for aggregate spread rates. Load repetitions to failure for all three seal types. Temperature: 25°C (S1,S2) & 10°C (S4). Base stiffness: 200 MPa. Traffic load: 20 kN-800 kPa at 80 km/h.

The single seal exhibits an increase in the shear stress response with an increasing spread rate, while a reduction is obtained within double seal for similar reasons as discussed in Section 10.1.1. The cape seal exhibits a similar trend compared to the double seal, but with a greater number of load repetitions to failure. It should be noted that the cape seal analysis was conducted at $10°C$ in comparison to $25°C$ of the single and double seals.

The reverse is observed in comparing the three seals with respect to ALD as illustrated in Figure 10.13. Here, the single seal response exhibits a slight decrease in shear stress response with increasing ALD, while the double seal displays an increase. A steeper decline is observed for the cape seal load repetitions to failure in comparison to the double seal. This suggests that thickness or height of a cape seal affects its resistance to cohesive fatigue.

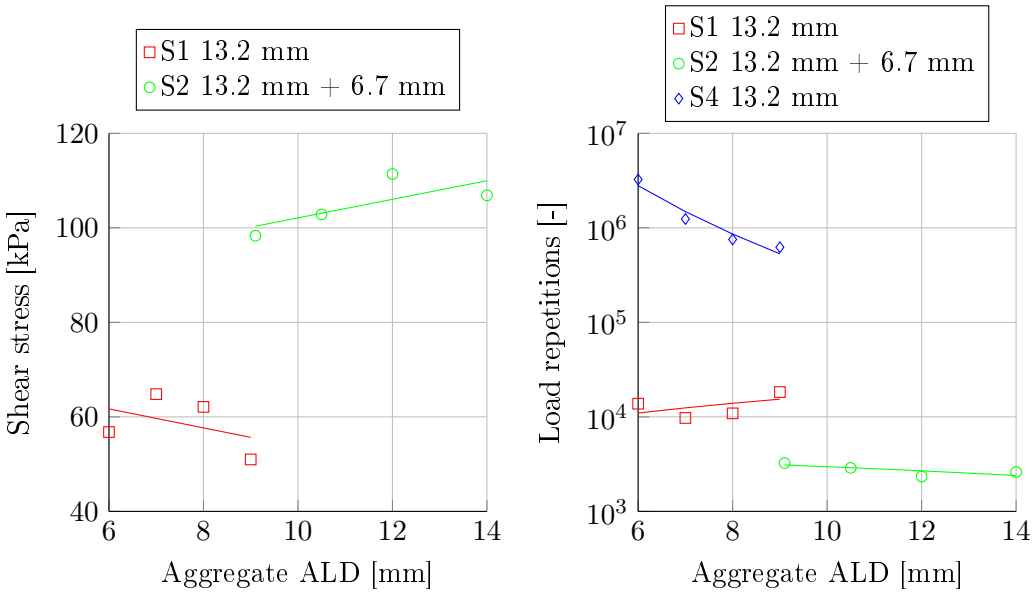

Figure 10.13: Shear stress comparison between S1 and S2 for aggregate ALDs. Load repetitions to failure for all three seal types. Temperature: 25°C (S1,S2) & 10°C (S4). Base stiffness: 200 MPa. Traffic load: 20 kN-800 kPa at 80 km/h.

The latter statement is supported by Figure 10.14, which illustrates the notion that height affects the cape seal's performance. The 'binder application rate' should read, 'cured slurry application', in this case. This parameter was estimated from the initial surface texture for comparison purposes and contrary to expectation a reduction in load repetitions to failure is observed with increasing slurry application. This result emanates from the hypothesis that the slurry supports only a fraction of the load and therefore greater slurry application rates i.e. smaller surface textures exhibit more dissipated energy, resulting in a reduction of load applications to fatigue failure.
The single and double seals indicates a reduction in the shear stress response as the binder application rates increase. The single seal exhibits a greater range of shear stress response compared to the double seal. This suggests that a single seal is more sensitive to changes in the binder application rate. The double seal analyses had an approximate 55/45 (tack coat/penetration coat) application split.
The discussion on the hypothesis that the radius of curvature (ROC) can be utilised

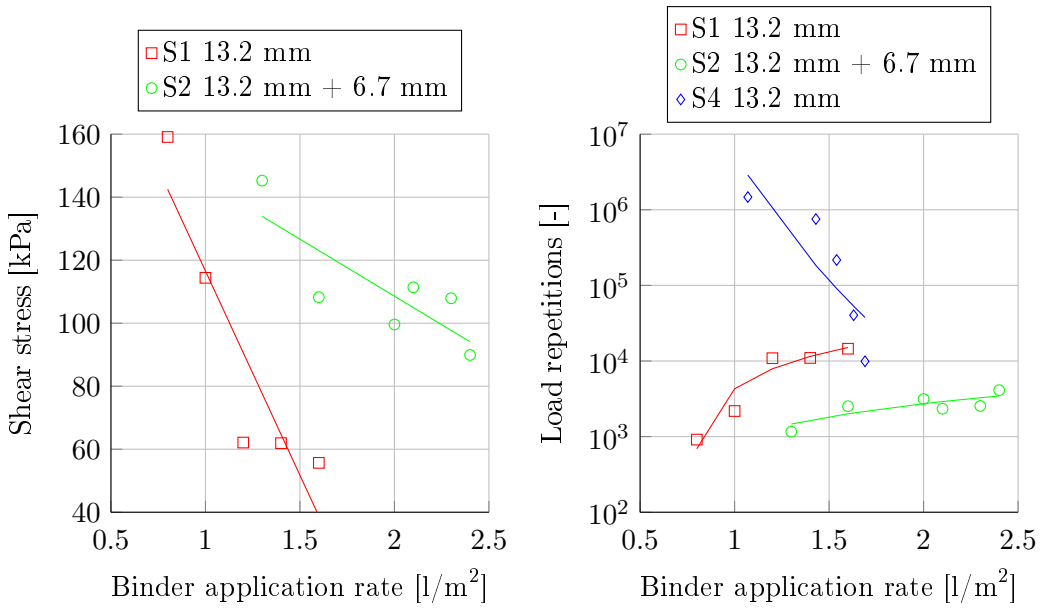

Figure 10.14: Shear stress comparison between S1 and S2 for binder application rates. Load repetitions to failure for all three seal types. Temperature: 25°C (S1,S2) & 10°C (S4). Base stiffness: 200 MPa. Traffic load: 20 kN-800 kPa at 80 km/h.

as an indication for the probability of cohesive failure continues in Figure 10.15, where the thicker double seal responds with a greater shear stress in comparison to the thinner single seal. This phenomenon signifies a beam stiffness effect and

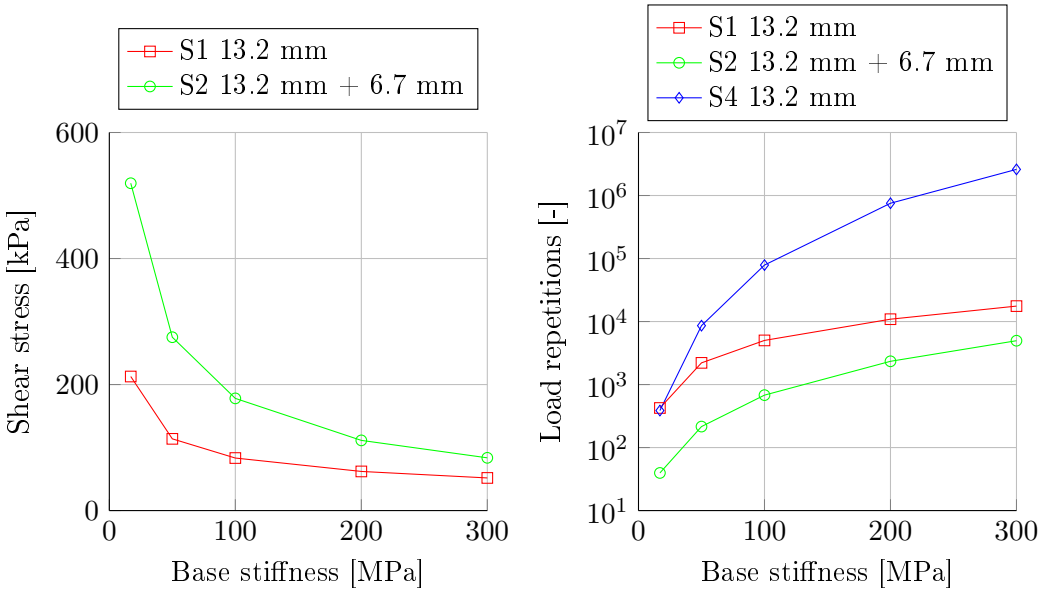

Figure 10.15: Shear stress comparison between S1 and S2 for a variation in base stiffness. Load repetitions to failure for all three seal types. Temperature: 25°C (S1,S2) & 20°C (S4). Traffic load: 20 kN-800 kPa at 80 km/h.

indicates that the double seal responds with more resistance to a vertical deflection than the single seal when subjected to the same load. All three models however, indicate that weaker bases i.e. greater vertical deflection, result in a reduction in the number of load repetitions to failure. This reaffirms the sentiment that the $d_0 - d_{127}$ ROC parameter has the potential to provide suitable information on the prediction of cohesive failure as discussed in Section 6.2.1, Figure 6.3. The offset in Figure 10.16 between the single and double seal originates therefore more from a structural difference perspective than a difference in temperature. Lower temperatures however, exaggerate this offset, though both seals respond with similar trends to a change in temperature.

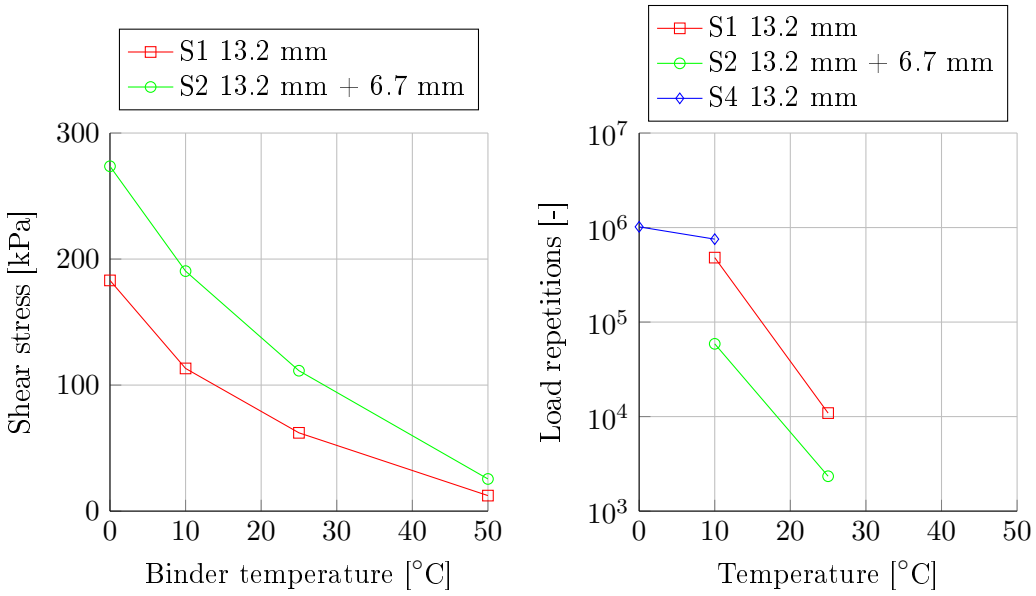

Figure 10.16: Shear stress comparison between S1 and S2 for binder temperatures. Load repetitions to failure for all three seal types. Base stiffness: 200 MPa. Traffic load: 20 kN-800 kPa at 80 km/h.

An objective comparison between all three seals is illustrated in Figure 10.16 at $10°C$. The more rigid cape seal exhibits the most significant number of load repetitions to failure, followed by the single seal and concluding with the double seal. Not surprising then is a similar ranking with reference to aging as illustrated in Figure 10.17. Although both single and double seals indicate similar response trends to a change in the G-R parameter which represents aging, Figure 10.17 is reminiscent of the discussion on the beam stiffness effect. Since the slurry aging process was not converted to G-R parameters, Figure 10.17 illustrates the load repetitions to failure for virgin conditions and includes a PAV condition for slurries only. The same ranking as with temperature is obtained for aging, where the more rigid cape seal

exhibits the most number of load repetitions to failure, followed by the single seal and ending with the double seal. It should be noted that Huurman (2008) estimates the PAV age of the slurry to be approximately seven years.

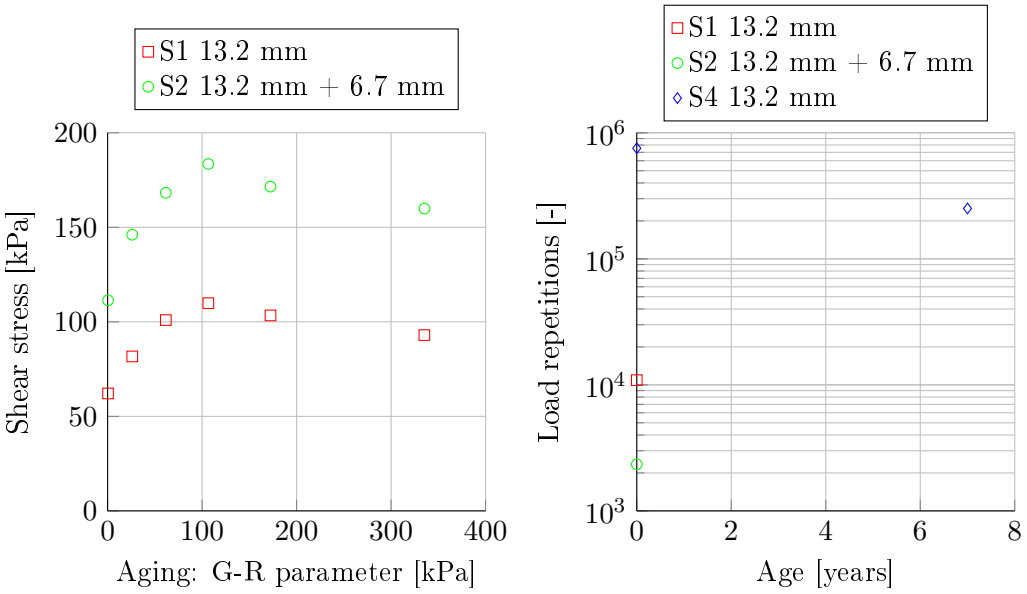

Figure 10.17: Shear stress comparison between S1 and S2 for various binder ages. Load repetitions to failure for all three seal types. Temperature: 25°C (S1,S2) & 10°C (S4). Base stiffness: 200 MPa. Traffic load: 20 kN-800 kPa at 80 km/h.

Contrary to the adhesive failure comparison, the shear stress response of the double seal within the cohesive failure comparison is by far more significant in comparison to the single seal response with reference to the tyre contact stress as illustrated in Figure 10.18. This suggests that a double seal is more prone to fatigue cracking than a single seal and both seal types have and increased risk of cracking under heavier loads than lighter loads. The cape seal shares the latter sentiment as illustrated in Figure 10.18 at a lower temperature ($10°C$) with an increased number of load repetitions to failure.

A unique difference in the cohesive failure mechanisms is illustrated in Figure 10.19, where an increase in the travelling speed result in either a decrease in the number of load applications for single and double seals or an increase for a cape seal. This contradiction emanates from the different damage models utilised for single, double and cape seals respectively. The cape seal makes use of a dissipated energy response parameter, which is transferred by a damage function to an equivalent number of load repetitions to failure. A slower travelling load results in a greater dissipated energy parameter compared to a faster load. The greater dissipated energy parameter translates to fewer equivalent load repetitions to failure. Although single and

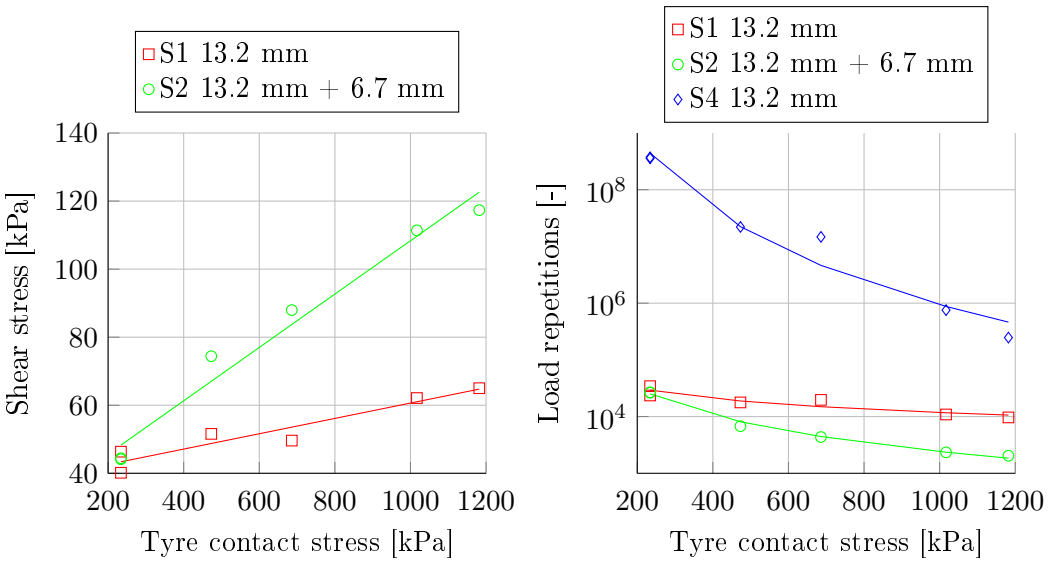

Figure 10.18: Shear stress comparison between S1 and S2 for tyre inflation pressures. Load repetitions to failure for all three seal types. Temperature: 25°C (S1,S2) & 10°C (S4). Base stiffness: 200 MPa. Travelling speed: 80 km/h.

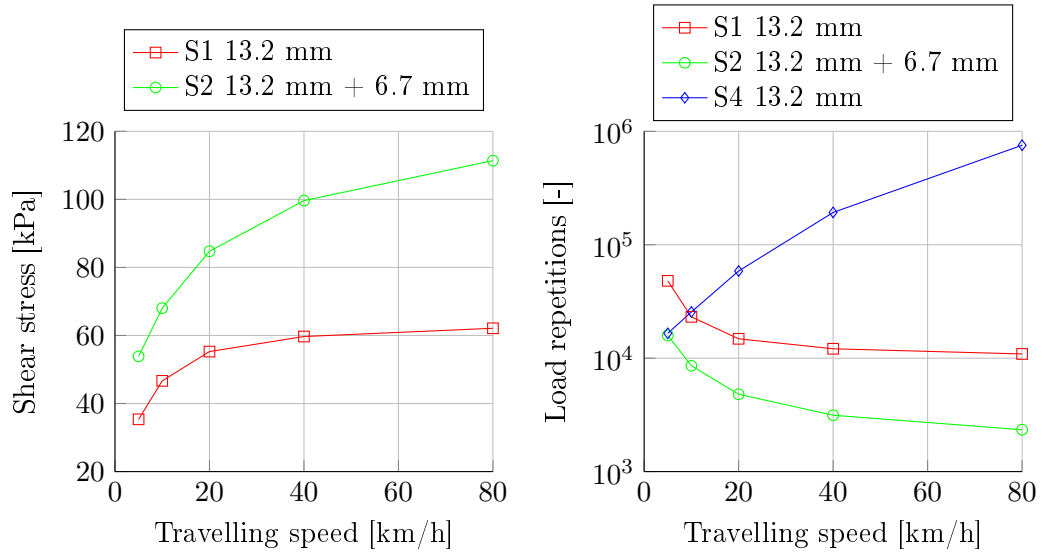

Figure 10.19: Shear stress comparison between S1 and S2 for travelling speeds. Load repetitions to failure for all three seal types. Temperature: 25°C (S1,S2) & 10°C (S4). Base stiffness: 200 MPa. Traffic load: 20 kN-800 kPa.

double seals utilise a similar transfer approach, the shear stress response parameter does not consider the loading time. Shear stress increase with loading rate is a result of the vicoelastic properties of bitumen and translates to fewer equivalent load applications to failure, thus explaining the contradiction observed in Figure 10.19.

10.2.2 Primary cohesive response models

The cohesive response model development followed a similar approach to the development of the adhesive response models. Multiple linear regression analyses resulted in simple models that are implementable in the SARDS simulations. The primary cohesive response model expressions for single, double and cape seals are presented in Equation 10.6 to Equation 10.8 respectively, while the observed versus predicted response results and associated residual error distributions are illustrated in Figure 10.20 to Figure 10.22. The regression model coefficients are summarised in Table 10.4 and the statistic thereof presented in Table 10.5. These models have the same variable description as presented in Table 10.1, with a natural logarithmic transformation of the base stiffness X_4.

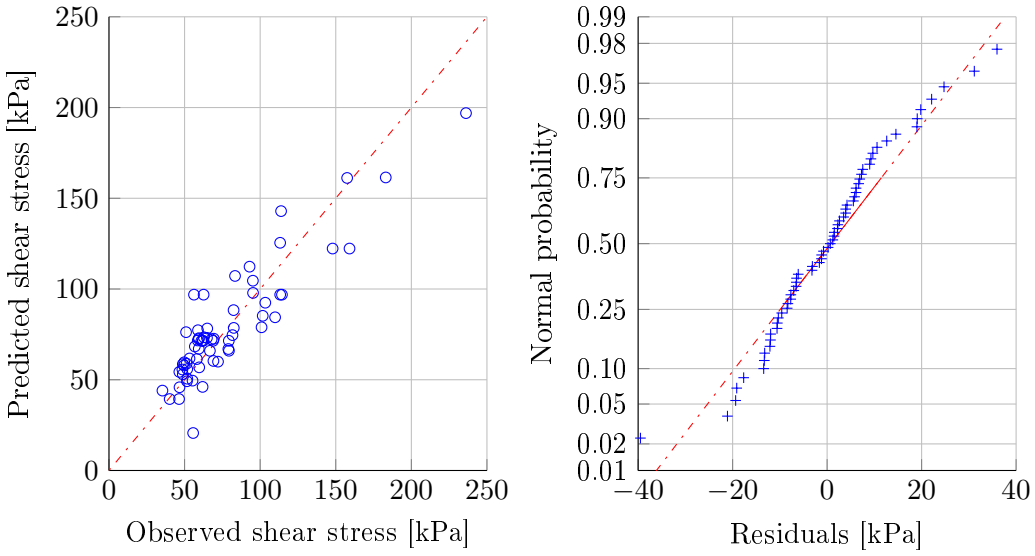

Figure 10.20: Predicted and observed response and residual distribution of the primary cohesive response model for single seals (S1).

$$\tilde{Y}_{S1} = \beta_0 + \beta_1 X_1 + \beta_2 X_2 + \beta_3 X_3 + \beta_4 ln(X_4) + \beta_5 X_5 + \beta_6 X_6 + \beta_7 X_7 + \beta_8 X_8 \quad (10.6)$$

Table 10.4: Model coefficients of the multiple linear regression analyses for the cohesive failure results.

Seal	β_0	β_1	β_2	β_3	β_4	β_5	β_6	β_7	β_8
S1	359.12	34.53	17.45	-127.06	-51.54	-3.60	0.122	0.041	0.366
S2	940.45	–	-5.35	-12.40	-138.04	-5.57	0.228	0.081	0.659
S4	71.58	–	–	-23.13	-8.97	0.219	–	0.004	-0.103

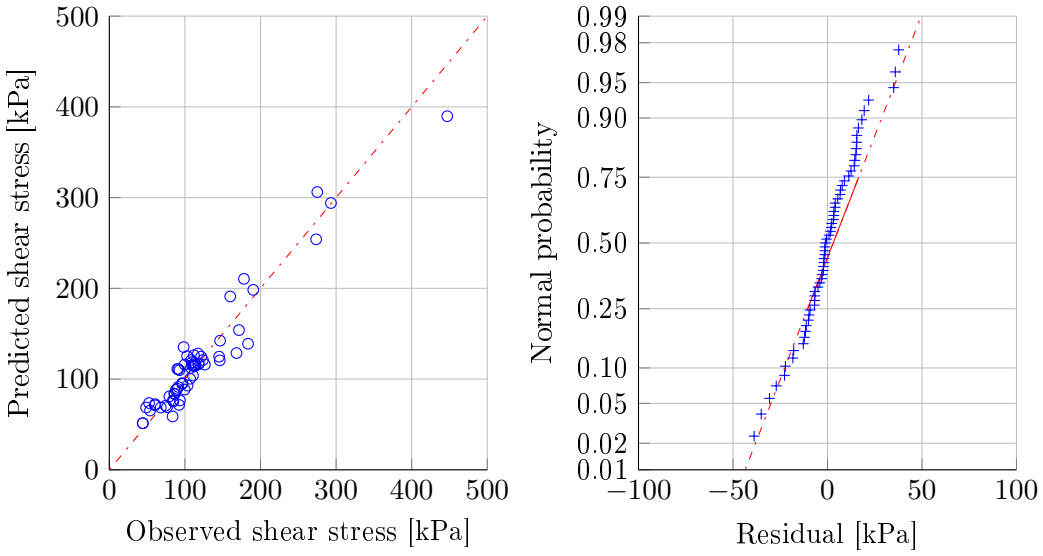

Figure 10.21: Predicted and observed response and residual distribution of the primary cohesive response model for double seals (S2).

$$\tilde{Y}_{S2} = \beta_0 + \beta_2 X_2 + \beta_3 X_3 + \beta_4 ln(X_4) + \beta_5 X_5 + \beta_6 X_6 + \beta_7 X_7 + \beta_8 X_8 \qquad (10.7)$$

Table 10.5: Statistical summary of the multiple linear regression models for the cohesive failure results.

Seal	R^2	R^2-adjusted	F-value	P-value	RMSE
S1	0.805	0.777	28.83	0.000	17.52
S2	0.921	0.911	91.80	0.000	19.74
S4	0.875	0.859	54.66	0.000	1.86

All three regression models illustrate a good fit, since 80% to 90% of the variation (R^2) in the response parameter $\tilde{Y}$ is accounted for by the independent variables. The single seal regression model includes all the available variables in its expression, while aggregate spread rate (X_1) was excluded from the double seal expression. More variables in an expression do not necessarily mean a better model, the contrary is actually the aim: the simplest model, with the least amount of variables that can accurately and reliability define the underlying relationship between the DV and IVs is deemed the best model.

This study, however, aimed at including at least one structural, one time related and one traffic orientated variable per regression model, thereby ensuring that geometry, age and load effects are represented by the primary response models. The latter statement is however only valid for the adhesive and cohesive failure mechanisms,

since some variables do not contribute, with statistical significance, to the development of embedment. This was also the case in the development of the cape seal cohesive response model as defined in Equation 10.8.

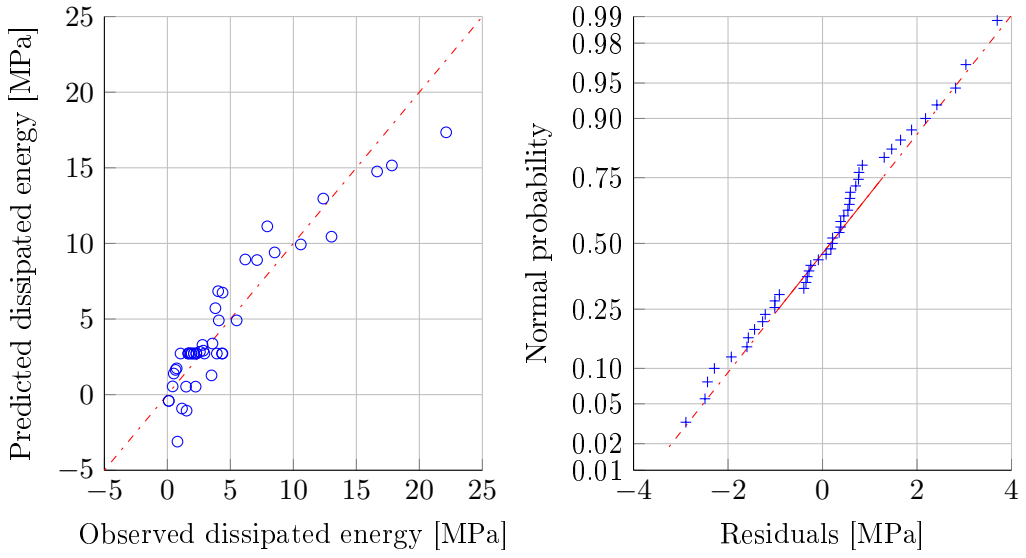

Figure 10.22: Predicted and observed response and residual distribution of the primary cohesive response model for cape seals (S4).

$$\tilde{Y}_{S4} = \beta_0 + \beta_3\sqrt{X_3} + \beta_4 ln(X_4) + \beta_5 X_5 + \beta_7 X_7 + \beta_8 X_8 \tag{10.8}$$

The aggregate spread rate (X_1), ALD (X_2) and slurry age (X_6) did not attain statistical significance i.e. P-value < 0.05 and were therefore not included in the regression analysis. An additional square root transformation was applied to the initial surface texture (X_3) to obtain statistical significance of that parameter. Although the cohesive response parameter indicates a good fit, negative values are predicted at a high base stiffness and low tyre inflation pressure. This may be a cause of concern, but since the cape seal models are based on mortar properties developed for porous asphalt concrete, this current model will suffice as a substitute until actual slurry characterisation testing is conducted.

10.3 Embedment failure comparison

It is important to note that embedment development is quantified by surface texture loss, although adjudicating embedment with remaining surface texture is devious, since remaining texture is a function of a list of variables such as the: initial surface texture, aggregate nominal size, ALD, spread rate, aggregate orientation etc. This section therefore presents the embedment comparison between the single (S1), double (S2) and cape seals (S4). The critical variables incorporated in the primary embedment response model were identified according to the vertical deflection and not the remaining surface texture or load repetitions to failure.

10.3.1 Critical embedment response parameter analysis

Similar to the previous comparisons a 13.2 *mm* single and cape seal and a 13.2 *mm* + 6.7 *mm* double seal were compared to obtain an objective comparative perspective as illustrated in Figure 10.23, where the vertical deflection of the three seals are compared as a function of the aggregate spread rate. The aggregate spread rate has a minimal influence on the single and double seal, but does affect the cape seal.

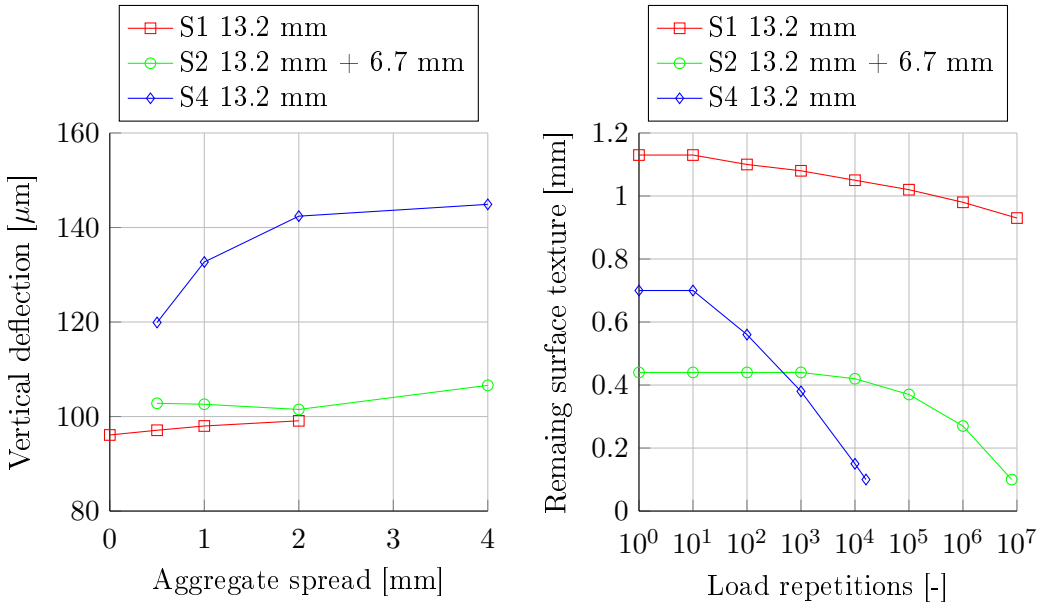

Figure 10.23: Deflection comparisons between S1, S2 & S4 for aggregate spread rates and corresponding load repetitions to failure. Temperature: 25°C (S1,S2) & 10°C (S4). Base stiffness: 200 MPa. Traffic load: 20 kN-800 kPa at 80 km/h.

Similar to the dissipated energy discussion the hypothesis that a fraction of the load is supported by the slurry, is supported by an increase in the vertical deflection as the spread rate increases. The associated remaining surface texture illustrates the

quantification of the vertical deflections for the single seal with a spread of 0.5 *mm* and the double and cape seal with a spread of 1.0 *mm* (Figure 10.23). The quantification calculation is based on the assumption that the permanent vertical deformation results in an upward surge of binder and thus a loss of initial surface texture. Uncertainty remains however, regarding the extent to which the cape seal aggregate will embed as the slurry fully cures and hardens, but Figure 10.23 indicates that the cape seal has a greater embedment rate in comparison to the other two seals. If the embedment development reaches a stage where the binder upsurge infiltrates the remaining surface texture of the double seal; a greater texture loss rate is observed in comparison to the single seal.

Increase in the aggregate ALD increases the vertical deflection response of all three seal types, although, minimal increases are observed for single and double seals as illustrated in Figure 10.24. A moderate increase in the vertical deflection, results in a decrease in the number of load repetitions to failure for the cape seal. Failure is defined at 0.1 *mm* for the minimum surface texture. The opposite trend is observed for the double seal, while the single seal never reaches the failure criterion.

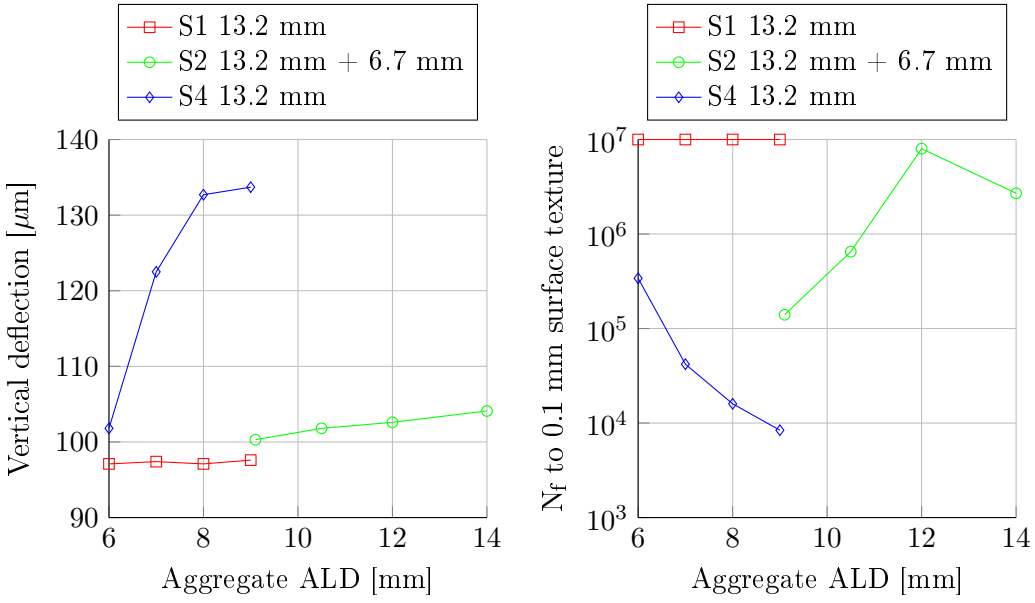

Figure 10.24: Deflection comparisons between S1, S2 & S4 for aggregate ALD and corresponding load repetitions to failure. Temperature: 25°C (S1,S2) & 10°C (S4). Base stiffness: 200 MPa. Traffic load: 20 kN-800 kPa at 80 km/h.

A summary of the texture loss development is therefore presented in Table 10.6, which provides insight into the misconception that surface texture loss depicts about embedment. The single seals possessed the highest initial surface texture and revealed the greatest measure of embedment (permanent deformation). Since it never

reached the failure criterion, it was the best performer of the three. The insight obtained from Table 10.6 suggests that selecting a certain combination of structural variables on an adequate base will reduce the risk of surface texture loss or bleeding, although the development of embedment is present.

Increasing one of the structural variables such as the binder application rate, as illustrated in Figure 10.25, results in a dramatic increases to the risk of bleeding for all the seals. A compromise is therefore reached in seal construction between sufficient binder application rates to ensure proper aggregate adhesion without increasing the risk of bleeding as result of embedment. The excessive increase in the vertical deflection of the cape seal as the 'cured-slurry-application' rate increases, is again ascribed to the loading hypothesis of cape seals. The associated load repetitions to failure however, are in close comparison to the single seals.

No other variable has as a significant influence on the embedment development as the base stiffness (Figure 10.26). The vertical deflection trends of all three seals indicate the non-linear response and sensitivity of embedment to a change in the base stiffness. In this case, the selection of 1.2 l/m^2 as the binder application rate for the single seal, allowed it to perform better than its counterparts, the double seal (2.1 l/m^2) and the cape seal (0.7 mm surface texture), with a variation in the base stiffness.

Table 10.6: Embedment comparisons for single, double and cape seal models.

Seal type	ALD [mm]	Initial texture	Remaining texture	Failure criteria[i]	PD [mm][ii]	Load repetitions
S1	6	0.75	0.58	0.1	2.26	1×10^7
S1	7	0.89	0.76	0.1	2.26	1×10^7
S1	8	1.0	0.86	0.1	2.26	1×10^7
S1	9	1.13	1.03	0.1	2.26	1×10^7
S2	9.1	0.33	0.1	0.1	1.56	1.4×10^5
S2	10.5	0.34	0.1	0.1	1.82	6.5×10^5
S2	12	0.44	0.1	0.1	2.23	8×10^6
S2	14	0.49	0.1	0.1	2.05	2.7×10^6
S4	6	0.7	0.1	0.1	1.71	3.4×10^5
S4	7	0.7	0.1	0.1	1.39	4.2×10^4
S4	8	0.7	0.1	0.1	1.23	1.6×10^4
S4	9	0.7	0.1	0.1	1.14	8.4×10^3

[i] Minimum surface texture of 0.1 mm or 10^7 load repetitions [ii] Permanent deformation

The vertical deflection in relation to the tyre contact stress was the final variable that was compared amongst the three seals, as illustrated in Figure 10.27. The deflection responses for low to medium contact stresses i.e LVs are almost similar for all three seals, while the cape seal deviates to higher deflection responses at increased

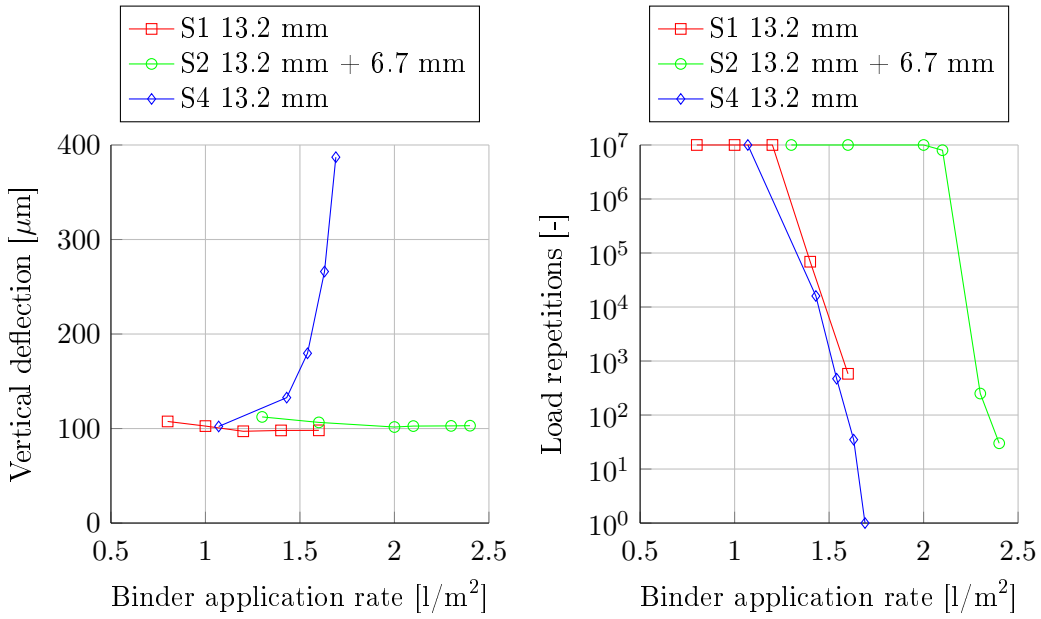

Figure 10.25: Deflection comparisons between S1, S2 & S4 for binder application rates and corresponding load repetitions to failure. Temperature: 25°C (S1,S2) & 10°C (S4). Base stiffness: 200 MPa. Traffic load: 20 kN-800 kPa at 80 km/h.

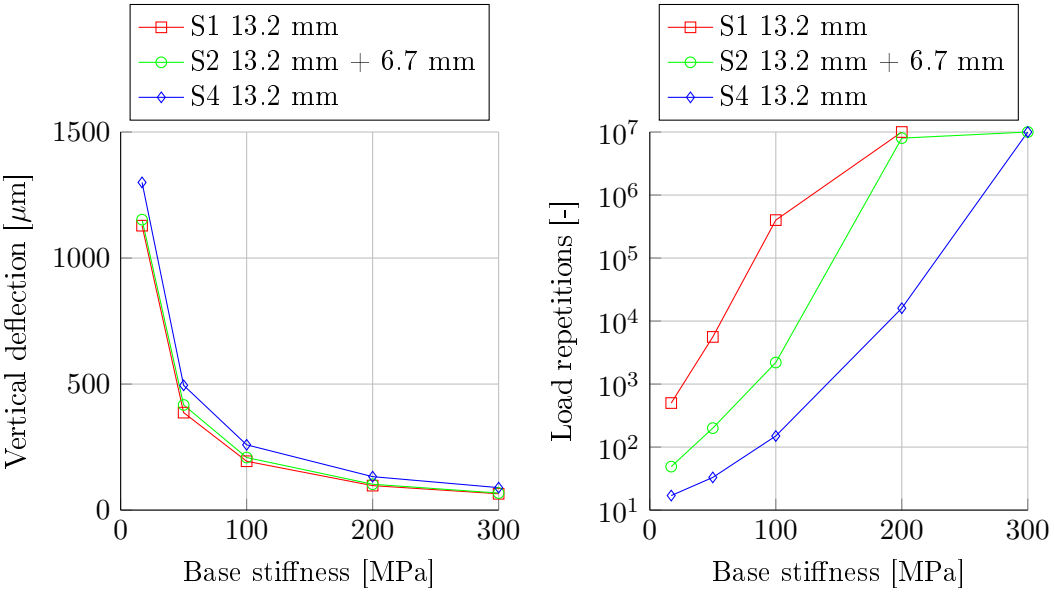

Figure 10.26: Deflection comparisons between S1, S2 & S4 for base stiffness and corresponding load repetitions to failure. Temperature: 25°C (S1,S2) & 20°C (S4). Traffic load: 20 kN-800 kPa at 80 km/h.

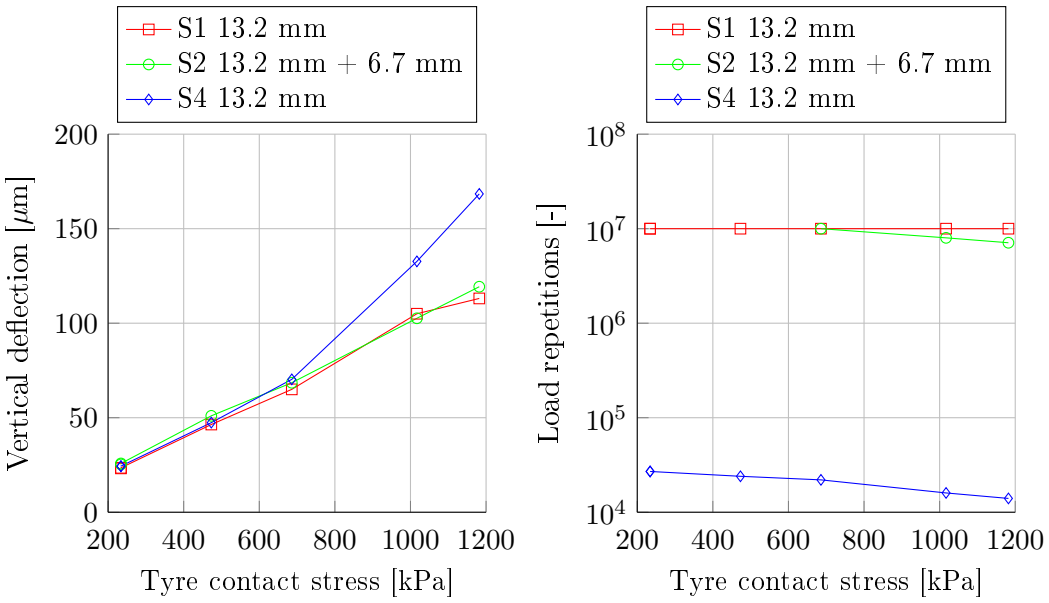

Figure 10.27: Deflection comparisons between S1, S2 & S4 for tyre inflation pressures and corresponding load repetitions to failure. Temperature: 25°C (S1,S2) & 20°C (S4). Base stiffness: 200 MPa. Travelling speed: 80 km/h.

tyre contact stresses in comparison with the other two seals. Figure 10.27 indicates that a change in the tyre contact stress does not have a significant impact on the number of load repetitions to failure, while the offset of the cape seal's load repetitions to failure is reminiscent of the discussion on Table 10.6. The three remaining variables from Table 10.1: temperature, binder age and travelling speed, did not contribute significantly to the embedment development in this study and were therefore not considered for inclusion as critical variables in the development of the primary embedment response models.

10.3.2 Primary embedment response models

The base stiffness parameter dictates the embedment response parameter almost entirely, yet embedment cannot develop without a corresponding load parameter. The tyre contact stress and base stiffness variables were therefore included in the embedment response model development. In the case of the cape seal, the initial surface texture had a significant influence on the deflection response and was therefore also included in the development process. A summary and description of all the variables are presented in Table 10.7.

Notable non-linearity obtained in the deflection response as a result of variation in base stiffness, required a multiple non-linear regression analysis to imitate the observed response results. The predicted versus observed deflections and associated

residual error distributions for the single, double and cape seals are illustrated in Figure 10.28 to Figure 10.30 respectively. The corresponding model expressions are defined in Equation 10.9 to Equation 10.11, with the model coefficients presented in Table 10.8. A statistical summary of each model is presented in Table 10.9.

Table 10.7: Variable description of the non-linear regression models for the embedment deflection results.

Variable	Description	S1-range	S2-range	S4-range
X_1	Tyre contact stress $[kPa]$	200 - 1200	200 - 1200	200 - 1200
X_2	Initial surface texture $[mm]$	NA	NA	0.1 - 1
X_3	Base stiffness $[MPa]$	50 - 450	50 - 450	50 - 450

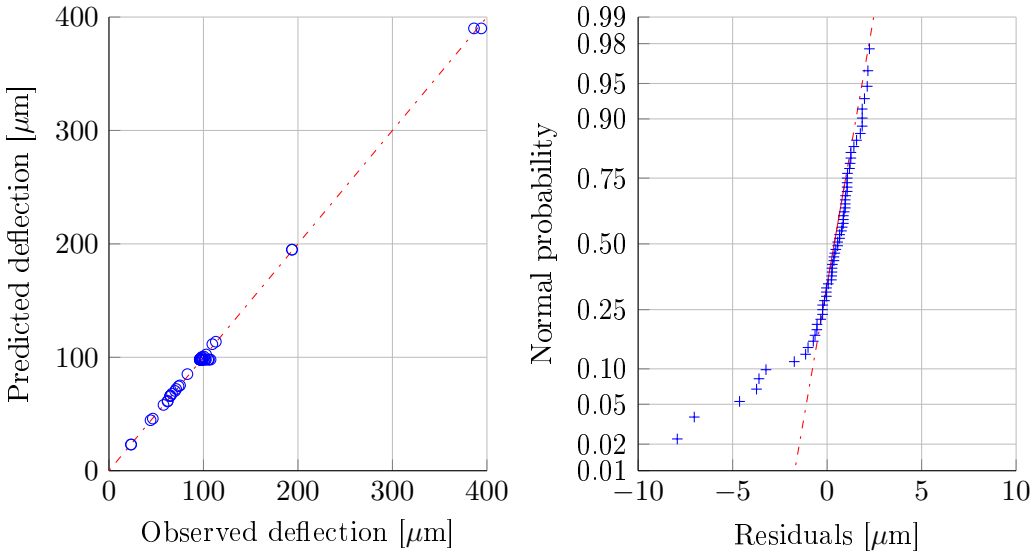

Figure 10.28: Predicted and observed response and residual distribution of the primary embedment response model for single seals (S1).

$$\tilde{Y}_{S1} = \beta_0 + \beta_1 X_1 + \beta_3 X_3^{\alpha} \tag{10.9}$$

Table 10.8: Model coefficients of the non-linear linear regression analyses for the embedment deflection results.

Seal	β_0	β_1	β_2	β_3	α
S1	-94.96	95.64E-03	–	20102	-1.0093
S2	-107.33	100.54E-03	–	17766	-0.9612
S4	73.19	156.30E-03	-341.54	18464	-0.9182

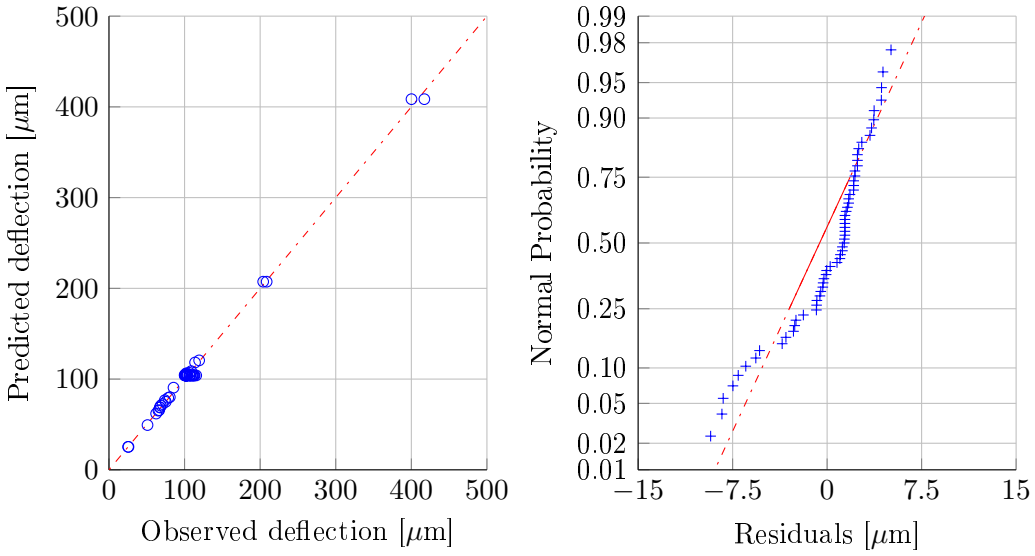

Figure 10.29: Predicted and observed response and residual distribution of the primary embedment response model for double seals (S2).

$$\tilde{Y}_{S2} = \beta_0 + \beta_1 X_1 + \beta_3 X_3^{\alpha} \tag{10.10}$$

Table 10.9: Statistical summary of the non-linear models for the embedment deflection results.

Seal	R^2	R^2-adjusted	F-value	P-value	RMSE
S1	0.998	0.998	4.03e+04	0.000	2.32
S2	0.996	0.996	1.54E+04	0.000	3.89
S4	0.979	0.978	2.0E+03	0.000	16.3

All three models exhibit an extremely close fit with 97% to 99% of the variance in the dependent variable accounted for by the independent variables. Although the single and double seal regression models do not include a term which describes a structural property, the final models remain simplistic with root mean square errors (RMSE) below 3 μm and 4 μm respectively.

The cape seal regression model on the other hand does include a term ($\beta_2 X_2$) which represents a measure of the structural properties. The initial surface texture is included in the primary embedment response model for cape seals. This model as illustrated in Figure 10.30, exhibits a greater RMSE of 16.3 μm compared to the single and double seal regression models.

$$\tilde{Y}_{S4} = \beta_0 + \beta_1 X_1 + \beta_2 X_2 + \beta_3 X_3^{\alpha} \tag{10.11}$$

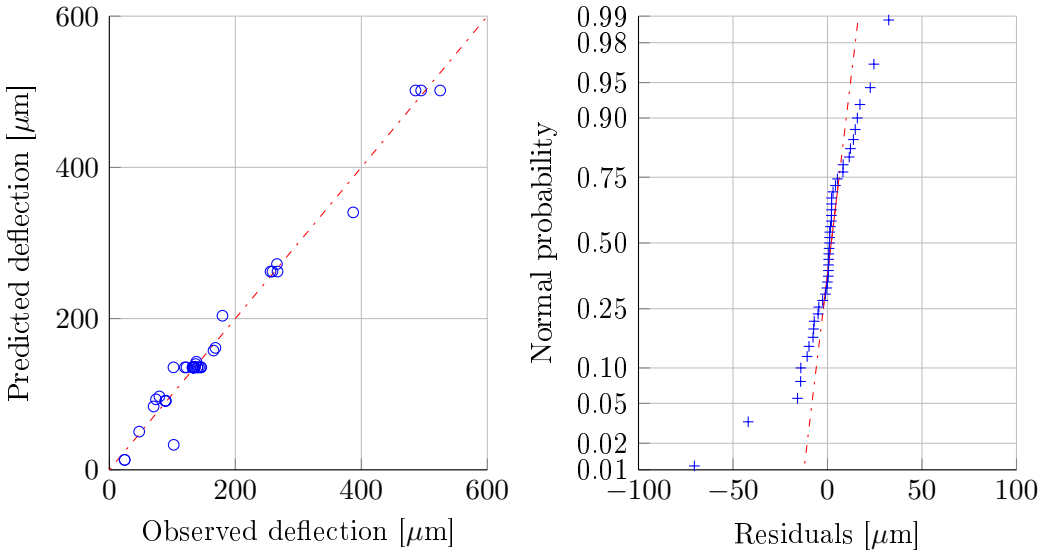

Figure 10.30: Predicted and observed response and residual distribution of the primary embedment response model for cape seals (S4).

10.4 Inter-PSRM failure comparison

As outlined at the introduction of this chapter, the PSRM consists of nine regression equations. The development process of these equations have been illustrated and thoroughly discussed. This section presents the application of the PSRM equations, by selecting two cases per seal type and comparing the response outcome. This section aims to clarify any ambiguity regarding model and material parameters utilised in computing the number of load repetitions to failure for each of the three failure mechanisms.

10.4.1 Single seal models

The variables of the two single seal cases are summarised in Table 10.10. The aim of this exercise is to investigate whether Case 1, with a weaker base support, exhibits any signs of fatigue prior to Case 2, which has a stronger base support.
Adhesive, cohesive and embedment response characteristics are determined by implementing the variables obtained from Table 10.10 into Equation 10.3, Equation 10.6 and Equation 10.9 respectively. The response results are summarised in Table 10.11 and indicate that Case 1 responds with greater shear stress values than Case 2. This is as expected since Case 1 has a weaker support structure than Case 2 and therefore exhibits also a greater deflection response.
Obtaining the number of load repetitions to the initiation of adhesive failure requires the utilisation of the adhesive transfer function as defined in Equation 4.4 of which

Table 10.10: Variable description for the single seal inter-failure comparison.

Variable	Case 1	Case 2
Aggregate nominal size $[mm]$	13.2	13.2
Aggregate spread rate $[mm]$	0.5	0.5
Aggregate ALD $[mm]$	8	8
Binder application rate $[l/m^2]$	1.0	1.2
Base stiffness $[MPa]$	50	200
Binder temperature $[°C]$	25	25
G-R parameter $[kPa]$	0.48	0.48
Tyre contact stress[i] $[kPa]$	1017	1017
Travelling speed $[km/h]$	80	80

[i] 20kN-800kPa, Table B.2, Appendix B

Table 10.11: Primary single seal response model results.

Response type	Description	Case 1	Case 2
Adhesion	Shear stress $[kPa]$	157.1	102.7
Cohesion	Shear stress $[kPa]$	168.3	71.5
Embedment	Vertical deflection $[\mu m]$	390	98

Equation 10.12 is a copy and re-printed for convenience. Since the binder temperature is at $25°C$, the material parameters a and b are selected from Table 4.6 as 3.448 MPa and -0.287 respectively. Parameter a is adjusted to kPa, while the response stresses of Case 1 and Case serve as the independent variable τ.

$$N_f = (\frac{\tau}{a})^{\frac{1}{b}} - 1 \tag{10.12}$$

Obtaining the number of load repetitions to the initiation of cohesive failure follows exactly the same process with exception that the material damage parameters a and b are selected from Table 4.4 as 2.119 MPa and -0.379 respectively. Computing the permanent deformation (embedment) from the deflection response, requires three steps of transformation as discussed in Chapter 3, Section 3.2.1.

Step 1

Convert the vertical deflection response to the permanent deformation of the initial cycle with Equation 3.25 of which Equation 10.13 is a copy and re-printed for convenience. The model parameters a_1, a_2 and b_2 are selected from Table 5.4 as 0.999, -3×10^{-5} and -0.007 respectively, while the applied load F is the applied force per aggregate in the first layer (bottom layer) of aggregates. A summary of the expected concentrated loads are presented in Table 10.12.

$$u_p = a_1 u_e + b_1 \tag{10.13}$$

Table 10.12: Expected concentrated loads per aggregate.

Nominal size	HV load [N]	LV load [N]
6.7	7.5	2.8
9.5	10	3.6
13.2	14	5
19	20	7.1

Step 2

Calculate the deformation ratio (DR) with Equation 3.27 of which Equation 10.14 is a copy and re-printed for convenience, where $PD_{N=1}$ is equal to u_p.

$$DR = \frac{PD_{N=1}}{ball\ pen.\ value} \times 100 \tag{10.14}$$

Select the appropriate model parameters b_4, a_5 and b_5 according to the base stiffness for Equation 3.29 and Equation 3.30. Make use of Table 5.4 and linear interpolation, where a weak base strength equates to 17 MPa and a strong base equals 300 MPa. In the case of model parameter a_4 use the exponential decay model as defined in Equation 10.15. Extrapolation of all model parameters are valid up to a base stiffness strength of 450 MPa. A summary of the back calculated base stiffness and corresponding ball penetration values for this study is presented in Table 10.13.

$$a_4 = 0.7797e^{-0.008(base\ stiffness)} \tag{10.15}$$

Table 10.13: Base stiffness and corresponding ball penetration values (BPV).

Base stiffness [MPa]	BPV [mm]
17	6.3
50	5.9
100	5.3
200	4.0
300	2.8
450	1.0

Step 3

Calculate the permanent deformation (embedment) of the associated deformation ratio with Equation 3.28 of which Equation 10.16 is a copy en re-printed for convenience.

$$PD = a_3 ln(N) + b_3 \tag{10.16}$$

Quantification of the response results in Table 10.11 is presented in Table 10.14 in terms of load repetitions to failure. Case 1 fails prior to Case 2 for all three modes. This is as expected since Case 1 had a weaker base in comparison to Case 2 and highlights the importance of a proper support structure.
Cohesive failure adjustments for self-healing and lateral wandering were discussed in Chapter 7. The cohesive results of Table 10.14 remain unadjusted. Adjusting the results would increase the number of load repetitions to cohesive failure to 2.25E+05 and 2.15E+06 for Case 1 and Case 2 receptively. It is reiterated that these adjustments are only for indication purposes since the factors were obtained from asphalt fatigue testing, nevertheless, the adjustments demonstrate the importance of self-healing and lateral wander.

Table 10.14: Quantification of the primary single seal response model results.

Failure Mechanism	Quantification	Case 1	Case 2
Adhesive failure	Number of load cycles to failure	4.71E+04	2.07E+05
Cohesive failure	Number of load cycles to failure	7.89E+02	7.53E+03
Embedment	Permanent deformation [mm] after; 10^7 load cycles or 0.3 mm remaining texture	5.92	2.26

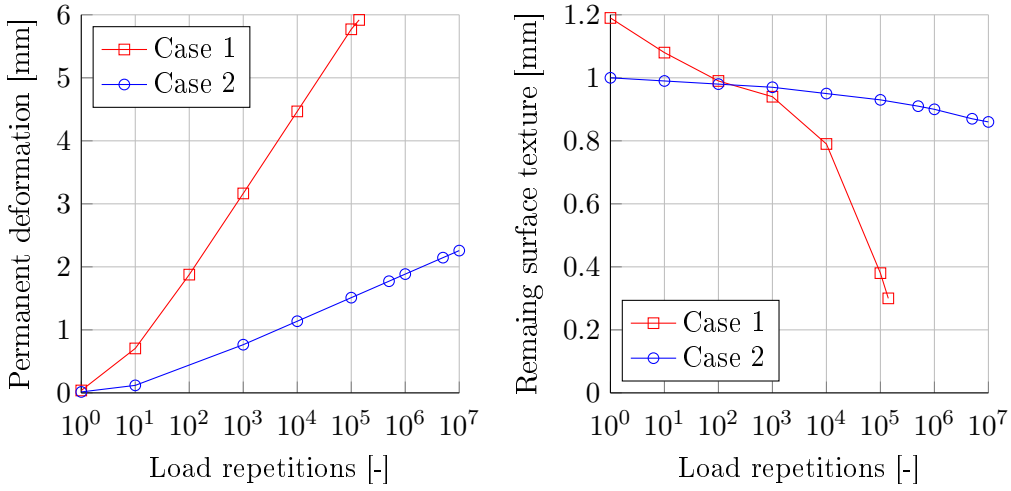

Figure 10.31: Embedment development and associated remaining surface texture for the single seal cases.

The embedment development and associated remaining surface texture for each case are illustrated in Figure 10.31. The initial 2 mm of embedment for both cases resulted in a surface texture loss of approximately 0.2 mm. Continual embedment thereafter, resulted in a greater decline of surface texture as revealed by Case 1.

10.4.2 Double seal models

The variables of the two double seal cases are summarised in Table 10.15. The aim of this exercise is to investigate the difference between a smaller and bigger double seal as represented by Case 1 and Case 2.

Adhesive, cohesive and embedment response characteristics are determined by implementing the variables obtained from Table 10.15 into Equation 10.4, Equation 10.7 and Equation 10.10 respectively. The response results are summarised in Table 10.16 and indicate that Case 1 responded with lower adhesive stress, yet a greater cohesive stress in comparison to Case 2. The smaller aggregate of Case 1 responded with a lower vertical deflection than the larger aggregate of Case 2.

Table 10.15: Variable description for the double seal inter-failure comparison.

Variable	Case 1	Case 2
Aggregate nominal size $[mm]$	13.2+6.7	19.0+9.5
Aggregate spread rate $[mm]$	1.0	1.0
Aggregate ALD $[mm]$	12	18
Binder application rate $[l/m^2]$	2.1	2.6
Base stiffness $[MPa]$	300	300
Binder temperature $[°C]$	25	25
G-R parameter $[kPa]$	0.48	0.48
Tyre contact stress[i] $[kPa]$	1017	1182
Travelling speed $[km/h]$	80	80

[i] 20kN-800kPa & 20kN-1000kPa, Table B.2, Appendix B

Table 10.16: Primary double seal response model results.

Response type	Description	Case 1	Case 2
Adhesion	Shear stress $[kPa]$	67.91	130.42
Cohesion	Shear stress $[kPa]$	58.82	33.88
Embedment	Vertical deflection $[\mu m]$	68.8	85.4

Table 10.17: Quantification of the primary double seal response model results.

Failure Mechanism	Quantification	Case 1	Case 2
Adhesive failure	Number of load cycles to failure	8.74E+05	9.00E+04
Cohesive failure	Number of load cycles to failure	1.26E+04	5.38E+04
Embedment	Permanent deformation $[mm]$ after; 10^7 load cycles or 0.1 mm remaining texture	1.04	1.04

Quantification of the response results in Table 10.16 in terms of load repetitions to failure, follows the same procedures as discussed for the single seal cases and is presented in Table 10.17. Case 2 is more susceptible to aggregate loss compared to Case 1, while Case 2 with a slightly greater load provides more resistance to cohesive fatigue in comparison to Case 1. The later results are again unadjusted for self-healing and lateral wander. Neither case shows any signs of aggravated embedment, resulting in unchanged remaining surface texture within 10 million load applications as illustrated in Figure 10.32.

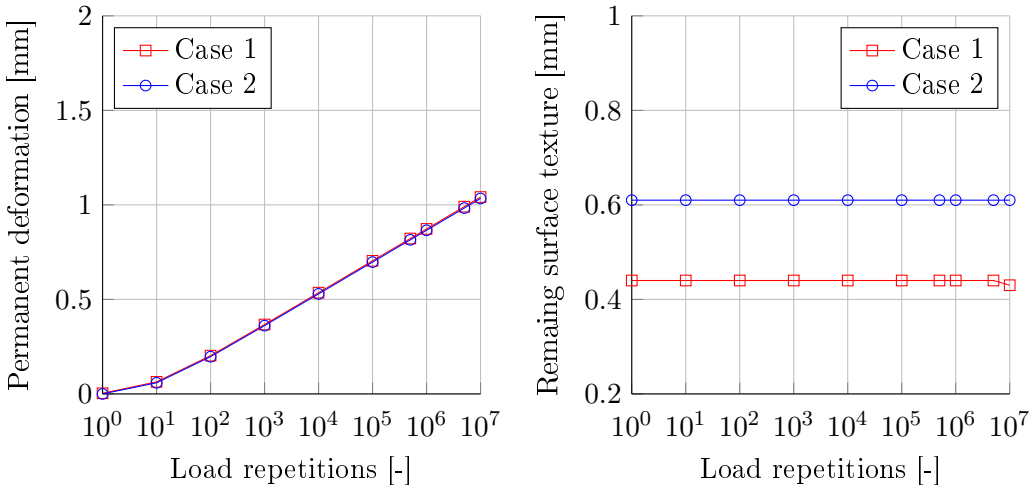

Figure 10.32: Embedment development and associated remaining surface texture for the double seal cases.

10.4.3 Cape seal models

The variables of the two cape seal cases are summarised in Table 10.18. The aim of this exercise is to investigate the difference between light vehicle (LV) and heavy vehicle (HV) wheel loads on a cape seal as represented by Case 1 and Case 2. Adhesive, cohesive and embedment response characteristics are determined by implementing the variables obtained from Table 10.18 into Equation 10.5, Equation 10.8 and Equation 10.11 respectively. The response results are summarised in Table 10.19 and indicate that all the response parameters of Case 1 is lower when compared to Case 2. This is as expected since Case 1 represents LV loads and Case 2 represents HV loads.

Obtaining the number of load repetitions to the initiation of adhesive failure, requires the implementation of the adhesive response parameter into Equation 4.10 of which Equation 10.17 is a copy and re-printed for convenience. Here, the parameter

Table 10.18: Variable description for the cape seal inter-failure comparison.

Variable	Case 1	Case 2
Aggregate nominal size $[mm]$	13.2	13.2
Aggregate spread rate $[mm]$	1.0	1.0
Aggregate ALD $[mm]$	8	8
Initial surface texture $[mm]$	0.7	0.7
Base stiffness $[MPa]$	200	200
Slurry temperature $[°C]$	10	10
Binder age $[years]$	1	1
Tyre contact stress[i] $[kPa]$	400	1017
Travelling speed $[km/h]$	80	80

[i] 6.0kN-360kPa & 20kN-800kPa, Appendix B

Table 10.19: Primary cape seal response model results.

Response type	Description	Case 1	Case 2
Adhesion	Equivalent tensile stress $[MPa]$	0.501	1.488
Cohesion	Dissipated energy $[MPa]$	0.252	2.720
Embedment	Vertical deflection $[\mu m]$	39.1	135.5

$\dot{D}$ is the damage rate, while n_0 and σ_0 are obtained from Equation 4.12 and Equation 4.13 for virgin conditions at $10°C$. Multiplying the damage rate $\dot{D}$ with the loading time and obtaining the reciprocal, results in the number of equivalent load applications to failure initiation.

$$\dot{D}(\sigma_e) = \left(\frac{\sigma_e}{\sigma_0}\right)^{n_0} \tag{10.17}$$

Obtaining the number of load repetitions to the initiation of cohesive failure, requires the implementation of the cohesive response parameter into Equation 4.5 of which Equation 10.18 is a copy and re-printed for convenience. The material parameters n and W_0 are obtained from Equation 4.6 and Equation 4.7 for virgin conditions at $10°C$.

$$N_f = \left(\frac{W_0}{W_{in}}\right)^{n} \tag{10.18}$$

Computing the permanent deformation (embedment) from the deflection response, follows the procedures as discussed for the single seal cases. The permanent deformation results are summarised with the adhesive and cohesive quantification results in Table 10.20. From this table it can be deduced that HV loads cause more damage when compared to LV loads, roughly a 100 to 150 times more.
In terms of equivalent damage factors, cape seals therefore respond differently compared to single (2 to 4 times) and double seals (8 to 14 times). The different methods

of failure quantification between the cape and single or double seals should be noted and recognised. The embedment developments however, are virtually the same for both cases as illustrated in Figure 10.33. Both cases fail in the same order: surface texture loss, ravelling and fatigue cracking.

Table 10.20: Quantification of the primary cape seal response model results.

Failure Mechanism	Quantification	Case 1	Case 2
Adhesive failure	Number of load cycles to failure	1.2E+07	1.4E+05
Cohesive failure	Number of load cycles to failure	6.4E+07	4.4E+05
Embedment	Permanent deformation $[mm]$ after; 10^7 load cycles or 0.1 mm remaining texture	1.24	1.24

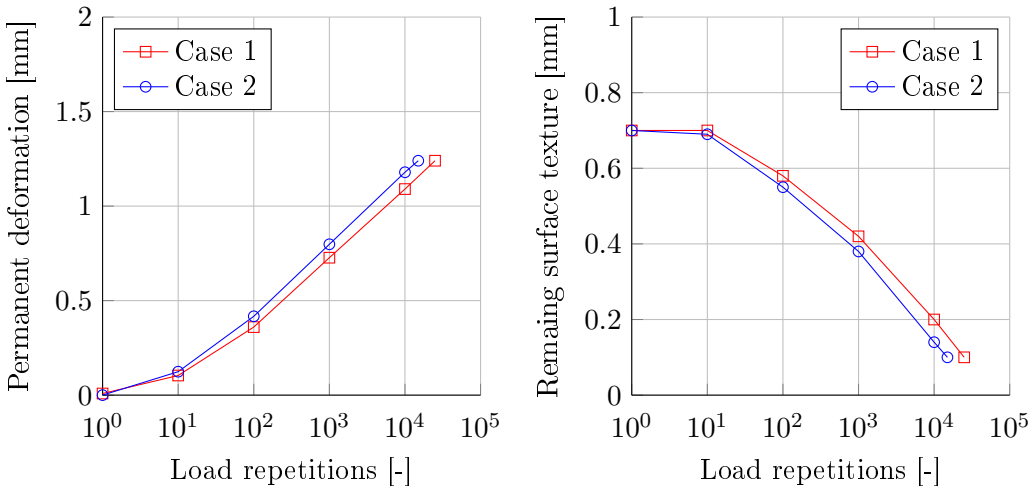

Figure 10.33: Embedment development and associated remaining surface texture for the cape seal cases.

10.5 Closure

Three different seal types were compared and discussed categorically by comparing the response and damage results according to the three failure mechanisms as presented in this study. The single and double seals respond with a shear stress parameter that represents the adhesive and cohesive critical failure parameters, while the cape seal responds with an equivalent tensile stress and dissipated energy parameter as its critical response parameters. All three seals respond with a vertical deflection parameter to signify the embedment response.

Nine regression analyses were developed, which as a collective represents the primary seal response model. These regression models relate a number of seal variables to a

primary response per damage mechanism and seal type. The responses are translated to equivalent damage via transfer functions. This study acknowledges that the response models for the cape seal were developed with mortar properties as a substitute for slurry properties in the absence of material characteristics for slurries. The overall findings will be address in the following chapter which deals with the conclusions and recommendations of this study.

11. Conclusions and recommendations

The problem statement and research objectives were defined at the introduction of this study. This chapter concludes this study by summarising the relevant findings and concluding the research objectives. Furthermore, comments are made regarding the contribution of this study towards science and recommendation towards future topics are presented to promote the research of seal models.

11.1 Summary of findings

A summary of the findings acquired throughout the finite element (FE) seal model analyses is presented in this section. Each item is addressed according to the associated failure mechanism which includes surface ravelling, surface cracking and surface texture loss.

11.1.1 Surface ravelling

The general response, obtained at the adhesive zone of the respective seal structure, is discussed in this section according the seal model variable of influence.

- **Aggregate ALD:** A general increase in the seal structure's critical response parameter was observed with an increase in the aggregate ALD for similar binder application rates. Elongated aggregate offers greater binder contact area than rounder, more cubical aggregate and results in a reduction in the critical response parameter.
- **Aggregate spread rate:** Inconsistent observations were made regarding aggregate spread rate with various seal types. Single seals illustrated and increase in the critical response parameter, while double and cape seals depicted increases and reductions of the critical response parameter, depending on the aggregate nominal size.

- **Application rates:** Reduction in the critical response parameters were observed with an increase in binder or slurry application rates. Greater application rates result in greater binder-aggregate contact area, reducing the critical response parameter.

- **Base stiffness:** A reduction in the base stiffness, increases the risk to surface ravelling of seals. Base stiffness is the most significant variable of all the seal variables investigated in this study.

- **Binder aging:** The Glower-Rowe (G-R) parameter was utilised to represent aging and indicated that an increase G-R results in an initial increase of the critical response parameter, followed by a reduction.

- **Temperature:** An increase in temperature significantly increases the risk of surface ravelling.

- **Traffic:** The tyre contact stress and not the vertical load is indicative to the risk of ravelling. A heavy vehicle (HV) does not induce 40 times more damage than one light vehicle. The damage ratios differ for the various failure mechanisms as presented in Table 11.1.

- **Vehicle speed:** Contradictory observations were obtained for an increase in speed with the different seal structures. Single and double seals indicated an increase to the risk of ravelling with increasing speeds, while the cape seal illustrated a reduction in ravelling risk with increasing speed.

- **Rolling wheel motion:** Single seals are more susceptible to ravelling than double and cape seals with regard to wheel motion conditions such as, acceleration, deceleration and traction on inclines.

11.1.2 Surface cracking

Critical responses within the binder and slurry material, indicated similar trends as observed for surface ravelling (Section 11.1.1). However, in some cases differences or anomalies were obtained. These will be discussed in this section according the seal model variable of influence.

- **Aggregate spread rate:** Double and cape seals indicated a general decrease in the respective critical response parameters, thereby reducing the risk to surface cracking with an increase in the aggregate spread rate. Single seals indicated an increase in the critical response parameter and therefore increased risk to failure.

- **Aggregate ALD:** Contradictory results were obtained amongst the three seal structures with increasing ALD. Double and cape seals indicated a general increase in the critical response parameters, while single seals illustrated a reduction of the critical response parameter.

- **Application rates:** An anomaly was observed for cape seals. An increase in the slurry application rate resulted in greater risk to surface cracking.

Table 11.1: Equivalent LV:HV damage ratios per seal type and failure mechanism.

Seal type	Adhesion	Cohesion	Embedment
Single	4.1 : 1	2.3 : 1	1 : 1
Double	14 : 1	8.5 : 1	1.2 : 1
Cape	160 : 1	330 : 1	1.6 : 1

11.1.3 Surface texture loss

Surface texture loss consists of four mechanisms as discussed in Section 2.1.3. Findings with regard to surface texture loss emanating from aggregate emebedment are discussed in this section according the seal model variable of influence.

- **Initial surface texture:** The combination of aggregate size, spread, ALD and binder application rate establishes the initial surface texture. The initial surface texture determines the maximum allowable embedment.

- **Base stiffness:** A decrease in the base stiffness dramatically increases the embedment rate and subsequent surface texture loss. The base stiffness is the single most significant parameter investigated by this study for surface texture loss.

- **Voids:** In some seal structures such as double or multiple seals, aggregate embedment is present without indications of surface texture loss. The upsurging binder first has to infiltrate the voids in the seal structure, before reducing the initial surface texture.

- **Construction embedment:** The notion that 50% of embedment occurs during construction is challenged by findings in this study which indicate that 14% of the total embedment occurs after 100 applications with a 20 ton pneumatic roller on an adequate base structure.

11.2 Conclusions

Four research objectives were set out for this study. This section presents concluding remarks regarding the research objectives and contributing aspects.

11.2.1 Objective 1 - Seal model generator

Software code was developed on a MATLAB platform that is capable of generating the architecture file, known as the input file, for a finite element simulation in ABAQUS. Conclusions regarding the seal model generator are presented in this section.

- **Graphical user interface:** The graphical user interface (GUI) greatly facilitates the compilation of the ABAQUS input files. It is user friendly and presents a large selection of seal design variables.

- **Seal structures:** The major seal structures are included in the seal model generator. These structures include: single, double and cape seals. A variation of the double seal known as the multiple seal is also included in version 1.0 of the seal model generator.

- **Geometry:** Only idealised geometrical shapes in 2D are currently used to represent the individual seal components such as the aggregate, binder coatings and base layers. Memory allocations are reserved for expansion of the seal model generator to arbitrary aggregate shapes and binder positioning, would further research commence.

- **Materials:** Quick accessing of seal materials are possible by selecting the desired combinations from the associated drop-down menus at the appropriate temperatures. The seal model generator includes a wide range of 70-100 penetration grate bitumen possibilities and reserved memory allocations for additional binder properties, would additional testing be conducted.

- **Traffic:** Measured traffic loading data, emanating from the stress in motion (De Beer and Fisher, 2013) system, forms the traffic loading signals in the 2D vertical longitudinal plane. A large range of traffic load conditions is possible and can be selected from the GUI. The FE seal models, created by the seal model generator, allow only one wheel pass per simulation.

11.2.2 Objective 2 - FE seal model analysis

Following the FE seal model simulations, vast amounts of data was post processed which resulted in attaining the final outcome of this study. Conclusions regarding this process are presented in this section.

- **Post processing:** Processing the FE seal simulation data to a single representative critical response parameter per failure mechanism, was necessary for comparison purposes. Stress conditions at the elements of interest were statistically analysed and proved successfully in providing representative response parameters for the respective failure mechanisms.

- **Seal performance:** The mechanisms for surface ravelling and cracking i.e. adhesive and cohesive failure, occur in close proximity to each other and exhibit similar response and damage trends as summarised in Section 11.1. Conclusions are drawn from the latter findings.
  a) Single seals are more sensitive to changes in the binder application rates than double seals. Low application rates dramatically increases the risk of cohesive failure for single seals.
  b) Double seals are thicker and more sensitive to vertical deflections in comparison to the more flexible single seals. Greater deflections increases the risk of cohesive failure for double seals.
  c) Double seals with greater aggregate nominal sizes are more susceptible to ravelling in comparison to double seals with smaller aggregate nominal sizes, however, more resistant to cohesive failure.
  d) The cohesive performance ranking of similar sized seals are as follows: cape, single and double seal.
  e) The difference in the cape seal transfer functions in relation to the transfer functions of the single and double seals, resulted in anomalies for comparisons in binder application rates and travelling speed.
  f) In relating LV damage to HV damage, it necessary to define the type of failure and this study indicates that different LV:HV equivalent damage ratios exists between the various seal types and failure mechanisms (Table 11.1).

- **Seal variables:** Finite element simulations per seal type were conducted according to a predefined list of variables, trimmed to allow an attainable outcome within the designated time restraints, but able to give a comprehensive overview of the seal responses with reference to geometric, material and load associated variations. This study concludes that each simulation represents a moment in time i.e a 'snap-shot'. By arranging these moments according to a

reference variable for example binder age, it becomes possible to observe the seal response over time.

- **Transfer functions:** Applying laboratory developed material damage functions to transfer the seal response to a quantifiable unit, allow the direct comparison to field or empirical data. The transfer functions of Mukandila (2015) utilised in this study are limited to a small set of materials and very conservative. Concerns were raised in Chapter 4. The conservative nature of the transfer functions hindered the model validation process. This study notes that the shear stress critical response parameters used in the transfer functions do not necessarily capture the full extent of damage caused by the traffic loads.

- **Model validation:** The FE seal model responses were within the linear viscoelastic range (Figure 4.2), verifying the model setup. The individual failure mechanisms are discussed categorically:
  a) Adhesive failure - The aggregate ALD orientation of the model excludes the possibility of isolated asperities, therefore, not creating a simulation environment that results in single load rip-off effects. Fatigue of the binder-aggregate bond is far below the results of the HDM-4 ravelling initiation calculations and is directly related to the associated transfer function.
  b) Cohesive failure - The FE seal models demonstrated that fatigue cracking validation by means of the D_0 - D_{127} radius of curvature parameter is feasible (Figure 6.3). Subsequent FE seal model response transformations with Mukandila's (2015) transfer functions, resulted in very conservative calculations that did not correspond to field observed results. Adjustments to the FE model results, to compensate for omitted fatigue characteristics such as self-healing, aging and loading rates, indicated that the validation process is fundamentally sound, but requires additional work on the transfer functions.
  c) Embedment - Single and double seal models indicated embedment results likened to results obtained in the field. No embedment validation was conducted for cape seals, since no field data for cape seals was recorded by van Zyl (van Zyl, 2015).

11.2.3 Objective 3 - Conceptual embedment model

Surface texture loss quantification as a result of aggregate embedment was not possible without the development of a conceptual embedment model. This section presents concluding remarks regarding the embedment model.

- **Concept:** A repeated load ball penetration test, demonstrated that it can be

used to link the ball penetration test values with the base material properties and embedment potential thereof.

- **Ball penetration FE model:** A FE model of the ball penetration test facilitated the back calculation process of the base material properties with the associated ball penetration values.
- **Results:** Repeated load ball penetration testing was limited to a single granular material, but provided sufficient data for a prove of concept. Ball penetration values are able to indicate the response properties of the base and the embedment potential thereof.
- **Limitations:** Machine compliance issues hindered very accurate load control. Testing was limited to limestone granular material and by expanding the base material selection would result in a more robust embedment model.

11.2.4 Objective 4 - Primary seal response model

Response relationships were defined per failure mechanism and seal type. A statistical approach resulted in the development of the primary seal response model (PSRM) that can be used to predict the critical seal response parameter, given a number of seal design variables. Conclusions are as follow:

- **Statistical approach:** Multiple linear and non–linear regression analyses were the simplest means by which the underlying relationship between the response variable and independent seal design variables could be defined. The greater the dataset, the more reliable the determined relationships become.
- **PSRM:** The PSRM is a prerequisite for this study and consists of nine regression equations, each relating a combination of variables per seal type and damage mechanism to a critical response parameter. Variables included in the regression analyses aimed at describing the seal's geometry, material condition and traffic load effects.
- **Implementation:** The PSRM is implementable into the South African Road Design System (SARDS), providing that necessary seal design variables are available. Details on SARDS falls outside the scope of this study.

11.3 Summary of contributions

The summary of contributions is divided into two categories. The first category reflects on the contribution to science of this study, while the second category considers the practical implications thereof.

11.3.1 Contribution to science

The contribution to science in the sense of bituminous surfacing seal science is twofold:

- **Seal model generator:** The seal model generator is the first of its kind that is able to generate single, double and cape seal models according to the same ideology, thereby allowing comparative analysis amongst the three different seal types. FE simulations of these models are able to give subjective insight into the responses of the respective seal seal structures according to the user selected material properties.

- **PSRM:** In the case where users do not possess FE software, the PSRM gives a predicted response for a limited number of seal design variables, with which to compare different seal designs.

11.3.2 Practical implications

Apart form the PSRM's implementation into SARDS other implications are as a result of this study.

- **LV:HV damage ratio:** This study challenges the 40:1 LV:HV equivalent damage ratio as referenced in the TRH3 (2007).

- **Construction embedment:** This study also challenges the notion that 50% of emebedment occurs during construction. This study further indicates that embedment is only one of four components that determines surface texture loss.

- **Surface deterioration models:** Pending additional work on the seal performance functions, this study demonstrated the use of FE models in providing an alternative approach to existing surface deterioration models.

11.4 Recommendations for future research

Recommendations for future research comments on the overlapping fields of model development, material testing and seal performance functions for the advancement of surfacing seal modelling.

11.4.1 Model development

Future model developments should consider cross-platform analyses to address the damage mechanisms identified in this study. Recommendations on seal modelling are as follow:

- **Surface cracking and ravelling:** The finite element method (FEM) is a good approach to investigate surface deterioration aspects due to mechanical loading, but can be combined with a computational fluid dynamic (CFD) analysis to investigate the extend of damage due to water ingress.
- **Surface texture loss:** Surface texture loss can be modelled by combining a CFD analysis with the discrete element method (DEM), since an up-surge of bitumen is expected during the aggregate orientation and the initial embedment process.
- **3D models:** Future model generation should be advanced to 3D modelling which includes arbitrary shaped aggregates with asperities, while simulating an actual rubber wheel across the surface. This has the potential to lend great insight into single load rip-off effects i.e catastrophic adhesive failure. The stress condition within the seal layer between a dual wheel load setup can also be analysed with a 3D model.
- **Test specimens:** As with the repeated ball penetration test, this study strongly advises that laboratory tests should also be modelled to develop constitutive material models that can be implemented into other meso-scale structural models.

11.4.2 Material testing

Recommendations on laboratory material testing includes three aspects and are discussed in this section.

- **Binders:** Binder testing should expand to include modified binders and bitumen rubbers. Cold, intermediate and high temperature testing should be conducted such that the corresponding master curve construction can be spaced at intervals of 5°C. Field recovered binders can be used to establish aging protocols for PAV aged binders according to the Glower-Rowe parameter.
- **Slurries:** There is a great need for constitutive material models of slurries that can be implemented into FE cape seal modelling.

- **Bases:** Repeated ball penetration tests in future should include substructures such as existing seals, asphalt surface and different granular bases. The test setup should be expanded to include a variation in the applied load rate.

11.4.3 Performance function development

The main obstacle in the FE seal model validation process was the conservative nature of the adhesive and cohesive transfer functions. It is the recommendation of this study that more efforts be applied in developing verified performance functions for the following failure mechanisms:

- **Adhesion:** The binder-aggregate adhesion bond should be investigated according to material type, aggregate surface micro texture, bond thickness, temperature and loading rate. The critical response parameter should include tensile as well as shear stress developments. A performance function should be developed and verified that is able to transfer the seal model response to measured field data results within adequate accuracy.
- **Cohesion:** A similar approach to the binder-aggregate bond is required for a cohesion performance function. Additional effects such as environmental loading and binder aging should be included. Four point bending beam performance functions have successfully been implemented for asphalt beams and may serve as a reference for seal performance functions.
- **Surface texture loss:** A performance function should be developed for surface texture loss that is able to differentiate between aggregate orientation and embedment development for various types of bases, tyre contact stresses and seal aggregate sizes.

11.5 Closure

This study quantified single, double and cape seal deterioration according to three failure mechanisms: surface ravelling, surface cracking and surface texture loss. Each seal type was modelled with the finite element method to investigate the structural response and performance in accordance with a predefined list of seal design variables. This process demonstrated that finite element surfacing seal models can reflect reality and serve as a powerful tool to investigate seal design adequacy prior construction.

List of References

Airey, G.D., Rahimzadeh, B. and Collop, A.C. (2002). Linear viscoelastic limits of bituminous binders (with discussion). *Journal of the Association of Asphalt Paving Technologists*, vol. 71.

Araya, A., Molenaar, A. and Houben, L. (2010). Characterization of unbound granular materials using repeated load cbr and triaxial testing. In: *GeoShanghai 2010 International Conference*, pp. 355–363.

Bagampadde, U., Isacsson, U. and Kiggundu, B. (2005). Influence of aggregate chemical and mineralogical composition on stripping in bituminous mixtures. *The international journal of pavement engineering*, vol. 6, no. 4, pp. 229–239.

Bahia, H.U. and Anderson, D.A. (1995). The pressure aging vessel (pav): a test to simulate rheological changes due to field aging. *ASTM Special Technical Publication*, vol. 1241, pp. 67–88.

Budavari, S. (1983). *Rock mechanics in mining practice*. 5. South African Institute of Mining and Metallurgy.

Burger, A. and van Zyl, G. (2004). Hdm4 summary on preventive and resealing work effects.

Cesbron, J., Anfosso-Ledee, F., Duhamel, D., Ping Yin, H. and Le Houedec, D. (2009). Experimental study of tyre/road contact forces in rolling conditions for noise prediction. *Journal of sound and vibration*, vol. 320, no. 1, pp. 125–144.

Cesbron, J., Anfosso-Lédée, F., Yin, H.P., Duhamel, D. and Le Houedec, D. (2008). Influence of road texture on tyre/road contact in static conditions: Numerical and experimental comparison. *Road Materials and Pavement Design*, vol. 9, no. 4, pp. 689–710.

Collop, A.C., Scarpas, A., Kasbergen, C. and de Bondt, A. (2003). Development and finite element implementation of stress-dependent elastoviscoplastic constitutive model with damage for asphalt. *Transportation Research Record: Journal of the Transportation Research Board*, vol. 1832, no. 1, pp. 96–104.

da Silva, L.F. and Campilho, R.D. (2012). *Advances in numerical modelling of adhesive joints*. Springer.

Das, P.K., Kringos, N. and Birgisson, B. (2013). Towards a multi-scale framework to optimize ageing resistance of asphaltic materials. In: *Multi-Scale Modeling and Characterization of Infrastructure Materials*, pp. 285–295. Springer.

De Beer, M. and Fisher, C. (2013). Stress-in-motion (sim) system for capturing tri-axial tyre–road interaction in the contact patch. *Measurement*, vol. 46, no. 7, pp. 2155–2173.

De Beer, M., Sadzik, E., Fisher, C. and Coetzee, C. (2005). Tyre-pavement contact stress patterns from the test tyres of the gautrans heavy vehicle simulator (hvs) mk iv+.

Frolov, A., Vasil'eva, V., Frolova, E. and Ovchinnikova, V. (1983). Strength and structure of asphalt films. *Chemistry and Technology of Fuels and Oils*, vol. 19, no. 8, pp. 415–419.

Haney, P. (2003). *The racing and high-performance tire*. TV MOTORSPORTS and SAE.

Hanson, F.M. (1934). Bituminous surface treatment of rural highways. *Transportation Research Record: Journal of the Transportation Research Board*, vol. 21, pp. 89–220.

Henderson, R., Morgan, P., Abbott, P., Watts, G., Burke, C., Harmer, C., Herrington, P. and Patrick, J. (2006). Finite-element modelling of a chip-seal road surfacing: a preliminary study. *Road and Transport Research*, vol. 15, no. 3.

Hintz, C. (2012). *Understanding Mechanisms Leading to Asphalt Binder Fatigue*. Ph.D. thesis, University of Wisconsin–Madison.

Horak, E. (1987). *Aspects of deflection basin parameters used in a mechanistic rehabilitation design procedure for flexible pavements in South Africa*. Ph.D. thesis, Department of Civil Engineering, University of Pretoria, South Africa.

Huang, Y.H. (1993). *Pavement analysis and design*.

Huurman, M. (1997). *Permanent Deformation in Concrete Block Pavements*. Ph.D. thesis, Faculty of Civil Engineering and Geosciences, Delft University of Technology, P.O.Box 5048, 2600 GA Delft, Netherlands.

Huurman, M. (2008). Lifetime optimisation tool, lot, main report, report 7-07-170-1. Tech. Rep., Delft University of Technology, Delft, NL.

Huurman, M. (2010). Developments in 3d surfacing seals fe modelling. *International Journal of Pavement Engineering*, vol. 11, no. 1, pp. 1–12.

Huurman, M., Scarpas, T., Kasbergen, C. and Milne, T. (2003). Development of a structural fem for road surfacing seals. In: *Proceedings of the 2003 International Conference on Computational and Experimental Engineering and Sciences (ICCES), Greece.(On CD-ROM.)*.

Huurman, M. and Woldekidan, M. (2007). Lot, mortar response; measurements, test interpretation and determination of model parameters, report 7-07-170-3. Tech. Rep., Delft University of Technology, Delft, NL.

ISOHDM (2004). *The Highway Development and Management Series. ISOHDM Technical Secretariat.* University of Birmingham, Edgbaston, Birmingham, United Kingdom.

Kannemeyer, L. (2014 20 May). Road network condition and mtf budget. provincial and national. In: *27th Road Pavement Forum.*

Kathirgamanathan, P., Herrington, P.R. and McIver, I. (2012). Chip seal finite element model. *Seventh International Conference on Maintenance and Rehabilitation of Pavements and Technological Control, Issue 00073.*

Kringos, N. (2007). *Physical and mechanical moisture susceptibility of asphaltic mixtures.* Ph.D. thesis, Faculty of Civil Engineering and Geosciences, Delft University of Technology, P.O.Box 5048, 2600 GA Delft, Netherlands.

Li, Y.H. and Liu, Y.X. (2011). Finite element simulation analysis of ball penetration test on asphalt pavement. *Advanced Materials Research*, vol. 243, pp. 4080–4084.

Little, D.N. and Jones, D. (2003). Chemical and mechanical processes of moisture damage in hot-mix asphalt pavements. In: *Proceedings of the Moisture Sensitivity of Asphalt Pavements–A National Seminar*, pp. 37–71.

Lombard, L. (2015). *Influence of surface seal variables on the bitumen bond strength properties.* Master's thesis, Civil Engineering, University of Stellenbosch, South Africa.

Miller, S.L., Youngberg, B., Millie, A., Schweizer, P. and Gerdes, J.C. (2001). Calculating longitudinal wheel slip and tire parameters using gps velocity. In: *American Control Conference, 2001. Proceedings of the 2001*, vol. 3, pp. 1800–1805. IEEE.

Milne, T. (2004). *Towards a performance related seal design method for bitumen and modified road seal binders.* Ph.D. thesis, Civil Engineering, University of Stellenbosch, South Africa.

Milne, T. (2010). *Revision of the South African Flexible Pavement Design Method. Inception report for Project PB/2006/D-1: Improved Damage Models for Bitiminious Materials. Part 2 - Thin Surfacings.* CSIR, South Africa.

Mo, L. (2010). *Damage development in the adhesive zone and mortar of porous asphalt concrete.* Ph.D. thesis, Faculty of Civil Engineering and Geosciences, Delft University of Technology, P.O.Box 5048, 2600 GA Delft, Netherlands.

Mo, L., Huurman, M., Wu, S. and Molenaar, A. (2008). 2d and 3d meso-scale finite element models for ravelling analysis of porous asphalt concrete. *Finite elements in analysis and design*, vol. 44, no. 4, pp. 186–196.

Molenaar, A. (2007). *Lecture notes CT 4860. Structural pavement design. Design of flexible pavements.* Delft University of Technology, Delft, NL.

Moore, D.F. (1975). *The friction of pneumatic tyres.* Elsevier Sceintific Publishing Company.

Mukandila, E. (2015). *Investigation of rheological response fatigue cohesion and adhesion of bituminous road seal materials.* Ph.D. thesis, Civil Engineering, University of Pretoria, South Africa. To be published.

Onifade, I., Jelagin, D., Guarin, A., Birgisson, B. and Kringos, N. (2013). Asphalt internal structure characterization with x-ray computed tomography and digital image processing. In: *Multi-Scale Modeling and Characterization of Infrastructure Materials*, pp. 139–158. Springer.

Paige-Green, P., Coetzer, K., Lea, J. and Semmelink, C. (2009). Appropriate use of locally available materials in concrete, bituminous surfacings and layerworks for roads in rural areas. Tech. Rep. PR93/263, Department of Tansport, Pretoria.

Pauli, T., Grimes, W., Wang, M., Lu, P. and Huang, S.-C. (2013). Development of an adherence energy test via force-displacement atomic force microscopy (fd-afm). In: *Multi-Scale Modeling and Characterization of Infrastructure Materials*, pp. 273–284. Springer.

Petersen, J., Robertson, R., Branthaver, J., Harnsberger, P., Duvall, J. and Kim, S. (1994). Binder characterisation, volume 4: test methods. *Strategic Highways Research Program, Rep. No. SHRP-A-370, National Research Council, Washington, DC.*

Poulikakos, L. (2011). *A multi-scale fundamental investigation of moisture induced deterioration of porous asphalt concrete.* Ph.D. thesis, ETH Zurich.

Rajamani, R. (2011). *Vehicle dynamics and control.* Springer.

Read, J. and Whiteoak, D. (2003). *The shell bitumen handbook.* 5th edn. Thomas Telford, 1 Heron Quay, Londen E14 4JD. ISBN 072773220X.

Rowe, G. (2015). Linear visco-elastic binder properties and asphalt pavement cracking. In: *Proceedings of the 11th Conference on Asphalt Pavements for Southern Africa CAPSA 2015.*

Rowe, G., King, G. and Anderson, M. (2014). The influence of binder rheology on the cracking of asphalt mixes in airport and highway projects. *Journal of Testing and Evaluation*, vol. 42, no. 5, pp. 1–10.

Rowe, G.M. and Brown, S.F. (1997). Fatigue life prediction using visco-elastic analysis. *Proc., International Society of Asphalt Pavements.*

SANS-3001-BT10:2013 (2013). *SOUTH AFRICAN NATIONAL STANDARD. Civil engineering test methods. Part BT10: Ball penetration test for the design of surfacing seals.* SABS Standards Division, Private Bag X191 Pretoria 0001 South Africa, 1st edn.

SAPEM (2014). *South African Pavement Engineering Manual. Chapter 4: Standards.* South African National Roads Agency Ltd, 2nd edn.

Shan, L., Tan, Y., Underwood, S. and Kim, Y.R. (2010). Application of thixotropy to analyze fatigue and healing characteristics of asphalt binder. *Transportation Research Record: Journal of the Transportation Research Board*, vol. 2179, no. 1, pp. 85–92.

Tabatabaee, H.A. and Bahia, H.U. (2014). Establishing use of asphalt binder cracking tests for prevention of pavement cracking. *Road Materials and Pavement Design*, , no. ahead-of-print, pp. 1–21.

Tehrani, F.F., Allou, F., Absi, J. and Petit, C. (2013). Investigation on mechanical properties of bituminous materials through 2d/3d finite element numerical simulations. In: *Multi-Scale Modeling and Characterization of Infrastructure Materials*, pp. 79–87. Springer.

TG1 (2007). *Technical Guideline: The use of Modified Bituminous Binders in Road Construction*. Asphalt Academy c/o CSRI Built Environment, Second Edition.

Theyse, H. (2008). *Revision of the South African Flexible Pavement Design Method, Project SAPDM - LP, System Design: HDM4 Deterioration Models - Part 1 Pavement Models*. Pavement Modelling Corporation, 1397 Starkey Ave Waverley 0186 South Africa.

Thomas, J., David, W. and Frank, S. (2006). Minnesota seal coat handbook. Tech. Rep., Minnesota: Minnesota Local Road Research Board.

Thothela, T., Robertson, G. and Jenkins, K. (2011). Improving the durability of seal aggregate by precoating.

Tielking, J.T. and Roberts, F.L. (1987). Tire contact pressure and its effect on pavement strain. *Journal of Transportation Engineering*, vol. 113, no. 1, pp. 56–71.

TRH3 (2007). *Technical Recomendations for Highways. Design and Construction of Surfacing Seals*. South African National Roads Agency Ltd, Version 1.5, PO Box 415 Pretoria 0001 South Africa.

van den Berg, J. (2014). *The influence of filler content on the performance of unbound granular material in pavement layers*. Master's thesis, Civil Engineering, University of Stellenbosch, South Africa.

van Zyl, G. (2007). Measurement and interpretation of input parameters used in the sa surface seal design method. In: *Procedings of the 9th Conference on Asphalt Pavements for Southern Africa (CAPSA'07)*, pp. 159–179. Document Transformation Technologies cc. ISBN 978-1-920017-32-3.

van Zyl, G. (2015). *Overview of long term seal performance*. Ph.D. thesis, Civil Engineering, University of Stellenbosch, South Africa. To be published.

van Zyl, G., Muller, J. and Sadler, D. (2012). Bitumen emulsion in sprayed seals: Experience and current best practice in south africa. Unpublished document.

Woldekidan, M.F. (2011). *Response Modelling of Bitumen, Bituminous Mastic and Mortar*. Ph.D. thesis, Faculty of Civil Engineering and Geosciences, Delft University of Technology, P.O.Box 5048, 2600 GA Delft, Netherlands.

Woodside, A., Wilson, J. and Xin Liu, G. (1992). The distribution of stresses at the interface between tyre and road and their effect on surface chippings. In: *International Conference on Asphalt Pavements, 7th, 1992, Nottingham, United Kingdom*, vol. 3.

Woodward, W., Woodside, A., Yacoob, H. and Maguire, S. (2005). Smaller stone size surface dressings for high stone surface mixes. Tech. Rep., Transport and Road Assesment Centre, University of Ulster, Northern Ireland.

Yaacob, H., Woodward, D. and Woodside, A. (2007). Predicting chip seal embedment. In: *Fifth International Conference on Maintenance and Rehabilitation of Pavements and Technological Control (MAIREPAV5)*.

Zelelew, H., Mahmoud, E. and Papagiannakis, A. (2013). Micromechanical simulation of the permanent deformation properties of asphalt concrete mixtures. In: *Multi-Scale Modeling and Characterization of Infrastructure Materials*, pp. 421–432. Springer.

Zelelew, H. and Papagiannakis, A. (2011). A volumetrics thresholding algorithm for processing asphalt concrete x-ray ct images. *International journal of pavement engineering*, vol. 12, no. 6, pp. 543–551.

Appendices

A. Surfacing deterioration models

Illustrations and variable definitions pertaining to this study and utilised in the HDM-4 (ISOHDM, 2004) pavement deterioration models of surfacing seals are presented in this appendix. This appendix is a summary of extracts emanating from the pavement deterioration models draft report as prepared by Theyse (2008).

A.1 Performance simulation

This section focuses on the HDM-4 material classification system as well as the definitions of several general variables related to traffic, climate and project history. These variables are used in the formulation of the pavement structure and deterioration models.

A.1.1 HDM-4 material classification

The HDM-4 pavement classification system for bituminous pavements is summarised in Table A.1, while Table A.2 provides a description of the material codes used by HDM-4.

Table A.1: HDM-4 bituminous pavement classification.

Surface type	Surface material	Base type	Base material	Pavement type
ST	SBSD, PM, DBSD, SL, CAPE, etc.	GB	NG, CRS, WBM, etc.	STGB
		AB	AB, EB, etc.	STAB
		SB	CS, LS, etc.	STSB
		AP	TNA, FDA, etc.	STAP
		RB	JUC, RBC, CUC, etc.	STRB

Table A.2: HDM-4 material classification.

Surface type	**Surface material**
ST - Surface treatment	SBSD - Single bituminous surface dressing PM - Penetration macadam DBSD - Double bituminous surface dressing SL - Slurry seal CAPE - Cape seal
Base type	**Base material**
GB - Granular base	NG - Natural gravel CRS - Crashed stone WM - Waterbound macadam
SB - Stabilised base	CS - Cement stabilised LS - Lime stabilised
AB - Asphalt base	AB - Asphalt base EB - Emulsified base
AP - Asphalt pavement	TNA - Thin asphalt surfacing FDA - Full depth asphalt
RB - Rigid base	JUC - Jointed un-bonded concrete RBC - Reinforced bond concrete CUC - Continuously un-bonded concrete

A.1.2 Construction quality indicators

The HDM-4 uses three construction quality indicators:

a) CDS - The construction defects indicator for bituminous surfacing layers.

b) CDB - The construction defects indicator for base layers.

c) COMP - The relative compaction indicator.

The CDB is a continuous variable ranging from 0 (no defects) to 1.5 (several defects). The foactors affecting the value of the CDB indicator are listed in Table A.4 and the contributions from the individual defects are added to obtain the total CDB.

Table A.3: Construction defects indicator for bituminous surfacing layers.

Condition	**Description**	**CDS**
Dry/brittle	Binder content about 10% below optimal aged binder	0.5[i]
Normal	Fresh binder at optimal binder content	1.0
Rich/soft	Binder content about 10% above optimal	1.5

[i] 0.5 indicating worst condition and 1.5 indicating best condition

Table A.4: Construction defects indicator for base layers.

Base construction defect	CDB
Poor gradation of material	0.5
Poor aggregate shape	0.5
Poor compaction	0.5

Table A.5: Relative compaction values.

Compliance with density specification	COMP(%)
Full compliance in all layers	100
Compliance in some layers	95
Reasonable compliance in most layers	90
Poor compliance in most layers	85

A.1.3 Summary of traffic, climate and history variables

Table A.6 provides a summary of the traffic, climate and history variables used by the HDM-4 and this study. Figure A.1 provides more detail on the history variables. The AGE1 variable is reset at any activity ranging from preventative maintenance to reconstruction or new construction. The AGE2 variable is reset if any activity ranging from reseal to new construction is performed. AGE3 is rest in case of an overly, reconstruction or new construction while AGE4 is reset in case of reconstruction or new construction.

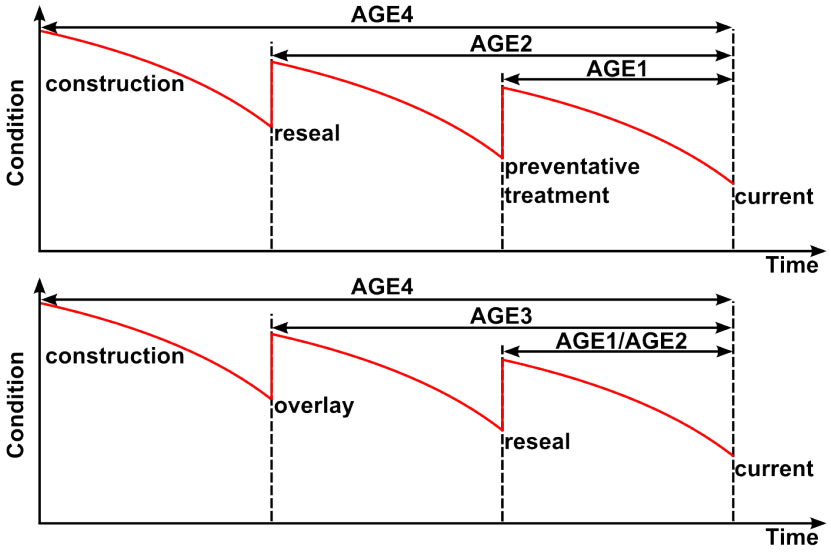

Figure A.1: Illustration of history variables.

Table A.6: Definition of traffic, climate and history variables.

Category	Description	Variable
Traffic	Annual average daily traffic in both directions	AADT
	Total number of axles for all vehicles per year (million/lane)	YAX
	Total number of axles per year for vehicle class 'k' (million/lane)	YAX_k
	Annual traffic volume for vehicle class 'k'	T_k
	Number of axles per vehicle for vehicle class 'k'	$NAXLES_k$
	Effective number of lanes for the road section	ELANES
	Number of standard axles per heavy vehicle for vehicle class 'k'	$ESALF_k$
	Annual total number of equivalent standard axles (million/lane)	YE4
	Cumulative number of equivalent standard axles since last rehabilitated (million/lane)	NE4
	Flow of heavy commercial vehicles (vehicles/lane/day)	QCV
	Average daily heavy vehicles (>3.5 tonne) in both directions	ADH
	Number of equivalent light vehicle passes per year	△NELV
	Average daily light vehicles (>3.5 tonne) in both directions	ADL
Climate	Mean monthly precipitation (mm/month)	MMP
History	Preventative treatment age	AGE1
	Surfacing age	AGE2
	Rehabilitation age	AGE3
	Base age	AGE4

A.2 Surface deterioration models

The HDM-4 presents a number of surface deterioration models. The models that are of particular interest for this study includes: crack initiation, ravelling initiation and texture depth loss. These models are presented in this section. Models that are not discussed here can be found elsewhere (ISOHDM, 2004).

A.2.1 Crack initiation

Structural cracking is effectively load, age and environmental associated cracking (ISOHDM, 2004). The model calculates the surface deterioration in two phase. The fist phase calculates the number of years to crack initiation. The second phase determines the crack progression as a percentage of total carriageway area. The HDM-4 makes further distinction by characterising the severity of the crack width as follows and have separate models for the initiation and progression of 'all' and 'wide' cracking classes:

a) Class 1: Crack width $\leq$ 1 mm

b) Class 2: 1 mm $<$ Crack width $\leq$ 3 mm

c) Class 3: Crack width > 3 mm without spalling

d) Class 4: Crack width > 3 mm with spalling

Wide structural cracking and crack progression are not considered in this study since fatigue cracking i.e. initiation of material micro cracking is the focus area for the cohesive failure criterion. Calculations for wide cracking and crack progression can be found elsewhere (ISOHDM, 2004). Figure A.2 illustrates the logic for calculating the crack initiation for all structural cracks (ICA). The input variables presented in Figure A.2 are direct input variables while other variables are derived as illustrated Figure A.3.

$$ICA = K_{cia}\{CDS^2 a_0 e^{\left[a_1 SNP + a_2\left(\frac{YE4}{SNP^2}\right)\right]} + CRT\} \tag{A.1}$$

$$\begin{aligned} ICA =& K_{cia}\{CDS^2[max(max\left\{\left(1-\frac{PCRW}{a_3}\right),0\right\} \\ & \times a_0 e^{\left[a_1 SNP + a_2\left(\frac{YE4}{SNP^2}\right)\right]}, a_4 HSNEW)] + CRT\} \end{aligned} \tag{A.2}$$

$$\begin{aligned} ICA =& K_{cia}\{CDS^2[max(max\left\{\left(1-\frac{PCRW}{a_3}\right),0\right\} \\ & \times a_0 e^{\left[a_1 SNP + a_2\left(\frac{YE4}{SNP^2}\right)\right]}, a_4)] + CRT\} \end{aligned} \tag{A.3}$$

$$ICA = K_{cia}\{CDS^2 a_0 e^{a_1 HSE + a_2 lnCMOD + a_3 (YE4)(DEF)} + CRT\} \tag{A.4}$$

$$\begin{aligned} ICA =& K_{cia}\{CDS^2[(0.8KA + 0.2KW)(1 + 0.1HSE) + (1 - KA) \\ & \times (1 - KW) a_1 HSE + a_2 lnCMOD + a_3 (YE4)(DEF)] + CRT\} \end{aligned} \tag{A.5}$$

Table A.7: Definitions of variables utilised in the ICA crack initiation models.

Description	Variable
Time (years) to crack initiation for all structural cracks	ICA
Construction defects indicator for seals	CDS
Annual number of equivalent standard axles (millions/lane)	YE4
Average annual adjusted structural number of pavement	SNP
Mean Benkelman beam deflection in both wheel paths (mm)	DEF
Resilient modulus of stabilised material (GPa)	CMOD
Thickness of most resent surfacing (mm)	HSNEW
Combined thickness of previous underlying surfacing layers (mm)	HSOLD
Area of all structural cracking before most recent reseal (%)	PCRA
Area of wide structural cracking before most recent reseal (%)	PCRW
Crack retardation time (years) due to maintenance	CRT

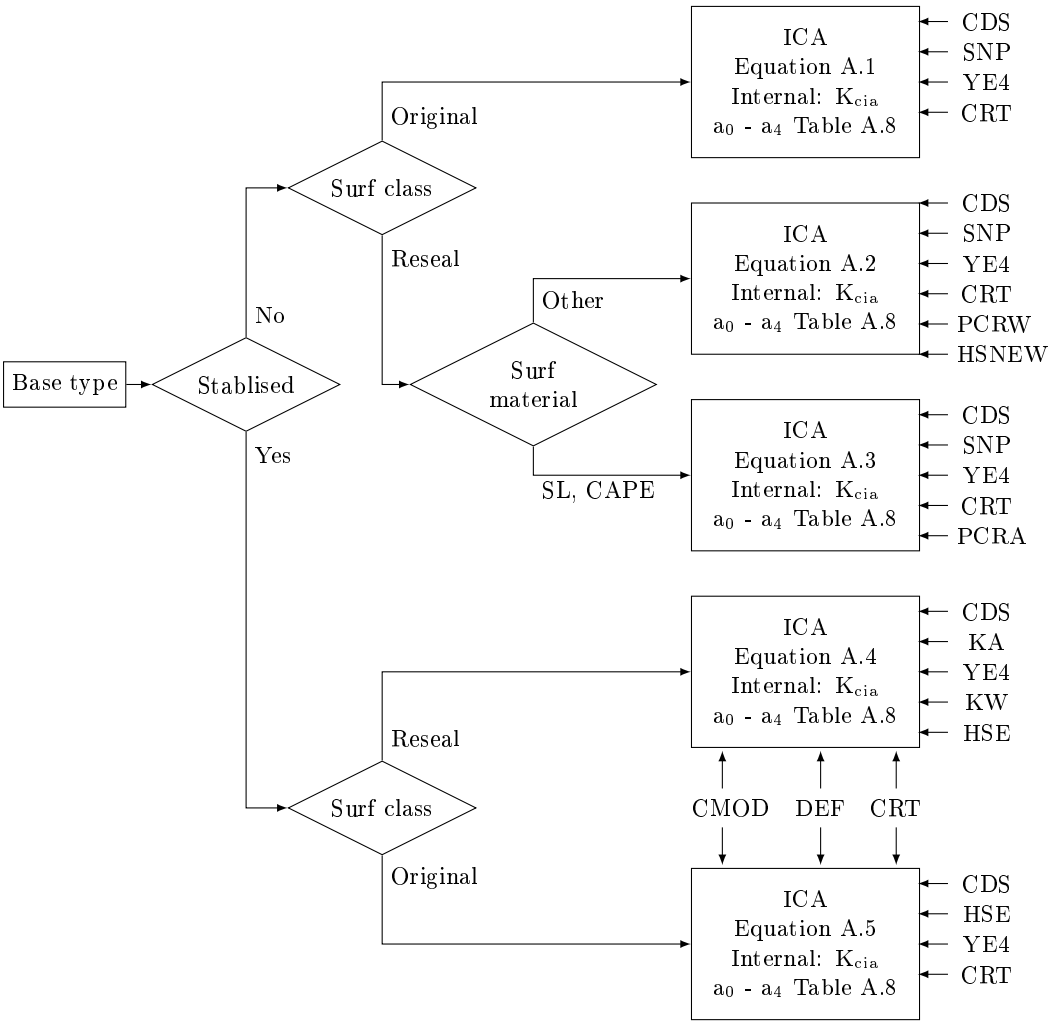

Figure A.2: Flowchart for the HDM-4 crack initiation models - all structural cracks.

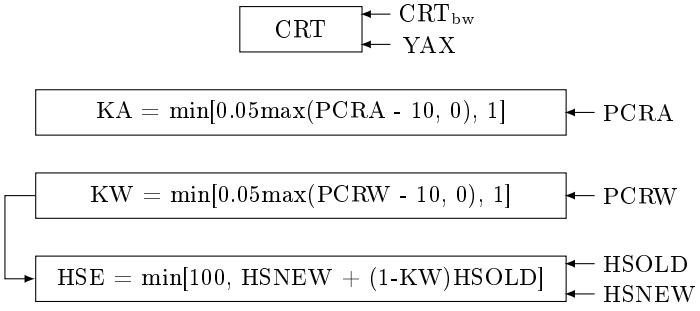

Figure A.3: Derived variables for crack initiation - all structural cracks.

Table A.8: Coefficients for all structural crack initiation.

Pavement type	Surface material	HSOLD	Equation	a_0	a_1	a_2	a_3	a_4
STGB	All	0	A.1	13.2	0	-20.7	-	-
	All except SL, Cape	> 0	A.2	13.2	0	-20.7	20	0.22
	SL, Cape	> 0	A.2	13.2	0	-20.7	20	1.4
STAB	All	0	A.1	13.2	0	-20.7	-	-
	All except SL, Cape	> 0	A.2	4.21	0.14	-17.1	20	0.12
	SL, Cape	> 0	A.3	4.21	0.14	-17.1	30	.022
STAP	All	> 0	A.2	4.12	0.14	-17.1	20	0.12
STSB	All	0	A.4	1.12	.035	.371	-.42	-2.9
		> 0	A.5	1.12	.035	.371	-.42	-2.9

A.2.2 Ravelling initiation

The HDM-4 ravelling initiation model estimates the number of years to ravelling initiation (IRV). The diagram for ravelling initiation is illustrated in Figure A.4, while the variables used in the model are listed in Table A.9. The modelling of ravelling initiation also uses a ravelling retardation factor RRF which is a function of the maintenance.

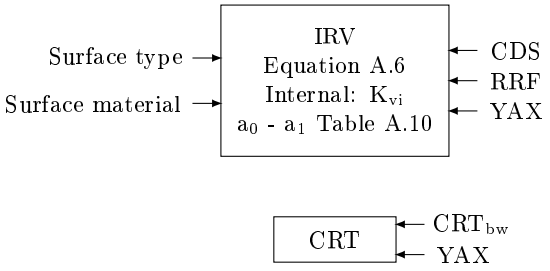

Figure A.4: Flowchart for the HDM-4 ravelling initiation model.

Table A.9: Definitions of variables utilised in the ravelling initiation model.

Description	Variable
Time (years) to ravelling initiation	IRV
Construction defects indicator for seals	CDS
Annual number of axles for all vehicle classes (million/lane) in analysis year	YAX
Ravelling retardation factor	RRF

$$IRV = K_{vi}(CDS)^2 a_0 (RRF) e^{a_1 YAX} \tag{A.6}$$

Table A.10: Coefficients for the initiation of ravelling.

Surface type	Surface material	a_0	a_1
ST	All except SL, Cape	10.5	-0.156
	SL, Cape	14.1	-0.156

A.2.3 Texture depth loss

The initial surface texture depth emanates from the sand patch test. The logic for the HDM-4 texture depth loss model is illustrated in Figure A.5, while Table A.11 defines the variables that are utilised in the texture depth deterioration model.

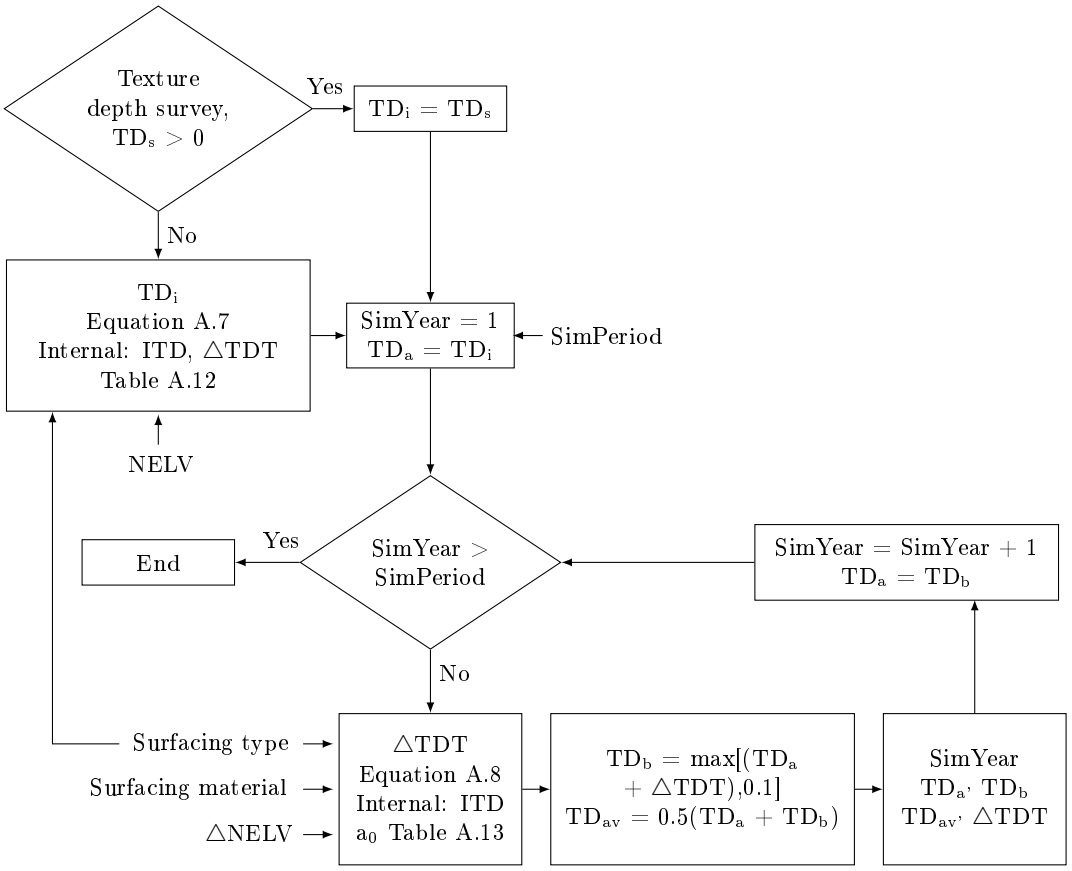

Figure A.5: Flowchart for the HDM-4 texture loss model.

$$TD_i = ITD(1 - \triangle TDT log NELV) \tag{A.7}$$

$$\triangle TD = K_{td}\{ITD - TD_a - a_0 ITD log(10^{\frac{ITD-TD_a}{a_0 ITD}} + \triangle NELV)\} \tag{A.8}$$

Table A.11: Definitions for variables in the HDM-4 texture depth loss model.

Description	Variable
Texture depth (mm) measured at the time of design investigation	TD_s
Initial value of the texture depth (mm) used in simulation	TD_i
Initial texture depth (mm) at the time of surfacing layer construction	ITD
Rate of texture depth change	$\triangle$TDT
Number of equivalent light vehicle passes since construction of surface layer	NELV
Number of equivalent light vehicle passes for analysis year	$\triangle$NELV
Texture depth (mm) at the start of the analysis year	TD_a
Texture depth (mm) at the end of the analysis year	TD_b
Incremental change (mm) in the texture depth for the analysis year	$\triangle$TD
Annual average texture depth for the analysis year	TD_{av}

Table A.12: Coefficients for the HDM-4 initial texture depth at simulation start.

Surface type	ITD	$\triangle$TDT
SL	0.7	0.006
SBSD & DBSD	1.5 (fine)	0.120
	2.5 (course)	0.120

Table A.13: Coefficients for the HDM-4 texture depth deterioration model.

Surface type	Surfacing material	ITD	a_0
ST	SBSD	2.5	0.120
	DBSD	2.5	0.120
	CAPE	0.7	0.006
	SL	0.7	0.006
	PM	1.5	0.008

B. Seal model generator

A graphical user interface (GUI) was developed during this study to assist with quick compilation of 2D Abaqus seal model input files. The GUI was developed in Matlab and included a wide spectrum of variables with sub-variations. This appendix gives an overview of Seal_Generator (Figure B.1), a finite element model creator for seals.

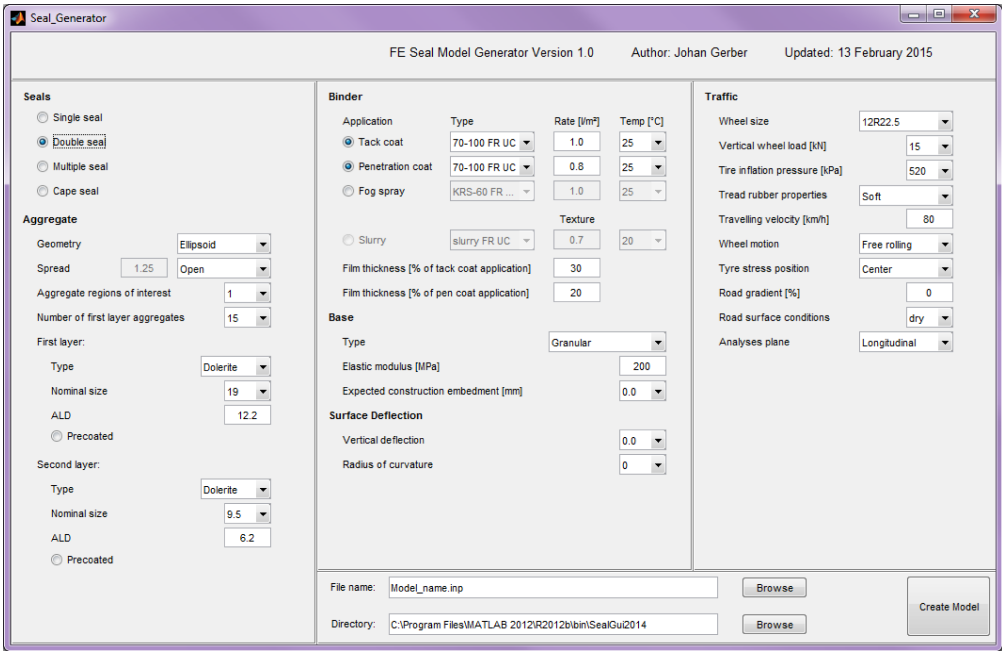

Figure B.1: Idealised seal model generator front end.

B.1 Seal selection

The GUI requires the user to select one of four seal types by selecting the desired radio button as illustrated in Figure B.2. The seal type selection dictates the variable requirements for a successful input file.

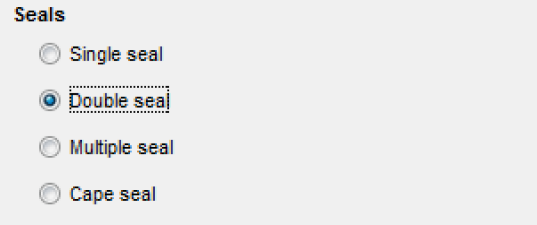

Figure B.2: GUI seal selection.

B.2 Aggregate selection

Aggregate selection consist of three parts: General properties, First layer and Second layer aggregate properties.

B.2.1 General properties

The general properties includes a drop-down menu to select the geometry of the aggregate. Only ellipsoids are currently available. The user can define the adjacent aggregate to aggregate spacing (spread) in millimetres. Predefined sets in the corresponding drop-down menu includes: Open, Interlock and Offset. An open spread is available for all seal types, while interlock i.e. aggregate to aggregate edge contact is only allowed for single seals. Offset, is a user-defined distance that is greater than 0 mm.

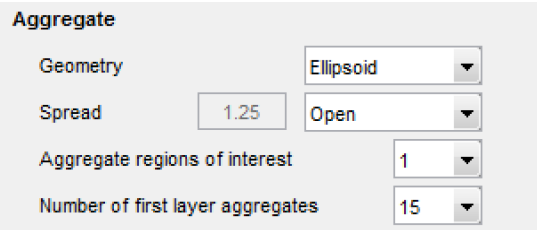

Figure B.3: Aggregate general properties.

The regions of interest are used to define the number of aggregates that require an adhesive zone. The number can be selected from the drop-down menu. The reference aggregate is at the centre of the FE model and additional pairs are allocated outwardly conforming to model symmetry around the centre aggregate. The number of first layer (bottom layer) aggregates can also be selected from the corresponding drop-down menu, with the minimum being 5 and the maximum 99. When selecting a seal type, a default number of aggregates for that seal are prescribed, but can be overridden by the user.

B.2.2 Firsts layer

Single and cape seals have only one layer of aggregate. The type and dimensions of the representative ellipsoid are defined under the properties of the first layer. The GUI makes provision for three aggregate types, but only properties for dolerite is currently available. The nominal aggregate size (mm) can be selected from the corresponding drop-down menu, while the ALD (mm) is a user defined parameter (Figure B.4). The first layer aggregates are replicates off each other.

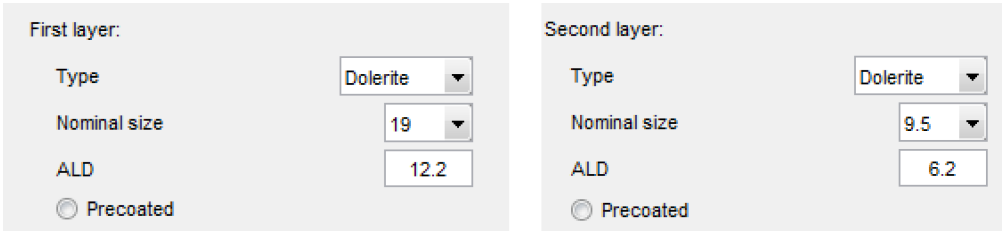

Figure B.4: First and second layer aggregate properties.

B.2.3 Second layer

The second layer of aggregates are reserved for double and multiple seals. The number of aggregates depend on the number of first layer aggregates. These aggregates are not identical in size but are controlled by the ALD (mm) and nominal size (mm). Seal_Generator runs a number of iterations to pack the top structure according to the specifications of the top and bottom structures. In both the first and second layers, Seal_Generator makes provision for pre-coated aggregates, however, no properties are currently installed in the model architecture. This option is therefore not yet available.

B.3 Binder selection

The binder type, application rates and operating surface temperatures can be selected by the user for the various binder coatings in a seal structure. These variables can be selected with their corresponding drop-down menus or adjusted in the user-defined text-boxes as illustrated in Figure B.5. Some restriction apply however and is discussed below at the relevant application.

B.3.1 Tack coat

All seal structures require a tack coat. Each binder type is represented by its corresponding Prony series for the selected operating temperature. The architecture

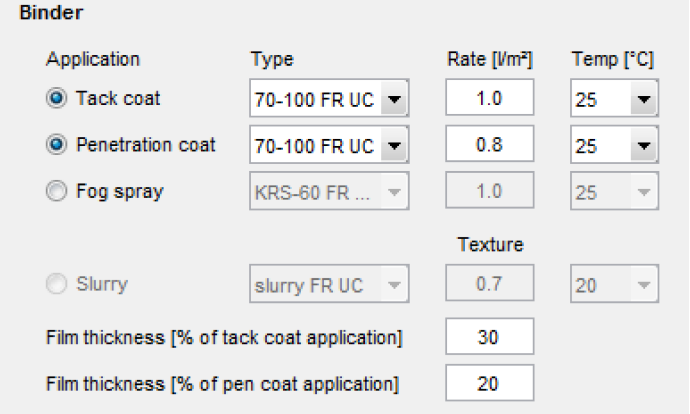

Figure B.5: Binder selection properties.

currently includes a complete set of the 70-100 penetration grade binder for virgin, PAV and field extracted data. Memory allocations are preserved, would additional binder testing commence. A complete temperature set ranges from 0°C to 50°C. The minimum and maximum tack coat application rates are defined at 0.5 l/m^2 and 3.3 l/m^2.

B.3.2 Penetration coat

The penetration coat is reserved for double and multiple seals. The same restrictions apply for the penetration coat than for the tack coat. However, the maximum application rates are reduced in cases where 3.3 l/m^2 exceed the available voids between the aggregates.

B.3.3 Fog spray

A fog spray layer is reserved for single, double and multiple seals. However, in the case of adjacent aggregate to aggregate edge contact for single seals, a fog spray layer is currently not allowed due to FE computational difficulties. The minimum and maximum fog spray application rates are defined at 0.8 l/m^2 and 1.2 l/m^2.

B.3.4 Slurry application

A slurry application is reserved for a cape seal. Contrary to binder application rates which is measured in l/m^2, the slurry application is controlled by the remaining surface texture of a cured application. The minimum surface texture is defined at 0.1 mm according to the sand patch test.

B.3.5 Film thickness

The tack coat film thickness is a user defined fraction that describes the minimum film thickness measured between the bottom of the seal aggregate and base layer. In the case of double and multiple seals, a penetration coat fraction is also specified by the user which describes the minimum film thickness of the penetration coat between the first and second layer of aggregates.

B.4 Base properties

The base properties allow the selection of the base type with a drop-down menu. The drop-down menu selection includes granular and stabilised options, but stabilised is currently only a place holder for future developments (Figure B.6). The elastic modulus of the upper 30 mm is a user-defined variable as well as the expected construction embedment. The measure of construction embedment can be selected from the corresponding drop-down menu.

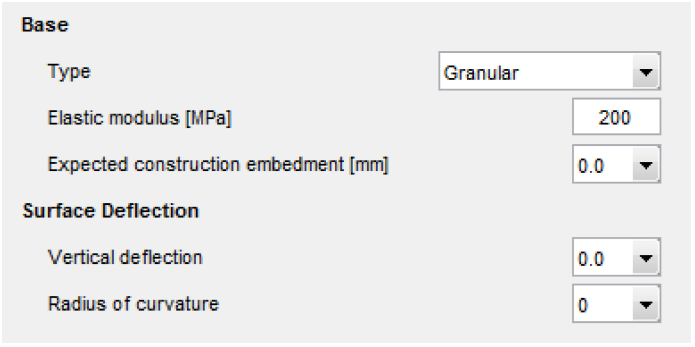

Figure B.6: First and second layer aggregate properties.

B.5 Surface deflection

Earlier developments allowed the user to control the surface deflection by specifying the maximum vertical deflection and corresponding radius of curvature (Figure B.6). This practice is outdated and the model has developed significantly since then. The developmental remnants, however, are still visible on the GUI.

B.6 Traffic selection

The traffic selection are divided in three categories: wheel load properties, wheel motion properties and the road surface conditions (Figure B.7).

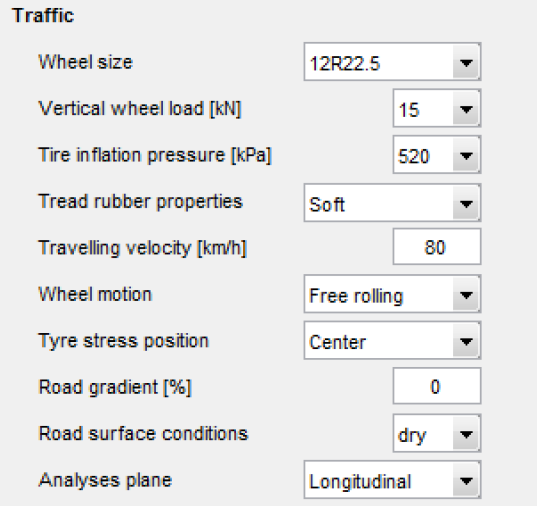

Figure B.7: Traffic variable selection.

B.6.1 Wheel load properties

The wheel load properties consists of the wheel size, vertical wheel load, tyre inflation pressure (TiP), analysis plane and the stress position within the tyre contact patch. Table B.1 summarises the wheel load combinations. Any one of the latter traffic load combinations can be acquired by adjusting the corresponding drop-down menus and selecting the desired value. Table B.2 presents the peak forces per wheel load case for the vertical-longitudinal (z-x) plane. The model was restricted to this plane and was not developed further for the vertical-lateral (z-y) plane.
The peak wheel load forces (Table B.2 to Table B.6) were obtained form Tyre Stress SEAL as discussed in Section 3.2.3. Additional adjustments are made to these forces with regard to surface texture according to Equation 2.6.

Table B.1: Wheel size and load combination as derived from Tyre Stress Seal.

Size	Class	Vertical load [kN]	TiP [kPa]
12R22.5	HV	15 20 35 40 50	520 620 720 800 950 1000
315-80R22.5	HV	20 35 40 50 75 100	520 620 720 800 950 1000
265-65R17	LV	5.4	190
245-70R16C	LV	5.4	190
195R15C	LV	6.0	360

Table B.2: Peak force conditions and contact stress per load case.

Size	Vertical load [kN]	TiP [kPa]	Position	Z-force [N]	X-force [N]	Contact stress [kPa]
12R22.5	15	520	centre	10.6	0.58	771
		620	centre	12.0	0.57	873
		720	centre	12.8	0.62	936
		800	centre	14.3	0.73	1045
		950	centre	14.4	0.86	1053
		1000	centre	14.6	0.81	1064
12R22.5	20	520	centre	9.4	0.75	686
		620	centre	10.8	0.68	791
		720	centre	13.1	0.62	960
		800	centre	13.9	0.62	1017
		950	centre	15.6	0.83	1141
		1000	centre	16.2	0.86	1182
12R22.5	35	520	centre	10.2	1.38	746
		620	centre	11.5	1.17	838
		720	centre	13.5	1.03	989
		800	centre	14.0	0.97	1021
		950	centre	16.2	0.78	1179
		1000	centre	15.9	0.75	1159
12R22.5	40	520	centre	9.4	1.38	686
		620	centre	10.9	1.31	792
		720	centre	12.7	1.17	927
		800	centre	13.8	1.13	1010
		950	centre	14.9	1.00	1089
		1000	centre	15.9	0.85	1162
12R22.5	50	520	centre	9.6	1.70	703
		620	centre	11.5	1.74	841
		720	centre	12.5	1.42	915
		800	centre	13.9	1.36	1018
		950	centre	-	-	-
		1000	centre	15.8	1.12	1152

Table B.3: Peak force conditions and contact stress per load case.

Size	Vertical load [kN]	TiP [kPa]	Position	Z-force [N]	X-force [N]	Contact stress [kPa]
12R22.5	15	520	edge	8.2	0.66	599
		620	edge	8.2	0.55	602
		720	edge	8.2	0.57	596
		800	edge	8.7	0.56	636
		950	edge	9.0	0.59	659
		1000	edge	8.6	0.60	631
12R22.5	20	520	edge	9.6	1.01	703
		620	edge	9.9	0.78	723
		720	edge	9.7	0.61	709
		800	edge	10.0	0.67	728
		950	edge	10.6	0.51	777
		1000	edge	10.7	0.55	779
12R22.5	35	520	edge	12.1	1.69	883
		620	edge	12.8	1.50	938
		720	edge	13.2	1.35	962
		800	edge	14.2	1.22	1036
		950	edge	14.6	0.98	1062
		1000	edge	14.3	0.87	1041
12R22.5	40	520	edge	13.2	2.05	962
		620	edge	13.8	1.70	1009
		720	edge	14.5	1.54	1059
		800	edge	15.1	1.43	1101
		950	edge	15.6	1.16	1141
		1000	edge	15.4	1.14	1121
12R22.5	50	520	edge	14.2	2.24	1037
		620	edge	14.8	1.99	1081
		720	edge	15.8	1.87	1156
		800	edge	16.7	1.70	1220
		950	edge	-	-	-
		1000	edge	17.2	1.47	1259

Table B.4: Peak force conditions and contact stress per load case.

Size	Vertical load [kN]	TiP [kPa]	Position	Z-force [N]	X-force [N]	Contact stress [kPa]
315-80R22.5	20	520	centre	9.0	0.67	659
		620	centre	10.7	0.72	779
		720	centre	12.2	0.86	893
		800	centre	12.6	0.82	919
		950	centre	14.5	1.01	1060
		1000	centre	15.6	1.04	1140
315-80R22.5	35	520	centre	9.1	0.95	663
		620	centre	10.5	0.91	767
		720	centre	12.7	0.73	929
		800	centre	13.4	0.69	978
		950	centre	14.8	0.72	1078
		1000	centre	16.8	0.96	1227
315-80R22.5	40	520	centre	9.1	1.05	667
		620	centre	10.5	1.05	764
		720	centre	12.8	0.87	932
		800	centre	13.7	0.81	997
		950	centre	15.1	0.82	1102
		1000	centre	17.1	0.92	1248
315-80R22.5	50	520	centre	9.6	1.31	703
		620	centre	10.9	1.18	799
		720	centre	12.3	1.21	895
		800	centre	14.1	1.25	1030
		950	centre	16.8	1.04	1223
		1000	centre	16.5	0.91	1205
315-80R22.5	75	520	centre	10.2	1.76	743
		620	centre	11.3	1.72	826
		720	centre	12.9	1.59	939
		800	centre	14.0	1.44	1025
		950	centre	16.4	1.40	1198
		1000	centre	16.8	1.35	1228
315-80R22.5	100	520	centre	10.8	2.08	786
		620	centre	11.6	2.09	845
		720	centre	13.3	1.86	971
		800	centre	14.1	1.62	1031
		950	centre	16.2	1.71	1186
		1000	centre	17.1	1.72	1248

Table B.5: Peak force conditions and contact stress per load case.

Size	Vertical load [kN]	TiP [kPa]	Position	Z-force [N]	X-force [N]	Contact stress [kPa]
315-80R22.5	20	520	edge	8.0	0.65	582
		620	edge	8.1	0.60	594
		720	edge	8.2	0.43	601
		800	edge	8.0	0.35	586
		950	edge	7.9	0.40	579
		1000	edge	8.2	0.38	597
315-80R22.5	35	520	edge	11.0	1.45	803
		620	edge	11.4	1.36	835
		720	edge	11.9	1.22	871
		800	edge	11.9	0.98	869
		950	edge	12.0	0.79	877
		1000	edge	12.4	0.98	902
315-80R22.5	40	520	edge	11.9	1.64	870
		620	edge	12.3	1.57	899
		720	edge	12.9	1.41	941
		800	edge	13.0	1.20	948
		950	edge	13.1	0.97	958
		1000	edge	13.6	1.17	991
315-80R22.5	50	520	edge	13.5	2.07	988
		620	edge	14.0	2.01	1022
		720	edge	14.5	1.70	1056
		800	edge	14.9	1.60	1087
		950	edge	15.3	1.43	1116
		1000	edge	15.5	1.36	1130
315-80R22.5	75	520	edge	16.3	2.93	1191
		620	edge	17.2	2.83	1254
		720	edge	17.9	2.47	1308
		800	edge	18.3	2.37	1337
		950	edge	19.4	2.17	1413
		1000	edge	19.7	2.12	1437
315-80R22.5	100	520	edge	18.2	3.50	1326
		620	edge	19.1	3.34	1395
		720	edge	20.1	2.97	1468
		800	edge	20.9	2.96	1522
		950	edge	22.3	2.72	1626
		1000	edge	22.7	2.67	1655

Table B.6: Peak force conditions and contact stress per load case.

Size	Vertical load [kN]	TiP [kPa]	Position	Z-force [N]	X-force [N]	Contact stress [kPa]
265-65R17	5.4	190	centre	3.2	0.72	234
		190	edge	3.7	0.62	268
245-70R16C	5.4	190	centre	3.2	0.94	234
		190	edge	2.5	0.59	183
195R15C	6.0	360	centre	6.5	0.82	473
		360	edge	5.5	0.81	399

B.6.2 Wheel motion properties

The wheel motion properties represents rolling conditions of the tyre. These properties include the travelling velocity and type of free rolling. The user can change the velocity by adjusting the corresponding text-box value. Three types of rolling can be selected by the user with a drop-down menu which includes: free rolling, driven and brake conditions. In the case of traction conditions (driven or brake), the load force distributions per load case (Table B.1) are adjusted according to Equation 3.34.

B.6.3 Road surface conditions

The final adjustments to the load force distributions are made with regard to the road surface conditions. The user can specify whether the tyre rolls on a flat surface or on an incline. If an incline is specified the the load force distributions are adjusted according to Equation 3.35. All calculations are conducted for dry surface conditions, however, provision is made in the architecture for wet conditions would research be expanded towards such conditions in future.

B.7 Model compilation

When the user is satisfied with all the model parameters a file name can be assigned to the input file and saved within the desired directory (Figure B.8). Selecting the 'Create Model' button initiates the input file compilation and meshing processes. A summary of all the input parameters is stored on the input file, including the number of FE model nodes.

Figure B.8: Input file directory and model compilation.

C. Prony series parameters

The bituminous material data utilised in this study is presented in this appendix. The data consist of: Prony series of binders and Prony series of mortar.

C.1 Prony series response parameters of binders

The Prony series consist of four parameters: the instantaneous shear modulus G_0, Poisson's ratio ν and a number of Maxwell elements which includes the normalised stiffness reduction α_i and the relaxation rate τ_i. The Prony series for each binder and condition as pertaining to this study were obtained from Mukandila (2015).
Field recovered binders are referenced to one of four acronyms which indicate the retrieval position. These acronyms include: shoulder (SHDR), outer wheel track (OWT), between wheel tracks (BWT) and the inner wheel track (IWT). The type of seal from which the field recovered binders was retrieved is indicated by: S1 for single seals, S2 for double seals and S4 for cape seals.

Table C.1: Prony series, virgin, 70-100 penetration grade binder tested at $0°C$ (Mukandila, 2015).

α_i	τ_i
0.205	0.000184
0.211	0.00117
0.203	0.007
0.198	0.0397
0.141	0.277
0.0368	3.37
0.00423	61.6
0.000259	993
1e-09	11200
3.29e-05	73800

$G_0 = 289\ MPa$, $\nu = 0.5$

Table C.2: Prony series, virgin, 70-100 penetration grade binder tested at $10^{\circ}C$ (Mukandila, 2015).

α_i	τ_i
0.21011338196	0.00015429156207
0.32354521754	0.0010102797631
0.19033392566	0.0014622459289
0.22564549883	0.066270832627
0.045804250757	0.59925712574
0.0041367859138	2.3444762768
1e-11	43.665448455
0.00041944893924	381.30502231
4.9029588556e-07	141500.63027
1e-11	15615106.516

$G_0 = 106\ MPa,\ \nu = 0.5$

Table C.3: Prony series, virgin, 70-100 penetration grade binder tested at $25^{\circ}C$ (Mukandila, 2015).

α_i	τ_i
0.61	0.000519
0.258	0.00186
0.0692	0.00399
0.00147	0.0161
0.0591	0.0307
2.9e-05	0.0883
0.00147	0.366
0.000173	3.41
6.75e-05	7.9
3.67e-05	50.1

$G_0 = 23\ MPa,\ \nu = 0.5$

Table C.4: Prony series, virgin, 70-100 penetration grade binder tested at $50^{\circ}C$ (Mukandila, 2015).

α_i	τ_i
0.97766184622	8e-05
0.021774201028	0.00012828875883
0.00039370411001	0.0012662370378
3.3022437703e-05	0.0067861026796
2.5908972986e-05	0.037076616245
1e-10	0.054067525529
0.00010313280756	0.16435669895
6.4381004463e-07	1.8860586114
7.5365794557e-06	16.557223266
9.27599e-12	47962068.575

$G_0 = 5\ MPa,\ \nu = 0.5$

Table C.5: Prony series, virgin, 70-100 penetration grade binder, conditioned with water, tested at $25^{\circ}C$ (Mukandila, 2015).

α_i	τ_i
0.728621	5.752529e-05
0.2032632	0.0005172197
0.05687996	0.004041032
0.01008511	0.03555186
0.001083925	0.3885253
6.516656e-05	6.399511
1.141118e-06	250.5894

$G_0 = 76\ MPa,\ \nu = 0.5$

Table C.6: Prony series, PAV aged, 70-100 penetration grade binder, tested at $25^{\circ}C$ (Mukandila, 2015).

α_i	τ_i
0.4476917221	0.000110610966
3.614875381e-05	0.001057901076
0.4528717429	0.001287662667
0.05740246157	0.02765649197
0.0384009113	0.09030354094
0.0001761367602	1.094246679
0.001714198892	2.00046612
2.90790265e-05	2.995386551
0.001608671496	8.917241168
6.78171538e-05	120.9861701

$G_0 = 61\ MPa,\ \nu = 0.5$

Table C.7: Prony series, PAV aged, 70-100 penetration grade binder, conditioned with water, tested at $25^{\circ}C$ (Mukandila, 2015).

α_i	τ_i
0.415761842065	0.000111829514498
3.61509571399e-05	0.00105790768659
0.484304186548	0.00141920233124
0.054438957477	0.0290297789905
0.0422908925925	0.102885015583
0.000176835521583	1.09439195742
0.00177441261963	1.87329307441
2.90924507615e-05	2.99405024362
0.00112235962012	21.2390138518
6.52701478444e-05	117.646986764

$G_0 = 65\ MPa,\ \nu = 0.5$

Table C.8: Prony series, 3 years, 70-100 penetration grade binder, S2, BWT, tested at $25°C$ (Mukandila, 2015).

α_i	τ_i
0.538585	0.000384911
3.95819e-05	0.00105781
0.229869	0.00274007
0.194804	0.0369434
0.000226515	1.42145
0.0335606	1.44365
3.22459e-05	3.35106
0.000803169	15.5143
0.00198686	124.082
7.69161e-05	655.881

$G_0 = 122\ MPa,\ \nu = 0.5$

Table C.9: Prony series, 3 years, 70-100 penetration grade binder, S2, OWT, tested at $25°C$ (Mukandila, 2015).

α_i	τ_i
0.499082	0.000320128
3.961e-05	0.00105782
0.266981	0.00279149
0.205717	0.0280908
0.0265143	0.696643
0.000226318	1.41684
3.22255e-05	3.34848
0.000736889	14.4791
0.000600965	61.9013
6.74954e-05	614.97

$G_0 = 105\ MPa,\ \nu = 0.5$

Table C.10: Prony series, 4 years, 70-100 penetration grade binder, S4, SHDR, tested at $25°C$ (Mukandila, 2015).

α_i	τ_i
0.592645	0.000320037
3.96078e-05	0.00105782
0.214948	0.00278394
0.165352	0.0279277
0.0253516	0.69421
0.000226226	1.41681
3.22235e-05	3.34847
0.000599856	11.8457
0.000736721	14.4844
6.74331e-05	614.464

$G_0 = 79\ MPa,\ \nu = 0.5$

Table C.11: Prony series, 4 years, 70-100 penetration grade binder, S4, OWT, tested at 25°C (Mukandila, 2015).

α_i	τ_i
0.659708	0.000320048
3.96057e-05	0.00105782
0.175233	0.00278378
0.138856	0.0279211
0.000226154	0.506797
0.0244987	0.693897
3.2222e-05	0.748465
0.000599279	2.84422
0.000736442	14.482
6.73797e-05	400.04

$G_0 = 79\ MPa,\ \nu = 0.5$

Table C.12: Prony series, 5 years, 70-100 penetration grade binder, S2, BWT, tested at 25°C (Mukandila, 2015).

α_i	τ_i
0.574449	0.00060417
3.98984e-05	0.00105787
0.221275	0.00304273
0.170812	0.0287946
0.000231612	0.499725
0.031078	0.638169
3.23115e-05	0.747508
0.000657623	3.53288
0.00135841	30.4919
6.37049e-05	479.425

$G_0 = 75\ MPa,\ \nu = 0.5$

Table C.13: Prony series, 5 years, 70-100 penetration grade binder, S2, IWT, tested at 25°C (Mukandila, 2015).

α_i	τ_i
0.65238	0.000293381
3.96068e-05	0.00105782
0.18332	0.00279386
0.136768	0.027913
0.000226239	0.506929
0.0257958	0.725014
3.22244e-05	0.748514
0.000602612	2.8615
0.000763187	14.9964
7.09221e-05	416.588

$G_0 = 92\ MPa,\ \nu = 0.5$

Table C.14: Prony series, 6 years, 70-100 penetration grade binder, S2, BWT, tested at 25°C (Mukandila, 2015).

α_i	τ_i
0.515678	5.00066e-05
0.379519	0.00103558
3.96284e-05	0.0010578
0.00304059	0.0301167
0.0999172	0.0905705
0.000227816	0.504482
3.22259e-05	0.996148
0.000796798	16.2665
0.000675305	20.9456
7.13562e-05	412.208

$G_0 = 124\ MPa,\ \nu = 0.5$

Table C.15: Prony series, 6 years, 70-100 penetration grade binder, S2, IWT, tested at 25°C (Mukandila, 2015).

α_i	τ_i
0.644994	0.000202834
3.96395e-05	0.00105784
0.190812	0.0027862
0.13265	0.0259923
0.000226969	0.506091
0.0299631	0.564312
3.22355e-05	0.798296
0.000700732	13.8225
0.000515354	34.6947
6.38189e-05	389.548

$G_0 = 114\ MPa,\ \nu = 0.5$

Table C.16: Prony series, 9 years, 70-100 penetration grade binder, S4, BWT, tested at 25°C (Mukandila, 2015).

α_i	τ_i
0.650576	0.000202836
3.96392e-05	0.00105784
0.18753	0.00278625
0.130504	0.0259968
0.000226959	0.506093
0.029809	0.564759
3.22353e-05	0.798297
0.000700937	13.8287
0.000515735	37.7253
6.38918e-05	389.994

$G_0 = 114\ MPa,\ \nu = 0.5$

Table C.17: Prony series, 9 years, 70-100 penetration grade binder, S4, OWT, tested at 25°C (Mukandila, 2015).

α_i	τ_i
0.674347	0.000202934
3.96383e-05	0.00105784
0.172298	0.00278763
0.122461	0.0260187
0.000226929	0.506094
0.029312	0.564905
3.22347e-05	0.798297
0.000700961	13.8288
0.000515601	39.7264
6.38902e-05	389.999

$G_0 = 114\ MPa,\ \nu = 0.5$

Table C.18: Prony series, 9 years, 70-100 penetration grade binder, S4, IWT, tested at 25°C (Mukandila, 2015).

α_i	τ_i
0.674348	0.000202934
3.96383e-05	0.00105784
0.172298	0.00278763
0.122461	0.0260188
0.000226929	0.506094
0.029312	0.564906
3.22347e-05	0.798297
0.000700962	13.8288
0.000515602	39.7265
6.38903e-05	390

$G_0 = 113\ MPa,\ \nu = 0.5$

Table C.19: Prony series, 10 years, 70-100 penetration grade binder, S4, OWT, tested at 25°C (Mukandila, 2015).

α_i	τ_i
0.674125	0.000239551
3.96496e-05	0.00105786
0.167407	0.00285248
0.130201	0.0242176
0.000226831	0.505879
0.0267734	0.554638
3.22337e-05	0.798478
0.000704153	12.8837
0.00042733	59.1643
6.19156e-05	403.845

$G_0 = 110\ MPa,\ \nu = 0.5$

Table C.20: Prony series, 10 years, 70-100 penetration grade binder, S4, SHDR, tested at 25°C (Mukandila, 2015).

α_i	τ_i
0.669952	0.000202934
3.96385e-05	0.00105784
0.175035	0.00278764
0.124007	0.0260192
0.000226936	0.506094
0.029423	0.56497
3.22349e-05	0.798297
0.000701074	13.8297
0.000515868	69.7657
6.39016e-05	390.065

$G_0 = 115\ MPa,\ \nu = 0.5$

Table C.21: Prony series, 10 years, 70-100 penetration grade binder, S1, BWT, tested at 25°C (Mukandila, 2015).

α_i	τ_i
0.494264	0.000120142
3.98473e-05	0.00105734
0.350671	0.00171196
0.124292	0.045968
0.000256465	0.473244
3.26375e-05	0.788171
0.0256236	1.09674
0.00386728	17.83
0.000763457	161.663
0.000180322	2115.94

$G_0 = 89\ MPa,\ \nu = 0.5$

Table C.22: Prony series, 10 years, 70-100 penetration grade binder, S1, IWT, tested at 25°C (Mukandila, 2015).

α_i	τ_i
0.498816	0.00026416
3.98227e-05	0.0010575
0.349411	0.00337758
0.118791	0.0599806
0.000255849	0.474209
3.26334e-05	0.788498
0.0276574	1.39886
0.00400333	19.4972
0.000806298	165.882
0.00017527	1812.05

$G_0 = 74\ MPa,\ \nu = 0.5$

Table C.23: Prony series, virgin, CRS-60% emulsion at 25°C (Mukandila, 2015).

α_i	τ_i
0.753	7.46e-05
0.168	0.000738
0.000434	0.0018
0.0603	0.00495
0.0144	0.0396
0.00277	0.291
0.000429	2.36
5.66e-05	18.7
5.4e-06	213
2.32e-07	4240

$G_0 = 62\ MPa$, $\nu = 0.5$

C.2 Prony series response parameters of mortar

The viscoelastic response properties of virgin and aged mortar were translated into two term Prony series (Huurman and Woldekidan, 2007). Mortar responses were selected to represent slurries in the finite element modelling of cape seals. Mortar responses were therefore selected at $0°C$, $10°C$ and $20°C$. This section presents the mortar Prony series as pertaining to this study.

Table C.24: Prony series of virgin mortar at 0°C (Huurman and Woldekidan, 2007).

α_i	τ_i
0.7456	0.0192
0.1771	0.3693

$G_0 = 1873\ MPa$, $\nu = 0.45$

Table C.25: Prony series of virgin mortar at 10°C (Huurman and Woldekidan, 2007).

α_i	τ_i
0.9469	0.0162
0.025	0.3115

$G_0 = 1463\ MPa$, $\nu = 0.45$

Table C.26: Prony series of virgin mortar at $20°C$ (Huurman and Woldekidan, 2007).

α_i	τ_i
0.9734	0.0078
0.005	0.1499
$G_0 = 414\ MPa,\ \nu = 0.45$	

Table C.27: Prony series of aged mortar at $0°C$ (Huurman and Woldekidan, 2007).

α_i	τ_i
0.3996	0.0059
0.3598	0.0692
$G_0 = 1374\ MPa,\ \nu = 0.45$	

Table C.28: Prony series of aged mortar at $10°C$ (Huurman and Woldekidan, 2007).

α_i	τ_i
0.2493	0.001
0.6482	0.0114
$G_0 = 1018\ MPa,\ \nu = 0.45$	

Table C.29: Prony series of aged mortar at $20°C$ (Huurman and Woldekidan, 2007).

α_i	τ_i
0.1861	0.0006
0.7696	0.0069
$G_0 = 411\ MPa,\ \nu = 0.45$	

D. Miscellaneous

Miscellaneous sections are addressed in this appendix. It includes a brief summary on traffic wandering as discussed by Huurman (1997) and bitumen self-healing shift factors according to the work of Molenaar (2007).

D.1 Traffic wander

Real traffic will not travel exactly in one wheel track and as a result, a transverse distribution of the wheel loads will develop. For motorway traffic this phenomenon was investigated by the Road and Hydraulic Engineering Division of the Dutch Ministry of Transport and Public Works (Huurman, 1997). The research indicated that the measured lateral wheel shift patterns can be described by normal distributions. The standard deviation of the normal distributions depends amongst other things heavily on the lane width as presented in Table D.1. Considering that the typical 12R22.5 HV tyre has a 200 mm contact width, calculations with regard to the number of wheel passes over a unique point per lane with can easily be determined.

Table D.1: Cohesive failure validation traffic volumes and growth rates.

Lane width [m]	Standard deviation of lateral wander [m]
3.00	0.24
3.25	0.26
3.50	0.29

D.2 Self-healing

Self-healing of an asphalt mixture has to do with the fact that asphalt mixtures have the capacity to repair themselves. This self repair mechanism occurs when the material is not subjected to loading. It has been shown that the ratio between the rest period and loading period is important. If this ratio is at approximately 20,

the self repairing capacity has reached its maximum (Molenaar, 2007). Furthermore, self-healing depends on the amount and type of bitumen used in the mixture. It can be shown that the maltene phase of bitumen is responsible for self-healing, implying that softer bitumens show better healing performance than harder bitumens. Figure D.1 illustrates the effect of the amount of bitumen on self-healing and the effect of rest periods for the type of bitumen.

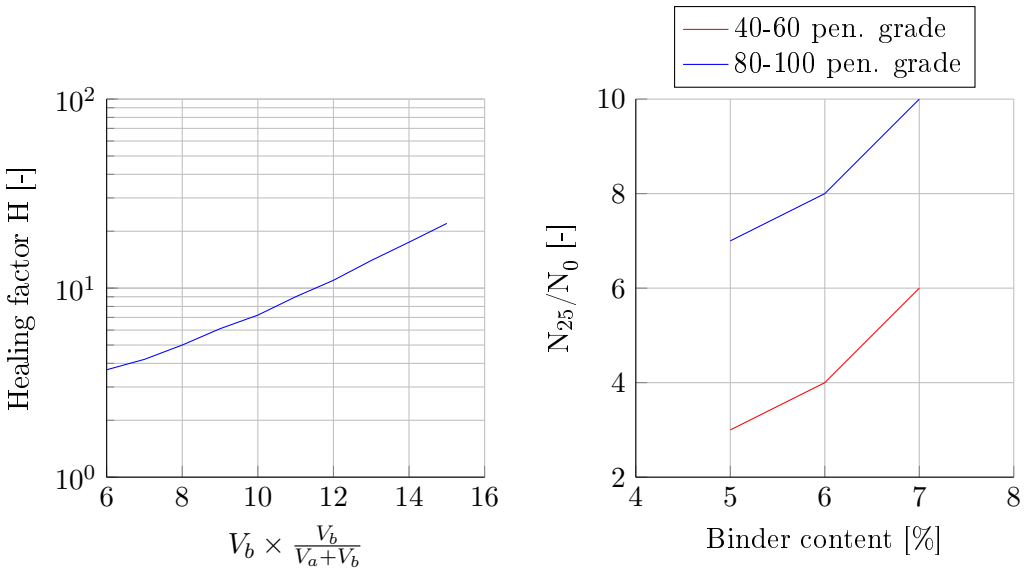

Figure D.1: Self-healing adjustment factors: Effect of the amount of bitumen (left); Rest period, bitumen content and type of bitumen in asphalt mixtures (right).

The term $V_b \times \frac{V_b}{V_a+V_b}$ as used in Figure D.1 is known as the degree to which voids are filled in the aggregate skeleton with bitumen. Figure D.1 was developed from data obtained on four mixtures which included bitumens with penetration values ranging from 47 to 80. Figure D.1 is based on fatigue data from Shell, where N_0 indicates the number of load repetitions to failure when no rest periods are applied (Molenaar, 2007). N_{25} indicates the number of load repetitions to failure with a rest period : loading period ratio of 25.